

Morphology, fragmentation, and  
dynamic balance: an investigation into  
early stages of structure formation in  
molecular clouds

INAUGURAL-DISSERTATION

zur  
Erlangung des Doktorgrades  
der Mathematisch-Naturwissenschaftlichen Fakultät  
der Universität zu Köln



vorgelegt von

**Shashwata Ganguly**  
aus Kolkata, Indien

Köln, 2022

Berichterstatter (Gutachter):  
Prof. Dr. Stefanie Walch-Gassner  
Prof. Dr. Peter Schilke

Vorsitzender der Kommission:  
Prof. Dr. Susanne Crewell

Tag der mündlichen Prüfung:  
30. Mai 2022

*Für meine Eltern*



## ABSTRACT

---

How molecular clouds fragment and create the dense structures which go on to eventually form stars is an open question. This thesis numerically investigates various aspects of fragmentation and structure formation in young molecular clouds based on the SILCC-Zoom and SILCC deep-zoom simulations. The SILCC-Zoom simulations follow the self-consistent formation of molecular clouds in a few hundred parsec sized region of a stratified galactic disc, which include (self-) gravity, magnetic fields, supernova driven turbulence, as well as a non-equilibrium chemical network and treatment of the interstellar radiation field, with resolutions of  $\sim 0.1$  parsec. The SILCC deep-zoom simulations are an extension of the cloud scale SILCC-Zoom simulations and allow us to resolve structures with a maximum resolution of 0.0078 parsec ( $\sim 1600$  AU). We identify 3D volumes inside the simulated clouds as structures using dendrograms and analyze their behaviour. By considering the energetic balance of cloud scale sub-structures, we find that our molecular clouds are dominated by the interplay of turbulence and self-gravity - with self-gravity becoming dynamically dominant only over time. This supports the gravo-turbulent scenario of structure formation. By tracing the morphology of cloud scale structures, we evaluate our clouds to be sheet-like on larger scales, likely tracing the shells of bubbles driven by supernovae. We estimate the effect of magnetic fields in molecular clouds and their atomic envelopes and find that magnetic fields alter the nature of fragmentation at low densities, slow down the formation of denser structures, but do not seem to be dynamically important in the further evolution of these potentially star forming sub-structures. We extend the study of energetics and morphology to sub-pc scale structures using the novel SILCC deep-zoom simulations. We find different methods of forming filaments - fragmentation of mostly self-gravitating structures, as well as shock compression. Moreover, we find that gravitationally bound, spheroidal cores emerge at  $\sim 0.1$  parsec scales and are embedded inside gravitationally dominated filaments.

# CONTENTS

1	INTRODUCTION	1
1.1	Composition of the ISM	3
1.2	Physics of the ISM	5
1.2.1	Phases of the ISM	5
1.2.2	Heating and cooling processes	6
1.2.3	Turbulence	8
1.2.4	Magnetic fields	10
1.3	Molecular clouds	14
1.3.1	Cloud formation	16
1.3.2	Cloud evolution and star formation	18
1.3.3	Cloud destruction	23
2	METHODOLOGY	26
2.1	Magneto-Hydrodynamics	26
2.1.1	Assumptions of ideal MHD	26
2.1.2	Equations of ideal MHD	27
2.1.3	Limitations	28
2.1.4	Description of shocks	29
2.2	FLASH 4	30
2.3	Simulation setup	33
2.3.1	SILCC	33
2.3.2	SILCC-Zoom	35
2.3.3	SILCC deep-zoom	36
2.4	Analysis method	37
2.4.1	Structure identification and classification	39
2.4.2	Gravity tree	42
2.4.3	Virial analysis	43
2.4.4	Tidal analysis	48
3	THE RESEARCH	51
4	SILCC-ZOOM: THE DYNAMIC BALANCE IN MOLECULAR CLOUD SUBSTRUCTURES (PAPER I)	53
5	UNRAVELLING THE STRUCTURE OF MAGNETIZED MOLECULAR CLOUDS WITH SILCC-ZOOM: SHEETS, FILAMENTS AND FRAGMENTATION (PAPER II)	74
6	SUB-STRUCTURES IN SILCC DEEP-ZOOM	91
6.1	The scope of the deep-zoom simulations	91
6.2	General overview	93

---

6.3	Virial analysis	96
6.3.1	Structures dominated by kinetic energy	96
6.3.2	Structures dominated by thermal energy	97
6.3.3	Structures dominated by magnetic energy	99
6.3.4	Structures dominated by gravitational energy	100
6.3.5	Virial balance	102
6.4	Morphology of structures	104
6.4.1	Cores	106
6.4.2	Filaments	110
6.5	Summary	117
7	SUMMARY AND CONCLUSION	<b>119</b>
7.1	Summary	119
7.2	Conclusion	121
7.3	Outlook	122
A	APPENDIX	<b>124</b>
A.1	Distance measure for uniformly accreting ideal filaments	124
	ABBREVIATIONS	<b>126</b>

# List of Figures

1	Image of the star forming region Orion B in optical (left) and far-infrared (right). . . . .	2
2	Map of the planar magnetic field toward the molecular cloud Taurus, from <a href="#">Planck Collaboration et al. (2016)</a> . . . . .	12
3	Snapshot of the SILCC simulations, adapted from <a href="#">Walch et al. (2015)</a> , Fig. 4. Part of the simulation box of size $0.5 \text{ kpc} \times 0.5 \text{ kpc} \times 2 \text{ kpc}$ , is shown. The panels show, from left to right, gas density slice, column density projection, gas temperature slice, and column densities of $\text{H}^+$ , $\text{H}$ and $\text{H}_2$ , and $\text{CO}$ . All slices are taken at $y = 0$ for the elongated panels, or at $z = 0$ for the square panels, respectively. Similarly, the column density is projected along the $y$ - or $z$ -axis. . . . .	34
4	SILCC-Zoom cloud MC1-MHD at $t_{\text{evol}} = 3 \text{ Myr}$ , from different viewing angles. Adapted from Fig. 2 of <a href="#">Seifried et al. (2019)</a> . . . . .	37
5	The length scales of the SILCC, SILCC-Zoom, and the SILCC deep-zoom simulations. <b>Left:</b> A $500 \times 500 \text{ pc}$ region of the SILCC disc shown as a projection with the deep-zoom region MC1-MHD highlighted as a black outlined box. <b>Middle:</b> A $50 \times 50 \text{ pc}$ portion of the SILCC-Zoom region MC1-MHD with part of a deep-zoom region shown. <b>Right:</b> A typical $4 \times 4 \text{ pc}$ deep-zoom portion used for analysis. Note that the actual deep-zoom region is much larger compared to the right box shown. . . . .	38
6	Relation between the simulation start time $t$ , SILCC-Zoom evolution time for the two deep-zoom clouds $t_{\text{evol}}$ and the deep-zoom evolution time $t_{\text{deep}}$ . . . . .	38
7	Left: Cartoon illustration of a hypothetical 2D intensity distribution. Right: The resulting dendrogram tree. The large-scale, low intensity structure is picked up as a trunk. Further nested branches show the hierarchical nature of the structure. Structures which contain no further sub-structures are called leaves. Both figures adapted from the <a href="#">astrodendro</a> website. . . . .	39
8	Relation between $\alpha_{\text{vir}}$ and $\Theta_{\text{VT}}$ , adapted from <a href="#">Dib et al. (2007)</a> . . . . .	47
9	Projection of the SILCC deep-zoom clouds . . . . .	93
10	Projected view of different analyzed regions from the SILCC deep-zoom simulations . . . . .	94
11	Gradual refinement of the right region for the cloud MC1-MHD, projected along the $x$ -axis . . . . .	95
12	Two examples of kinetically bound structures from SILCC deep-zoom . . . . .	98
13	$\rho_{\text{thr}}$ vs size $R$ (left) and mean temperature distribution of (right) all deep-zoom structures . . . . .	98



14	Two examples of magnetically confined structures from SILCC deep-zoom . . . . .	100
15	Two examples of self-gravity dominated structures from SILCC deep-zoom . . . . .	101
16	$\rho_{\text{thr}}$ vs size $R$ for only the gravity dominated leaf structures and their parent structures for MC1-MHD-Ra (left) and MC1-MHD-Rc (right) .	102
17	Two examples of external gravity dominated structures from SILCC deep-zoom . . . . .	103
18	The absolute value of the virial ratio for SILCC deep-zoom regions . .	103
19	The cumulative distribution of the types of structures, plotted against $\rho_{\text{thr}}$ (left), and against $R$ (right) . . . . .	105
20	Two examples of small scale core-like structures from SILCC deep-zoom . . . . .	106
21	Family tree of core-like structures and their parents . . . . .	107
22	$\dot{M}$ against $M$ (left), and ratio of $\dot{M}$ to $\dot{M}_{\text{Bondi}}$ (right) for core-like structures . . . . .	108
23	Fraction of surface cells with inflowing mass for MC1-MHD-Ra (left) and MC1-MHD-Rc (right) . . . . .	109
24	Mass-length relation for all (left) and only gravity dominated (right) deep zoom filaments at $t_{\text{deep}} = 0.8$ Myr. The dotted line represents $l_{\text{fil}} \propto M^{1/2}$ . The dashed line represents the best fit in each case. . . . .	111
25	Line mass, critical line mass and temperature distribution of filamentary structures in SILCC deep-zoom . . . . .	113
26	$\dot{\lambda}_{\text{fil}}$ vs $\lambda_{\text{fil}}$ for all accreting filaments ( $\dot{\lambda}_{\text{fil}} > 0$ ). The dotted lines represent different constant $\tau_{\text{acc}}$ . The gravity dominated filaments accrete at a higher rate, and the accretion timescale for all the structures is around $\tau_{\text{acc}} \sim 0.1$ Myr, with considerable scatter. . . . .	113
27	Cumulative PDF of the distance measure $d_S$ for different accreting SILCC deep-zoom filaments . . . . .	115
28	Two panels from Fig. 8, bottom panel, in <b>paper I</b> showing the evolution of $\alpha_{\text{vir}}^{\text{vol}}$ (Eq. 2.58) for MHD sub-structures at $t_{\text{evol}} = 2$ Myr (top) and 3.5 Myr (bottom). Bound structures appear over time below the $\alpha_{\text{vir}}^{\text{vol}} = 1$ line. . . . .	119
29	Panel from Fig. 4 in <b>paper II</b> showing the 3D view of the sheet-like nature of the cloud MC1-MHD (in blue) and a prominent filamentary structure inside (in red). . . . .	120

## INTRODUCTION

---

Do stars form at all? If so, how do they form? Such questions have been at the heart of astronomy since antiquity. In the old worldview, stars were heavenly bodies, not subject to change under the influence of mere physical forces. That stars can form, and that they are forming even today, is a relatively recent discovery, and one that needed a significant shift in our perspective of the universe and our place in it.

Even until the early 1950s, the prevailing idea was that all star formation occurred shortly after the beginning of the universe and that stars are not really forming today. A number of key observations changed this world view and led to field that we call star formation.

One of the first clues that stars might still be forming in today's universe came about due to the work of Viktor Ambartsumian in 1949, where he estimated the age of a certain type of star cluster called OB clusters ([Ambartsumian, 1949](#)). He found that the cluster age was only  $\sim 10^6$  years, far less compared to the then perceived age of the universe,  $10^9$  years. This suggested that there must at least be some stars that formed relatively recently.

For the first direct observations of a forming star, however, we would have to wait almost twenty further years. In 1967, Becklin & Neugebauer found an infrared black body source in the Orion nebula that had no optical counterpart ([Becklin & Neugebauer, 1967](#)). This was the first direct sign of a star currently forming and opened up a wide range of observational and theoretical avenues to study the conditions and processes of star formation. We took a step forward, moving from wondering whether stars are forming at all, to investigating how they come about.

Today, we know that stars form from interstellar gas - a medium that permeates the space between stars, typically called the interstellar medium (ISM). On the face of it, the contrast in density and temperature between a star and the interstellar medium is huge - interstellar gas has an average number density of  $\sim 1 \text{ cm}^{-3}$ , while our sun, for example, has the average number density of around  $\sim 10^{23} \text{ cm}^{-3}$ , comparable to water. The problem of understanding star formation is to understand the relation between the rare and multi-faceted interstellar medium and the stars that form inside it.

A particularly important clue to this puzzle can be obtained from studying a certain phase of the ISM - called molecular clouds (MCs). Molecular clouds are regions of cold, dense ( $\gtrsim 100 \text{ cm}^{-3}$ ) gas that act as nurseries of newly born stars. In optical observations, they typically appear as dark patches in the sky. The newly forming stars are embedded inside these gaseous clouds and are therefore hard for us to observe in their early forming stages.

An example of such a molecular cloud region is shown in Fig. 1, which shows the optical (left) and far-infrared observations of the Orion B molecular cloud region. In the optical image, the Orion nebula at the top half of the picture catches the eye immediately. However, below it we can see dark lanes where no stars are visible. In longer wavelengths, these dark patches reveal the dense structure of dust and gas in these regions.



Figure 1: Image of the star forming region Orion B. **Left:** optical image obtained from DSS2 data from European Southern Observatory. **Right:** Herschel far infrared observations of the same region. Both maps were obtained through [ESA skymap](https://sky.esa.int)<sup>1</sup> of the European Space Agency. The optical image shows dark patches where no stars are visible, which reveal rich, complex dust lanes in far infrared wavelengths. The Orion nebula is visible at the top part of the image.

In this thesis, we attempt to investigate the structures that form inside a molecular cloud which will go on to eventually form stars. By analyzing the early stages of structure formation in simulated molecular clouds, this thesis will attempt to answer the following principal questions:

- What is the relative importance of different dynamical forces (gravity, turbulence, magnetic fields etc.) in terms of structure formation inside molecular clouds?
- How does the presence of magnetic fields affect the morphology and fragmentation of the medium?
- How are these dynamical and morphological properties related from larger cloud-scale (tens of parsecs) to smaller core-scale (sub parsec) sub-structures?

The remainder of this thesis is structured to provide the background to these questions, formulate them in a more nuanced manner, and to answer these as well as other subordinate questions that arise from the attempt to answer them.

In **Chapter 1**, we introduce the interstellar medium, and its relation to molecular clouds and the formation of stars. The components of the ISM are described in Section 1.1. We then move on to describe the relevant physical processes for our purpose in Section 1.2. This includes description of the different states of the ISM and how they are maintained (Section 1.2.1 and 1.2.2); detailed discussion on the roles of turbulence (Section 1.2.3) and magnetic fields (Section 1.2.4). After discussing the physics that governs the ISM, we delve into how they are combined in the

---

<sup>1</sup><https://sky.esa.int>

formation, evolution, and eventual destruction of molecular clouds (Section 1.3). In each stage we will attempt to connect the discussions back to the initial questions we have already formulated.

We elaborate on the methods used to model and analyze the physics of the simulations in **Chapter 2**. In Section 2.1, we dwell on the equations of ideal magnetohydrodynamics (MHD), including the assumptions that go into them as well as their limitations. This is paramount as all the simulations in this thesis are based on solving the equations of ideal MHD, and understanding the limitations of our equations helps us understand the limitations of our simulations. In Section 2.2, we highlight the details of the code FLASH used for the simulations. Section 2.3 describes the simulation setups themselves. We detail the methods used to analyze the simulations in 2.4.

**Chapters 3** through **6** provide the main results of this thesis. Chapter 3 connects the introduction and methods to the results, highlighting the key points for the two papers included in this thesis. The two papers are included in Chapter 4 and 5, respectively, and relate to the first two of the three questions highlighted above. Paper I investigates the dynamic balance between different force terms, while paper II looks at the role of magnetic fields. Chapter 6 investigates the physics of molecular clouds at sub-parsec scales, and attempts to relate it to the physics of the ISM at cloud scales.

Finally, we present the summary and conclusion of this work, as well as its future outlook in **Chapter 7**.

## 1.1

### COMPOSITION OF THE ISM

#### *Gas*

From the standpoint of earth, the space between stars can seem empty. The density of particles in the solar system is far lower than the best vacuums we can create on earth. However, the vast expanse of the Galaxy means that the apparently "empty" space can add up to have a significant amount of mass. The total gas mass in the Milky Way is estimated to be close to  $10^{10} M_{\odot}$  (Kalberla & Kerp, 2009). Of this vast reservoir of gas, mass wise roughly 70% is in the form of hydrogen, 28% as helium, and all the other heavier elements (typically called 'metals') contribute to the other 2% (Draine, 2011).

Hydrogen is the most abundant element in the universe, and therefore also in the ISM. Ionized hydrogen ( $H^+$ ) fills most of the volume of the galaxy, with a volume filling fraction of 0.64, while atomic (H) and molecular ( $H_2$ ) forms have volume filling fractions of around 0.31 and 0.05, respectively (Spitzer, 1978; Tielens, 2005). If we look at the mass distribution, however, the picture is quite different. Around 60% of hydrogen mass is in its atomic form, while 23% is in ionized, and 17% in the molecular state (Draine, 2011).

The metals, although 2% in terms of mass, hold significant sway over the thermal processes in the ISM. The metals are produced in stars, in complex thermonuclear processes, and are ejected into the interstellar medium through stellar winds, as well as in explosive events such as supernovae. The metallicity in the ISM generally increases over cosmic time as more and more stars form, while there are also significant deviations in the ISM of a single galaxy. For the Milky Way, the metallicity in the central bulge of the Galaxy (the so called Central Molecular Zone or CMZ)

is twice the value of that in the solar neighbourhood (Ferrière et al., 2007), while further away in the outer galaxy, it is sub-solar (Rudolph et al., 2006).

#### *Dust*

We can estimate the amount of metals produced by stars, for example, by studying the spectra of B-type stars (e.g. Rolleston et al., 2009). On the other hand, we can determine the amount of metals available in the ISM in their elemental form from ultraviolet (UV) absorption lines. Comparing the two values, we arrive at the conclusion that most heavy elements are depleted from the gas phase. This can be explained by assuming that much of the heavier elements are bound in the form of interstellar ‘dust’ - solid particles made of metals, usually of size 5-250 nm (Draine & Lee, 1984; Weingartner & Draine, 2001). The dust contribution to the total mass in the ISM is estimated to be  $\sim 1\%$  of the total gas mass (Hildebrand, 1983; Klessen & Glover, 2016).

#### *Radiation field*

The thermal and chemical state of the interstellar gas is controlled largely by the interaction of both gas and dust with the interstellar radiation field (ISRF). The ISRF is a combination of various radiation contributions, which we summarize here from Draine (2011):

- The **cosmic microwave background** represents the relic radiation from the early stages of the universe, and in the present day corresponds to a black body temperature of 2.725 K (Fixsen & Mather, 2002). It dominates the ISRF at wavelengths between 600  $\mu\text{m}$  and 30 cm.
- The **infrared dust emission** is the reprocessed radiation emitted by dust grains (from absorbing starlight, for example), and dominates the ISRF between roughly 5  $\mu\text{m}$  and 600  $\mu\text{m}$ , in the infrared and far-infrared regime.
- **Starlight** makes important contribution to the ISRF in the visible, as well in the near-infrared and the soft ultraviolet (UV) wavelengths (roughly between 0.09 – 1.25  $\mu\text{m}$ ). Energetic photons from massive stars can also create ionized bubbles in the dense ISM and affect their dynamics.
- **Nebular emission**, corresponding to the continuum obtained from bound-bound, bound-free and free-free emissions from warm ionized plasma at temperatures  $\sim 10^4$  K
- **X-ray** emission from hot plasma at temperatures  $\sim 10^5$  K or above, typically from supernovae remnants or X-ray binaries
- **Galactic synchrotron emission** in radio wavelength from relativistic electrons

Since we are interested in the hydrogen chemistry, of particular interest to us is the strength of the radiation field in the ultraviolet regime. This is typically represented by  $G_0$ , the radiation field strength in 4-13.6 eV regime (13.6 eV is the ionization energy of the H atom). In the solar neighbourhood conditions,  $G_0 = 1.7$  in Habing units, where 1 Habing unit =  $5.29 \times 10^{-4}$  erg  $\text{cm}^{-3}$  (Draine, 1978).  $G_0$ , however, is highly localized and varies widely.

*Magnetic fields*

Magnetic fields are an important component of the ISM, and affect gas dynamics by channeling gas flow, acting as a preventive pressure term, redistributing angular momentum, and significantly affecting the behaviour of charged energetic particles such as cosmic rays (see, e.g. [Crutcher \(2012\)](#) for a general review, also see below). They are an integral part of the investigations performed in this thesis, and are explored in greater detail in Section 1.2.4.

*Cosmic rays*

The final important component of the ISM is cosmic rays. Cosmic rays are relativistic particles, with energies from 100 MeV to more than 1 TeV. They are composed of  $\sim 1\%$  relativistic electrons,  $\sim 1\%$  metal nuclei,  $\sim 10\%$  alpha particles, while the remaining are mostly energetic protons ([Draine, 2011](#)). Their energy density is comparable to the mean thermal energy in the ISM, making them important contributors to the energy balance of interstellar gas. Cosmic rays are mostly tied to the local magnetic field, resulting in repeated scattering in the galactic disk. They are usually treated as a fluid with a uniform energy density. Cosmic rays can penetrate deep into the dense parts of the ISM, and interact with molecular gas to produce ions, thereby maintaining charged particles in a mostly neutral environment.

One remarkable result of the different energetic components of the ISM is that cosmic rays, the ISRF, and the kinetic, thermal, and magnetic energy of the gas are all remarkably in rough energetic equipartition. This implies that none of the components can simply be ignored as irrelevant. A summary of the energy densities of the different components in the ISM can be found in Table 1.1.

Component	Energy density ( $\text{erg cm}^{-3}$ )
Cosmic microwave background	$4.2 \times 10^{-13}$
Dust far infrared	$5.0 \times 10^{-13}$
Starlight (photon energy $< 13.6$ eV)	$8.6 \times 10^{-13}$
Nebular emission (bound-free, free-free, bound-bound)	$6.3 \times 10^{-15}$
Soft X-rays	$10^{-17}$
Synchrotron	$2.7 \times 10^{-18}$
Magnetic fields	$1.4 \times 10^{-12}$
Cosmic rays	$2.2 \times 10^{-12}$
Thermal energy	$7.8 \times 10^{-13}$
Kinetic energy	$3.5 \times 10^{-13}$

Table 1.1: Energy densities in the ISM. Adapted from [Klessen & Glover \(2016\)](#) and [Draine \(2011\)](#). Thermal and kinetic energies refer to the gas component of the ISM.

## 1.2

## PHYSICS OF THE ISM

## 1.2.1

## PHASES OF THE ISM

We have described above the components that make up the ISM. An often useful description of the ISM is to describe it in terms of different phases. [Field et al.](#)

(1969) proposed that if we assume the interstellar gas to be atomic and in thermal equilibrium, then there exist two stable solutions: warm, diffuse gas at temperatures of  $\sim 10^4$  K (now identified as warm neutral medium or WNM) and cold, dense gas at temperatures of  $\sim 100$  K (cold neutral medium or CNM). These two phases would be in pressure equilibrium, and any intermediate gas would either heat up to the WNM or cool down and become denser to the CNM phase.

McKee & Ostriker (1977) pointed out that supernova explosions must create large swathes of ionized volume, violating the assumption of charge neutrality in the original two-phase model. This led to the third quasi-stable phase of hot ionized gas (called hot ionized medium or HIM) at temperatures of around  $10^6$  K. The gas between  $10^6$  and  $10^4$  K has a much shorter cooling time compared to the HIM, setting the temperature of the HIM at  $\sim 10^6$  K.

Additionally, observations such as the dispersion of radio signals from pulsars (Reynolds, 1989; Gaensler et al., 2008), free-free absorption of the galactic synchrotron background (Hoyle & Ellis, 1963), and optical emission lines of  $O^+$  and  $N^+$  (Reynolds et al., 1973; Mierkiewicz et al., 2006) posited the existence of warm ionized medium (WIM). Gas in the WIM is typically ionized through collisions. The WIM has a density comparable to the WNM, and becomes increasingly important away from the galactic midplane. Haffner et al. (2009) show that nine tenths of the ionized gas in the galaxy is indeed located in the WIM phase.

Furthermore, the cold neutral medium is often separated between the atomic neutral medium, and the cold, dense, molecular gas hosted in regions called molecular clouds. Such molecular clouds are distributed in clumps in the Galaxy. For the Milky Way, they are most prominent in the central molecular zone, as well as along the spiral arms. A summary of the basic properties of the different phases of the ISM can be found in Table 1.2.

Phase	Temperature (K)	Density ( $\text{cm}^{-3}$ )	Ionization fraction
Molecular cloud	10-20	$>10^2$	$< 10^{-5}$
Cold neutral medium (CNM)	50-100	20-50	$\sim 10^{-4}$
Warm neutral medium (WNM)	6000-10000	0.2-0.5	$\sim 0.1$
Warm ionized medium (WIM)	$\sim 8000$	0.2-0.5	1.0
Hot ionized medium (HIM)	$\sim 10^6$	$\sim 10^{-2}$	1.0

Table 1.2: Different phases of the ISM. Adapted from Klessen & Glover (2016), based on Ferrière (2001), Caselli et al. (1998), Wolfire et al. (2003), and Jenkins (2013).

Owing to the fact that the ISM is a highly turbulent system out of equilibrium, there also exists a significant amount of gas in between the different phases, i.e. in thermally unstable regimes (see e.g. Seifried et al., 2011).

### 1.2.2

#### HEATING AND COOLING PROCESSES

The ISM phases differ in temperature, in ionization state of different elements, and even in elemental abundance. This naturally leads to quite different heating and cooling mechanism dominating in the different regimes. This is relevant for modelling the significant dynamic range of the ISM and setting the thermodynamic balance in numerical simulations. For more extensive details on the heating and cooling mechanisms, see, for example, section 3 of the review by Klessen & Glover (2016).

### Heating

**Photoelectric heating:** UV photons hitting dust grains in the ISM can eject electrons. The energy of such an electron equals the difference in energy of the incident photon with the energy barrier of the dust grain. This energy is then quickly distributed among the atoms and molecules near the dust grain as heat (Bakes & Tielens, 1994; Wolfire et al., 2003).

**Photodissociation of H<sub>2</sub>:** Incident UV rays can also dissociate H<sub>2</sub> molecules into atoms. The resulting atoms have a higher kinetic energy than that of the mean kinetic energy of the gas particles, which is then redistributed among other atoms or molecules in terms of heat through collisions. Averaged over such possible dissociative transitions, this inputs  $\sim 0.4$  eV energy per dissociation into the gas. (Black & Dalgarno, 1977)

**UV pumping:** An H<sub>2</sub> molecule absorbing a UV photon can decay radiatively back into the ground state. In denser gas ( $\gtrsim 10^4$  cm<sup>-3</sup>), the collisional de-excitation timescale is shorter than the radiative decay timescale, causing this energy to be redistributed as heat (Burton et al., 1990).

**Cosmic rays:** In well shielded gas, the ISRF is weak and a significant contribution to heating is provided by cosmic rays. Cosmic rays can penetrate deep into the dense ISM, and in collisions with atoms or molecules, typically impart a larger energy than simply their dissociation energy (Glassgold & Langer, 1973).

**X-rays:** X-rays provide heating in the ISM in a manner very similar to cosmic rays, by depositing kinetic energy in the gas. This is important in regions near to X-ray sources (for example, X-ray binaries or active galactic nuclei), as well as in the diffuse ISM.

**H<sub>2</sub> formation:** The formation of H<sub>2</sub> releases 4.48 eV energy per molecule. This energy, stored initially as an excited rotational or vibrational state of the molecule, can be redistributed through collisions and provide an important source of heating in rapidly H<sub>2</sub> forming regions. (Goldsmith & Langer, 1978)

**Dynamical heating:** Adiabatic compression caused by gravity or shocks can be a significant source of heating by converting bulk kinetic energy of the gas into random thermal motions, i.e. heat.

### Cooling

**Dipole transitions:** At high temperatures, in atomic or ionized gas, dipole-allowed electronic transitions are an important source of cooling. At around a temperature of  $10^4$  K, the Lyman- $\alpha$  cooling, where electrons return to the Hydrogen ground state by emitting a UV photon, dominates. At higher temperatures, cooling due to metals such as C, O, Ne and Fe become more important (Gnat & Ferland, 2012).

**Fine structure transitions:** Spin-orbit coupling for atoms and ions can cause small differences between energy levels that would otherwise have been degenerate (Atkins



& Friedman, 2010). These energies are typically of the order of  $10^{-2}$  eV, corresponding to temperatures of the order of 100 K. Therefore, even in temperatures below  $10^4$  K, when electronic transitions become rare, such fine structure transitions can occur and cool the gas. Since hydrogen and helium have no fine structure splitting in their ground states, such transitions are dominated by transitions of carbon and oxygen (Wolfire et al., 1995). The spontaneous transition rates for such transitions are, however, much smaller than the electric dipole transitions mentioned above.

**Molecular H<sub>2</sub>:** Hydrogen is the most abundant element in the universe. However, the spacing between different rotational energy levels of Hydrogen are relatively high ( $\Delta E/k_B \approx 170J$  K, for small rotational quantum number  $J$ ). Further, transitions from even to odd  $J$  states (and vice versa), called para-hydrogen and ortho-hydrogen states, respectively, are strongly forbidden. The first permitted rotational transition therefore corresponds to  $J = 2 \rightarrow 0$ , and has a  $\Delta E/k_B \approx 510$  K. This results in molecular H<sub>2</sub> cooling becoming unimportant for temperatures less than around 100 K. However for temperatures above 100 K, particularly in shock-heated molecular gas, molecular H<sub>2</sub> can act as an important coolant (Hollenbach & McKee, 1979, 1989).

**HD cooling:** Hydrogen deuteride (HD), although significantly less abundant compared to H<sub>2</sub>, can act as an important coolant in low temperatures. It has permitted transitions between rotational level  $J = 1$  and  $J = 0$ , and a smaller energy separation between rotational levels ( $\Delta E/k_B = 128$  K for  $J = 1$  to  $J = 0$ ). This results in HD becoming a better coolant than H<sub>2</sub> below 50 K, despite having  $10^4$  times smaller abundance (see e.g. Klessen & Glover, 2016).

**CO cooling:** CO has a low energy separation between its different rotational energy states. In molecular clouds, carbon often does not exist in neutral or ionized form, but is captured into CO, stopping the fine structure cooling mechanism described above. CO therefore often provides an important source of line cooling via rotational transitions. However, in dense regions of molecular clouds CO is often optically thick and cannot cool efficiently, or gets "frozen out" onto dust grains (Kramer et al., 1999; Goldsmith, 2001).

**Dust cooling:** Individual dust grains can efficiently radiate across the infrared continuum, and therefore help in cooling (see e.g. Leung, 1975). The temperature of dust grains is then determined by the balance of this cooling rate, and the heating caused by the incident ISRF. The dust is also coupled to the gas through collisions. Therefore, differences between the dust and gas temperature result in an energy flow between the gas and the dust. If the dust temperature is lower, this transfers heat energy from the gas to the dust, which is then radiated away, causing cooling. Below number densities of  $\sim 10^5$  cm<sup>-3</sup> in solar metallicity conditions, the coupling is weak enough to see this effect (Hollenbach & McKee, 1989; Goldsmith, 2001).

### 1.2.3

#### TURBULENCE

The different phases of the ISM are maintained by the heating and cooling balance discussed above. However, the different phases do not strictly exist in isolation, but are continuously mixed by turbulence in the gas. Thermal instabilities and stellar

feedback support and sustain turbulence (see also below for sources of turbulence). In the context of the present thesis, turbulence provides the primary source of kinetic energy, and the compressive velocity fluctuations can confine structures. We discuss here some general theory, and key observations related to turbulence.

### *General theory*

The interstellar medium is in a chaotic state, defined by a high Reynolds number ( $\sim 10^5 - 10^7$  in the cold ISM, as estimated by [Elmegreen & Scalo \(2004\)](#)), and great variations in density and pressure over both spatial and temporal scales. Such a behaviour is characteristic of a turbulent medium. Despite the chaotic nature, it is indeed possible to describe the velocities and energies of a turbulent medium in terms of spatial correlation in velocity and energy. The first theory of turbulence was described by [Kolmogorov \(1941\)](#), which describes the motion of fluids in isotropic, incompressible (where fluid velocities are smaller compared to their thermal velocities) turbulence. In the Kolmogorov theory of turbulence, the kinetic energy has a power law behaviour of the form  $E(k) \propto k^{-n}$  ( $k = 2\pi/l$  being the wave number, where  $l$  is the length scale) in the so called "inertial range", between a large scale injection scale and a small scale dissipation scale. For Kolmogorov turbulence,  $n = 5/3$ . The injection scale is the length scale at which energy is injected into the system, and the dissipation scale is where viscous dissipation converts the turbulent kinetic energy into heat. In the inertial range, larger turbulent eddies break down into smaller eddies as the energy injected into the system cascades down to smaller and smaller scales, right down to where the turbulent eddies are dissipated due to viscosity in the fluid.

The Kolmogorov theory of turbulence describes incompressible, isotropic fluids. In the interstellar medium, we often get velocities larger than the sound speed (Mach number  $\mathcal{M} > 1$ ), where the incompressible assumption does not apply. The high Mach number causes shocks, which dissipates the turbulent energy into heat. If the thermal pressure is negligible, the system of fluid can be described by a network of overlapping shocks. This state, called Burgers turbulence, has a power law of the form  $E(k) \propto k^{-2}$ . The steeper power law reflects that energy is dissipated in Burgers turbulence at every scale, in contrast to Kolmogorov turbulence.

The presence of magnetic fields breaks down the assumption of isotropy in the fluid. If the magnetic field is coupled to the motion of the fluid, then fluid motions parallel and perpendicular to the magnetic field direction must have different behaviours. For incompressible MHD turbulence, [Goldreich & Sridhar \(1995\)](#) find a relation between the spatial modes parallel and perpendicular to the magnetic field lines ( $k_{\parallel}$  and  $k_{\perp}$ , respectively), given by  $k_{\parallel} \propto k_{\perp}^{2/3}$ , with the perpendicular modes exhibiting a Kolmogorov type behaviour  $E(k_{\perp}) \propto k_{\perp}^{-5/3}$ .

### *Key observations*

Direct observational evidence of turbulence in the ISM comes from studying the linewidths of different lines (for example, CO lines in the dense ISM, or HI lines in the diffuse ISM). The linewidths exhibited are consistently broader compared to the thermal linewidth expected from the temperature (obtained, for example, by comparing the strength of different rotational transitions). [Zuckerman & Palmer \(1974\)](#) suggested that the supersonic linewidths in the dense ISM are representative of small scale turbulence acting as support against gravitational collapse. The turbulent nature of the ISM was established more firmly with the seminal work of

Larson (1981), who found that the velocity dispersion in different molecular clouds (representing the dense ISM) has a power law scaling with the size of the clouds, spanning many orders of magnitude. Similar scaling has since been confirmed by many, in both Milky Way and other galaxies (Myers, 1983; Dame et al., 1986; Solomon et al., 1987; Bolatto et al., 2008; Falgarone et al., 1995). Traditionally, such a scaling has been seen as the observational evidence of the cascading behaviour representing turbulence. More recently this view has come into question, and forms one of the principle questions related to the role and nature of turbulence. We discuss more details on the role of turbulence in structure formation in the dense ISM when discussing molecular clouds, in Section 1.3.2.

#### *Sources of turbulence*

Supersonic turbulence is distributed over a length scale  $l$  typically over the crossing scale  $t_{\text{crossing}} = l/v_l$ , where  $v_l$  is the typical eddy velocity at length scale  $l$ . In the absence of driving forces, supersonic turbulence also decays typically over a crossing time (Mac Low et al., 1998; Stone et al., 1998). This means that turbulence must constantly be driven by physical processes that inject energy and momenta into the system. The largest possible driving scale in the ISM is set by the disk height in case of a spiral galaxy, for example the Milky Way. Following section 4 of Klessen & Glover (2016), we highlight the possible key sources usually considered as energy source for the turbulence:

- gas accretion onto the galaxy through the cosmic web
- rotational energy of the galactic disk
- magnetorotational instabilities in the galactic disk
- feedback from stars, including supernova explosions, stellar winds, radiation from massive stars, protostellar jets and outflows

#### 1.2.4

##### MAGNETIC FIELDS

In conjunction with turbulence, magnetic fields are an important component of the ISM and their exact role in shaping and governing cloud dynamics forms one of the central questions of this thesis. Let us attempt to disentangle some key observations, as well as in what exact manner we expect magnetic fields to modify the behaviour of the turbulent ISM.

#### *Key observations*

The existence of magnetic fields in the ISM has been known since the works of Hiltner (1951) and Hall (1951). There are four primary methods we can use to appraise the strength of magnetic fields in the ISM.

- **Zeeman effect**, which estimates the line of sight component of the magnetic field by using the phenomenon of spectral line splitting in a magnetized medium
- **Davis-Chandrasekhar-Fermi method**, which estimates the plane of the sky component of the magnetic field ( $\mathbf{B}_{\text{pos}}$ ) by comparing the dispersion in polarization direction (corresponding to dispersion in direction of  $\mathbf{B}_{\text{pos}}$ ) with the dispersion in the velocity field

- **Faraday rotation** which uses the rotation in the polarization vector of starlight to estimate the strength of the magnetic field
- **Synchrotron observations**, where the magnetic field strength is estimated through the frequency of the emitted gyro-radiation

The last two methods are only applicable in the diffuse ISM. In addition to the strength, the morphology of the magnetic field can be obtained from dust polarization observations, or polarization of line emissions (Goldreich & Kylafis, 1981; Crutcher, 2012). While magnetic fields are difficult to observe and constrain, painstaking observations over the past decades allows us today an unprecedented accuracy in the measurement of the strength and morphology of magnetic fields from galactic scales down to prestellar and stellar scales (Crutcher, 1999; Bourke et al., 2001; Heiles & Troland, 2005; Troland & Crutcher, 2008; Crutcher et al., 2009; Planck Collaboration et al., 2016, 2020).

An example of the excellent measurements of magnetic field morphologies we obtain can be seen in Fig. 2. Taken from Planck Collaboration et al. (2016), the figure shows the column density map (obtained from dust opacity measurements) towards the direction of the Taurus molecular cloud. The wavy pattern, created using the technique of line integral convolutions (LIC, Cabral & Leedom (1993)), represents the orientation of the magnetic field in the plane of the sky, obtained from dust polarization measurements. Fig. 2 clearly illustrates the complicated field geometry that permeates the entire cloud. Let us attempt to understand the dependency of magnetic fields on various factors.

#### *Magnetic field vs density*

Magnetic fields in the ISM are coupled to the charged particles. The charged particles are in turn collisionally coupled to the neutral gas. At different scales in the ISM, as the density and ionization fraction changes, so too does the nature and extent to which magnetic fields affect the motion of the gas.

We can try to understand the relationship magnetic fields have to the density of the particles, assuming perfect collisional coupling, using some simple arguments. For particle density  $n$ , we assume that the magnetic field strength varies as  $B \propto n^\kappa$ . If gas contracts parallel to the field lines, the strength of the field does not enhance with density and  $\kappa = 0$ . This is indeed observed in the ISM up to densities of  $\sim 300 \text{ cm}^{-3}$  (Troland & Heiles, 1986; Crutcher et al., 2010). If a spherical cloud of radius  $R$  is uniformly collapsing, and the magnetic pressure is weak, we expect:

$$\begin{aligned} B &\propto R^{-2} \\ n &\propto R^{-3} \end{aligned} \tag{1.1}$$

from magnetic flux and mass conservation, respectively. This leads to  $\kappa = 2/3$ . If the magnetic field is non-negligible,  $B \propto n^{1/2}$  is expected, for example from energy equipartition between magnetic and kinetic energy (Hennebelle & Inutsuka, 2019). Crutcher et al. (2010) find  $\kappa = 2/3$  densities above  $300 \text{ cm}^{-3}$ , up to  $\sim 10^6 \text{ cm}^{-3}$ .

Generally speaking, 3D numerical ideal MHD turbulence simulations find good agreement with such relations. Mocz et al. (2017) find that for super-Alfvénic turbulence (Alfvénic Mach number  $\mathcal{M}_A > 1$ ), the clumps in their simulations follow  $B \propto n^{2/3}$ , while for sub-Alfvénic turbulence ( $\mathcal{M}_A < 1$ ) the result is consistent with the strong field limit of  $B \propto n^{1/2}$ . Simulations including both self-gravity and magnetic fields tend to find  $\kappa = 1/2$  in dense gas, while simulations without self-gravity

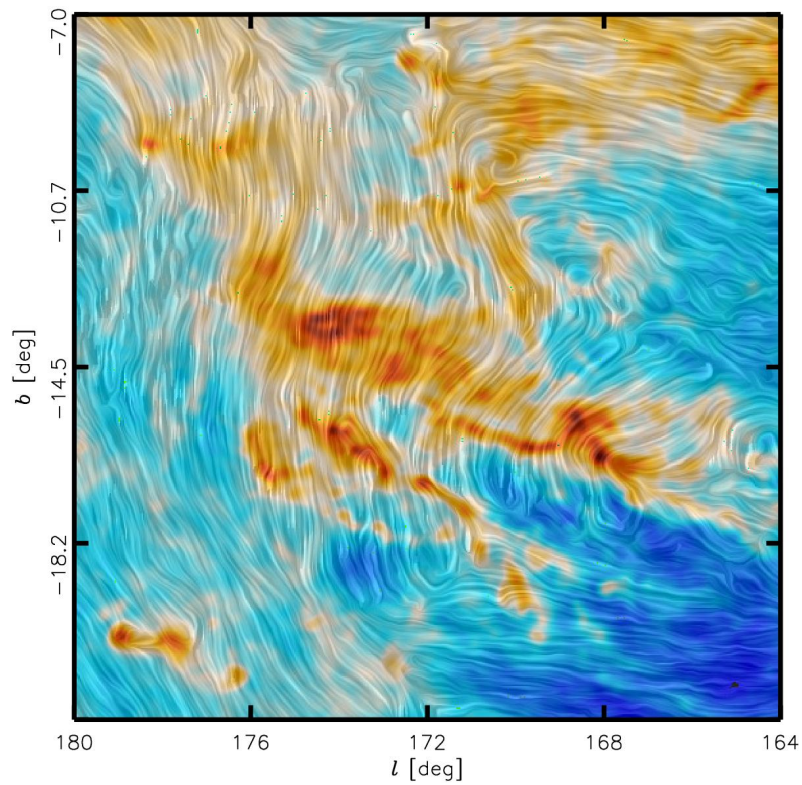


Figure 2: Map of the planar magnetic field toward the molecular cloud Taurus, from [Planck Collaboration et al. \(2016\)](#). The color represents the column density of the gas. The wavy pattern represents the morphology of the planar magnetic field obtained by using the technique of line integral convolutions (LIC). The magnetic field directions have been obtained from dust polarization. The box size here corresponds roughly to around 40 pc.

tend to find a weak correlation of  $\kappa \approx 0.1 - 0.2$  (Hennebelle et al., 2008; Banerjee et al., 2009). See the excellent review by Hennebelle & Inutsuka (2019), Section 5.1, for more extensive discussion on this topic.

#### *Magnetic field across scales*

**Cloud scale:** Is gas accretion onto the dense ISM sensitive to magnetic field strength and orientation? Planck Collaboration et al. (2016) analyze the relative orientation between the planar magnetic field and gradient of the column density for ten MCs, and find that magnetic fields tend to become perpendicular to the orientation of structures as we go towards higher column densities (see also the discussion on filament scales below). Li & Henning (2011) show through studies of CO line polarization that magnetic field directions are correlated with the spiral arm directions in six giant massive clouds (GMC) in M33. As discussed previously, Crutcher et al. (2010) find that up to densities of  $300 \text{ cm}^{-3}$ , the magnetic field is roughly constant at a strength of around  $10 \mu\text{G}$ . All these observations suggest that gas accretion primarily occurs along magnetic field lines for formation of molecular clouds, and that magnetic field lines are not simply randomized due to turbulence and other factors.

**Filament scale:** The dense ISM is highly fragmented and filamentary in nature (André et al., 2014). These filaments are often seen parallel to each other (Myers, 2009). Dynamically dominant magnetic fields are expected to play an important role in the formation of such parallel filaments - through either B-field channelled gravitational contraction (e.g. Nakamura & Li, 2008), or through anisotropic sub-Alfvénic turbulence (Stone et al., 1998). In the former method, flows along field lines causes elongated structures perpendicular to magnetic field lines, with multiple centres of contraction causing parallel filaments. In the latter method, anisotropic turbulent pressure extends the gas along the field lines and makes the dense gas elongated parallel to the magnetic field.

**Core scale:** Filamentary structures are threaded with sub-pc scale dense molecular cores, which act as nurseries of star formation. A sufficiently strong magnetic field can slow down the collapse of such cores to form stars, or even completely prevent them. This was for a long time thought to be an explanation as to how the star formation is so inefficient. Only  $\sim 1\%$  of gas mass inside molecular clouds actually end up inside stars in the Milky Way (Kennicutt, 1998; Genzel et al., 2010; Krumholz et al., 2012). If the mass to magnetic flux ratio is less than a critical value (such cores are called sub-critical cores), gravity cannot overcome magnetic pressure and the core can be magnetically supported. More recent observations, however, suggest that molecular clouds have supercritical mass to flux ratios, and magnetic fields are not strong enough to prevent collapse of cores (Crutcher, 1999; Crutcher & Troland, 2000; Bourke et al., 2001; Crutcher et al., 2009, 2010). However, cores are often elongated, and Tassis et al. (2009) find alignment between magnetic field direction and the short axis of the core, suggesting that magnetic fields channel the way gas is flowing and shaping such cores.

The discussion so far has assumed perfect coupling between magnetic fields and gas. At core scales, however, the ionization fraction is low enough that this assumption can break down. In such a scenario, ion-neutral drift occurs, causing the mass to magnetic flux ratio in cores to increase (which would be constant under perfect coupling). This is called ambipolar diffusion. At smaller scales of disc

formation around protostars, one must invoke further non-ideal MHD effects to explain magnetic dissipation and formation of discs: Ohmic diffusion and the Hall effect. A brief discussion on the non-ideal effects in terms of the MHD equations is presented in Section 2.1.3.

### 1.3

#### MOLECULAR CLOUDS

The previous sections have provided us a general overview of how energetic balance and gas flow is connected across various scales in the ISM. We can now attempt to connect it to the nurseries of forming stars, molecular clouds. Molecular clouds are part of the dense CNM, where most of the gas is in its molecular form. All stars form inside these cold dense gas clouds, and therefore understanding their formation, evolution, and destruction is critical to the field of star formation. Before we look in more details into the formation, evolution, and destruction of molecular clouds, let us have a brief look into the relevant physical length and timescales usually associated when discussing molecular clouds.

##### *Relevant length, mass and timescales*

The most important length scale for molecular clouds is called the Jeans length, or sometimes the thermal Jeans length. It defines the smallest length scale at which gravitational perturbations become important and grow over time, allowing for collapse of the mass confined within this length scale. The Jeans length  $\lambda_J$  is defined as

$$\lambda_J = \left( \frac{\pi c_s^2}{G\rho} \right), \quad (1.2)$$

where  $\rho$  is the background density of the medium, and  $c_s$  is the sound speed in the medium. Scales smaller than the Jeans length are stable to perturbations, while larger scales are not. This implies that the smallest length scale at which fragmentation of molecular clouds can occur is set by the Jeans length, which in turn depends on the temperature and density of the medium. Another useful way to define the same physics is to define a Jeans mass  $M_J$ , which represents the largest mass stable under perturbation. This is defined as follows:

$$M_J = \frac{4}{3} \pi \rho \left( \frac{\lambda_J}{2} \right)^3 = \frac{\pi^{5/2} c_s^3}{6G^{3/2} \rho^{1/2}}. \quad (1.3)$$

The Jeans mass and length, for example, quite naturally explain why star formation happens only in cold dense gas, i.e. molecular clouds. Since the temperature of the medium  $T \propto c_s^2$ ,  $M_J \propto T^{3/2} \rho^{-1/2}$ , which implies that the colder and denser the gas gets, the smaller the Jeans mass. Gas inside molecular clouds, therefore, is much more susceptible to collapse compared to for example in the WNM, where the Jeans mass would be several orders of magnitude higher.

In contrast to the more traditional thermal Jeans length, in presence of supersonic turbulence, one can also define a turbulent Jeans length  $\lambda_J^{\text{turb}}$  and a Jeans mass  $M_J^{\text{turb}}$ . This is obtained by assuming that the turbulent pressure acts in a similar manner to thermal pressure and corresponds to the primary resistive force to gravitational collapse. The sound speed  $c_s$  can under these assumptions be replaced by the supersonic velocity dispersion  $\sigma_{1D}$ , leading to the following expressions of

the Jeans length and mass, respectively:

$$\lambda_J^{\text{turb}} = \left( \frac{\pi \sigma_{1D}^2}{G \rho} \right) \quad (1.4)$$

$$M_J^{\text{turb}} = \frac{\pi^{5/2} \sigma_{1D}^3}{6 G^{3/2} \rho^{1/2}} \quad (1.5)$$

The Jeans fragmentation implicitly assumes a spherical geometry. However, we know that molecular clouds are very often highly filamentary (André et al., 2010; Molinari et al., 2010). For an elongated filamentary structure, the defining quantity related to filaments is the line mass.

Let us assume a filamentary structure with mass  $M$  and length  $l_{\text{fil}}$ . The line mass of this filament is then given by

$$\lambda_{\text{fil}} = M/l_{\text{fil}}. \quad (1.6)$$

For an isothermal cylinder in hydrostatic equilibrium, we can define a critical line mass  $\lambda_{\text{crit}}$ , such that filaments above the critical line mass are unstable to perturbations and therefore subject to fragmentation (Stodólkiewicz, 1963; Ostriker, 1964). This is defined as follows:

$$\lambda_{\text{crit}} = \frac{2c_s^2}{G}. \quad (1.7)$$

Filaments above the critical line mass become radially unstable and collapse (e.g. Hacar et al., 2022). Due to the assumption of hydrostatic equilibrium,  $\lambda_{\text{crit}}$  is often called the thermal critical line mass. Similar to the Jeans fragmentation, we can define a turbulent critical line mass if strong non thermal velocity dispersions are present. This is defined by

$$\lambda_{\text{crit}}^{\text{turb}} = \frac{2\sigma_{1D}^2}{G}. \quad (1.8)$$

For both Jeans mass and the critical line mass, it is also possible to add the thermal and non thermal component if both are dynamically relevant. In observations, this would be represented simply by the total line width of the observed line. For simulations, we can do this by using the total velocity dispersion  $\sigma_{\text{tot}}$  as follows:

$$\sigma_{\text{tot}}^2 = \sigma_{1D}^2 + c_s^2. \quad (1.9)$$

In terms of relevant timescales, a few timescales are quite naturally associated with molecular clouds. The natural timescale of gravitational contractions is given by the free fall time ( $t_{\text{ff}}$ ). It defines the timescale at which a mass of gas will collapse in the absence of any pressure. For a uniform density spherical gas cloud of density  $\rho$ , this remarkably depends only on the density itself, i.e.  $t_{\text{ff}} = [3\pi/32G\rho]^{1/2}$ . For fully molecular gas, we can define this in terms of the the number density of  $\text{H}_2$ ,  $n_{\text{H}_2}$ , as:

$$t_{\text{ff}} = 3.4 \left( \frac{100}{n_{\text{H}_2}} \right)^{1/2} \text{ Myr}. \quad (1.10)$$

For typical molecular clouds then, this is typically of the order of a few Myrs.

Another timescale is the crossing timescale, which defines the timescale over which supersonic turbulence dissipates in the molecular cloud. For a cloud of size



$R$  and velocity dispersion  $\sigma_v$ , this is defined as:

$$t_{\text{crossing}} = R/\sigma_v. \quad (1.11)$$

For a cloud in rough virial equilibrium,  $t_{\text{crossing}} \approx 2t_{\text{ff}}$  (Dobbs et al., 2014).

With these scales in mind, now let us attempt to understand the life-cycle of molecular clouds themselves.

### 1.3.1

#### CLOUD FORMATION

##### *Formation of $H_2$*

Molecular clouds are defined by their chemical content, i.e. the presence of primarily molecular  $H_2$ . One way to think of molecular cloud formations, then, is by trying to understand the formation of  $H_2$  itself. Molecular  $H_2$  can form in various pathways, for example by radiative association:



or by ion-neutral reaction pathways:



and



However, it is difficult to produce an  $H_2$  fraction of more than 0.01 in such gas phase methods (Tegmark et al., 1997). Most of the molecular  $H_2$  instead forms through gas grain chemistry (Gould & Salpeter, 1963). H atoms are adsorbed by dust grains, and these H atoms react to form  $H_2$  molecules.

The molecular fraction is maintained by the balance between creation and destruction of said molecules. The principal method of the destruction of  $H_2$  is through photo-dissociation, where UV photons with energy  $E > 11.2$  eV can dissociate the  $H_2$  molecule. In warm dense gas, dissociation through collisions also become effective (Kwan et al., 1977; Flower et al., 2003).

The amount of molecular gas is sensitive to the temperature, as well as the incident ISRF. In regions of high column density, much of the UV radiation is attenuated due to the line absorption by  $H_2$  at the edge of the molecular clouds. This is called self-shielding of the gas and is an important component to treat molecular chemistry in MCs.

Further, interstellar dust also shields the gas by attenuating the incident ISRF, allowing molecules to form. A useful way to define how "embedded" a certain star or molecular cloud is to study its column density and relate it to the visual extinction  $A_V$  (Draine & Bertoldi, 1996; Glover et al., 2010) :

$$A_V = \frac{N_{H,\text{tot}}}{1.87 \times 10^{21} \text{cm}^{-2}}, \quad (1.15)$$

where  $N_{H,\text{tot}}$  is the total hydrogen column density. The transition to molecular  $H_2$

occurs at typically  $A_V \sim 0.1 - 0.2$  (Krumholz et al., 2008). Since molecular  $H_2$  is difficult to observe, another way to define the molecular state of the gas is to use the formation of tracer molecules such as CO to define the molecular cloud. The transition from atomic and ionized carbon to CO happens at around  $A_V \sim 1$  (Wolfire et al., 2010). However, the highly fragmented and filamentary nature of molecular clouds means that the incident ISRF is not isotropic, and radiation could still reach denser parts through holes and gaps in the fractured medium.

#### *Formation mechanism*

Understanding the chemical pathways of molecule formation do not necessarily give us insight into how MCs physically form. It only pushes the question further: which physical processes in the galaxy lead to conditions which facilitate such favourable conditions? Any model of MC formation must explain a number of key observations related to them - the lifetime of molecular clouds varies from a few Myrs to few tens of Myrs for so called giant molecular clouds (GMC) (Blitz et al., 2007; Murray, 2011; Heyer & Dame, 2015), they are usually embedded in an extended envelope of atomic hydrogen, and the number of molecular clouds  $N$  at different masses shows a remarkable power law behaviour

$$\frac{dN}{dm} \propto m^{-\alpha_m}, \quad (1.16)$$

with  $\alpha_m \approx 1.7$  (Solomon et al., 1987; Heithausen et al., 1997; Heyer et al., 2001; Rosolowsky, 2005).

The original proposition of Oort (1954), the so called coagulation model, suggests that molecular clouds form due to thermal instability in warmer atomic gas (Field, 1965), and collisions between clouds efficiently dissipate energy, and "stick together" to form larger MCs. However, it is difficult to explain the formation of the largest GMCs in this method, especially given their relatively short lifetime.

Even accepting this scenario, a fundamental question remains. What mechanism drives such converging flows? There are a number of possible candidates:

- Large scale gravitational instability in the galactic disk. Gravitational instabilities are commonly associated in smaller scales, for example in protostellar disks, with the formation of secondary stars or gas giants, and the scale-up version of a similar method may be responsible for creating MCs.
- Parker instability in spiral galaxies (Parker, 1966). Perturbations in the magnetic field cause the field lines to bend, allowing gas to fall towards the disk midplane and causing gas accumulation.
- Compression due to supernovae. Supernovae sweep up vast swathes of gas, and converging flows may occur in the dense shells of such bubbles, or in the interaction of multiple such bubbles. This forms the basis of the bubble driven filament formation scenario explaining the filamentary MCs (Inutsuka et al., 2015)

## 1.3.2

## CLOUD EVOLUTION AND STAR FORMATION

*Molecular cloud properties*

What is the nature of molecular clouds? How do they evolve and form denser structures, and eventually stars? Are molecular clouds bound entities? Investigating the answers to these questions lie at the heart of this thesis. Let us attempt to examine a few key observations related to the nature of MCs.

Larson (1981) found a number of widespread relationships between molecular cloud properties. Larson's first law proposes that the velocity dispersion  $\sigma_v$  in molecular clouds is related to the size  $R$  of the molecular cloud, with  $\sigma_v \propto R^n$ , where Larson found  $n = 0.38$ . This value was refined by Solomon et al. (1987) based on GMCs in the first galactic quadrant to

$$\sigma_v = (0.72 \pm 0.07) R_{\text{pc}}^{0.5 \pm 0.05} \text{km s}^{-1}. \quad (1.17)$$

A Burgers type cascading turbulence, energy equipartition between kinetic and potential energy, and even gravitational infall all are consistent with this  $\sigma_v \propto R^{1/2}$  kind of power law.

Larson's second law states that GMCs are gravitationally bound, with the kinetic virial parameter  $\alpha_{\text{vir}} \approx 1$ . Other observations have confirmed the rough equipartition in molecular clouds between kinetic and potential energies (Dame et al., 1986; Solomon et al., 1987; Blitz et al., 2007).

These two relations lead to Larson's third law, that all GMCs are at roughly the same column densities of  $\bar{\Sigma} \approx 170 M_{\odot} \text{pc}^{-2}$ . Larson's third law has been challenged arguing that it reflects selection biases (Kegel, 1989; Scalo, 1990). We know now that MCs exist in a variety of different surface densities.

Heyer et al. (2009) show that a better fit of Larson's linewidth-size relation is obtained if we assume that it has a dependency on the column density  $\Sigma$  of the gas as

$$\frac{\sigma_v}{R^{1/2}} \propto \Sigma^{1/2}. \quad (1.18)$$

This naturally implies that MCs can exist in different column densities. Indeed GMCs in the outer galaxy have lower surface density compared to those in the inner galaxy in general. Clouds at low column densities typically also tend to have an excess of kinetic compared to potential energy (Kauffmann et al., 2013; Leroy et al., 2015).

*Structure formation*

Any theory of structure formation in molecular clouds must be able to explain these observations, along with some other key observations mentioned before: (1) supersonic linewidths in MCs (2) low star formation efficiency. We discuss here two main competing theories as to the interpretation of these observations - the gravo-turbulent scenario, and the global hierarchical collapse scenario.

**Gravo-turbulent scenario:** The gravo-turbulent (GT) scenario of structure formation in molecular clouds was proposed originally by Zuckerman & Evans (1974) as a solution to the observations of supersonic linewidths in MCs. The original interpretation of Goldreich & Kwan (1974) was that the supersonic linewidths represent molecular clouds in global gravitational infall. Zuckerman & Palmer (1974) pointed

out that such a global infall would result in two observations: (1) high star formation efficiency as opposed to the observed  $\sim 1\%$ , and (2) cloud scale radial motions would result in redshifted absorption lines compared to the emission lines from the star-forming region itself, which were not observed. Based on these arguments, [Zuckerman & Evans \(1974\)](#) discounted radial infall and instead suggested that the supersonic linewidths represent small-scale turbulence that acts as a kinetic pressure and prevents the molecular cloud collapse. This idea has been refined much since (see e.g. excellent reviews by [Mac Low & Klessen, 2004](#); [Ballesteros-Paredes et al., 2007](#); [McKee & Ostriker, 2007](#); [Hennebelle & Falgarone, 2012](#)).

In the present day scenario of this model, the molecular cloud structure represents a turbulent cascade. Larger scale dynamics (for example supernovae) drive turbulent energy into the dense ISM. This turbulent energy cascades down from molecular cloud scales all the way down to core scales ( $\sim 0.1$  pc). Structures at every length scale are supersonically turbulent, and this generates support against gravitational collapse of the structure. Denser structures are created by turbulent compression, which can become gravitationally bound, collapse, fragment, and eventually form stars. This turbulent cascade is represented by a Larson-like power law. The scale of transition from supersonic to subsonic turbulence (the so-called sonic scale, usually predicted to be around  $\sim 0.1$  pc) represents the scale at which gravitationally bound cores emerge ([Arzoumanian et al., 2013](#)). The elongated filamentary structures are a natural result of the inhomogeneous nature of turbulent interaction.

In this scenario, the lack of global collapse is explained by the fact that clouds are held up by turbulent pressure. Dense, self-gravitating structures form only when turbulent compression makes them gravitationally bound, naturally leading to low star formation efficiencies.

The matter of explaining how the Larson coefficient  $\sigma_v/R^{1/2}$  can depend on the surface density is trickier in the classical turbulence picture, as a purely cascading turbulence does not lead to such a dependency. Indeed, [Heyer et al. \(2009\)](#) interpreted this as a signature that GMCs are in virial equilibrium. [Hennebelle & Falgarone \(2012\)](#) propose that using the full virial analysis by treating the external pressure might solve the apparent discrepancy, if the external pressure scales with the gas surface density in a suitable way. [Padoan et al. \(2016\)](#) find that if they exclude clouds with equivalent radius smaller than 4 pc citing insufficient velocity resolution, both outer galaxy clouds as well as clouds on the galactic ring (at 5 kpc radius) are consistent with a constant  $\sigma/R^{1/2}$ , despite being at different column densities.

**Global hierarchical collapse (GHC) scenario:** The original global infall model was discarded based on the arguments of [Zuckerman & Palmer \(1974\)](#). However, a more nuanced picture of MCs in gravitationally collapse can deal with the principal objections. A complete overview of the GHC scenario can be obtained in [Vázquez-Semadeni et al. \(2019\)](#), based on previous works by [Vázquez-Semadeni et al. \(2007, 2009, 2010, 2017\)](#); [Heitsch & Hartmann \(2008\)](#); [Heitsch et al. \(2009\)](#); [Ballesteros-Paredes et al. \(2011\)](#); [Camacho et al. \(2016\)](#) etc.

The GHC scenario argues that molecular clouds are not supported at all, but are instead undergoing multi-scale, multi-epoch gravitational collapse. This is characterized by a mass and energy cascade across scales, reminiscent of the turbulent cascade in the gravo-turbulent picture. The collapse is highly non-linear and asymmetric. Smaller denser structures collapse on a much shorter timescale, creating massive stars whose feedback disperses the parent cloud and keeps the star form-

ation efficiency low. The turbulence shapes the density profile of the cloud, but is mildly supersonic ( $\mathcal{M} \sim 3$ ) and not strong enough to support the collapse of GMCs. Shortly after acquiring more than their thermal Jeans mass, the molecular cloud therefore begins to collapse in a non-linear fashion. The supersonic linewidths are a sign of this gravitational collapse, but systematic redshift is masked due to the non-spherical geometry of the cloud. The collapse at any scale occurs when the mass exceeds a few times the thermal Jeans mass at that corresponding density. The collapse is initially slow, but accelerates towards the end of a cloud's lifetime before being dispersed by feedback. The motion inside the cloud therefore consists of an overlapping motion of large scale inflow directed towards global potential wells, overlapped with gas motion towards smaller-scale potential minima.

This naturally leads to a Heyer-like relation where the coefficient  $\sigma/R^{1/2} \propto \Sigma^{1/2}$ . The exact scaling, however, would be slightly different compared to assuming virial equilibrium. Velocities due to gravitational infall would be a factor of  $\sqrt{2}$  higher compared to velocity expected from virial balance, and the one suggested by Heyer et al. (2009). However, Ballesteros-Paredes et al. (2011) argue that the uncertainties in Heyer et al. (2009) are high enough that it could allow the velocity dispersion  $\sigma_v$  to represent free fall velocity instead of virial balance.

**Predictions of gravo-turbulent vs GHC scenario:** The GHC scenario predicts that clouds are bound under self-gravity. Some recent observations of gravitational accretion flows seem to support this behaviour (Kirk et al., 2013; Chen et al., 2019; Shimajiri et al., 2019). Chevance et al. (2022), however, point out that the observations tend to focus on denser regions of clouds, and it is unclear if the behaviour is similar for the entire cloud. In contrast to overall gravitational contraction, the gravo-turbulent scenario allows for overall unbound or close to virialized clouds, with local regions becoming bound. This is the primary tool of investigation implemented in paper I for distinguishing between the two scenarios. Another prediction of the GHC scenario is that, as the cloud is overall collapsing, this should lead to an accelerated star formation until the cloud is dispersed by stellar feedback (Vázquez-Semadeni et al., 2019). The GT scenario does not predict any such trend. In the GT scenario, the star clusters that eventually form should have largely random motions to each other, while in the GHC scenario, due to the nature of collapse there should be a strong radial component. The evidence on this is fractured. Observations based on Gaia data fail to observe such radial motions (see e.g. Kounkel et al., 2018), while some clusters tend to show radial expansion (Lim et al., 2020; Swiggum et al., 2021).

#### *Cloud properties at filament scales*

The study of the filamentary nature of ISM structures has been a matter of active study based on data from Herschel Gould belt survey (Arzoumanian et al., 2011, 2019; Benedettini et al., 2015), galactic plane surveys such as HiGal (Molinari et al., 2010), ATLASGAL (Schuller et al., 2009; Li et al., 2016), and the CO survey SEDI-GISM (Schuller et al., 2017; Mattern et al., 2018). Filaments based on Herschel dust emission maps of nearby molecular clouds tend to find a filament width of  $\sim 0.1$  pc (Arzoumanian et al., 2011, 2019), although it is a matter of much discussion whether such a typical width exists (Panopoulou et al., 2017; Ossenkopf-Okada & Stepanov, 2019). If such a typical width exists, it is often associated with a transition from supersonic to subsonic regime (see e.g. Arzoumanian et al., 2011).

**Filament formation:** A number of possibilities have been proposed as methods of filament formation. This is of particular interest in the context of this thesis, which we will explore in greater detail in Chapter 6. Following [Hacar et al. \(2022\)](#), we here highlight some frequently invoked mechanisms for filament formation:

- Gravitational instability in sheet-like structures, leading to filaments with density enhancements towards its end ([Burkert & Hartmann, 2004](#); [Hartmann & Burkert, 2007](#))
- Network of filaments caused by interaction of turbulent flows (see e.g. [Clarke et al., 2017](#))
- Shock compression of clumpy structures in the presence of magnetic fields ([Inoue & Fukui, 2013](#))
- Pressure compression driven by stellar feedback (e.g. [Suri et al., 2019](#))
- Galactic shear resulting in  $\sim 100$  pc scale filaments ([Wada et al., 2002](#); [Smith et al., 2014](#))

**Accretion onto filaments:** The different possible mechanisms of filament formation naturally lead to different dynamical behaviours. Filaments forming through turbulent interactions, for example, could be kept confined by ram pressure even when they are not sustained by gravity (e.g. [Heitsch, 2013](#)). Filaments forming through gravitational instability, on the other hand, are expected to accrete more through their ends. The accretion rate of filaments tend to be of the orders of few 10 to few 100  $M_{\odot} \text{ Myr}^{-1} \text{ pc}^{-1}$  ([Kirk et al., 2013](#); [Palmeirim et al., 2013](#); [Bonne et al., 2020](#)). The mass flow onto and along filaments naturally also implies an accretion of kinetic energy, that is a possible source of driving turbulence inside filaments. It is generally expected that such accretion driven turbulence is solely not enough to sustain the dynamic balance of the filament.

**Fragmentation to core formation:** If filaments exceed their critical line mass (see Section 1.3 for discussion), they are expected to fragment and form equally spaced cores. However, presence of a turbulent environment considerably complicates the picture. [Clarke et al. \(2016\)](#) show that accretion onto filaments considerably changes the nature of fragmentation expected from quiescent filaments ([Inutsuka & Miyama, 1992](#)). We will also investigate how different cores form in the context of the SILCC deep-zoom simulations in Chapter 6.

#### *Cloud core to star formation*

While molecular clouds exhibit supersonic motions, the dense cores that act as sites of star formation have subsonic or transsonic motions ([Kirk et al., 2007](#); [André et al., 2007](#); [Rosolowsky et al., 2008a](#)). Some of them also show signs of inflow. Any scenario of how stars form inside cores needs to explain a few principal observations, the most important of which is the stellar initial mass function (IMF).

The stellar IMF is the distribution in stellar masses at birth. The IMF is often said to be universal, in the sense that it shows remarkably similar behaviour over a wide range of environments. The most unique feature of the IMF is that for masses above roughly  $\sim 1M_{\odot}$ , the number of stars at different mass ranges shows a power law behaviour of  $dN/dM \propto M^{-\alpha}$  with  $\alpha \approx 2.3$  ([Salpeter, 1955](#); [Kroupa, 2001](#)). This

remarkable scale-free behaviour requires theories that too are The IMF also shows a turnover at a mass of  $\sim 0.1M_{\odot}$ .

A second important observation that needs to be explained is the remarkable similarity between the IMF and the mass distribution of cores where the stars form, called core mass function or CMF (Klessen & Glover, 2016). The CMF is typically of a similar shape as the IMF, but scaled up by a factor of  $\sim 3$  (e.g. Klessen & Glover, 2016). There are two primary theoretical frameworks that attempt to explain the origin of the IMF: competitive accretion and turbulent fragmentation. We present the two theories briefly below.

In the **competitive accretion** scenario, the peak of the IMF is set by the Jeans length of the medium. Gravitational instabilities lead to "seed" protostars that accrete in a collective and competitive manner from a common gas reservoir. If we consider such seed protostars of mass  $M$  accreting from the environment, we can assume that the more massive seeds will accrete in faster manner, i.e.

$$\frac{dM}{dt} \propto M^{\eta}, \quad (1.19)$$

with  $\eta > 0$ . In the simplest assumption, if a seed protostar accretes homogeneously from a uniform density ambient medium, this leads to spherical Bondi-Hoyle accretion with  $\eta = 2$  (Hoyle & Lyttleton, 1941; Bondi, 1952). The mass distribution of stars in such a case can be shown to be (see e.g. Krumholz, 2015, chapter 13) following

$$\frac{dM}{dt} \propto M^{-2}. \quad (1.20)$$

This is close to the observed power law slope of 2.3. The difference in the slope of the power law can be explained by a combination of factors, such as tidal effects due to the presence of numerous accreting cores (Krumholz, 2015). In the original competitive accretion scenario, the seed masses were all considered to be almost of equal mass, set by the Jeans mass in the medium. A more realistic scenario, encapsulating the fragmentation process, suggests that cloud fragmentation creates a mass distribution that lacks the power law tail of the stellar IMF, which is then set by competitive accretion among competing masses (Klessen & Glover, 2016). In this phase, protostars with masses close to the Jeans mass of the medium compete for gas at the center of the forming cluster. Gas is fed onto the cluster through gravitational channeling, and protostars that remain in the cluster manage to get massive, while protostars that are ejected by N-body interactions in the forming cluster remain low mass. In this scenario, the similarity between the CMF and the IMF does not contain any significant physical meaning, as there is no direct mapping between the CMF and the IMF.

In contrast to the gravitational accretion theories, another scale-free theory that has often been evoked to explain the shape of the IMF is the theory of **turbulent fragmentation**. In this scenario, turbulence in the molecular gas creates a number of density enhancements, typically called clumps. The distribution of clumps can be obtained from assumptions on the density distribution of the gas (Padoan et al., 1997; Padoan & Nordlund, 2002; Hennebelle & Chabrier, 2008; Hopkins, 2012). However, not all clumps are collapsing. Only a subset of clumps are gravitationally bound, and these are typically referred to as cores. Such gravitationally bound cores collapse and form stars, with a certain fraction of the mass of the core ending

up in the forming star. In the simpler forms of this scenario, the apparent similarity between the CMF and the IMF is a direct consequence of this one to one mapping between cores and the stars that form inside them.

For the purpose of this thesis, we will study the distribution of forming cores, their gravitational boundness, and the nature of their accretion in Chapter 6. A detailed comparison of turbulent fragmentation and competitive accretion, however, is beyond the scope of this present work.

### 1.3.3

#### CLOUD DESTRUCTION

##### *Molecular cloud lifetimes*

Many theories of molecular cloud formation and evolution rely critically on how long a molecular cloud lives. Intuitively, this is easy to understand - a long living molecular cloud implies that star formation is inefficient because it is extremely slow, while if a molecular cloud lives a much shorter time (comparable to the dynamical free fall timescale), then the low inefficiency can be explained also through theories where the star formation rate inside clouds is much higher. We present here a brief summary of the theories regarding molecular cloud lifetimes.

Molecular clouds are often detected in the inter arm region of spiral galaxies such as our own galaxy, the Milky Way. Since the transit time between two spiral arm passages is  $\sim 10^8$  Myr, based on this one can argue that molecular clouds live longer than 100 Myrs. [Scoville & Hersh \(1979\)](#) applied this argument for the Milky way, and [Koda et al. \(2009\)](#) found a similar behaviour for the galaxy M51. This would imply that that molecular clouds live much longer compared to their free fall times, requiring them to have some form of support against gravity. In this scenario, during spiral arm passage, large GMCs are built up rapidly from already existing molecular clouds. However, for this scenario to happen, it is enough that the hydrogen molecules themselves survive (as opposed to entire clouds) the spiral arm passage and have a lifetime of 100 Myrs.

Based on CO line emission survey of the dwarf galaxy LMC, [Kawamura et al. \(2009\)](#) observe three different phases of GMCs: type I clouds with no signature of massive star formation, type II clouds containing ionized HII bubbles signifying the birth of massive stars, and type III clouds with developed stellar clusters. The relative ratio of the three types of clouds tells us their relative lifetimes, as cloud stages observed less frequently must have a shorter lifespan. By dating the age of the star clusters for type III clouds, one can determine the absolute age of the type III clouds and therefore also the other two. [Kawamura et al. \(2009\)](#) find that from this they estimate the lifetime of MCs to be  $\sim 25$  Myrs.

In the solar neighbourhood, we can observe smaller molecular clouds with much greater spatial resolution and date the age of clouds by dating the position of the embedded stars in the Hertzsprung-Russell (HR) diagram ([Elmegreen, 2000](#); [Hartmann et al., 2001](#); [Ballesteros-Paredes & Hartmann, 2007](#)). For solar neighbourhood GMCs, this yields a MC lifetime of  $\sim 10$  Myrs.

MC lifetime estimates, therefore, seem to vary quite a bit. However, if we consider that different molecular clouds live in different environments and can have quite different average densities, and as a result have very different free fall times, it is perhaps possible to reconcile the galactic observations with the extra galactic ones. [Tan et al. \(2006\)](#) argue that the lifetime of a molecular cloud is roughly  $\sim 10$



times its free fall timescale, for all clouds, both galactic and extragalactic.

#### *Dispersion by stellar feedback*

Molecular clouds form stars. These stars, particularly the massive ones (typically mass  $> 8 M_{\odot}$ ) eject energy and momentum into the surrounding molecular cloud in the form of stellar winds, ionizing radiation, radiation pressure, and supernovae. These feedback processes can heat up, ionize, erode and even completely destroy the parent cloud. This thesis looks at early stages of MC evolution, and therefore does not include any stellar feedback. Their inclusion would be particularly interesting in the context of further evolution of the deep-zoom simulations. We briefly consider the most important of the different feedback mechanisms and their various consequences.

**Supernovae:** Massive stars can explode as supernovae. Typical core collapse supernovae release  $2\text{--}5 M_{\odot}$  mass at high velocities of  $6000\text{--}7000 \text{ km s}^{-1}$  (Janka, 2012). This releases massive amounts of energy and momentum into the ISM. If a supernova occurs inside a molecular cloud, it can potentially destroy the entire cloud. Supernovae typically consists of different phases. In the initial free expansion phase, the ejected material expands without meeting any resistance. When the mass in the swept up shell equals the ejected mass, the supernova enters an energy conserving Sedov-Taylor phase. The forward shock imparts most of the radial momentum due to supernovae in this phase to the ambient medium. As time passes, more mass accumulates in the shell and radiative cooling becomes increasingly important and the supernova enters the pressure driven snowplow phase where the shell expands due to the homogeneous pressure inside the shell. Finally, when the pressure in the shell becomes equal to the pressure in the ambient medium, then the supernova enters into a momentum conserving snowplow phase where the shell is not expanding due to a pressure gradient, but carries on due to its previously gained momentum (McKee & Ostriker, 1977; Cioffi et al., 1988; Haid et al., 2016). In this entire process, typically a large amount of energy of  $\sim 10^{51}$  erg is injected into the ISM. The ambient medium is heated to temperatures above  $10^6$  K. When supernovae explode inside molecular clouds, they incur significant radiative losses, and the energy conserving phase is shorter (Gatto et al., 2015; Girichidis et al., 2016). They can nonetheless destroy the parent MCs (Iffrig & Hennebelle, 2015; Gatto et al., 2015; Walch et al., 2015), while the shock waves can also help trigger the condensation and formation of new clouds.

**Stellar wind:** All stars continuously eject material in the form of stellar winds. For massive O- and B-type stars, such radiation driven stellar winds can have important consequences for the ambient medium. The mass ejection rate in winds is typically of the order of  $\sim 1 M_{\odot} \text{ Myr}^{-1}$ , while the ejection velocity is also typically a few thousand  $\text{km s}^{-1}$ . Over a star's lifetime, the total energy output can be similar to that in a supernova explosion at  $\sim 10^{51}$  erg for the most massive of stars (Puls et al., 1996; Naab & Ostriker, 2017). Stellar winds can reduce the density of the ambient medium, increase the temperature, and therefore change the nature and effect of a supernovae explosion in such a medium. Further, the momentum ejected by stellar winds can be more important compared to even supernovae.

**Ionizing radiation and radiation pressure:** In terms of total energy input, ionizing radiation is the most energetic stellar feedback process. Over its lifetime, a massive

star typically ejects  $\sim 10^{53}$  erg of energy in Lyman continuum photons. The ejection of these photons ionizes a portion of the parent molecular cloud, up until the so called Strömgren radius where the recombination rate of ionized hydrogen equals the dissociation rate due to the incident photon field. Part of the residual energy from the ionizing photons is converted into heat and raises the temperature of the medium, as well as raising the pressure inside the HII bubble and driving a shock that can travel into the ISM up to a radius of 100 pc (Strömgren, 1939; Spitzer, 1978; Hosokawa & Inutsuka, 2006). It is not completely clear how much of the photon momentum is converted into bulk momentum of the gas. If the method is efficient, it could possibly also help drive and maintain turbulence inside the clouds (Murray et al., 2005, 2010, 2011; Agertz & Kravtsov, 2015; Geen et al., 2015). Ionizing radiation lowers the density of inside the MC in regions of massive star formation, and can make the effects of supernovae far more drastic.

Photons, whether energetic enough to ionize hydrogen atoms or not, can still impart momentum to the gas. This effect can be quantified as a pressure due to the electromagnetic photon field. This radiation pressure on gas particles, as well as dust grains can impart momentum. In typical ISM densities, this effect is negligible (Arthur et al., 2004; Krumholz & Matzner, 2009; Sales et al., 2014). However, when the environment is dense, such as in the dense MCs, such a radiative pressure can help drive turbulence (Gritschneder et al., 2009) as well as modify the mass distribution in the environment by moving gas away from the star.

The discussion above completes the introductory part of this work. In this chapter, we have discussed the physics of the ISM and focused on the formation, evolution, and destruction of its dense molecular component - the molecular clouds. In each stage, we have tried to highlight some of the key observations and competing theories. The primary scientific goals of the present work relate to understanding structure formation in the early stages of cloud evolution (Section 1.3.2). In the following chapter, we delve into the necessary numerical tools required for this task.

## METHODOLOGY

---

In the methodology section, we describe the critical aspects related to the simulations and their analysis. In Section 2.1, we detail the equations of ideal magnetohydrodynamics (MHD), including their assumptions, limitations, and how fluid discretizations deal with discontinuities such as shocks. We then describe the FLASH code that is used to solve the MHD equations in Section 2.2. In Section 2.3, we highlight the setup of the simulations used for this present work. We then move on to highlight some key aspects of how we have analyzed the results in Section 2.4.

### 2.1

#### MAGNETO-HYDRODYNAMICS

The work for this thesis is based on solving the equations of ideal MHD. Let us consider the assumptions that go on into describing astrophysical fluids using this approximation.

##### 2.1.1

###### ASSUMPTIONS OF IDEAL MHD

The dynamics of most astrophysical systems can be adequately described by non-relativistic Newtonian mechanics. Notable exceptions to this are near compact objects such as black holes or neutron stars, or in fast moving relativistic jets. In most astrophysical systems including star formation, however, gas densities and velocities are low enough that we can describe the dynamics of physical systems as an interactions of discrete classical particles.

Moreover, the length scales of our interest (AU to kilo-parsec scale, or higher) are many orders of magnitude larger than the typical particle separation (typically of the order of 1 cm or less), while collisional time scales between particles are much shorter than any timescale we are interested in. This allows us to describe the dynamics of discrete particles using a continuous approximation, i.e. by equations of fluid dynamics.

The most complete description of a classical fluid is obtained using the Navier-Stokes equation (Landau & Lifshitz, 1959). In astrophysical fluids, however, very often further approximation can be made. Apart from shocks, or dense planetary discs, bulk viscosity plays little role in astrophysics. The Reynolds number  $R_e$  in the interstellar medium is high (for example, Elmegreen & Scalo (2004) estimate that in the cold ISM,  $R_e \sim 10^5 - 10^7$ ) implying that the ISM is highly turbulent, and viscous dissipation length scales are small, in practice much smaller than any length scale of interest, as well as smaller than the best resolution any star formation simulation can numerically resolve. We can therefore generally ignore viscosity while numerically evolving astrophysical fluids, and use the much simpler Euler equations (Choudhuri, 1998).

Additional assumptions are needed when we add magnetic fields. Under the further assumptions of infinite conductivity of the ISM (Stahler & Palla, 2004), and perfect collisional coupling between charged particles and neutral gas, we can simplify Maxwell's equations and arrive at the equations of ideal MHD.

### 2.1.2

#### EQUATIONS OF IDEAL MHD

For a fluid parcel of density  $\rho$ , velocity  $\mathbf{v}$ , total energy  $e_{\text{tot}}$ , and magnetic field strength  $\mathbf{B}$  (zero if pure hydrodynamics), the equations for ideal MHD are as follows:

$$\frac{\partial \rho}{\partial t} + \nabla \cdot (\rho \mathbf{v}) = 0, \quad (2.1)$$

$$\frac{\partial \rho \mathbf{v}}{\partial t} + \nabla \cdot \left[ \rho \mathbf{v} \otimes \mathbf{v} + \left( P + \frac{B^2}{8\pi} \right) \mathbf{I} - \frac{\mathbf{B} \otimes \mathbf{B}}{4\pi} \right] = \rho \mathbf{g}, \quad (2.2)$$

$$\frac{\partial e_{\text{tot}}}{\partial t} + \nabla \cdot \left[ (e_{\text{tot}} + P) \mathbf{v} - \frac{(\mathbf{B} \cdot \mathbf{v}) \mathbf{B}}{4\pi} \right] = \rho \mathbf{v} \cdot \mathbf{g} + \dot{u}_{\text{heat}}, \quad (2.3)$$

$$\frac{\partial \mathbf{B}}{\partial t} - \nabla \times (\mathbf{v} \times \mathbf{B}) = 0. \quad (2.4)$$

Here Eqs. 2.1 through 2.4 represent conservation of mass, momentum, energy, and magnetic flux, respectively.  $P$  is the thermal pressure,  $\mathbf{g}$  is the local gravitational acceleration,  $u$  is the internal energy, and  $\dot{u}_{\text{heat}}$  is the internal energy input rate due to heating/cooling processes. The  $\otimes$  represents outer product (i.e.  $(\mathbf{a} \otimes \mathbf{b})_{ij} = a_i b_j$ ).

The total energy and the pressure are computed as follows:

$$e_{\text{tot}} = u + \frac{1}{2} \rho v^2 + \frac{1}{8\pi} B^2, \quad (2.5)$$

$$P = (\gamma - 1)u, \quad (2.6)$$

with  $\gamma$  being the adiabatic index. For magnetic fields, the divergence constraint on magnetic field is maintained by

$$\nabla \cdot \mathbf{B} = 0. \quad (2.7)$$

The local gravitational acceleration can be obtained from the solution of the Poisson equation. If the gravitational potential at the location of the fluid parcel is  $\Phi$ , then from the Poisson equation:

$$\nabla^2 \Phi = 4\pi G \rho, \quad (2.8)$$

$$\mathbf{g} = -\nabla \Phi. \quad (2.9)$$

$G$  here is the universal gravitational constant. The contribution to the potential  $\Phi$  can include other components apart from the gas itself, such as old stars, dark matter, or star clusters represented by sink particles. We go more into the details pertaining to our simulations when we discuss code-specific computation of gravitational terms in Section 2.2.

## 2.1.3

## LIMITATIONS

The ideal-MHD equations are not valid in situations where the assumptions behind them break down: in relativistic conditions, for example. In addition, the inclusion of magnetic fields under the assumptions of infinite conductivity and perfect coupling between charged particles and the mostly neutral gas leads to additional caveats. These limitations can be divided into two categories: physical and numerical. Let us briefly consider these limitations, particularly in the context of our simulations.

**Physical limitations:** The ionization fraction inside dense molecular clouds is low. For example, [Caselli et al. \(1998\)](#) estimate the ionization fraction to be in the range of  $10^{-6}$  to  $10^{-8}$ , while [Goicoechea et al. \(2009\)](#) find that in the Horsehead nebula, the values follow a gradient from  $10^{-4}$ , to values as low as  $10^{-9}$ . This can result in situations where particularly in the dense ISM, the gas and charged particles are imperfectly coupled ([Elmegreen, 1979](#); [Mathis et al., 1977](#); [Nishi et al., 1991](#)). The charged ions can then experience an ion neutral drift, where the neutral particles have a drift motion with respect to the charged particles. This mechanism, called **ambipolar diffusion**, can cause magnetically sub-critical structures to become super-critical and collapse, and is not taken into account in the ideal MHD equations.

The derivation of the ideal MHD equations assumes that the conductivity of the medium is close to infinity (e.g. [Stahler & Palla, 2004](#)). In dense cores, this assumption may not be valid, and would lead to dissipation of magnetic energy. This is called **ohmic dissipation**. However, Ohmic dissipation is expected to become important only at particle densities above  $10^{11} \text{ cm}^{-3}$  ([Nakano et al., 2002](#); [Kunz & Mouschovias, 2010](#); [Li et al., 2011](#)), a number at least two orders of magnitude higher than the highest values we reach.

A further third non ideal MHD effect relevant for star formation is **Hall diffusion**. The Hall effect is the phenomenon that in the presence of magnetic fields, moving charged particles can create an electric field perpendicular to both the direction of the current and the magnetic fields, thereby violating the infinite conductivity assumption of ideal MHD. This can occur in discs around forming stars due to relative diffusion of oppositely charged ions in presence of magnetic fields, and introduces a further non-ideal term similar to resistivity ([Wardle, 2004](#)).

Of the three effects, the ambipolar diffusion is active on cloud scales at relatively lower densities ( $< 10^7 \text{ cm}^{-3}$ , [Nakano et al. \(2002\)](#)), ohmic dissipation is relevant for dense cores, while the Hall effect is important for the intermediate range, in particular for forming discs around protostars ([Li et al., 2011](#)). For the densities and length scales investigated in our simulations, we expect only the ambipolar diffusion to have any possible impact on our results.

**Numerical limitations:** The primary numerical limitations in ideal MHD simulations arise from difficulties in maintaining the  $\nabla \cdot \mathbf{B} = 0$  constraint. We must discretize the equations of ideal MHD in order to solve them, and this results in numerical errors. Left unchecked, this can generate non-zero  $\nabla \cdot \mathbf{B}$  values in the flow of the fluid, leading to spurious unphysical forces ([Derigs et al., 2017](#)). Any numerical solution to the ideal MHD equations therefore requires careful treatment of the divergence errors. To treat this, the MHD simulations in this thesis have been run with the so called ES solver, which guarantees positive pressure and entropy,

and allows for the least possible diffusion (Derigs et al., 2016, 2018).

#### 2.1.4

##### DESCRIPTION OF SHOCKS

We have above discussed the ideal MHD equations and their possible limitations. Another important detail when treating with the equations of MHD is how to deal with shocks. This is particularly relevant in the astrophysical context.

One of the key assumptions that allows us to describe astrophysical fluids using the Euler equations is that the mean free path of particles is much smaller than relevant length scales, and therefore can be approximated as evolution of continuous fluid parcels. If there is a discontinuity in quantities such as pressure or density in the fluid, the continuity assumption is violated. Such discontinuities, called shocks, therefore need careful treatment.

Astrophysical situations often contain shocks. Physically, a shock is a thin layer of fluid where the mean free path of the fluid particles is comparable to the width of the layer. On both sides of the shock (called pre-shock and post-shock fluid, depending on if the shock has already passed through the region), the continuous fluid description we have discussed is valid. At the shock layer, however, viscosity becomes important and ordered gas motion (kinetic energy) gets converted into random thermal motions (internal energy).

Fortunately, shocks can still be treated in a meaningful way by approximating the discontinuity in the solution to the Euler equations. The bulk fluid quantities in the pre-shock and the post-shock fluid can be related by simple considerations of mass, momentum, and energy conservation. If the fluid flow direction is perpendicular to the shock front, then in absence of magnetic fields, the density, velocity and pressure are related in the following way:

$$\rho_1 v_1 = \rho_2 v_2, \quad (2.10)$$

$$P_1 + \rho_1 v_1^2 = P_2 + \rho_2 v_2^2 \quad (2.11)$$

$$\frac{1}{2} v_1^2 + \frac{\gamma}{\gamma - 1} \frac{P_1}{\rho_1} = \frac{1}{2} v_2^2 + \frac{\gamma}{\gamma - 1} \frac{P_2}{\rho_2} \quad (2.12)$$

where the suffixes 1 and 2 refer to the pre- and post-shock gas, respectively; the velocities are computed in the frame of the shock (shock velocity  $v_{shock} = 0$ ), and the three relations reflect mass, momentum, and energy conservation, respectively. These conditions together are called Rankine-Hugoniot jump conditions. The density, velocity and pressure contrasts can be expressed in terms of the Mach number of the incoming flow  $\mathcal{M}_1 = v_1/c_{s,1}$ ,  $c_{s,1}$  being the sound speed of the pre-shock medium.

$$\frac{\rho_2}{\rho_1} = \frac{v_1}{v_2} = \frac{(\gamma + 1)\mathcal{M}_1^2}{2 + (\gamma - 1)\mathcal{M}_1^2} \quad (2.13)$$

$$\frac{P_2}{P_1} = \frac{2\gamma\mathcal{M}_1^2 - (\gamma - 1)}{\gamma + 1} \quad (2.14)$$

$$\frac{T_2}{T_1} = \frac{(2\gamma\mathcal{M}_1^2 - (\gamma - 1))(2 + (\gamma - 1)\mathcal{M}_1^2)}{(\gamma + 1)^2\mathcal{M}_1^2} \quad (2.15)$$

This tells us, for example, that for highly supersonic shocks ( $\mathcal{M}_1 \gg 1$ ), the density

contrast approaches  $\frac{\gamma+1}{\gamma-1}$ , something that can be tested in numerical implementations. For monoatomic gas,  $\gamma = 5/3$ , and the density contrast becomes  $\rho_2/\rho_1 \approx 4$ .

If  $\mathcal{M}_1 = 1$ , then  $\rho_2 = \rho_1$ ,  $P_2 = P_1$  and  $T_2 = T_1$ , i.e. there is no shock. Therefore shocks can only occur when the pre-shock gas is supersonic. If the pre-shock gas is subsonic, then the solution generated by the jump conditions suggests that the temperature and therefore the entropy of the post shock gas lower than the pre-shock gas, i.e. that the second law of thermodynamics is violated. Shocks are therefore solely associated with supersonic flows.

So far we have considered a situation when the flow of gas is perpendicular to the shock front. If this is not the case, then such shocks are called oblique shocks. In this case, the component of the flow parallel to the shock front has no discontinuities in velocity, i.e.

$$v_{2,\parallel} = v_{1,\parallel} = v_1 \cos\phi, \quad (2.16)$$

where  $\phi$  is the angle between the incident velocity direction and the shock front. In contrast, the component of the flow perpendicular to the front follows the same jump conditions described above, provided that the perpendicular component of the velocity,  $v_1 \sin\phi$ , is still supersonic.

Shocks become considerably more complicated when magnetic fields are present. This can be understood by the fact that in the hydrodynamic case, we have one characteristic velocity: the sound speed, and the shock is associated with a jump in the fluid velocity from above the sound speed in the pre-shock gas, to below. In presence of magnetic fields, we have two additional characteristic velocities: the velocity of the fast and slow magnetosonic waves (see e.g. [Goossens, 2003](#)). This results in six possible shock configurations, each associated with the jump of the flow velocity from above a given phase velocity (fast wave or slow wave velocity, or the sound speed) to below the phase velocity of the same or a different wave, subject to the overall velocity actually decreasing.

## 2.2 FLASH 4

We have discussed so far the primary equations of ideal MHD that we solve to numerically evolve astrophysical fluids. In this section, we provide a short overview of FLASH 4, the code used for the simulations performed and analyzed in this thesis. FLASH is highly parallelizable, 3D, adaptive mesh refinement (AMR) based magneto-hydrodynamic code developed by the FLASH Center for Computational Science of the University of Chicago. We describe some of the key modules in the context of this present thesis below. More details on the architecture and modules of FLASH can be found in [Fryxell et al. \(2000\)](#) and [Dubey et al. \(2008\)](#).

### GENERAL DATA STRUCTURE

FLASH organizes data in a tree-based structure, based on basic units called "blocks", representing nodes in the tree structure. The PARAMESH library based grid unit (see [MacNeice et al., 2000](#), for details of PARAMESH) organises the computational domain hierarchically into blocks. The block that contains the entire computational domain is called a root block and corresponds to refinement level  $l = 1$ . A root block can be subdivided into 8 blocks with the same cubic shape, and these would correspond to blocks at a refinement level  $l = 2$ . This tree-based structure generates

the adaptive nature of the FLASH grid. Each block contains  $8^3$  cells, although this number is modifiable.

#### MHD SOLVER

The core of evolving the magneto-hydrodynamic equations of fluid dynamics is solving the equations between two neighbouring cells. This is done using the Riemann solver. The Riemann solver computes the mass, momentum, energy and magnetic field flux between two neighbouring cells. The hydrodynamic simulations analyzed in this thesis were all run with the directionally split Bouchut 5-wave HLL5R MHD solver, with the magnetic field set to zero (Bouchut et al., 2007; Waagan, 2009; Bouchut et al., 2010; Waagan et al., 2011). The Bouchut 5 solver is a stable, approximate Riemann solver which preserves positive density and entropy for highly supersonic flows. For the MHD simulations, we use the ES solver to evolve the gas (Derigs et al., 2016, 2017, 2018). In addition to the advantages mentioned above, the ES solver accomodates minimum possible dissipation, and treats the errors in the magnetic field divergence in a manner consistent with the second law of thermodynamics. In FLASH, both schemes are performed in a directionally split manner, in the sense that along all three dimensions, a 1D Riemann problem is solved subsequent to each other.

#### GRAVITY

The gravitational potential and acceleration are obtained by the gravity module of FLASH. The gravitational potential can be considered a sum of the self-gravity, sink particles representing stellar clusters (when included), and an external potential. For the present simulations, the external potential represents the potential due to old stars in the galaxy. The stellar potential is calculated according to a stellar surface density of  $30 M_{\odot} \text{ pc}^{-2}$ , with a scale height of 100 pc according to Spitzer (1942). The contribution to variations in potential due to the presence of dark matter has been ignored. The present simulations do not include any sink particles, so no contribution from sink particles needs to be included.

The self-gravity from the gas is calculated based on Eqs. 2.8 and 2.9. The implementation in FLASH is performed using TreeRay, an OctTree based solver developed by Wünsch et al. (2018) that uses the hierarchical tree structure of FLASH data to calculate gravitational acceleration. For evaluation of acceleration at a given point, the solver ‘opens’ a block starting from the root level block, depending on if the block fulfills the chosen multipole acceptance criterion (MAC) or not. Details of the tree solver can be found in Wünsch et al. (2018).

#### HEATING, COOLING, AND CHEMICAL EVOLUTION

The simulations also use a simplified non-equilibrium chemical network, the so called NL97 network based on Nelson & Langer (1997) and Glover & Mac Low (2007a,b). The chemical network traces the evolution of  $\text{H}_2$ ,  $\text{H}$ ,  $\text{H}^+$ ,  $\text{CO}$ ,  $\text{C}^+$ ,  $\text{e}^-$  and  $\text{O}$ . A given chemical species is evolved according to its conservation equation, analogous to the mass conservation equation of 2.1. For species  $i$ , then,

$$\frac{\partial \rho_i}{\partial t} + \nabla \cdot (\rho_i \mathbf{v}) = C_i(\rho, T, \dots) - D_i(\rho, T, \dots), \quad (2.17)$$



where  $\rho_i$  is the density of the  $i$ th species, and  $C_i$  and  $D_i$  are the creation and destruction rates of the given species, respectively, depending on the temperature, its density, as well as densities of other species. In order to solve the equations, the advection and the source terms are treated separately. The advection terms, representing the species as if its abundance were constant, can be solved as the solution of a scalar conservation equation similar to Eq. 2.1:

$$\frac{\partial \rho_i}{\partial t} + \nabla \cdot (\rho_i \mathbf{v}) = 0. \quad (2.18)$$

The right hand side of Eq. 2.17 can then be treated as a set of coupled ordinary differential equations:

$$\frac{d\rho_i}{dt} = C_i(\rho, T, \dots) - D_i(\rho, T, \dots). \quad (2.19)$$

These equations are solved simultaneously with the heating and cooling. The net heat (positive or negative) generated in the chemical reactions contributes to the  $\dot{u}_{\text{heat}}$  term in equation 2.3.

The gas in the simulation is set to solar metallicity, with fixed elemental abundances of carbon, oxygen and silicon with respect to hydrogen ( $x_{\text{C}} = 1.14 \times 10^{-4}$ ,  $x_{\text{O}} = 3.16 \times 10^{-4}$ ,  $x_{\text{Si}} = 1.5 \times 10^{-5}$ ). The dust to gas ratio is set to 0.01. At the beginning of the simulation, all H and C are assumed to be in their ionized form.

There is further an interstellar radiation field (ISRF) of strength  $G_0 = 1.7$  in Habing units (Habing, 1968; Draine, 1978). The ISRF is attenuated depending on the column density of the gas, thereby allowing for dust shielding as well as (self-) shielding for  $\text{H}_2$  and CO. This is implemented by the TREE-RAY OPTICAL DEPTH module, developed by Wunsch et al. (2018).

For each cell in the simulation domain, the OPTICAL DEPTH module calculates radiation intensity reaching the cell from every direction. This is done by creating a pixelized sphere around the cell using the HEALPIX algorithm. The module computes the column density of total hydrogen, molecular  $\text{H}_2$  and CO in each healpix pixel surrounding the cell. Based on this, OPTICAL DEPTH then stores the average visual extinction  $A_{\text{V},3\text{D}}$ , as well as shielding coefficients for  $\text{H}_2$  and CO.

The three dimensional  $A_{\text{V},3\text{D}}$  computed in this manner takes into account the three dimensional geometry and is different from the usual  $A_{\text{V}}$  computed by observers from total Hydrogen column density. The three dimensional visual extinction is given by

$$A_{\text{V},3\text{D}} = -\frac{1}{2.5} \ln \left[ \frac{1}{N_{\text{PIX}}} \sum_{i=1}^{N_{\text{PIX}}} \exp \left( -2.5 \frac{N_{\text{H},\text{tot},i}}{1.87 \times 10^{21} \text{cm}^{-2}} \right) \right], \quad (2.20)$$

where the sum is carried over each HEALPIX pixel,  $N_{\text{PIX}}$  is the total number of such pixels (usually 48), and  $N_{\text{H},\text{tot},i}$  is the column density computed for the  $i$ th pixel. The sum is exponential because intensity of radiation decreases in an exponential manner in the presence of gas. In essence this method can be thought of as analogous to someone sitting inside this given cell, and computing the column density of the gas in various directions, and then computing  $A_{\text{V},3\text{D}}$  based on the column density along each direction.

## 2.3

## SIMULATION SETUP

Any set numerical equations can be solved only by starting from the proper initial conditions. These initial conditions describe the set of the simulations involved. The results presented in this thesis are based on the SILCC-Zoom (Chapters 4 and 5) and SILCC deep-zoom simulations (Chapter 6). Both of these are in turn based on the SILCC simulations. In this section, we describe all three simulation setups. For a detailed description of the SILCC setup, please see [Walch et al. \(2015\)](#) and [Girichidis et al. \(2016\)](#). For more details on the SILCC-Zoom setup, see [Seifried et al. \(2017\)](#).

## 2.3.1

## SILCC

The SILCC simulations simulate the multi-phase ISM in a stratified galactic box of size  $500 \text{ pc} \times 500 \text{ pc} \times \pm 5 \text{ kpc}$  in the vertical direction. The setup is motivated to investigate ISM dynamics in parts of galaxies with solar neighbourhood conditions in the present day universe. This is modelled by keeping the initial gas surface density at  $\Sigma_{\text{gas}} = 10 \text{ M}_{\odot} \text{ pc}^{-2}$ , although extensions of the original work include runs with different surface densities. The multi phase ISM is created by driving supernova explosions in the galactic disc. The supernova rate is set following the gas surface density, based on the Kennicutt-Schmidt (KS) relation ([Kennicutt, 1998](#)). The strength of the interstellar radiation field is also set based on the same. An example of the spatial distribution of the gas in the SILCC simulations can be seen in Fig. 3, adapted from [Walch et al. \(2015\)](#).

*Density profile*

Initially, the vertical gas profile is set to model an exponential gas distribution:

$$\rho(z) = \max\left(\rho_0 \exp\left(-z^2/h_z^2\right), 10^{-28} \text{ g cm}^{-3}\right), \quad (2.21)$$

where the scale height of the disc  $h_z = 60 \text{ pc}$ , and the mid-plane density  $\rho_0 = 9 \times 10^{-24} \text{ g cm}^{-3}$ , in accordance with the chosen gas surface density. The max function ensures that the exponential does not go down to arbitrarily low values, but cuts off at a background density value of  $10^{-28} \text{ g cm}^{-3}$ . The total mass in the simulation domain is  $2.5 \times 10^6 \text{ M}_{\odot}$ .

*Magnetic fields*

For runs with magnetic fields, an initially uni-directional magnetic field is set along the x direction. The magnetic field strength varies vertically, according to:

$$\mathbf{B} = B_x \hat{x} \quad (2.22)$$

$$B_x(z) = B_{x,0} \left[ \frac{\rho(z)}{\rho_0} \right]^{1/2}, \quad (2.23)$$

where  $B_{x,0} = 3 \mu\text{G}$  is the initial midplane magnetic field strength. The values are chosen to be in accordance with recent observations ([Beck & Wielebinski, 2013](#)).

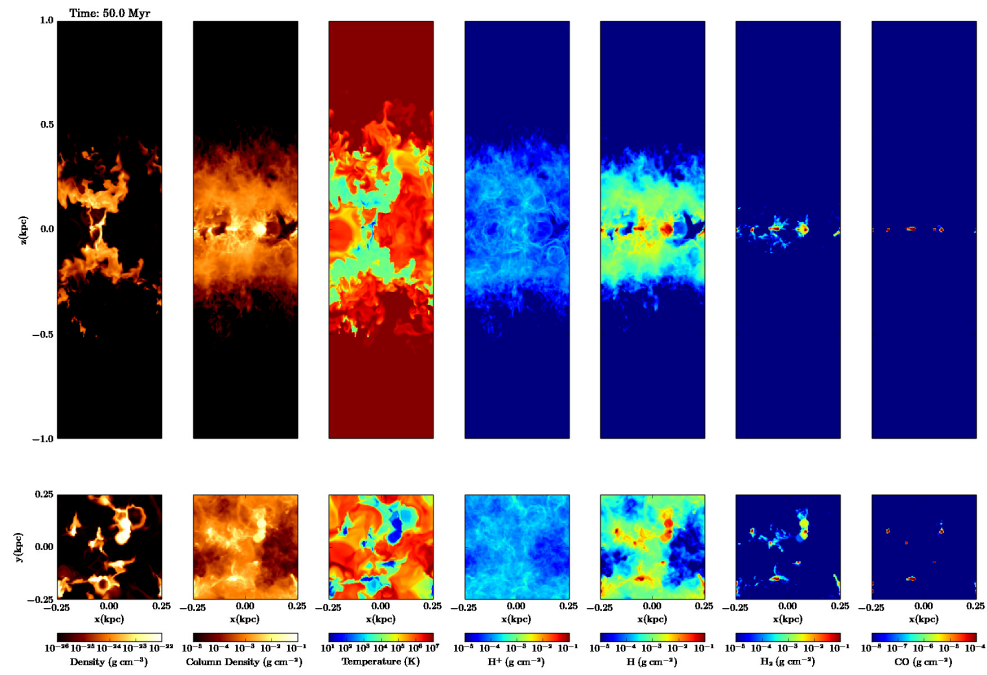


Figure 3: Snapshot of the SILCC simulations, adapted from [Walch et al. \(2015\)](#), Fig. 4. Part of the simulation box of size  $0.5 \text{ kpc} \times 0.5 \text{ kpc} \times 2 \text{ kpc}$ , is shown. The panels show, from left to right, gas density slice, column density projection, gas temperature slice, and column densities of  $H^+$ ,  $H$  and  $H_2$ , and  $CO$ . All slices are taken at  $y = 0$  for the elongated panels, or at  $z = 0$  for the square panels, respectively. Similarly, the column density is projected along the  $y$ - or  $z$ -axis.

*External gravitational potential*

The setup also includes a gravitational potential due to old stars in the galaxy. The stellar population is set to have a surface density of  $\Sigma_{\star} = 30 M_{\odot} \text{pc}^{-2}$ , with the vertical distribution following a  $\text{sech}^2$  profile with a scale height of 100 pc, set according to [Spitzer \(1942\)](#). The potential and gravitational acceleration due to the stars can be then computed by solving the Poisson equation, according to Eqs. 2.8 and 2.9. The stellar mass distribution is assumed to vary only in the z-direction, and therefore the resulting gravitational acceleration is also only in the vertical direction.

*Temperature*

The temperature of the gas near the midplane is set initially to 4500 K. The low density gas distant from the midplane (where the gas initially has the background density of  $10^{-28} \text{g cm}^{-3}$ ), is set at an initial temperature of  $4 \times 10^8 \text{K}$ , representing hot gas from the halo. All C is initially set to be in an ionized form, while the disc plane gas is set to consist initially of entirely atomic hydrogen.

*Supernovae*

Initially all gas is set at rest. The turbulence in the gas is driven by multiple supernova explosions. The runs used for SILCC-Zoom generally use mixed driving, where 50 percent of the supernova are exploded in local density peaks, while the other 50 percent are driven in random positions. The supernovae rate is chosen to be  $15 \text{Myr}^{-1}$ , consistent with the KS relation.

*Resolution*

The base resolution for the SILCC simulations is 3.9 pc near the midplane, and 7.8 pc for  $|z| > 2 \text{kpc}$ .

## 2.3.2

## SILCC-ZOOM

The supernovae explosions in the SILCC simulations drive the turbulence and create the multi-phase ISM. Although the gas initially starts either ionized or atomic, several cold and dense molecular clouds develop from the diffuse ISM. They accrete gas, occasionally merge, and are moved around by nearby supernovae. The so called SILCC-Zoom simulations intend to investigate the formation and evolution of such molecular clouds in greater detail and with a better spatial resolution.

*Refinement strategy*

In order to capture molecular cloud formation and early stages of their evolution, it is essential to study the molecular clouds with a better resolution before they have become well developed highly molecular entities. For this purpose, the SILCC-Zoom approach identifies regions where different molecular clouds are forming, and then rewind the simulations and run them from a time when the typical number density inside the zoom-in regions does not exceed a few times  $10 \text{cm}^{-3}$ . This represents the starting time  $t_0$  for the zoom-in simulations and is referred to as  $t_{\text{evol}} = 0$ .

Usually molecular clouds forming in isolation are chosen. FLASH allows custom sized boxes with their own refinement strategies. For the purpose of SILCC-Zoom

simulations, typically boxes of size  $\sim 100$  pc are chosen. The boxes are chosen by eye. At  $t_0$ , the gas inside the SILCC-Zoom boxes is allowed to refine to a higher resolution compared to the 3.9 pc resolution of the base SILCC grid. The gas is refined according to two different refinement criteria. Up to a resolution of 0.5 pc (3 refinement levels above base grid), the SILCC-Zoom box is refined according to variations in density. Following [Löhner \(1987\)](#), this approach refines based on the second derivative of the density field. A second refinement is performed using the criterion that the local Jeans length for each cell should be resolved by at least 16 cells in each dimension ([Truelove et al., 1997](#); [Federrath et al., 2011](#)). This refinement strategy is used to refine up to a resolution of 0.125 pc (5 levels above base grid).

An important question related to the zoom-in process is how to progress from the base grid resolution to the maximum resolution. If this is done instantaneously, it can possibly lead to numerical artefacts. While if this process is done over a time period comparably longer than the free fall time or the assemble time of the cloud, this might affect key features of the cloud. [Seifried et al. \(2017\)](#) found that the best results are obtained if during the zoom-in process, around  $n = 200$  time steps are spent on each intermediate refinement level, corresponding to a total zoom-in time of roughly 1-1.5 Myr. The present simulations follow this prescription. For the details of the effect of refinement time on the resulting features of the molecular cloud, please see Section 4.3 of [Seifried et al. \(2017\)](#).

#### *Analyzed clouds*

Chapters 4 and 5 (papers I and II) are based on the analysis of several hydrodynamic (HD), as well as MHD molecular clouds. We analyze a total of eight clouds (two HD and six MHD clouds). Each SILCC region typically includes two zoom-in regions. As a result, the different MHD runs differ in the initial turbulent seed to each other (as well as to the HD clouds), but otherwise contain identical initial conditions. The naming convention of the clouds followed in this thesis is as follows: the two HD clouds are named as MC1-HD and MC2-HD, while the various MHD clouds are named as MC1-MHD, MC2-MHD and so on. We highlight an example SILCC-Zoom cloud MC1-MHD in Fig. 4, adapted from Fig. 2 of [Seifried et al. \(2019\)](#), that shows the highly inhomogeneous and filamentary structure of the clouds. The relevant details related to the different clouds are presented in papers I and II. Further details of the different runs can be found in [Seifried et al. \(2017\)](#) for the HD clouds, and in [Seifried et al. \(2019\)](#) for the different MHD clouds.

### 2.3.3

#### SILCC DEEP-ZOOM

The SILCC deep-zoom simulations are a natural extension of the zoom-in method. Due to the relatively high computational cost of the SILCC-Zoom simulations, it is not feasible to run the entire SILCC-Zoom box to a much higher refinement. For this purpose, the deep-zoom simulations embed zoom-in boxes inside the SILCC-Zoom regions themselves. This allows us to have smaller regions with much higher resolution. For the purpose of this thesis, we have implemented such deep-zoom boxes of size  $\sim 50$  pc inside zoom in boxes, in order to capture and resolve structures such as filaments. We highlight the spatial extent of the SILCC deep-zoom simulations in Fig. 5. The left panel of Fig. 5 denotes the main stratified galactic disc, obtained from the larger SILCC environment. The black box denotes the central portion of the SILCC-Zoom cloud MC1-MHD, shown in the middle panel. The black box in

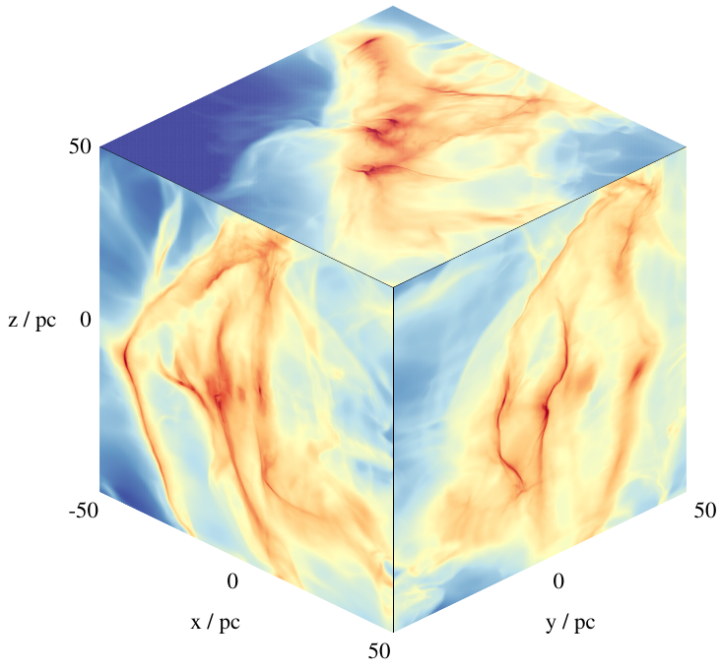


Figure 4: SILCC-Zoom cloud MC1-MHD at  $t_{\text{evol}} = 3$  Myr, from different viewing angles. Adapted from Fig. 2 of Seifried et al. (2019)

the middle panel highlights the typical scales analyzed for the SILCC deep-zoom analysis, shown in a larger view in the right panel. Note that the actual deep-zoom box is larger than the 4 pc region showed in the right panel.

In terms of refinement, the deep-zoom simulations implement a similar refinement strategy to the zoom-in simulations. The deep-zoom simulations presented in this thesis in Chapter 6, have a base grid refinement of up to level 9 (4 refinement levels above base grid), and a refinement based on Jeans criterion for up to level 14 (9 refinement levels above base grid). This corresponds to a maximum resolution of 0.0078 pc, or 1600 AU.

A natural question that arises is at what time do we choose to begin the refinement procedure. We choose this to be relatively soon after the SILCC-Zoom refinement has finished and the simulation has reached a maximum resolution of level 10, but all the cells are still well resolved in terms of their Jeans length.

In terms of the start of the original SILCC, the SILCC-Zoom, and the SILCC deep-zoom simulations, we therefore have three timescales. These are highlighted in Fig. 6. The overall simulation time  $t$  reflects the time from the beginning of the simulation.  $t_{\text{evol}}$  represents the time the SILCC-Zoom refinement starts. Shortly after the SILCC-Zoom refinement finishes, we start the evolution of the deep-zoom cloud regions. This start time is represented by  $t_{\text{deep}}$ .

## 2.4

### ANALYSIS METHOD

From the previous sections, we know how we model and evolve the relatively complicated ISM fluid. The complicated nature of the simulations themselves imply that

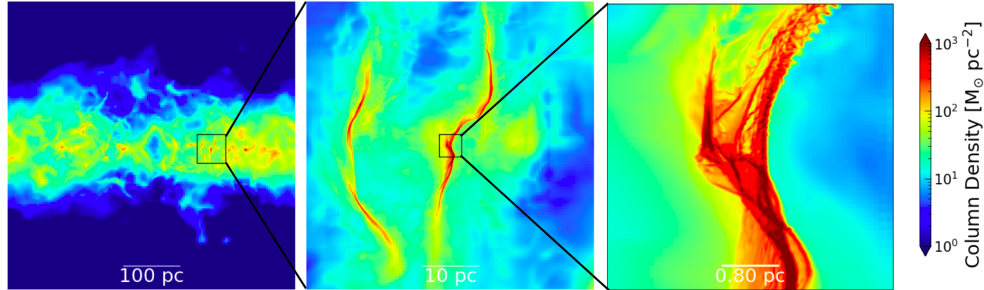


Figure 5: The length scales of the SILCC, SILCC-Zoom, and the SILCC deep-zoom simulations. **Left:** A  $500 \times 500$  pc region of the SILCC disc shown as a projection with the deep-zoom region MC1-MHD highlighted as a black outlined box. **Middle:** A  $50 \times 50$  pc portion of the SILCC-Zoom region MC1-MHD with part of a deep-zoom region shown. **Right:** A typical  $4 \times 4$  pc deep-zoom portion used for analysis. Note that the actual deep-zoom region is much larger compared to the right box shown.

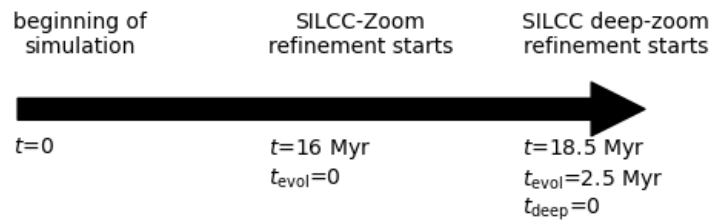


Figure 6: Relation between the simulation start time  $t$ , SILCC-Zoom evolution time for the two deep-zoom clouds  $t_{\text{evol}}$  and the deep-zoom evolution time  $t_{\text{deep}}$ .

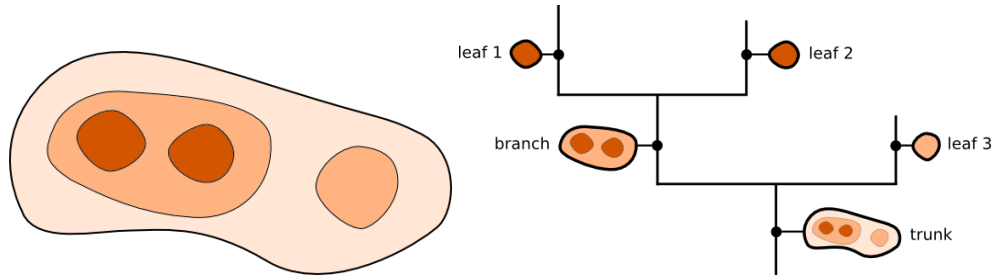


Figure 7: Left: Cartoon illustration of a hypothetical 2D intensity distribution. Right: The resulting dendrogram tree. The large-scale, low intensity structure is picked up as a trunk. Further nested branches show the hierarchical nature of the structure. Structures which contain no further sub-structures are called leaves. Both figures adapted from the [astrodendro](#) website.

we need to devise comprehensive methods of analysis. The basic analysis method we employ in Chapters 4 through 6 is as follows: we identify structures inside the simulations, and then analyze their shapes and their energetic behaviour. The layout of the analysis section is as follows: we explain how we identify structures and classify their shapes in Section 2.4.1. The computation of self-gravity of the individual structures, though simple in principle, are computationally demanding. This is explained in Section 2.4.2. The method of energetic analysis used primarily in paper I and Chapter 6, we elaborate in Section 2.4.3. In paper I we further use a method of tidal analysis. This is explained in Section 2.4.4.

### 2.4.1

#### STRUCTURE IDENTIFICATION AND CLASSIFICATION

##### *Identification*

The principal method that has been used in this thesis to investigate structures forming inside the simulated molecular clouds, is the method of dendrograms. Dendrograms are a model independent method to determine hierarchical structures in 2 and 3 dimensions (Rosolowsky et al., 2008b). Performed on a 3D density cube, the dendrogram algorithm essentially outputs a list of density iso-surfaces, and arranges them in a tree. This allows us to identify structures and analyze their dynamics in detail, without any assumption on their shape or profile.

Given a density cube, the output of the dendrogram essentially depends on three parameters: the initial starting threshold  $\rho_0$ , the density jump  $\Delta\rho$ , and the minimum number of cells (pixels for 2D data) any structure must contain  $N_{\text{cells}}$ . We briefly outline here the effect of varying these three parameters. The dendrogram analysis here was performed using `astrodendro`<sup>1</sup> (Robitaille et al., 2019), a Python package to compute dendrograms of observed and simulated data. A visual example of how dendrograms work for 2D data is shown as an example cartoon in Fig 7, taken from the `astrodendro` website<sup>1</sup>.

**Starting threshold  $\rho_0$ :** This parameter determines how much gas the dendrogram algorithm initially considers to find structures. Decreasing the starting threshold allows us to find lower and lower density structures. For the purpose of this thesis,

<sup>1</sup><http://www.dendrograms.org/>



we have primarily used a density threshold of  $\rho_0 = 10^{-22} \text{ g cm}^{-3}$ , while for probing lower density environments we have used  $\rho_0 = 10^{-24} \text{ g cm}^{-3}$ . For the deep-zoom runs, we have used a higher threshold, with  $\rho_0 = 10^{-20} \text{ g cm}^{-3}$ .

**Density jump  $\Delta\rho$ :** The density jump parameter controls what is the minimum density threshold difference between two levels of dendrogram structures (i.e. parent and children structure). Lowering this value increases the number of structures produced, and the number of structures between the large scale structures, and the smallest leaf structures that are no longer subdivided. Due to the high range in density of the medium, we have built the dendrogram on the logarithm of the densities, using  $\Delta\log_{10} \rho = 0.1$  or  $0.2$ . For  $\Delta\log_{10} \rho = 0.1$ , this produces a maximum possible of 10 structures between each order of magnitude (for example, between  $10^{-22} \text{ g cm}^{-3}$  and  $10^{-21} \text{ g cm}^{-3}$ ). Building the dendrogram on the density cube itself, instead of the logarithm, with a  $\Delta\rho = 10^{-22} \text{ g cm}^{-3}$ , produces more structures but the overall behaviour remains the same. Varying the  $\Delta\log_{10} \rho$  also modifies the number of structures, but keeps their statistical properties (scaling relations, density-size relations etc.) intact.

**Minimum number of cells  $N_{\text{cells}}$ :** The minimum cells criterion ensures that the dendrogram is not sensitive to noise in the data. Varying  $N_{\text{cells}}$  only affects the smallest scales in the dendrogram, and leaves the larger scales intact. We perform most of the dendrogram analysis with  $N_{\text{cells}} = 100$ , corresponding to a size of  $\sim 0.5$  pc for the SILCC-Zoom runs and  $\sim 0.03$  pc for the deep-zoom runs at the highest resolution. Note that the size-scale is  $(N_{\text{cells}})^{1/3}$  times higher than the maximum resolution for analysis in 3D. Apart from  $N_{\text{cells}} = 100$ , we test the analysis using  $N_{\text{cells}} = 1000$  when probing larger scales, and  $N_{\text{cells}} = 50$  for some test runs when performing a lower resolution analysis. This does not affect the general statistical properties of the results.

**Pruning peak  $\rho_{\text{prune}}$ :** Apart from the three main parameters, the dendrogram offers an additional pruning parameter  $\rho_{\text{prune}}$ . This defines the minimum value of peak density a structure must have in order to be considered an independent structure. If this is set equal to or lower than  $\rho_0$ , it plays no role at all. It can be used to prune lower density structures. For paper I of this analysis, we set this to  $10^{-21} \text{ g cm}^{-3}$ . This reduces the number of structures, by mostly getting rid of structures which have peaks just over  $10^{-22} \text{ g cm}^{-3}$ , or roughly  $\sim 100 \text{ cm}^{-3}$ .

Overall, while we have not performed a systematic investigation into the differences in behaviour from using different parameters, they do not seem to have any unexpected bearings on the results.

The choices of parameters are slightly different in the different analyses, depending on our necessities. For example, we use a pruning peak if we want to focus on the more denser end of the structures, and want to only get the large scale structures at or near the starting density threshold. The different parameters used for the analysis are summarized in Table 2.1.

### *Classification*

Once we obtain the dendrogram structures, we classify them using a fitting method based on the moment of inertia (MOI) of the structures. We compute an equivalent MOI ellipsoid, which has the same mass, center of mass, and MOI tensor as the

Used where	Resolution [pc]	$\rho_0$ [ $\text{g cm}^{-3}$ ]	$\Delta \log_{10} \rho$	$N_{\text{cells}}$	$\rho_{\text{prune}}$ [ $\text{g cm}^{-3}$ ]
Paper I	0.125	$10^{-22}$	0.1	100	$10^{-21}$
Paper II	0.125	$10^{-22}$	0.1	100	None
	0.25	$10^{-24}$	0.2	100	None
Chapter 6	0.0078	$10^{-20}$	0.1	100	None

Table 2.1: Information on the parameters used for the parameters of the dendrogram analyses used in the different investigations. From left to right are: in which investigation were these parameters used, the grid resolution at which it is performed, the starting density, the logarithmic density jump, the minimum number of cells in structures, the density of the pruning peak used.

original structure. For a uniform density ellipsoid of mass  $M$  and axes lengths  $a, b, c$  with  $a \geq b \geq c$ , the moments of inertia along the three principal axes are as follows:

$$\begin{aligned}
 I_a &= \frac{1}{5}M(b^2 + c^2), \\
 I_b &= \frac{1}{5}M(c^2 + a^2), \\
 I_c &= \frac{1}{5}M(a^2 + b^2),
 \end{aligned}
 \tag{2.24}$$

where  $I_c \geq I_b \geq I_a$ . If the principal moments of inertia of our given dendrogram structure are  $A, B$  and  $C$ , respectively, then the ellipsoid has an equivalent moment of inertia if

$$A = I_a, \quad B = I_b, \quad C = I_c. \tag{2.25}$$

This leads to the following equation for computing the axes lengths of the equivalent ellipsoids:

$$\begin{aligned}
 a &= \sqrt{\frac{5}{2M}(B + C - A)}, \\
 b &= \sqrt{\frac{5}{2M}(C + A - B)}, \\
 c &= \sqrt{\frac{5}{2M}(A + B - C)}.
 \end{aligned}
 \tag{2.26}$$

We then use the aspect ratio of the axes of the ellipsoid to categorize the different structures into four categories: sheets, curved sheets (sheet\_c from here on), filaments, and spheroids.

$$\begin{aligned}
 \text{sheet: } & \frac{a}{b} \leq f_{\text{asp}}, \frac{a}{c} > f_{\text{asp}} \\
 \text{filament: } & \frac{a}{b} > f_{\text{asp}} \\
 \text{spheroidal: } & \frac{a}{c} \leq f_{\text{asp}}, \text{ contains its own COM} \\
 \text{sheet\_c: } & \frac{a}{c} \leq f_{\text{asp}}, \text{ does not contain its own COM.}
 \end{aligned}
 \tag{2.27}$$

The aspect ratio factor  $f_{\text{asp}} = 3$  is a user defined parameter. The addition of the COM criterion allows us classify some curved sheet-like structures, which would

otherwise be identified as spheroids. If a sheet-like structure is highly curved, it is possible for this structure to have three comparable moments of inertia eigenvalues. Based solely on the aspect ratios, this structure would then be classified as a spheroid. If we add the additional criterion that the structure must contain its own center of mass in order to be classified as a spheroid, however, we can distinguish between the two situations.

Note that for a filament, even a curved one would typically still be a planar structure, and therefore would have at least one ellipsoid axis much shorter than the other two. In principle, this could posit certain situations where the filament is classified as a sheet. However, this seems to be a rather extreme case and we do not find obvious examples of this kind from visual inspection.

Finally, all such simplistic methods are of course limited as the filaments and sheets in the simulations can have very complex morphological shapes, particularly at larger scales, and a more thorough classification would require treating many of the structures individually. This is beyond the scope of this thesis.

#### 2.4.2

##### GRAVITY TREE

For the purpose of analyzing the energetics of the dendrogram structures, we often need to estimate the self-gravitational potential energy. Further, for performing a tidal analysis (see Section 2.4.4, as well as paper I), we need estimations of the acceleration vector for each point inside a given structure.

This is in principle quite straight forward. In a direct computation, at position  $\mathbf{r}_i$ , the potential  $\Phi_i$  and acceleration  $\mathbf{g}_i$  can be computed as follows:

$$\Phi_i = - \sum_{\substack{j=1 \\ j \neq i}}^N \frac{Gm_j}{|\mathbf{r}_i - \mathbf{r}_j|} \quad (2.28)$$

$$\mathbf{g}_i = - \sum_{\substack{j=1 \\ j \neq i}}^N \frac{Gm_j}{|\mathbf{r}_i - \mathbf{r}_j|^3} (\mathbf{r}_i - \mathbf{r}_j) \quad (2.29)$$

where  $N$  is the total number of cells,  $m_j$  is the mass of the  $j$ th cell and  $\mathbf{r}_j$  is its position vector. The total self-gravitational potential energy is given by

$$E_{\text{PE}} = \frac{1}{2} \sum_{i=1}^N m_i \Phi_i. \quad (2.30)$$

The factor  $1/2$  here ensures that we consider every mass particle pair only once while counting. While simple in nature, such a computation is an  $\mathcal{O}(N^2)$  calculation, and quite expensive for the largest structures, which have  $\sim 10^6$  or more cells. For this purpose, we perform this computation using a KD tree.

KD tree, short for k-dimensional tree is a data structure that partitions k-dimensional space and organizes points in a hierarchical tree manner. Each node in k-dimensional space (here 3 dimensional) can contain information such as mass and position of the nodes. It is created by recursively splitting each node in a binary fashion (i.e. each node is split into two children nodes). Typically, both children nodes contain roughly an equal number of points. The splitting plane is selected by cycling through the different spatial axes. Essentially, then, for a KD tree, we split the volume of the structure recursively along the  $x$ -,  $y$ - and  $z$ - direction, respect-

ively, each time dividing up the volume of the node into two roughly equal mass bins. For each node, we know from which node it was created (called parent node), and into which nodes it is partitioned into (children nodes). This gives us then the full hierarchical tree.

Once the tree is constructed, potential and acceleration at any given point can be estimated by walking the tree starting from the root node, representing in this case the entire dendrogram structure. To understand the process of walking the tree, let us imagine that we want to compute the potential at a point which is very far away from our structure. If this point is distant enough to our structure, we can treat our structure as a point source and use the information available only in the root node to approximate the value of the potential at this point. As we bring this point closer and closer together, this approximation will become worse and worse until it does not hold anymore. In such a case, we would have to "open" the node and access information of its two children nodes. To determine when we open a node, we use here a simple geometric opening angle criterion. The opening angle  $\theta_{\text{open}}$  for a given node and a given evaluation point  $\mathbf{r}_{\text{eval}}$  is calculated as follows:

$$\theta_{\text{open}} = \frac{\max(\Delta x, \Delta y, \Delta z)}{|\mathbf{r}_{\text{eval}} - \mathbf{r}_{\text{node}}|}, \quad (2.31)$$

where the position of the mode  $\mathbf{r}_{\text{node}}$  represents the center of mass of all the mass inside that node and  $\Delta x$ ,  $\Delta y$ ,  $\Delta z$  represent the maximum spatial extent of the node in the x-, y-, and z- directions, respectively. A node is opened if  $\theta_{\text{open}} \geq \theta_{\text{crit}}$ , where  $\theta_{\text{crit}}$  is some user defined parameter. If  $\theta_{\text{open}} < \theta_{\text{crit}}$ , then the mass in the node is sufficiently far enough that it can be treated as a point mass for evaluating the potential at that point. The potential and acceleration due to only the node at the evaluation point is then given by,

$$\Phi_{\text{eval,node}} = -\frac{Gm_{\text{node}}}{|\mathbf{r}_{\text{eval}} - \mathbf{r}_{\text{node}}|}, \quad (2.32)$$

$$\mathbf{g}_{\text{eval,node}} = -\frac{Gm_{\text{node}}}{|\mathbf{r}_{\text{eval}} - \mathbf{r}_{\text{node}}|^3}(\mathbf{r}_{\text{eval}} - \mathbf{r}_{\text{node}}). \quad (2.33)$$

Here,  $m_{\text{node}}$  is the mass contained in the node. The total potential and acceleration, then, is the sum of the contribution from the different nodes in the tree-walk:

$$\Phi_{\text{eval}} = \sum \Phi_{\text{eval,node}}, \quad (2.34)$$

$$\mathbf{g}_{\text{eval}} = \sum \mathbf{g}_{\text{eval,node}}. \quad (2.35)$$

Here, the sum is performed over each opened node. This can be further improved by consider higher multipoles, but was not necessary in our case. Using an opening angle of  $\theta_{\text{crit}} = 0.5$ , the difference in the computed potential energy was within  $\sim 1\%$  of the exact value computed using the direct sum.

### 2.4.3

#### VIRIAL ANALYSIS

A large part of the thesis, principally paper I and Chapter 6, is dependent upon an energetic analysis of cloud substructures. For this purpose, we give here a brief overview of the virial theorem.

The virial theorem describes the energetic balance of a mass of gas. This can

be described in Lagrangian form for a fixed mass of gas (Chandrasekhar & Fermi, 1953), or in Eulerian form, for a fixed volume (McKee & Zweibel, 1992). Since FLASH is a grid-based code, a Eulerian description suits our purpose more adequately.

Let us consider a fixed volume  $V$ , surrounded by a surface  $S$ . The center of mass of this volume is situated at  $\mathbf{r}_0$ . Within the volume, we have a well defined density field  $\rho(\mathbf{r})$ , and a velocity field  $\mathbf{v}(\mathbf{r})$ . For ease of computation, we define the position of each point within this volume with respect to the center of mass as

$$\tilde{\mathbf{r}} = \mathbf{r} - \mathbf{r}_0, \quad (2.36)$$

where  $\mathbf{r}$  is the position of the point in the reference frame. For this given configuration, the full Eulerian virial theorem is given as follows:

$$\frac{1}{2} (\dot{I}_E + \dot{\Phi}_I) = W + \Theta_{VT} \quad (2.37)$$

Here  $I_E = \int_V \rho \tilde{\mathbf{r}}^2 dV$  corresponds to the trace of the moment of inertia tensor  $\mathbf{I}$ , component wise defined as

$$I_{ij} = \int_V \rho (\delta_{ij} |\tilde{\mathbf{r}}|^2 - \tilde{r}_i \tilde{r}_j) dV. \quad (2.38)$$

$\Phi_I$  defines here the flux of moment of  $I_E$  through the surface  $S$  and is defined as

$$\Phi_I = \oint_S \rho |\tilde{\mathbf{r}}|^2 v_i \hat{n}_i dS, \quad (2.39)$$

where  $\hat{n}$  is the surface normal vector pointing outwards. The  $\dot{\Phi}_I$  term is a consequence of considering an Eulerian reference frame (i.e. with a fixed volume). The right hand side of Eq. 2.37 corresponds to the sum of the various volume and surface energy terms.  $W$  contains the effect of gravity, while  $\Theta_{VT}$  combines the effect of magnetic fields, thermal energy, and kinetic energy. Let us consider them one by one.

The term  $W$  corresponds to the gravitational energy of this fixed structure, caused by the overall gravitational field. This is defined as

$$W = - \int_V \rho \tilde{\mathbf{r}} \cdot \nabla \Phi_{\text{tot}} dV, \quad (2.40)$$

where  $\Phi_{\text{tot}}$  is the overall gravitational potential, due to matter both inside the fixed volume, as well as outside. The negative gradient of  $\Phi_{\text{tot}}$  corresponds to then the overall gravitational acceleration and can be divided into two parts: the self-gravitational acceleration  $\mathbf{g}_{\text{int}}$  and the gravity due to all matter outside the volume  $V$ ,  $\mathbf{g}_{\text{ext}}$ .

$$-\nabla \Phi_{\text{tot}} = \mathbf{g}_{\text{int}} + \mathbf{g}_{\text{ext}} \quad (2.41)$$

As a consequence, the total gravitational energy  $W$  can also be split into two parts:

$$W = E_{\text{PE}} + E_{\text{PE}}^{\text{ext}} \quad (2.42)$$

Here  $E_{\text{PE}}$  and  $E_{\text{PE}}^{\text{ext}}$  are the self-gravitational potential energy, and the gravitational

energy due to the external medium, respectively. They are defined as follows:

$$E_{\text{PE}} = \int_V \rho \tilde{\mathbf{r}} \cdot \mathbf{g}_{\text{int}} dV, \quad (2.43)$$

$$E_{\text{PE}}^{\text{ext}} = \int_V \rho \tilde{\mathbf{r}} \cdot \mathbf{g}_{\text{ext}} dV. \quad (2.44)$$

Note that this way of computing  $E_{\text{PE}}$  is equivalent to Eq. 2.30. The other term on the right hand side of Eq. 2.37 can be expanded in the following way:

$$\Theta_{\text{VT}} = 2(E_{\text{KE}} - E_{\text{KE}}^{\text{surface}}) + 2(E_{\text{TE}} - E_{\text{TE}}^{\text{surface}}) + (E_{\text{B}} + E_{\text{B}}^{\text{surface}}), \quad (2.45)$$

with the different terms corresponding to the volume and surface contribution of the kinetic, thermal, and magnetic energy, respectively. The volume terms are defined as follows:

$$E_{\text{KE}} = \frac{1}{2} \int_V \rho |\mathbf{v}|^2 dV, \quad (2.46)$$

$$E_{\text{TE}} = \frac{3}{2} \int_V P dV, \quad (2.47)$$

$$E_{\text{B}} = \frac{1}{8\pi} \int_V |\mathbf{B}|^2 dV. \quad (2.48)$$

Here  $P$  is the thermal pressure and  $\mathbf{B}$  is the magnetic field. Further, the velocity field is computed in the rest frame of the fixed volume.

The surface terms, although often ignored when discussing the virial theorem, relate to energy associated with the incoming flux. The kinetic, thermal, and the magnetic surface energies are computed as follows:

$$E_{\text{KE}}^{\text{surface}} = \oint_S \tilde{r}_i K_{ij} \hat{n}_j dS, \quad (2.49)$$

$$E_{\text{TE}}^{\text{surface}} = \frac{1}{2} \oint_S P \tilde{r}_i \hat{n}_i dS, \quad (2.50)$$

$$E_{\text{B}}^{\text{surface}} = \oint_S \tilde{r}_i T_{ij} \hat{n}_j dS. \quad (2.51)$$

Here,  $\mathbf{K}$  is the kinetic tensor and  $\mathbf{T}$  is the Maxwell stress tensor. The kinetic tensor is defined as follows:

$$\mathbf{K} = \frac{1}{2} \rho \mathbf{v} \otimes \mathbf{v}. \quad (2.52)$$

The Maxwell stress tensor in our case does not include the electric field (as the equations of ideal MHD assume infinite conductivity and therefore zero electric field) and can be written down as follows:

$$\mathbf{T} = \frac{1}{4\pi} \left( \mathbf{B} \otimes \mathbf{B} - \frac{1}{2} |\mathbf{B}|^2 \hat{\mathbf{I}} \right), \quad (2.53)$$

where  $\hat{\mathbf{I}}$  is the identity matrix.

Using the Gauss's divergence theorem, we can convert Eqs. 2.49, 2.50 and 2.51 from surface to volume integral for ease of computation. These are then written as

follows:

$$E_{\text{KE}}^{\text{surface}} = \int_V \tilde{r}_i \partial_j K_{ij} dV + E_{\text{KE}}, \quad (2.54)$$

$$E_{\text{TE}}^{\text{surface}} = \int_V \tilde{r}_i \partial_i P dV + E_{\text{TE}}, \quad (2.55)$$

$$E_{\text{B}}^{\text{surface}} = \int_V \tilde{r}_i \partial_j T_{ij} dV - E_{\text{B}}. \quad (2.56)$$

This completes the overview of the full virial equation. It is however, not immediately clear the full meaning of each term and how that relates to an energetic balance. Let us take a moment and ponder the implications of the different terms.

The two time derivative quantities  $\dot{I}_{\text{E}}$  and  $\dot{\Phi}_{\text{I}}$ , describe the change in moment of inertia over time, incorporating the mass flux into the fixed volume. For a structure in rough energetic equilibrium, the time average of this quantity is expected to be negligible, as it includes the details of the instantaneous fluctuations. In most virial analyses, these two terms are usually ignored.

The virial theorem is often considered in the context of gravitational boundedness. In that sense, the right hand side of Eq. 2.37 is often used to describe the boundness of a given structure.

A structure is considered to be gravitationally bound if  $|W| > |\Theta_{\text{VT}}|$  (Shadmehri et al., 2002; Dib et al., 2007). This allows us to define a virial term for gravitational equilibrium  $\alpha_{\text{vir}}$  as:

$$\alpha_{\text{vir}} = \frac{\Theta_{\text{VT}}}{|W|}. \quad (2.57)$$

Note that the virial ratio defined in this manner can be negative when strong, confining surface contributions are present. A structure is gravitationally bound if  $|\alpha_{\text{vir}}| < 1$ . However, Dib et al. (2007) point out that there might be other conditions of boundness even when  $|\alpha_{\text{vir}}| > 1$ , provided  $W + \Theta_{\text{VT}} < 0$ . In this case the structures might be bound by the surface contribution of the kinetic, thermal, or magnetic energies. In Fig. 8, we adapt a modification of Fig. 1 from Dib et al. (2007) to highlight this relation between  $W + \Theta_{\text{VT}}$  and  $\alpha_{\text{vir}}$ , according to 2.57. In Fig. 8, structures lying in the bottom two quadrants are instantaneously bound, either gravitationally (bottom left quadrant), or by other surface contributions (bottom right). Structures lying in the top half are unbound, either primarily by tidal forces (top left), or by  $\Theta_{\text{VT}}$  (top right).

In observations, the computation of the surface terms in Eq. 2.37 is usually not possible. Further, the tidal forces, represented by  $E_{\text{PE}}^{\text{ext}}$ , are usually hard to compute and ignored for considerations of boundness in molecular cloud sub-structures. From these considerations, we define a volume virial parameter  $\alpha_{\text{vir}}^{\text{vol}}$ , dependent on only the volume terms of Eq. 2.37 as follows:

$$\alpha_{\text{vir}}^{\text{vol}} = \frac{2E_{\text{KE}} + 2E_{\text{TE}} + E_{\text{B}}}{|E_{\text{PE}}|}. \quad (2.58)$$

In cases where only the self-gravity is relevant, and the surface terms of Eq. 2.37 can be neglected, Eq. 2.58 reflects the virial state of a sub-structure, and is often used in literature. Similar to the behaviour of the full virial parameter of Eq. 2.57,  $\alpha_{\text{vir}}^{\text{vol}} < 1$  expresses a gravitationally bound state.  $\alpha_{\text{vir}}^{\text{vol}}$  is primarily used in paper I.

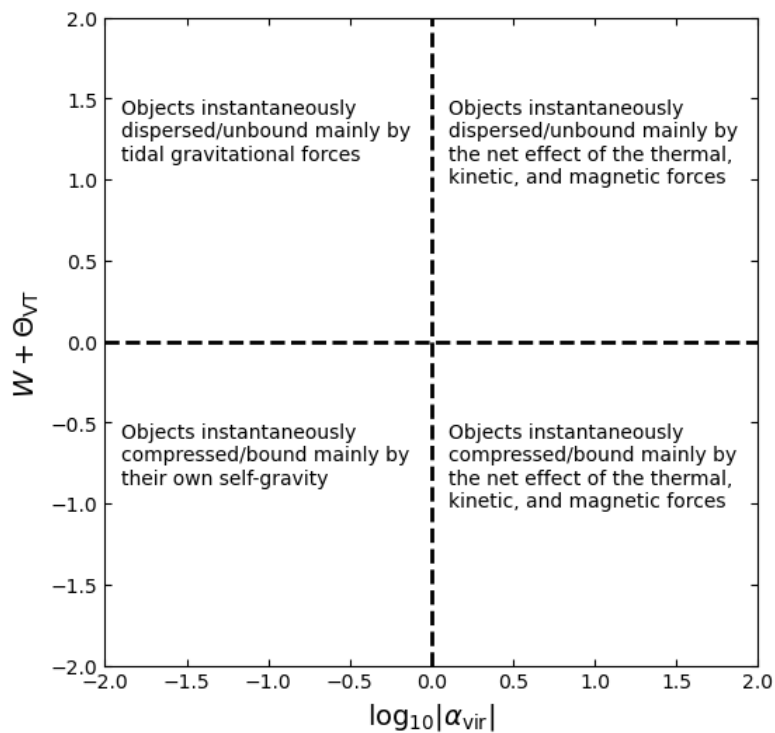


Figure 8: The relation between the virial parameter defined in Eq. 2.57 and the right hand side of the full virial equation, described by 2.37. The bottom two quadrants describe bound structures, with principally gravitationally bound structures occupying the bottom left quadrant, and kinetically, thermally, or magnetically bound structures appearing in the bottom right quadrant. Structures on the top half of the figure would be unbound, either by tidal forces (top left), or by the combined effect of thermal, magnetic, and kinetic forces (top right). Figure adapted from [Dib et al. \(2007\)](#).



### *Interpretation of the surface terms*

The volume terms of the virial analysis are quite intuitive to interpret. It is often enough to only consider them when considering gravitational equilibrium, especially if we have a well defined structure.  $E_{KE}$  represents the kinetic energy due to the velocity dispersion inside the structure, while  $E_{TE}$  and  $E_B$  represent energies associated with thermal and magnetic pressure, respectively.

If a structure does not possess a well defined "identity", the fluxes associated with the surface terms can often be of significant relevance.

The surface term of the kinetic energy represents the energy associated with ram pressure. Matter flowing into or out of a given volume will change the energetic state and therefore the equilibrium balance of a structure. For example, if a structure is at a point where different flows converge in a turbulent medium, this will result in a positive  $E_{KE}^{\text{surface}}$  that will help confine the structure.

The thermal surface term  $E_{TE}^{\text{surface}}$ , reflects in turn if a structure is being thermally confined. This can happen if for example for a structure, the temperature of the medium surrounding a structure is higher and therefore prevents the structure from expanding. This term could become important if there is rapid transition in temperature. In our case, this term is expected to be negligible as we do not form stars in the simulations which could create such a rapid temperature gradient.

The magnetic surface term  $E_B^{\text{surface}}$  is associated with the curvature of the magnetic field lines. Let us imagine a fixed volume inside a constant magnetic field. In such a case, the magnetic surface term defined such that it will be equal and opposite to the volume energy term, reflecting that a constant field neither helps nor hinders possible collapse under gravity. In truth, the field lines are affected by flows in the medium and in turn affect subsequent flows. The surface term of the magnetic field expresses magnetic tension, i.e. changes in the direction of the magnetic field lines, and can be both dispersive or confining. The magnetic surface term is explored in paper II of the present thesis. All the surface terms are included for a full virial analysis in Chapter 6.

#### 2.4.4

##### TIDAL ANALYSIS

In paper I, we perform an analysis based on the gravitational tidal field. Apart from in the relevant sections in the paper, we here present a brief review of the methods used to perform this analysis. The tidal field due to a given gravitational potential can be expressed using the tidal tensor  $\mathbf{T}$ , which is defined as:

$$T_{ij} = -\partial_i \partial_j \Phi = \partial_i g_j. \quad (2.59)$$

Here,  $\Phi$  is the gravitational potential, and  $g_j$  is the  $j$ -th component of the gravitational acceleration  $\mathbf{g} = -\nabla\Phi$ . The tidal tensor at a point encodes the deformation solely due to the gravitational field. Since the tidal tensor is symmetric and real-valued, it can be diagonalized. The eigenvalues and eigenvectors of the diagonalized tidal tensor represent the degree and direction of compression/extension due to the tidal field, respectively. For example, the tidal tensor at a point  $(x, 0, 0)$

( $x > 0$ ) due to a point of mass  $M$  at  $(0, 0, 0)$  is given by:

$$\mathbf{T} = \begin{bmatrix} \frac{2GM}{x^3} & 0 & 0 \\ 0 & -\frac{GM}{x^3} & 0 \\ 0 & 0 & -\frac{GM}{x^3} \end{bmatrix} \quad (2.60)$$

A positive eigenvalue here represents extension, and negative eigenvalue represents compression. The tidal tensor here represents that the nature of deformation due to tidal forces is extensive along the direction joining the point mass and the evaluation point, and compressive in the two orthogonal directions perpendicular to it. A spherical test mass will then be flattened and elongated at the same time, i.e. become sort of "spaghettified" due to the tidal field of a distant point mass body.

Further, the trace of the tidal tensor represents the Poisson equation and contains information on the local density field.

$$\text{Tr}(\mathbf{T}) = -\nabla^2\Phi = -4\pi G\rho \quad (2.61)$$

The trace is therefore non-zero only when there is mass distribution at the point of evaluation. For any mass distribution, the tidal tensor outside the mass distribution will always be zero, and as a consequence include both compressive and extensive modes.

In order to perform the tidal analysis on structures picked out by the dendrogram, we compute an average tidal tensor over an entire structure:

$$\langle T \rangle_{ij} = \frac{1}{V} \int_V \partial_i g_j d^3r. \quad (2.62)$$

This is necessary as we are interested in the compression and shear experienced by the structure as a whole, and not at every individual point. The potential at every point inside a given structure can be thought of as the sum of the structure's own self-gravity  $\Phi_{\text{int}}$  and the potential due to the external mass distribution  $\Phi_{\text{ext}}$ . The total potential  $\Phi_{\text{tot}}$  then is given by

$$\Phi_{\text{tot}} = \Phi_{\text{int}} + \Phi_{\text{ext}}. \quad (2.63)$$

As a consequence, the average tidal tensor can also be split into the total, internal, and external component, related by:

$$\langle \mathbf{T} \rangle_{\text{tot}} = \langle \mathbf{T} \rangle_{\text{int}} + \langle \mathbf{T} \rangle_{\text{ext}}. \quad (2.64)$$

Here  $\langle \mathbf{T} \rangle_{\text{tot}}$  represents the deformation due to the entire gravitational field,  $\langle \mathbf{T} \rangle_{\text{int}}$  due to the mass distribution of only the structure, and  $\langle \mathbf{T} \rangle_{\text{ext}}$  due to the external medium. The traces of these three terms are given by

$$\begin{aligned} \text{Tr}(\langle \mathbf{T} \rangle_{\text{tot}}) &= -4\pi G\rho_{\text{avg}}, \\ \text{Tr}(\langle \mathbf{T} \rangle_{\text{int}}) &= -4\pi G\rho_{\text{avg}}, \\ \text{Tr}(\langle \mathbf{T} \rangle_{\text{ext}}) &= 0, \end{aligned} \quad (2.65)$$

where  $\rho_{\text{avg}} = \frac{1}{V} \int_V \rho dV$  is the average density of the structure. The external gravitational field has trace zero as it computes the tidal tensor at the position of the structure due to all the mass outside it.

One can also associate a timescale with each eigenvalue of the tidal tensor.

As the magnitude of the eigenvalue  $\lambda$  represents the strength of the compression/extension, the associated timescale represents a deformation timescale.  $\lambda$  has the dimension of  $[\text{time}]^{-2}$ , and therefore a tidal timescale can be formulated as:

$$t_{\text{tidal}} = |\lambda|^{-1/2}. \quad (2.66)$$

To understand how the eigenvalues  $\lambda$  are related to a deformation timescale, let us perform a simple one dimensional thought experiment. Let us imagine a structure has an eigenvalue of the tidal tensor  $\lambda$  along the eigenvector direction  $(1, 0, 0)$ . The acceleration at position  $x$ ,  $g(x)$  is then given by

$$g(x) = g_0 + \lambda x, \quad (2.67)$$

$g_0$  being some constant and the equations reflects the fact that  $\lambda$  is essentially the gradient of the acceleration. If  $\lambda$  is positive, this implies that the acceleration increases linearly along  $x$ . In the absence of any other forces, the general equation of motion of a test particle along this eigenvector direction is given by

$$\frac{d^2 x}{dt^2} = g(x). \quad (2.68)$$

The solution is given by

$$x = C_1 e^{\sqrt{\lambda}t} + C_2 e^{-\sqrt{\lambda}t} - \frac{g_0}{\lambda}, \quad (2.69)$$

where  $C_1$  and  $C_2$  depend on the starting position and velocity of the test particle. If we imagine two test particles at  $t = 0$ , starting from  $x = 0$  and  $x = \Delta x_0$ , with zero velocities, then for the two particles, the position is given as:

$$\begin{aligned} x_1(t) &= \frac{g_0}{2\lambda} \left( e^{\sqrt{\lambda}t} + e^{-\sqrt{\lambda}t} - 2 \right) \\ x_2(t) &= \frac{g_0}{2\lambda} \left( e^{\sqrt{\lambda}t} + e^{-\sqrt{\lambda}t} - 2 \right) + \frac{1}{2}\Delta x_0 \left( e^{\sqrt{\lambda}t} + e^{-\sqrt{\lambda}t} \right). \end{aligned} \quad (2.70)$$

The distance between the two particles will then evolve as

$$\Delta x(t) = \frac{1}{2}\Delta x_0 \left( e^{\sqrt{\lambda}t} + e^{-\sqrt{\lambda}t} \right). \quad (2.71)$$

For short timescales,  $t \ll |\lambda|^{-1/2}$ , and

$$\Delta x(t) - \Delta x_0 \approx \lambda \frac{\Delta x_0 t^2}{2}. \quad (2.72)$$

$\lambda$  therefore determines the rate at which the two test particles drift apart or get closer, corresponding to deformation of the structure. As a consequence, the deformation timescale of the structure due to the tidal field can be estimated by  $|\lambda|^{-1/2}$ .

## THE RESEARCH

---

In the previous chapters, we have discussed the physics of the ISM, focusing on the early stages of molecular clouds. We have also had a detailed overview of the equations, numerical methods, and analysis tools we will need for understanding the results of this thesis. This chapter will attempt to provide a connection between the introduction and methods of the previous chapters, and the questions investigated in the following.

Molecular clouds are nurseries of star formation. Many aspects related to the multi-scale nature of structure formation in MCs remain poorly understood and are the focus of this thesis. Molecular clouds are permeated with elongated structures, such as filaments (André et al., 2010; Molinari et al., 2010; Arzoumanian et al., 2011; André et al., 2014; Hacar et al., 2022). The process of structure formation in molecular clouds is not well understood. There are two primary competing theories - the global hierarchical collapse scenario (e.g. Vázquez-Semadeni et al., 2019) and the gravo-turbulent scenario (see e.g. Mac Low & Klessen, 2004), which differ in the key question regarding whether molecular clouds are overall gravitationally bound entities or not. **Paper I (Chapter 4)** primarily investigates this question.

This is done by analyzing seven different clouds from the SILCC-Zoom simulations at different times in the early stages of structure formation. Structures inside clouds are identified using a dendrogram algorithm (Section 2.4.1), and an energetic analysis is performed. The key figures in this regard are the bottom panels of Figs. 7 and 8, showing the evolution of the virial parameter.

In typical virial analyses, the effects of tidal forces are often ignored. They have been shown to be important at smaller scales and have been evoked as a possible mechanism in shaping the initial mass function of star formation (Lee & Hennebelle, 2018; Colman & Teyssier, 2020). **Paper I** also discusses the effect of tidal effects due to the gas at cloud scales.

A key energetic term related to clouds are magnetic fields. They have been related to the formation of elongated structures (e.g. Inoue & Fukui, 2013), slowing down gravitational collapse (e.g. Heitsch et al., 2001), hindering formation of dense, (Hill et al., 2012) as well as molecular gas (Girichidis et al., 2018), and altering fragmentation (Commerçon et al., 2011). It is also unclear if this influence extends to dense gas. The dense, star forming gas found at the higher density end of mass distributions of MCs is often expected not to be influenced by the presence of magnetic fields (Klessen & Burkert, 2001; Slyz et al., 2005; Schneider et al., 2015). **Paper II (Chapter 5)** evaluates the influence of magnetic fields at the diffuse atomic envelope of molecular clouds ( $\sim 1 - 100 \text{ cm}^{-3}$ ), as well as in the denser structures ( $\gtrsim 100 \text{ cm}^{-3}$ ) in terms of shaping cloud structures (Fig. 5), governing their dynamics (Fig. 6), and influencing their fragmentation (Fig. 9). The analysis is done on the same set of SILCC-Zoom data as in paper I, with an additional dendrogram analysis performed at the low density range.

The properties of cloud scales (typically  $> 1$  pc) are directly related to the smaller filamentary structures, as well as cloud cores. Structure formation at this smaller sub-pc scale is analyzed through the analysis of two MHD clouds from the SILCC deep-zoom simulations, building upon the framework of the previous SILCC-Zoom runs. This is presented in **Chapter 6**. The results of the chapter are divided roughly into two parts - energetics and morphology. In terms of energetics, Chapter 6 focuses on the ways in which gravitationally bound sub-pc scale structures emerge. With regards to morphology, we attempt to primarily investigate the properties of filaments and cores and relate them to the possible scenarios of their formation.

SILCC-ZOOM: THE DYNAMIC BALANCE IN  
MOLECULAR CLOUD SUBSTRUCTURES (PAPER I)

---

# SILCC-Zoom: the dynamic balance in molecular cloud substructures

Shashwata Ganguly,<sup>1</sup>\* S. Walch,<sup>1,2</sup> S. D. Clarke<sup>1,3</sup> and D. Seifried<sup>1,2</sup>

<sup>1</sup>*Physikalisches Institut, Universität zu Köln, Zùlpicher Str. 77, 50937 Köln, Germany*

<sup>2</sup>*Cologne Centre for Data and Simulation Science, University of Cologne, Cologne, Germany*

<sup>3</sup>*Academia Sinica, Institute of Astronomy and Astrophysics, Taipei, Taiwan*

Accepted XXX. Received YYY; in original form ZZZ

## ABSTRACT

How molecular clouds fragment and create the dense structures which go on to form stars is an open question. We investigate the relative importance of different energy terms (kinetic, thermal, magnetic, and gravity - both self-gravity and tidal forces) for the formation and evolution of molecular clouds and their sub-structures based on the SILCC-Zoom simulations. These simulations follow the self-consistent formation of cold molecular clouds down to scales of 0.1 pc from the diffuse supernova-driven interstellar medium in a stratified galactic disc. We study the time evolution of seven molecular clouds (five with magnetic fields and two without) for 1.5–2 Myr. Using a dendrogram, we identify hierarchical 3D sub-structures inside the clouds with the aim to understand their dynamics and distinguish between the theories of gravo-turbulent fragmentation and global hierarchical collapse. The virial analysis shows that the dense gas is indeed dominated by the interplay of gravity and turbulence, while magnetic fields and thermal pressure are only important for fluffy, atomic structures. Over time, gravitationally bound sub-structures emerge from a marginally bound medium (virial ratio  $1 \leq \alpha_{\text{vir}}^{\text{vol}} < 2$ ) as a result of large-scale supernova-driven inflows rather than global collapse. A detailed tidal analysis shows that the tidal tensor is highly anisotropic. Yet the tidal forces are generally not strong enough to disrupt either large-scale or dense sub-structures but cause their deformation. By comparing tidal and crossing time scales, we find that tidal forces do not seem to be the main driver of turbulence within the molecular clouds.

**Key words:** MHD – methods; numerical – stars: formation – ISM: clouds – ISM: kinematics and dynamics

## 1 INTRODUCTION

Star formation occurs inside cold, dense and mostly molecular gas in the interstellar medium (ISM) - in so-called molecular clouds (MCs). They are typically thought of as the largest structure that can decouple from galactic dynamics (Chevance et al. 2020). The nature of MCs, their lifetime, formation mechanism, and whether they are bound or not, all have direct consequences on our understanding of the possible ways in which dense structures and eventually stars can form inside these clouds.

Several key discoveries over the past decades have facilitated and developed our understanding of molecular clouds. We know that they are in rough energy equipartition between kinetic and potential energy (e.g. see Dame et al. 1986; Solomon et al. 1987; Blitz et al. 2007). Only a small fraction of gas inside these clouds eventually ends up in stars (Kennicutt 1998; Genzel et al. 2010; Krumholz et al. 2012), which leads to a low star formation efficiency of the order of a few percent, although with some variation (Murray 2011). Molecular clouds are known to exhibit supersonic linewidths (Larson 1981; Orkisz et al. 2017), but generally lack a clear collapse signature such as redshifted lines (Zuckerman & Evans 1974). While this has recently been challenged with observations of gravity driven flows (Kirk et al. 2013; Peretto et al. 2014; Chen et al. 2019; Shimajiri et al. 2019), it is unclear if such flows extend to entire clouds (Chevance

et al. 2022). The linewidth is related to the mass and size of the molecular clouds themselves (Larson 1981; Solomon et al. 1987; Brunt 2003). The original power-law exponents proposed by Larson (1981) have since been revised and challenged. For example, Heyer et al. (2009) show that the Larson coefficient has a dependency on the MC surface density, and there have been studies pointing out that the Larson relation may not hold inside a single cloud (Wu et al. 2010; Traficante et al. 2018).

There are several possible ways to interpret these key observations. The traditional view, originally proposed by Zuckerman & Evans (1974), is that the supersonic linewidths in observed clouds are caused by small scale turbulence that provides overall support and prevents the entire cloud from freely collapsing under gravity. In this so-called gravo-turbulent (GT) scenario, clumps and cores inside molecular clouds form as a result of compression in the highly turbulent gas (see e.g. Klessen 2001; Padoan & Nordlund 2011). Only a few of the compressed regions become gravitationally bound structures, which collapse and form stars. In this scenario, the Larson-like power law connecting the turbulent velocity dispersion,  $\sigma_v$ , and the linear size of the cloud,  $R$ , i.e.  $\sigma_v \propto R^{0.5}$ , originates from a turbulent cascade of large-scale motions (see e.g. excellent reviews by Mac Low & Klessen 2004; Ballesteros-Paredes et al. 2007; McKee & Ostriker 2007; Hennebelle & Falgarone 2012).

This view has since been challenged. Magnetic fields have been proposed as a possible mechanism to provide support against gravitational collapse (Mouschovias 1976a,b; Padoan & Nordlund 2011;

\* E-mail: ganguly@ph1.uni-koeln.de

Federrath & Klessen 2012; Ibáñez-Mejía et al. 2022). However, after the emergence of key observations suggesting that most cloud structures are magnetically supercritical, it is generally accepted that magnetic fields cannot be solely responsible for the observed, low star formation efficiency (Crutcher 1999; Bourke et al. 2001; Troland & Crutcher 2008; Falgarone et al. 2008; Crutcher et al. 2010).

It is unclear if MCs need any support at all. Several studies suggest that MCs are transient entities, and that their lifetimes are short enough that they may not need any support (Bash et al. 1977; Leisawitz et al. 1989; Elmegreen 2000; Hartmann et al. 2001; Engargiola et al. 2003; Kawamura et al. 2009; Meidt et al. 2015; Mac Low et al. 2017).

In recent years, chaotic, hierarchical gravitational collapse has emerged as another possible alternative to the gravo-turbulent scenario. The hierarchical collapse scenario, originally developed by Hoyle (1953) and suggested as a mechanism for the collapse of a cloud by Goldreich & Kwan (1974), has been considered briefly over the past decades (e.g. Elmegreen 2000; Hartmann et al. 2001; Vázquez-Semadeni et al. 2007). In its most recent form, the so-called global hierarchical collapse (GHC) scenario (see e.g. Vázquez-Semadeni et al. 2019), the interstellar turbulence produces nonlinear density fluctuations, which facilitate a multi-scale hierarchical collapse of the entire molecular cloud through a mass cascade across scales. The chaotic nature of the collapse masks any obvious signatures of global collapse, and the low efficiency of star formation is explained by the fact that stellar feedback from the first generation of massive stars disperses the cloud before it can convert more of its gas mass into stars (see e.g. Vázquez-Semadeni et al. 2009, 2017; Ballesteros-Paredes et al. 2011; Kuznetsova et al. 2015, 2018).

Most analyses of the evolution of MCs focus on the self-gravity of the gas itself (Dobbs et al. 2011). The complex nature of the medium, however, implies that tidal forces can have a potentially significant sway over the gas dynamics. For example, stability produced by tidal forces has been invoked to explain the peak of the initial mass function on core-scales (Lee & Hennebelle 2018; Colman & Teysier 2020). For star clusters, it has been shown that fully compressive tides can slow down the dissolution of clusters (Renaud et al. 2011), and that young clusters are preferentially located in fully compressive regions of galaxies (Renaud et al. 2009). We aim to consider tidal forces here in the context of the (internal) dynamics of MCs.

In the presented work, we perform a detailed energy analysis of self-consistently formed MCs and their sub-structures based on the SILCC-Zoom simulations (Seifried et al. 2017). The MCs are situated inside a larger scale multi-phase ISM environment (Walch et al. 2015; Girichidis et al. 2016). This allows us to do a rigorous analysis of the MC dynamics and to test whether the GT or the GHC scenario are in control. We apply a three-dimensional dendrogram algorithm to define hierarchical structures (Rosolowsky et al. 2008).

The paper is structured as follows. We first present the details of the numerical setup in section 2. In section 3, we highlight the different scaling relations (Larson’s velocity-size and mass-size relations, and the Heyer relation). We then discuss the energetic balance between self-gravity, kinetic, magnetic, and thermal energy in section 4. By studying the dynamic balance of these structures, we find that larger scale and denser, molecular structures are primarily governed by the interaction of the turbulent kinetic energy and self-gravity, with magnetic and thermal energies playing a subservient role. In section 5, we discuss the relative importance of self-gravity and the gravity from the surrounding medium, by both a direct comparison of acceleration terms as well as a more detailed tidal analysis. From the direct comparison of the acceleration vectors, we find that bound and marginally bound structures are dominated by self-gravity over

external gravity. We further assess the nature and extent of deformation caused by the gravity of the surrounding clumpy medium by performing a tidal analysis, and find that the overall gravitational field is highly anisotropic but still mostly fully compressive. Finally, we present the summary of our findings in section 6.

## 2 NUMERICAL METHODS AND SIMULATION

We present results based on the SILCC-Zoom simulations (Seifried et al. 2017). The SILCC-Zoom simulations are zoom-in simulations of MCs forming self-consistently within the larger-scale, multi-phase ISM SILCC simulations (Walch et al. 2015; Girichidis et al. 2016). In this section, we highlight some key features of the simulations. Further details regarding the simulations can be found in Seifried et al. (2017). For description of the hydrodynamic (HD) and magnetohydrodynamic (MHD) clouds used for the present analysis, see Seifried et al. (2017) and Seifried et al. (2019), respectively.

All simulations were performed using the adaptive mesh refinement (AMR) code FLASH, version 4 (Fryxell et al. 2000; Dubey et al. 2008). We present results from runs with and without magnetic fields. The hydrodynamic cloud simulations have been performed using the MHD ‘Bouchut 5-wave solver’ (Bouchut et al. 2007; Waagan 2009), with magnetic field strength set to zero. The MHD simulations have been run using an entropy-stable solver which guarantees positive pressure and minimizes dissipation (Derigs et al. 2016, 2017, 2018).

The entire simulation domain consists of a box of size  $500 \text{ pc} \times 500 \text{ pc} \times \pm 5 \text{ kpc}$ , with the long axis representing the vertical  $z$ -direction of the stratified galactic disc. The box is set with periodic boundary conditions in the  $x$ - and  $y$ -directions, and outflow boundary conditions in  $z$ -direction. The initial gas surface density is set to  $\Sigma_{\text{gas}} = 10 M_{\odot} \text{ pc}^{-2}$  which corresponds to solar neighbourhood conditions. The vertical distribution of the gas is modelled as a Gaussian, i.e.  $\rho = \rho_0 \exp(-z^2/2h_z^2)$ , where  $h_z = 30 \text{ pc}$  is the scale height and  $\rho_0 = 9 \times 10^{-24} \text{ g cm}^{-3}$  is the midplane gas density. The initial gas temperature is set to 4500 K. For runs with magnetic fields, the magnetic field is initialized along the  $x$ -direction, i.e.  $\mathbf{B} = (B_x, 0, 0)$  with  $B_x = B_{x,0} \sqrt{\rho(z)/\rho_0}$  and the magnetic field strength in the midplane  $B_{x,0} = 3 \mu G$ . The field strength is chosen to be in accordance with recent observations (e.g. Beck & Wielebinski 2013).

All simulations include self-gravity as well as an external galactic potential due to old stars. The external potential is calculated using the assumption of a stellar surface density of  $\Sigma_{\text{star}} = 30 M_{\odot} \text{ pc}^{-2}$  with a scale height of 100 pc. The self-gravity of the gas is computed using the Octtree-based algorithm by Wünsch et al. (2018).

Apart from the dynamics of the gas, we also model its chemical evolution using a simple non-equilibrium chemical network based on hydrogen and carbon chemistry (Nelson & Langer 1997; Glover & Mac Low 2007; Glover et al. 2010). For this purpose, we follow the abundance of ionized, atomic, and molecular hydrogen ( $\text{H}^+$ ,  $\text{H}$ ,  $\text{H}_2$ ), carbon-monoxide (CO), ionized carbon ( $\text{C}^+$ ), free electrons ( $\text{e}^-$ ), and atomic oxygen (O). At the beginning of the simulation, hydrogen is fully atomic within the disc midplane and carbon is fully ionized. The simulations also include an interstellar radiation field (ISRF), with strength of  $G_0 = 1.7$  in Habing units (Habing 1968; Draine 1978). The ISRF is attenuated depending on the column density of the gas, thereby accounting for dust shielding as well as (self-) shielding of  $\text{H}_2$  and CO. This is accounted for using the TREE-RAY OPTICAL DEPTH module developed by Wünsch et al. (2018) and takes into account the 3D geometry of the embedded region.

The turbulence in the simulations is generated by supernova ex-



plosions (SNe). The explosion rate is set to 15 SNe per Myr, which is consistent with the star formation rate surface density expected for the given gas surface density from the Kennicutt-Schmidt relation (Schmidt 1959; Kennicutt 1998). 50% of the SNe are placed following a Gaussian random distribution with a scale height of 50 pc along the  $z$ -direction, while the other 50% are placed at density peaks of the gas. This prescription of mixed supernova driving creates a multiphase turbulent ISM which can be used as initial condition for the zoom-in simulations (Walch et al. 2015; Girichidis et al. 2016).

For the SILCC-Zoom simulations, we drive the medium with SNe up to a certain time  $t_0$ . Up to  $t_0$ , the uniform grid resolution is 3.9 pc. At  $t_0$ , the SNe are stopped and multiple regions are identified for the zoom-in process, primarily due to their molecular gas content at a later simulation time, when the simulation has been continued on the coarse resolution. This corresponds to the start of the evolution of the zoom-in regions, and we refer to this point as  $t_{\text{evol}} = 0$ . The total simulation time  $t$  is related to the cloud evolution time  $t_{\text{evol}}$  as

$$t = t_0 + t_{\text{evol}}. \quad (1)$$

The different simulations are compared at similar  $t_{\text{evol}}$ . For tracing the evolution of the clouds, in the selected regions, the AMR grid is allowed to refine to a higher resolution in order to capture the internal structure of the forming MCs. These regions are referred to as "zoom-in regions". In each SILCC box we run two zoom-in regions simultaneously, such that we follow eight zoom-in regions in total. The different MHD runs are seeded with a different set of random supernovae. All other initial conditions are the same. All the runs presented here have an effective spatial resolution of 0.125 pc. For more details on the zoom-in process see Seifried et al. (2017).

## 2.1 Cloud selection

For the analysis presented in this work, we look at eight different  $(62.5 \text{ pc})^3$  zoom-in regions. Each zoom-in region contains one molecular cloud (called 'MC1', 'MC2', and so on). Six simulations include magnetic fields (run names with '-MHD'), while the other two are of hydrodynamic nature ( $B = 0$ ; run names with '-HD'). We present some basic information of the different MCs in Table 1, and a projected view of all eight clouds at time  $t_{\text{evol}} = 3.5$  Myr in Fig. 1. The clouds we analyze have total gas masses of  $5.4 - 10.1 \times 10^4 M_{\odot}$ , and  $\text{H}_2$  masses between  $0.9 - 2.1 \times 10^4 M_{\odot}$  at  $t_{\text{evol}} = 2$  Myr. Note that the time at which we begin the zoom-in,  $t_0$ , varies for the different simulations (see Table 1). The evolution time  $t_{\text{evol}}$ , which we refer to throughout the paper when comparing the results for the different MCs, represents the "age" of the molecular cloud and corresponds to the time that has passed since the start of the zoom-in.

We perform a detailed analysis of the various clouds at different times between  $t_{\text{evol}} = 1.5 - 3.5$  Myr for the two hydrodynamic clouds, as well as for  $t_{\text{evol}} = 2 - 3.5$  Myr for the MHD clouds. We include the earlier time step for the hydrodynamic clouds as they evolve more rapidly compared to their MHD counterparts and show discernible structures early on. We do not include sink particles in these simulations, and hence the end time is chosen such that the cloud sub-structures are still well resolved with respect to the local Jeans length (Truelove et al. 1997). Of the eight simulations, we find that even at  $t_{\text{evol}} = 3.5$  Myr, MC3-MHD has a very low molecular gas fraction ( $\sim 1900 M_{\odot}$  molecular  $\text{H}_2$  of a total mass of  $\sim 20,000 M_{\odot}$ , see Table 1). The resulting dendrogram analysis is rather incomplete because this cloud lacks discernible dense structures. Therefore, we omit MC3-MHD from our further analysis.

Run name	MHD	$t_0$ [Myr]	Total mass [ $10^4 M_{\odot}$ ]	$\text{H}_2$ mass [ $10^4 M_{\odot}$ ]
MC1-HD	no	12	7.3	2.1
MC2-HD	no	12	5.4	1.6
MC1-MHD	yes	16	7.8	1.3
MC2-MHD	yes	16	6.2	0.86
(MC3-MHD) <sup>a</sup>	yes	16	2.0	0.19)
MC4-MHD	yes	11.5	6.8	1.2
MC5-MHD	yes	11.5	10.1	1.6
MC6-MHD	yes	16	6.6	1.4

**Table 1.** Basic information on the eight analyzed simulations. From left to right we list the run name, whether it is a magnetized run or not, the time when the AMR zoom-in started, as well as the total mass and the molecular hydrogen mass at  $t_{\text{evol}} = 2$  Myr.

<sup>a</sup>We discard MC3-MHD from our further analysis because of its low molecular gas content and lack of dense structures (see also Fig. 1).

## 2.2 Sub-structure identification and modelling

To identify structures in the MCs, we use a dendrogram algorithm (Rosolowsky et al. 2008). Dendrograms are a model independent method to determine hierarchical structures. We specifically use the python package *astrodendro* (Robitaille et al. 2019) and apply the method to find density (sub-)structures in 3D. For this purpose, we convert the AMR data to a uniform grid at our effective spatial resolution of 0.125 pc. Given the initial density cubes, our dendrogram analysis essentially depends on three free parameters: the initial starting threshold  $\rho_0$ , the density jump  $\Delta\rho$ , and the minimum number of cells included in a structure,  $N_{\text{cells}}$ . For the analysis presented here, unless otherwise stated, we use  $\rho_0 = 10^{-22} \text{ g cm}^{-3}$ ,  $\Delta(\log_{10} \rho) = 0.1$  and  $N_{\text{cells}} = 100$ . Defining  $\Delta(\log_{10} \rho)$  implies that the dendrogram is built on the logarithm of the density. In order to reduce the number of random fluctuations, we only retain those structures in the dendrogram tree, which eventually reach a density of  $\rho_{\text{peak}} > 10^{-21} \text{ g cm}^{-3}$ . A view of the resulting dendrogram tree can be seen in the left panel of Fig. 2 for MC1-MHD at  $t_{\text{evol}} = 2$  Myr. We highlight two branches of the dendrogram tree to show the hierarchical nature of the structures, a larger scale structure in blue, and a contained denser filamentary structure in red. The projections of these two structures can be seen in the right panel of Fig. 2, as contours over column density maps projected along the  $x$ -,  $y$ -, and  $z$ -direction, respectively.

We note that we varied the three free parameters within a reasonable range in order to test the robustness of our results. Increasing  $N_{\text{cells}}$  washes out the smallest sub-structures, while decreasing  $\rho_0$  results in larger structures on the largest scales, but leaves the smaller scales unaffected. Increasing the minimum value of  $\Delta\rho$  causes fewer structures to be identified but does not affect the general trends for different sub-structures. We have also performed the dendrogram analysis by using linear density jumps (i.e. dendrogram built on the density field instead of the logarithmic density field) of  $\Delta\rho = 10^{-22} \text{ g cm}^{-3}$  and  $\Delta\rho = 10^{-23} \text{ g cm}^{-3}$ , in addition to using logarithmic density bins. This also leaves the statistical properties of the resulting structures basically unaffected.

Examples of the resulting dendrogram structures can be seen in Fig. 3, for MC5-MHD at  $t_{\text{evol}} = 3.5$  Myr. Projections of different dendrogram leaf structures (i.e. structures that contain no further sub-structures inside them) are plotted over the column density as contours. We differentiate between sub-structures based on their molecular content. Molecular structures ( $\text{H}_2$  mass fraction  $> 0.5$ ) are

4 *S. Ganguly et al.*

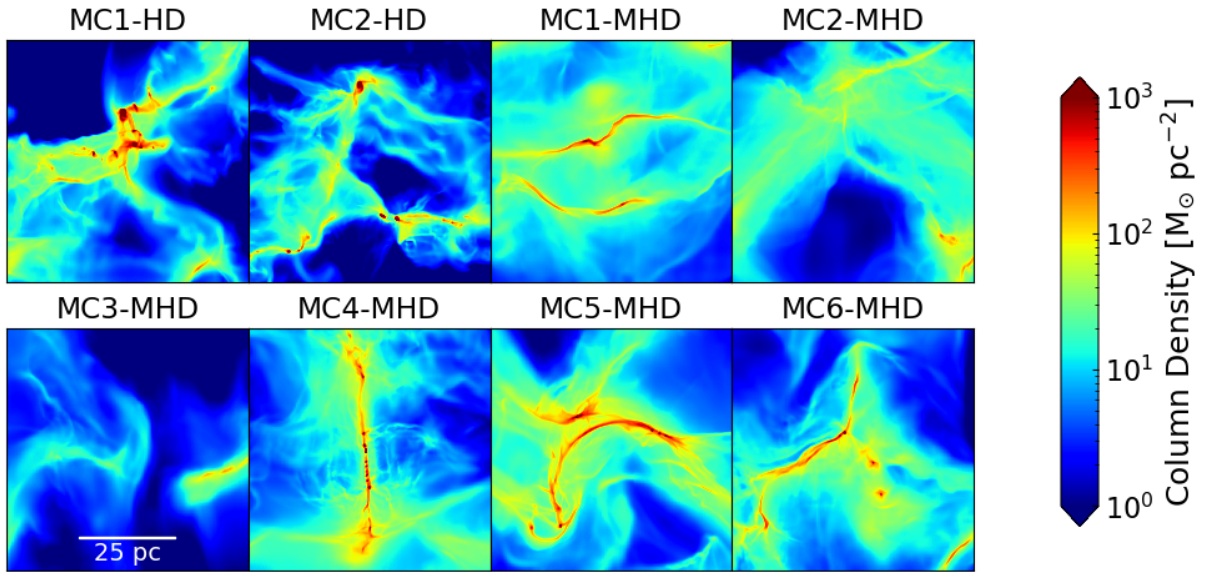


**Figure 1.** Column densities of the analyzed clouds, each projected along the  $x$ -axis at  $t_{\text{evol}} = 3.5$  Myr. The side length of each plot is  $62.5$  pc. The MHD clouds (top right, and bottom row) have elongated filamentary structures with extended diffuse envelopes, while the hydrodynamic clouds (top left) appear to be more clumpy and fragmented. Note that MC3-MHD has been excluded in further analysis due to its lack of discerning structures and low molecular gas content (see Table 1).

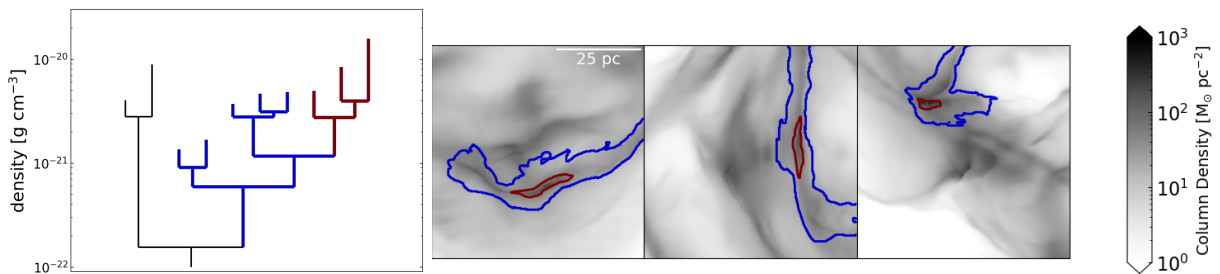


**Figure 2.** Left: Dendrogram tree with two sub-structures highlighted in blue and red for MC1-MHD at  $t_{\text{evol}} = 2$  Myr, plotted using *astrodendro*. Right: We depict these two sub-structures as contours on the column density maps of MC1-MHD projected along the  $x$ -,  $y$ -, and  $z$ -axis, respectively. The blue and red contours correspond to the branches of the same colour from the left panel. It is apparent that the structures look filamentary on the  $x$ -,  $y$ -projections, but rather clumpy on the  $z$ -projection.

plotted in solid lines, while atomic ( $\text{H}_2$  mass fraction  $< 0.5$ ) structures are plotted in dashed lines. Visually, we see that the molecular structures trace the denser spine of the cloud, while the atomic structures represent more the surrounding envelope. The number of total, as well as molecular structures for the various analyzed MCs can be seen in Table 2 for  $t_{\text{evol}} = 3.5$  Myr. From Table 2, we can see that apart from the more diffuse MC2-MHD, almost all the clouds are primarily dominated by molecular structures at the latter stage. The exact number of structures depends on the dendrogram parameters chosen, but the fraction of molecular and atomic structures is nonetheless indicative of the chemical state of the clouds.

Once we obtain the dendrogram, we aim to approximate the density sub-structures as ellipsoids. In a companion paper (Ganguly et al., in prep.), we use this method to classify the morphology of the given structures. For the present paper, however, it allows us to compute

a number of physical quantities dependent on the shortest axis of a given structure (such as the crossing time, see Fig. 16).

For each structure, we compute an equivalent ellipsoid that has the same mass and the same moments of inertia as the original structure. Let us consider a uniform density ellipsoid of mass  $M$  and semi-axis lengths  $a, b, c$  where  $a \geq b \geq c$ . The moments of inertia along the three principal axes will be given as follows:

$$\begin{aligned} I_a &= \frac{1}{5}M(b^2 + c^2) \\ I_b &= \frac{1}{5}M(c^2 + a^2) \\ I_c &= \frac{1}{5}M(a^2 + b^2) \end{aligned} \quad (2)$$

where  $I_c \geq I_b \geq I_a$ . If we now compute the principal moments of inertia of a given dendrogram structure to be  $A, B$ , and  $C$ , re-

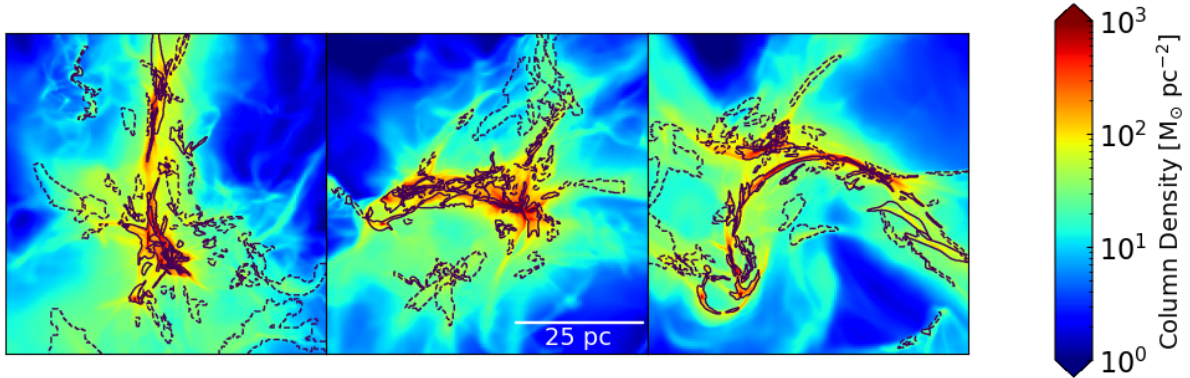


**Figure 3.** Left to right: Projections of MC5-MHD at  $t_{\text{evol}} = 3.5$  Myr along the  $x$ -,  $y$ -, and  $z$ -axis, respectively. The contours show the projections along the same axis of the leaf dendrogram structures. Molecular structures ( $> 50\%$   $\text{H}_2$ ) are plotted with solid lines, and atomic structures ( $< 50\%$   $\text{H}_2$ ) are plotted with dashed lines. The molecular structures nicely trace the dense spine of the cloud, while the atomic structures mostly represent the envelope.

Run name	Total structures	Molecular structures	Molecular structure fraction
MC1-HD	214	187	0.87
MC2-HD	138	113	0.81
MC1-MHD	52	37	0.71
MC2-MHD	127	36	0.28
MC4-MHD	172	122	0.71
MC5-MHD	208	136	0.65
MC6-MHD	120	97	0.81

**Table 2.** Information on the number of molecular structures obtained in the dendrogram analysis. From left to right are listed the run name, the number of total analyzed structures in each region, the number of structures which have  $> 50\%$  of their hydrogen mass in molecular form, and the fraction of such molecular structures at  $t_{\text{evol}} = 3.5$  Myr. The exact number of structures depends on the dendrogram parameters. The high fraction of molecular structures is partially a result of specifying that all structures should have a peak density  $\rho_{\text{peak}} > 10^{-21}$   $\text{g cm}^{-3}$ .

spectively, then the ellipsoid has an equivalent moment of inertia if

$$A = I_a, \quad B = I_b, \quad C = I_c. \quad (3)$$

This leads to the following equation for computing  $a$ ,  $b$ , and  $c$  of the equivalent ellipsoids:

$$\begin{aligned} a &= \sqrt{\frac{5}{2M}(B+C-A)}, \\ b &= \sqrt{\frac{5}{2M}(C+A-B)}, \\ c &= \sqrt{\frac{5}{2M}(A+B-C)}. \end{aligned} \quad (4)$$

We emphasize that the (sub-)structures identified with our dendrogram analysis represent volumina that are enclosed by the defined density contours. This does not imply that the structures are long-lived entities. They may either condense or diffuse and disperse completely. They may also accrete gas, grow in volume, merge with each other, or fragment. In the following, we analyse the dynamical state of the density (sub-)structures in detail and relate them with observed relations.

### 3 SCALING RELATIONS

In his seminal work, Larson (1981) showed that MCs follow a relation between their linewidth, representing the 1D gas velocity dispersion, and their linear size,

$$\sigma_{1D} \propto R^n. \quad (5)$$

While Larson (1981) originally found  $n = 0.38$ , this has later been revised to  $n = 0.5$  (Solomon et al. (1987), or more recently, Brunt (2003)) - roughly consistent with virialization (Solomon et al. 1987), turbulent cascade (Padoan et al. 2016), as well as gravitational collapse (Ballesteros-Paredes et al. 2011). More recently, for a single molecular cloud, a much flatter velocity dispersion-size relation has been observed when studying structures with high column density. This points towards a change in the cloud dynamics once self-gravity becomes dominant (Wu et al. 2010; Traficante et al. 2018). Re-examining Larson's laws, Heyer et al. (2009) show that this can be explained when taking into account the surface density of the structures. Here, we investigate the Larson and Heyer scaling relations of our dendrogram structures.

We compute the mass-weighted 1D velocity dispersion,  $\sigma_{1D}$ , from

$$\sigma_{1D}^2 = \frac{1}{3M} \int_V \rho (\mathbf{v} - \mathbf{v}_0)^2 d^3r, \quad (6)$$

where  $M$  is the total mass of the structure and  $\mathbf{v}_0$  is the velocity of its centre of mass, computed as

$$\mathbf{v}_0 = \frac{1}{M} \int_V \rho \mathbf{v} d^3r. \quad (7)$$

The integration is performed over the entire volume  $V$  of the structure. We choose a mass-weighted average because it roughly represents an intensity-weighted average, which is often used in observations. We estimate the linear size  $R$  from the volume of the structure as

$$R = V^{1/3}. \quad (8)$$

In Fig. 4, we plot  $\sigma_{1D}$  vs.  $R$  for different times (from left to right). The top row shows a compilation of all structures extracted from MC1-HD and MC2-HD, while the bottom row shows all structures found in the five MHD clouds. Note that we show slightly different times for the hydrodynamic ( $t_{\text{evol}} = 1.5, 2.0, 3.5$  Myr) and the MHD simulations ( $t_{\text{evol}} = 2.0, 2.5, 3.5$  Myr), owing to the fact that the

## 6 *S. Ganguly et al.*

former show discernible structures comparatively quicker (see below, also see [Seifried et al. \(2020\)](#)). We distinguish between mostly atomic structures (empty symbols) and mostly molecular structures (filled symbols) as defined in section 2.2 (see also Fig. 3). The colour bar shows the density threshold,  $\rho_{\text{thr}}$ , of each structure, defined as the minimum density value contained in the structure.

For early times, all structures seem to follow a power law relation for both HD and MHD clouds. The exponents were derived from fitting the logarithm of the data points with a non-linear least squares method. For the hydrodynamic clouds we find  $n = 0.61 \pm 0.03$ , which is slightly steeper than Larson's relation, while the best fit for the MHD clouds gives  $n = 0.54 \pm 0.03$  in quite good agreement with the observed scaling relation (Eq. 5), although the scatter is significant.

At later times, high density structures tend to trail off to the left of the power law relation, as these sub-structures have decreasing size but retain a high (mass-weighted) velocity dispersion. We will later see that this is a sign of gravity becoming dynamically important. The obvious branch-like collections of points leading towards small scales are actually identified as those dendrogram branches which lead to the densest sub-structures. Due to the presence of these branches, the fitted power law slope is much steeper than the expected  $n = 0.5$  for later times. From these plots one can also clearly see that the MHD clouds evolve more slowly than the non-magnetized clouds, as the MHD clouds only show dense, flat branches at  $t = 3.5$  Myr, while these are already present at  $t_{\text{evol}} = 2.0$  Myr for the HD runs.

A similar behaviour is seen in the mass-size relation shown in Fig. 5. Apart from a best-fit power law, based on a non-linear least squares fit on the logarithm of the values (similar to discussed above), we also plot here lines corresponding to  $M \propto R$  and  $M \propto R^2$  in dash-dotted and dotted lines, respectively. The overall fitted slope is generally steeper compared to the  $M \propto R^2$  expected from the Larson relation. This steeper slope rather describes the inability of a single exponent to explain the behaviour of all the structures. Visually, the less dense and mostly atomic structures seem to fit better with a  $M \propto R^2$  type power law. The denser structures on the other hand clearly branch off to follow a much shallower power law more similar to  $M \propto R$ . This is reminiscent of more centrally condensed profiles such as Bonnor-Ebert spheres ([Ebert 1955](#); [Bonnor 1956](#)), although in our case the structures are far from spherically symmetric.

Larson's velocity dispersion-size relation was later modified by [Heyer et al. \(2009\)](#) to show that the Larson coefficient  $\sigma_{\text{1D}}/R^{1/2}$  can depend on the surface density,  $\Sigma$ , of the structure. We plot the Heyer relation, i.e.  $\sigma_{\text{1D}}/R^{1/2}$  vs.  $\Sigma$  in figure 6. The surface density of a given structure is calculated as

$$\Sigma = \rho_{\text{avg}} R. \quad (9)$$

Here  $\rho_{\text{avg}}$  is the volume-average density of the structure:

$$\rho_{\text{avg}} = M/V. \quad (10)$$

The dash-dotted diagonal line represents the  $\sigma_{\text{1D}} = (\pi G/5)^{1/2} \Sigma^{1/2} R^{1/2}$  line from [Heyer et al. \(2009\)](#) representing virial equilibrium between kinetic energy and self-gravity ( $\alpha = 1$ , where  $\alpha$  is the kinetic virial parameter). Other values of  $\alpha$  correspond to lines parallel to the Heyer line in log-log space and are plotted with dotted lines. The virial parameter  $\alpha$  obtained in this manner is only a rough representation of the true virial equilibrium, and includes only the kinetic and potential energy terms. We find that at earlier times there is very weak, if any, trend along the Heyer line of  $\alpha = 1$  for both hydro and MHD structures. This picture evolves over time. At  $t_{\text{evol}} = 3.5$  Myr (figure 6, right column), we find two groups of structures: mostly molecular and dense structures

that follow the Heyer line, for both HD and MHD clouds and less dense, mostly (but not exclusively) atomic structures that show no correlation at all.

[Camacho et al. \(2016\)](#) have found similar differing behaviour when they look at structures at different density thresholds in turbulent box simulations. Similar results have been also found by [Weis et al.](#), in prep., when analyzing structures forming in colliding flow simulations. We additionally find that the molecular content of the gas is also tracing these two families of structures relatively well.

There are various possible interpretations for structures following the Heyer relation. The original interpretation of [Heyer et al. \(2009\)](#) was that they represent gravitational equilibrium. [Ballesteros-Paredes et al. \(2011\)](#) point out that, given the typical error estimates, they could also be consistent with gravitational infall, as the infall velocity and virial equilibrium velocity only differ by a factor of  $\sqrt{2}$ . A similar discussion was also presented in [Larson \(1981\)](#). In addition, the estimate of the surface density here is rather crude, and does not incorporate the fractal nature of the complicated medium. To investigate different possible scenarios, we perform an analysis on the different energy terms in the next section.

## 4 ENERGETICS

The interplay of various forces determines the dynamics of the structures involved. For a structure embedded in a more diffuse medium, we consider the self-gravity, kinetic energy, as well as thermal and magnetic energy (for the MHD runs) of the structure. We limit ourselves to the discussion of the various volume terms and do not consider the time dependent or the surface terms of the full virial theorem. Below, we briefly discuss how we determine the various terms.

### 4.1 Energy terms

The gravitational energy of a structure can be separated in two parts - the self-gravity due to its own mass, and the gravitational energy due to the fact that the structure is embedded in an asymmetric gravitational potential caused by the surrounding gas. For the analysis of this section, we have limited ourselves to considering only self-gravity for a more traditional virial analysis. In section 5, we analyse the relative importance of the external medium.

The self gravitational energy of the structure is defined as

$$E_{\text{PE}} = -\frac{1}{2} G \int_V \int_V \frac{\rho(\mathbf{r})\rho(\mathbf{r}')}{|\mathbf{r} - \mathbf{r}'|} d^3r d^3r'. \quad (11)$$

We compute this term by using a KD tree with a geometric opening angle of 0.5 radians. By comparing with the exact potential computed from a direct sum, we find that the errors introduced by the tree method are typically  $\sim 1\%$ .

We also compute the volume term of the magnetic energy, which can contribute to the important magnetic pressure term. This pressure term can act against compression and prevent a structure from collapsing. The magnetic energy of a given structure is computed as

$$E_{\text{B}} = \frac{1}{8\pi} \int_V |\mathbf{B}|^2 d^3r, \quad (12)$$

where  $|\mathbf{B}|$  is the magnitude of the magnetic field.

We compute the thermal energy of a structure as

$$E_{\text{TE}} = \frac{3}{2} \int_V P d^3r, \quad (13)$$

where  $P$  is the thermal pressure of the gas.

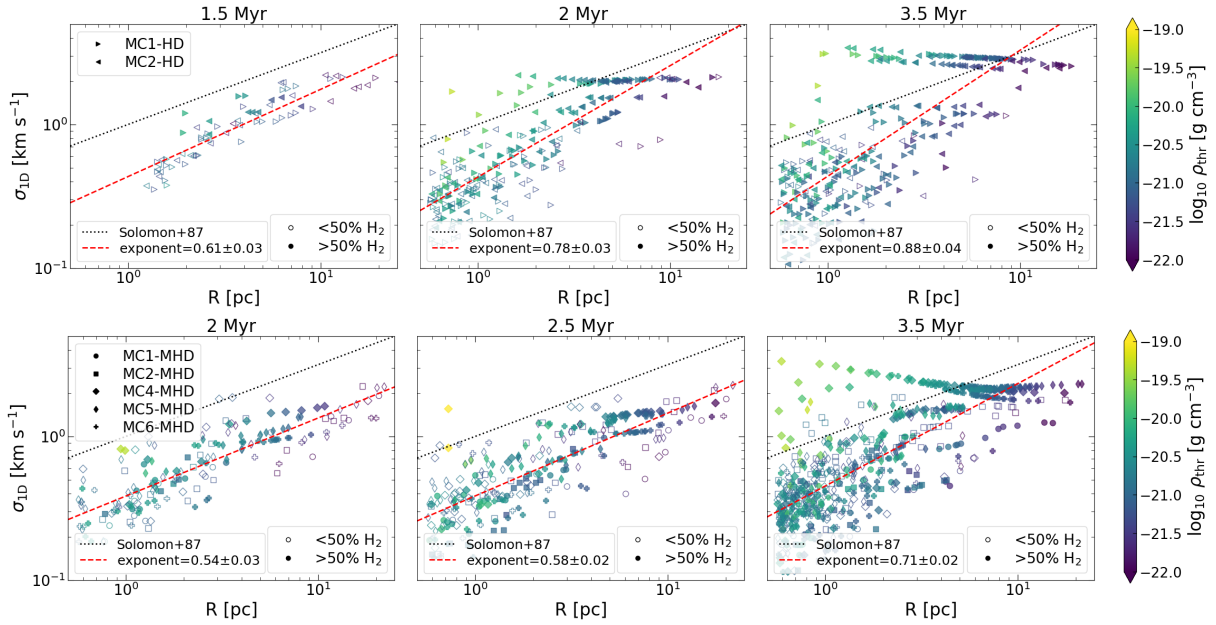


**Figure 4.** Time evolution of the velocity dispersion-size relation for HD clouds at 1.5, 2 and 3.5 Myr (top row, from left) and for MHD clouds at 2, 2.5 and 3.5 Myr (bottom row, from left). The colour bar represents the threshold (minimum) density inside each structure. Plotted as red, dashed and black, dotted lines are the best fit and the  $\sigma \propto R^{1/2}$  obtained by Solomon et al. (1987), respectively. We show the hydrodynamic clouds at an earlier time to highlight that they behave similar to the MHD clouds. Some denser branches trail off to the left, showing complete departure from a Larson-like power law. These dense branches are absent or less pronounced at earlier times.

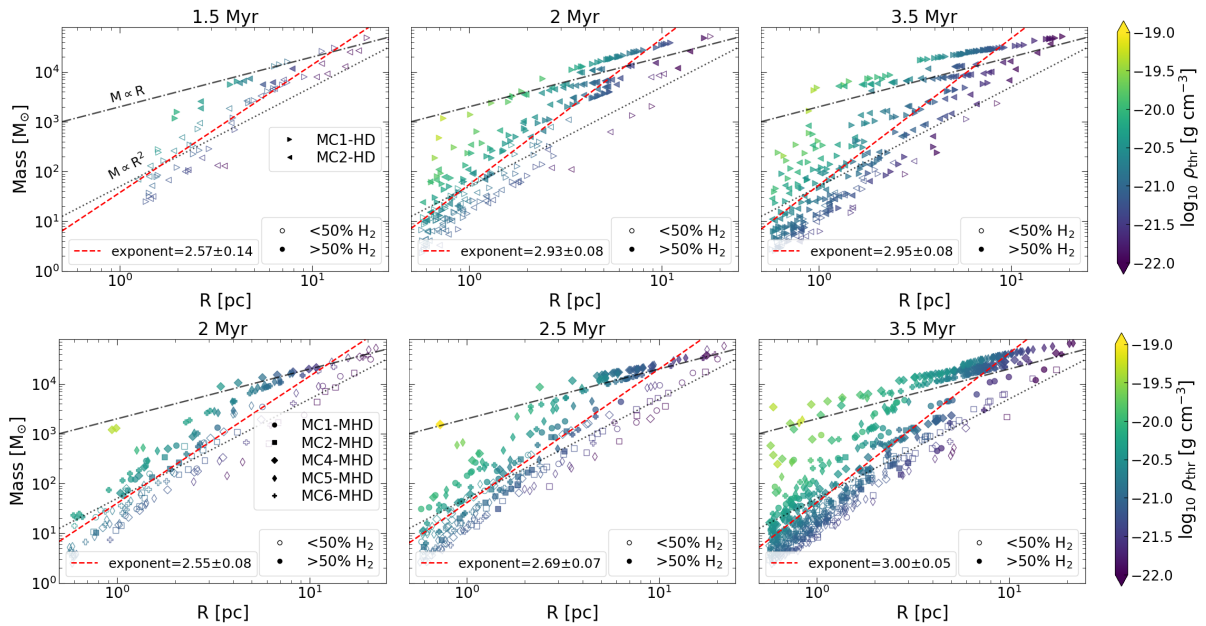


**Figure 5.** Same as in Fig. 4 but now for the mass-size relation. The red, dashed line represents the best-fit, while the black, dash-dotted and the black, dotted lines represent  $M \propto R$  and  $M \propto R^2$ , respectively. The denser branches follow roughly  $M \propto R$ , while the atomic structures seem to be more consistent with  $M \propto R^2$ .

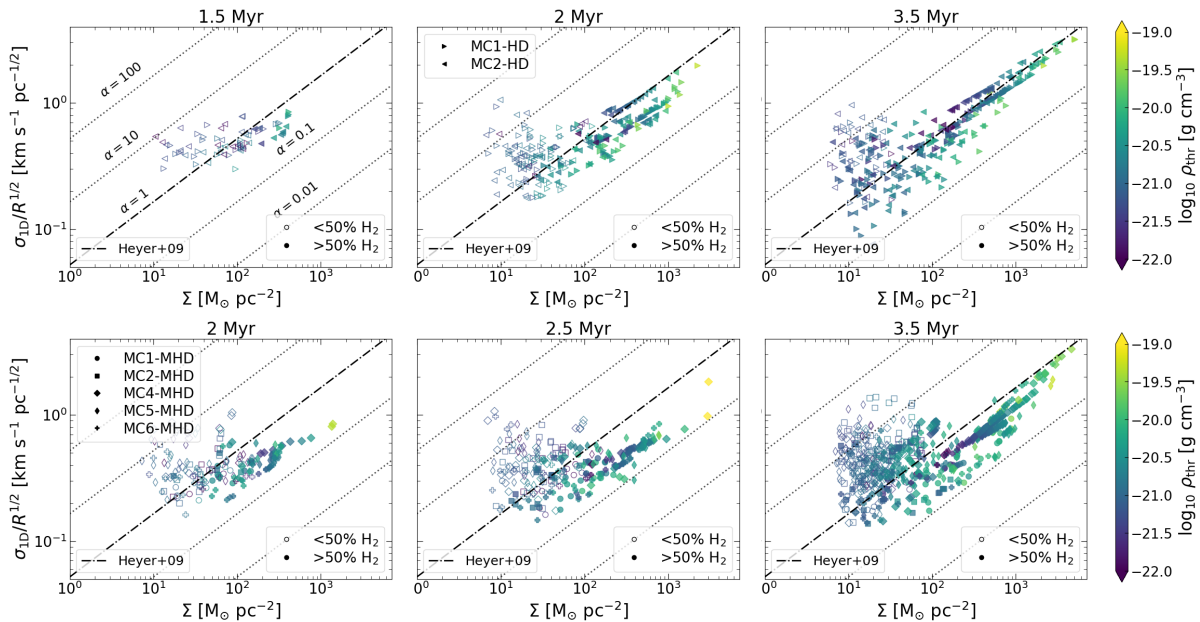


**Figure 6.** Same as in Fig. 4 but now for the Heyer relation. The dash-dotted line represents the  $(\pi G \Sigma / 5)^{1/2}$  line from Heyer et al. (2009) (corresponding to the virial parameter  $\alpha = 1$ ), while the parallel dotted lines represent other possible values of  $\alpha$  in a purely kinetic virial analysis. We find two populations of structures: denser and mostly molecular structures following the Heyer line towards higher  $\Sigma$ , and mostly atomic structures that show no correlation with surface density.

The computation of the kinetic energy,  $E_{\text{KE}}$ , of a structure is done as

$$E_{\text{KE}} = \frac{1}{2} \int_V \rho (\mathbf{v} - \mathbf{v}_0)^2 d^3r, \quad (14)$$

where  $\mathbf{v}_0$  is the bulk velocity computed from Eq. 7.

From the above quantities, we estimate a virial ratio of the volume energy terms:

$$\alpha_{\text{vir}}^{\text{vol}} = \frac{2E_{\text{KE}} + 2E_{\text{TE}} + E_{\text{B}}}{|E_{\text{PE}}|}. \quad (15)$$

The magnetic energy is absent for purely hydrodynamic simulations. Eq. 15 is a simplification of the full virial theorem (McKee & Zweibel 1992; Dib et al. 2007), which includes both time-dependent as well as surface terms, which is beyond the scope of this paper. However, we discuss the surface terms briefly at the end of Section 4.2.

We define bound structures as those with a virial ratio  $\alpha_{\text{vir}}^{\text{vol}} < 1$  and marginally bound structures as  $1 \leq \alpha_{\text{vir}}^{\text{vol}} < 2$ . The definition of marginally bound structures here is motivated by the fact that, in presence of only self-gravity and kinetic energy, a structure with  $\alpha_{\text{vir}}^{\text{vol}} = 2$  would have a net zero total energy,  $E_{\text{tot}}$ , i.e.

$$E_{\text{tot}} = E_{\text{KE}} + E_{\text{PE}} = 0, \quad (16)$$

and as a consequence,

$$\alpha = \frac{2E_{\text{KE}}}{|E_{\text{PE}}|}, \quad (17)$$

is reduced to  $\alpha = 2$ .

#### 4.2 Virial analysis

In Fig. 7, we show the time evolution of the ratio of different energy terms and the self gravitational energy, as well as  $\alpha_{\text{vir}}^{\text{vol}}$  (bottom row)

as a function of their size  $R$  (see Eq. 8) for the two hydrodynamic clouds and in Fig. 8 for the different MHD clouds. We plot the sub-structures at 2 Myr (left column) and at 3.5 Myr (right column). For the HD clouds (Fig. 7), the top two rows present the evolution of thermal and kinetic energy over  $E_{\text{PE}}$  as a function of size  $R$ . The colors represent the density threshold of each analyzed structure. For the MHD clouds (Fig. 8), we also plot the magnetic energy over  $E_{\text{PE}}$  in the top row. The red shaded region shows the marginally bound region. According to Eq. 15, for the ratio of magnetic to potential energy, marginally bound is where  $1 \leq E_{\text{B}}/|E_{\text{PE}}| < 2$ ; for the kinetic and thermal energies, this represents a region where  $0.5 \leq E_{\text{KE}}/|E_{\text{PE}}| < 1$  and  $0.5 \leq E_{\text{TE}}/|E_{\text{PE}}| < 1$ , respectively. This results  $1 \leq \alpha_{\text{vir}}^{\text{vol}} < 2$ .

For the sub-structures in the HD clouds (Fig. 7), we find that the thermal energy is mostly irrelevant for the large scale, as well as for the denser and molecular structures. However, it seems to be important for atomic structures on all scales and for some small-scale molecular structures, particularly at later times. The  $E_{\text{KE}}/|E_{\text{PE}}|$  ratio is far closer to unity for large scale ( $R > 10$  pc) and denser ( $\rho_{\text{thr}} \gtrsim 10^{-20}$  g cm $^{-3}$ ) structures. Due to the significant contribution of  $E_{\text{KE}}$ , we find that only a few structures seem to be bound, although the number of such structures increases from 2 to 3.5 Myr. When we consider the full virial parameter, the behaviour is quite similar to that of the kinetic energy, with the addition that even fewer structures are bound at all times. The emergence of gravitationally bound structures over time suggests a growing importance of gravity as the cloud becomes more evolved. This complements the picture we see in Larson's  $\sigma_{1D}$ - $R$  relation (Fig. 4), where a flat line-width size relation emerges for the densest branches over time.

For the MHD clouds (Fig. 8), the magnetic energy is relevant only for less dense and mostly atomic structures, and does not appear to be significant for the larger scale structures or the denser and potentially

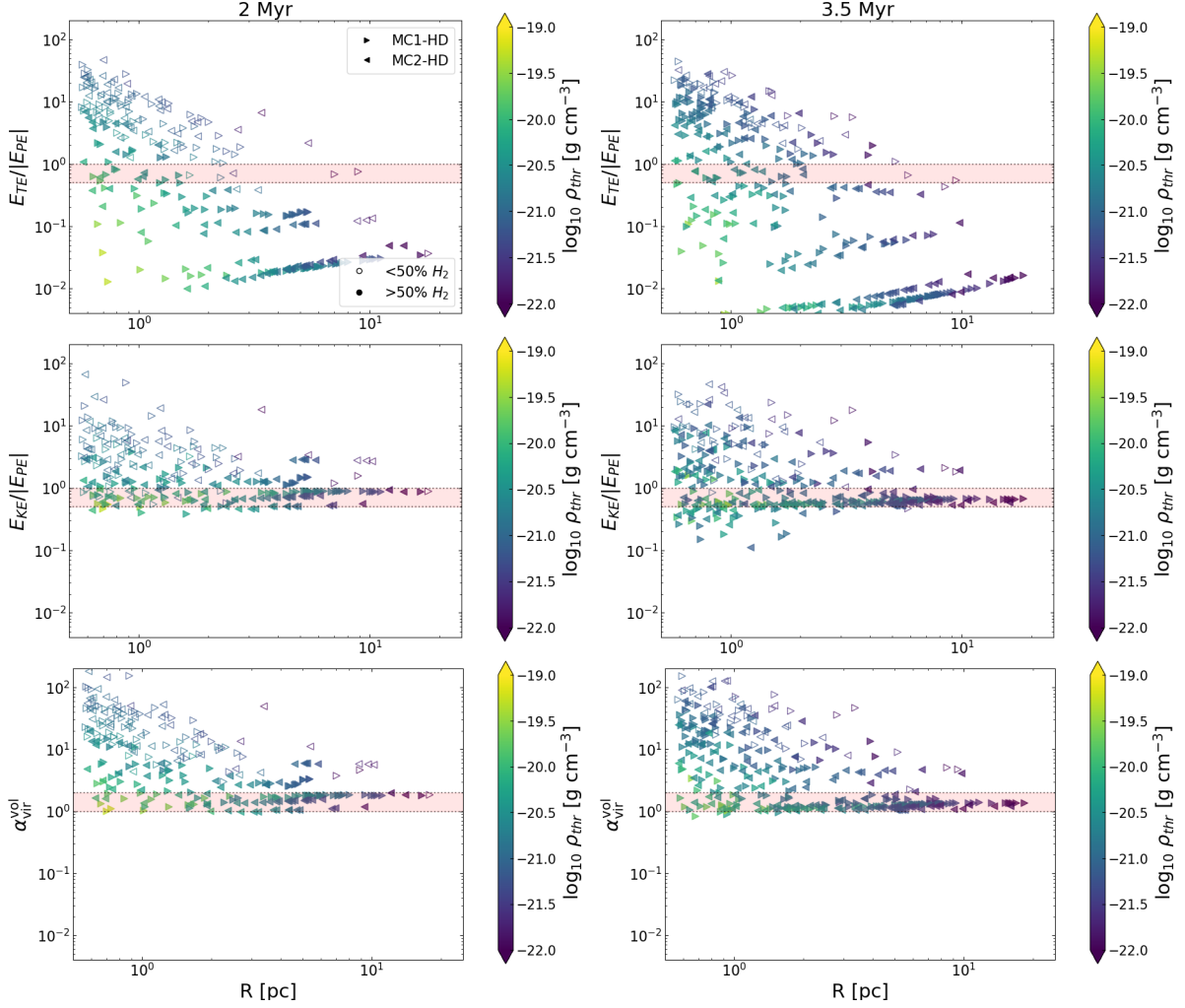


**Figure 7.** Energetics of the two HD clouds at  $t_{\text{evol}} = 2$  Myr (left column) and  $t_{\text{evol}} = 3.5$  Myr (right column). Each plot is a ratio of a different energy to the potential energy. The red shaded region represents the region between marginally bound and virialized ( $1 \leq \alpha < 2$ ) for that particular energy term. Large scale structures are marginally bound in the virial analysis. At smaller scales, most of the structures are kinetically dominated with only a few marginally bound structures, as well as a small number of bound structures.

star forming structures. This is true at earlier as well as later times. This behaviour is echoed in the evolution of  $E_{\text{TE}}/|E_{\text{PE}}|$ , which is quite similar to the behaviour in the hydrodynamic clouds. As in the hydrodynamic case, the dynamics of larger scale, as well as dense structures is mostly dominated by the interplay of  $E_{\text{KE}}$  and  $E_{\text{PE}}$ . The behaviour of  $\alpha_{\text{vir}}^{\text{vol}}$  for HD and MHD clouds is also similar and follows the overall trend of  $E_{\text{KE}}/|E_{\text{PE}}|$ . We note one exception to the purely hydrodynamic structures here though. While at earlier times, we barely have any bound structures at 2 Myr, this number is much higher at 3.5 Myr. This suggests that, with magnetic fields, bound structures form more slowly from a marginally bound environment.

The emergence of gravitationally bound structures over time from a marginally bound environment, suggests that gravity only gradually becomes important for the densest branches, but is not the primary driving force for the formation of the structures. Our findings are more in line with the GT scenario of structure formation, where

gravity takes over only once the turbulent structures are sufficiently compressed.

We stress that the aspect of gradually increasing boundness is essential here. If we look at only the relatively late stages at  $t_{\text{evol}} = 3.5$  Myr for the large-scale cloud structures, which are all molecular and lie close to  $\alpha_{\text{vir}}^{\text{vol}} = 1$ , it is difficult to distinguish between GT and GHC. This can be resolved only by looking at earlier times. The behaviour of the kinetic virial ratio, as well as  $\alpha_{\text{vir}}^{\text{vol}}$ , for the largest-scale structure in each cloud can be seen in Table 3. We find that at 2 Myr, almost all largest-scale structures, with the exception of MC6-MHD, have  $\alpha_{\text{vir}}^{\text{vol}} > 1.8$ , with three of the clouds having  $\alpha_{\text{vir}}^{\text{vol}} > 2$ . This is dramatically reduced at later times, with only MC2-MHD being unbound ( $\alpha_{\text{vir}}^{\text{vol}} > 2$ ) at  $t_{\text{evol}} = 3.5$  Myr.

The decrease in  $\alpha_{\text{vir}}^{\text{vol}}$  for large scale structures which are unbound or marginally bound suggests that the clouds are being compressed, likely by larger scale flows, towards becoming gravitationally bound (see also Section 4.3). While we explicitly show this here only for

10 *S. Ganguly et al.*

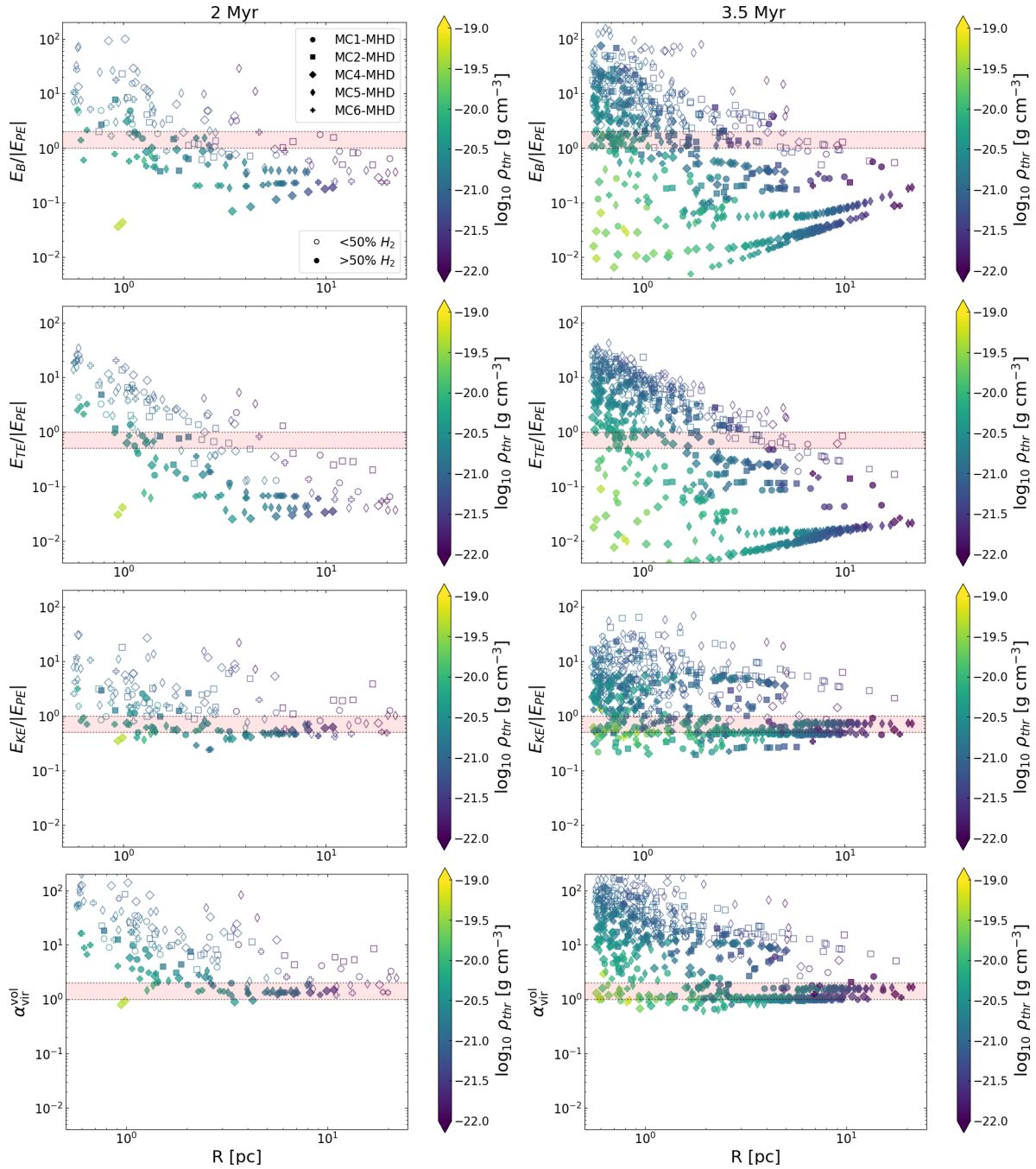


**Figure 8.** Same as in Fig 7 but now for the MHD clouds. Additionally  $E_B/|E_{PE}|$  is plotted in the top row. The red shaded region represents the region between marginally bound and virialized ( $1 \leq \alpha < 2$ ) for that particular energy term. Note that due to Eq. 15, this implies a factor of 2 difference between the energy ratios and  $\alpha_{vir}^{vol}$ , except for  $E_B/|E_{PE}|$ . Large scale structures are mostly marginally bound in the virial analysis. Gravitationally bound structures are few and emerge over time, suggesting their origin is from the dynamics of the marginally bound gas.



Run name	2 Myr		3.5 Myr	
	$2E_{\text{KE}}/ E_{\text{PE}} $	$\alpha_{\text{vir}}^{\text{vol}}$	$2E_{\text{KE}}/ E_{\text{PE}} $	$\alpha_{\text{vir}}^{\text{vol}}$
MC1-HD	1.77	1.85	1.35	1.39
MC2-HD	1.75	1.84	1.19	1.21
MC1-MHD	2.51	3.28	0.93	1.47
MC2-MHD	7.81	8.71	4.30	5.18
MC4-MHD	1.48	1.86	1.13	1.27
MC5-MHD	2.04	2.47	1.48	1.71
MC6-MHD	1.00	1.35	0.95	1.09

**Table 3.** The kinetic virial ratio and  $\alpha_{\text{vir}}^{\text{vol}}$  for the largest-scale ( $\sim 20$  pc) dendrogram structures for different HD and MHD clouds at 2 and 3.5 Myr. All large scale structures have  $\alpha_{\text{vir}}^{\text{vol}} > 1$ , but the value reduces considerably from 2 to 3.5 Myr.

the largest structures, the dependence of  $\alpha_{\text{vir}}^{\text{vol}}$  on  $R$  is relatively flat at large scales ( $R > 10$  pc, Figs. 7 and 8, bottom panels) and we can therefore conclude that this trend is not a consequence of e.g. the choice of our initial dendrogram threshold.

While over time we do see the emergence of individual structures below the bound line, as well as a decrease in the value of  $\alpha_{\text{vir}}^{\text{vol}}$  at large scales, the overall statistical behaviour of most of the cloud sub-structures remains more or less unchanged. This can be seen in Fig. 9, where we show the time evolution of the average of the logarithm of  $\alpha_{\text{vir}}^{\text{vol}}$ ,  $\langle \log_{10} \alpha_{\text{vir}}^{\text{vol}} \rangle$ , for atomic, molecular, and dense molecular structures (structures which are molecular and have a threshold density  $\rho_{\text{thr}} > 10^{-20} \text{ g cm}^{-3}$ ), respectively. Here, we sum over all the different cloud structures, differentiating only between hydrodynamic (Fig. 9, left panel) and MHD clouds (Fig. 9, right panel). The vertical error bar shows the standard error on the mean of  $\log_{10} \alpha_{\text{vir}}^{\text{vol}}$ . Fig. 9 illustrates that the atomic and molecular structures have clearly different energetic behaviour. We can attribute this to the fact that they trace different parts of the parent cloud, as can be visually seen in Fig. 3. The chemical evolution followed in the simulations seems to trace the dynamical difference of the cloud sub-structures in different environments. We further observe that, as we trace denser gas, the average value of  $\alpha_{\text{vir}}^{\text{vol}}$  decreases, suggesting that we trace gas which is close to being gravitationally bound.

As a conclusion to the virial analysis, we briefly remark on the expected behaviour of the surface terms which also contribute to the full virial ratio. Since we find that for most of the structures whose dynamics is important for eventual star formation (both large scale, as well as denser), the kinetic and the potential energy dominate their dynamics, we expect that their corresponding surface terms could be important as well. We perform a detailed analysis on the tidal effect of the external medium in Section 5.

### 4.3 Inflow or infall

The GHC scenario suggests that the high line-widths seen in MCs are a result of infalling gas. On the other hand, if gas is swept up due to larger scale flows, it could also result in possible signs of inflowing gas. To investigate this, we compute the radial velocity as

$$v_r = \frac{1}{M} \int_V \rho(\mathbf{v} - \mathbf{v}_0) \cdot \frac{(\mathbf{r} - \mathbf{r}_0)}{|\mathbf{r} - \mathbf{r}_0|} d^3r, \quad (18)$$

where  $\mathbf{r}_0$  is the position of the centre of mass of a given structure. We show the ratio of the radial velocity of the structures over their 1-dimensional velocity dispersion against  $R$  in Fig. 10. The color bar here represents  $\alpha_{\text{vir}}^{\text{vol}}$ , with bound structures ( $\alpha_{\text{vir}}^{\text{vol}} < 1$ ) marked with an additional black outline. The top row corresponds to all

sub-structures contained in the two hydrodynamic clouds at  $t_{\text{evol}} = 2$  (left) and 3.5 Myr (right), while the bottom row represents the MHD sub-structures. A negative value of  $v_r$  suggests that the gas inside the structure has motion towards the centre of mass while a positive value suggests the reverse. If the high kinetic energy in our dendrogram structures originates from inward motions due to gravitational collapse, we would expect more bound structures to have lower (more negative)  $v_r/\sigma_{1D}$  values. From Fig. 10, we do indeed see that the marginally bound points (reddish) tend to have a negative velocity, especially at larger scales, although the trend is far from clear.

In order to investigate which effect is dominating (gravitational infall or large-scale, compressive inflows), we perform a correlation analysis between  $\alpha_{\text{vir}}^{\text{vol}}$  and  $v_r/\sigma_{1D}$ . This can be seen in Table 4, where we compute the Kendall  $\tau$  parameter at 2 and 3.5 Myr for all (both HD and MHD) large-scale ( $R > 10$  pc) as well as bound and marginally bound ( $\alpha_{\text{vir}}^{\text{vol}} < 2$ ) sub-structures. In each case, we give the Kendall  $\tau$  coefficient,  $k_\tau$ , and the p-value.  $k_\tau$  quantifies the rank correlation between two quantities: +1 denotes perfect positive correlation and -1 perfect negative correlation (Kendall 1938).

Firstly, we note that for *all* structures, there is a statistically significant, mild positive correlation (0.19 at 2 Myr and 0.21 at 3.5 Myr) between  $v_r/\sigma_{1D}$  and  $\alpha_{\text{vir}}^{\text{vol}}$ . Since most of the sub-structures are unbound, this reflects rather the fact that structures with higher  $\alpha_{\text{vir}}^{\text{vol}}$  tend to have higher dispersive motions.

For large-scale structures, at 2 Myr, we do not find a statistically significant correlation (p-value of 0.46). However, at 3.5 Myr, there is a relatively strong anti-correlation ( $k_\tau = -0.43$ ). This implies that a more negative  $v_r/\sigma_{1D}$  is associated with a higher  $\alpha_{\text{vir}}^{\text{vol}}$ , i.e. at large scales the more unbound structures tend to feel a stronger inwards motion. This is contrary to our expectations of a gravitational infall, and rather suggest an inflow, where the stronger compression is associated with a higher kinetic energy, and consequently, a higher virial ratio.

Over all structures with  $\alpha_{\text{vir}}^{\text{vol}} < 2$ , we find an even milder or almost no correlation at both earlier and later times ( $k_\tau = -0.14$  at 2 Myr and  $-0.07$  at 3.5 Myr). The mild anti-correlation here is likely a result of the anti-correlation seen for the larger scale structures, which are mostly marginally bound.

### 4.4 Gravo-turbulence vs global hierarchical collapse

The gradual formation of dense, gravity dominated branches in Larson's  $\sigma_{1D}$ - $R$  relation (Fig. 4, see also Appendix A), the emergence of gravitationally bound structures over time (Figs. 7 and 8, bottom panel), the decrease in  $\alpha_{\text{vir}}^{\text{vol}}$  for large-scale unbound and marginally bound structures (Table 3), and the significant negative correlation between  $v_r/\sigma_{1D}$  and  $\alpha_{\text{vir}}^{\text{vol}}$  at large scales (Table 4) suggest that the dense molecular gas forms from the rarefied medium being swept up by large scale flows, likely originating from the supernovae being driven in the original SILCC simulations. We therefore conclude that our findings support the GT over GHC scenario of structure formation in our simulated clouds. Our results are in line with the new review by Hacar et al. (2022) on filamentary structures and their fragmentation, which provides independent evidence against GHC. In our companion paper (Ganguly et al., in prep.), we suggest that the MCs in our simulations rather form as sheet-like structures tracing the shells of expanding or interacting supernova bubbles, in agreement with the bubble-driven filament formation scenario of MCs (Koyama & Inutsuka 2002; Inoue & Inutsuka 2009; Inutsuka et al. 2015).

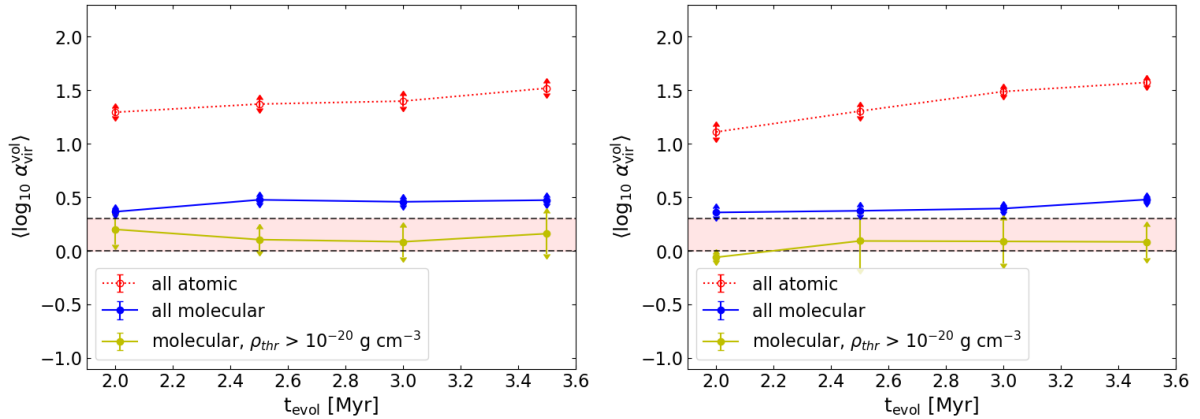


**Figure 9.** Time evolution of the average behaviour of  $\alpha_{\text{vir}}^{\text{vol}}$  for HD (left) and MHD clouds (right). The points represent the mean of  $\log_{10} \alpha_{\text{vir}}^{\text{vol}}$ , while the error bars represent the error on the mean. There is a clear distinction between the average behaviour of these ratios between atomic structures on the one side, and molecular as well as dense structures on the other side. This suggests that the molecular content helps us distinguish between two kinds of structures - unbound and mostly atomic, and marginally bound and mostly molecular.

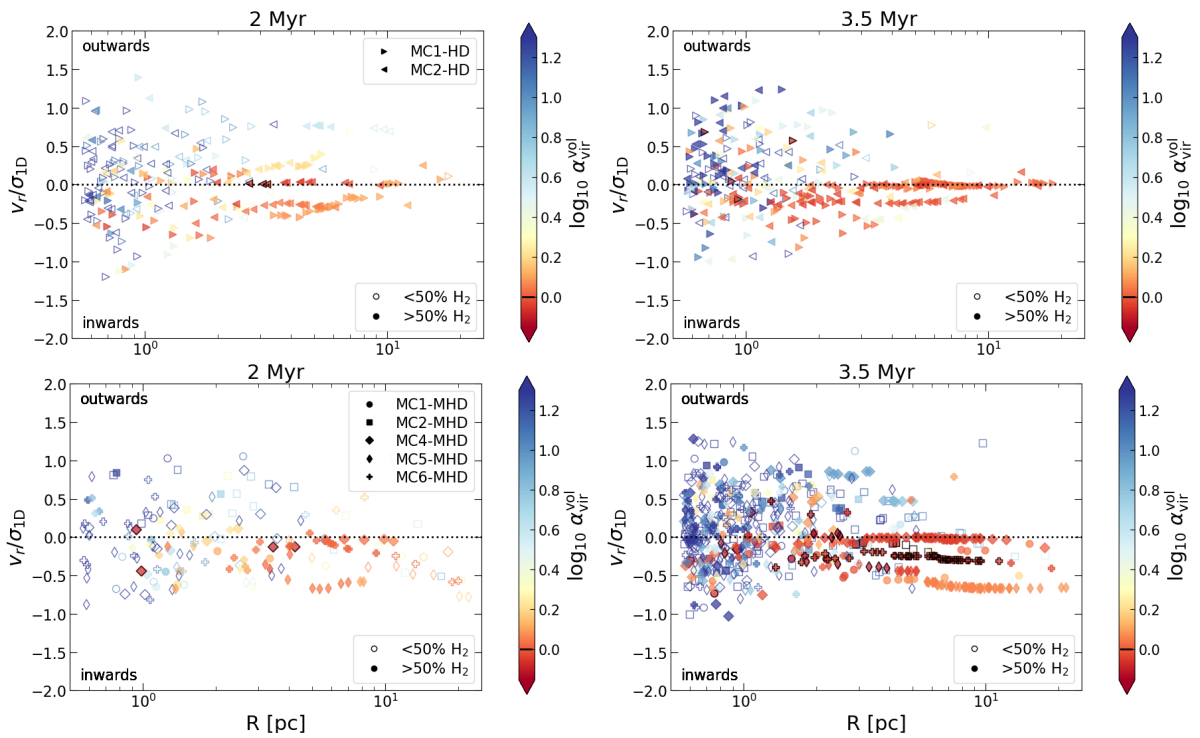


**Figure 10.** Radial velocity over 1D velocity dispersion plotted against the size for HD clouds at  $t_{\text{evol}}=2 \text{ Myr}$  (top left) and  $t_{\text{evol}}=3.5 \text{ Myr}$  (top right), and for MHD clouds at  $t_{\text{evol}}=2 \text{ Myr}$  (bottom left) and  $t_{\text{evol}}=3.5 \text{ Myr}$  (bottom right). A negative value means that the structure has overall a radial velocity towards its centre of mass (i.e. inflowing). The color-bar represents the boundness of the structures, with reddish structures representing  $\alpha_{\text{vir}}^{\text{vol}} < 2$ . The bound structures ( $\alpha_{\text{vir}}^{\text{vol}} < 1$ ), corresponding to points below the horizontal black bar in the color bar) are marked with black outlines. Large scale marginally bound structures show signs of inflowing velocity.

In similar simulations of forming MCs in a supernova-driven, stratified, turbulent medium, [Ibáñez-Mejía et al. \(2017\)](#) have found that their clouds remain overall gravitationally bound, and compressions due to supernovae are insufficient to drive the turbulence in the dense molecular gas. This is in contrast to our results. While it is

difficult to compare the simulations directly, we hypothesise that the difference between the results could lie in the technique of forming dense structures. [Ibáñez-Mejía et al. \(2017\)](#) have no self-gravity in the beginning and model gravitational interactions after the inception of the clouds. In contrast, our clouds include self-gravity from

$t_{\text{evol}}$ [Myr]	all		$R > 10$ pc		$\alpha_{\text{vir}}^{\text{vol}} < 2$	
	$k_{\tau}$	p-value	$k_{\tau}$	p-value	$k_{\tau}$	p-value
2	0.19	$3 \times 10^{-9}$	0.11	0.46	-0.14	0.009
3.5	0.21	$1.1 \times 10^{-24}$	-0.43	$1.1 \times 10^{-4}$	-0.07	0.03

**Table 4.** The Kendall  $\tau$  correlation values between  $v_r/\sigma_{1D}$  and  $\alpha_{\text{vir}}^{\text{vol}}$  for all, large scale, and bound structures at different times. In each case, the  $\tau$  statistic,  $k_{\tau}$ , and the corresponding p-value is shown. Overall, the structures show a weak correlation between  $v_r/\sigma_{1D}$  and  $\alpha_{\text{vir}}^{\text{vol}}$ , i.e. a larger  $\alpha_{\text{vir}}^{\text{vol}}$  leads to a larger outwards velocity. However, the large scale structures experiencing inflow show an anti-correlation at  $t_{\text{evol}} = 3.5$  Myr, i.e. less bound structures on the large scales have a higher inflow velocity, suggesting compression.

the very beginning and therefore form more self-consistently. This perhaps suggests that modelling gravitational interactions, including tidal effects, in the rare gas is important for consistently modelling the velocity structures and dynamics of the denser sub-structures that form later on. Once the dense, molecular gas has been formed, additional external nearby supernovae (at distances less than 50 pc) only drive turbulence for a short time (Seifried et al. 2018).

The role of supernovae in creating a turbulent cascade has been extensively discussed as a possible origin of the Larson-like scaling relations in simulated clouds (e.g. Kritsuk et al. 2013; Padoan et al. 2016). The role of the combined effect of supernova-driven turbulence and self-gravity has also been suggested with relation to the observed relations (see e.g. Izquierdo et al. 2021). Our findings are in agreement with these results.

## 5 INTERNAL VS EXTERNAL GRAVITY

### 5.1 Comparison of acceleration terms

In the analysis done so far, we have concentrated only on the self-gravity of individual structures. Due to the chaotic nature of the medium, the clumpy surrounding medium contributes to an asymmetric gravitational pull on any given structure, and thereby influences its dynamics. The gravity of the surrounding medium causes tidal effects within each structure, which can result in both, shear motions to tear a structure apart, as well as tidal compression to enhance its collapse along certain directions. Note that tidal compression due to the external medium can never be compressive from all directions, and rather deforms the mass distribution.

We highlight the relation between the acceleration due to self-gravity and the surrounding medium in Fig. 11. We consider a structure embedded in a more diffuse medium. For each point inside this structure, the total gravitational acceleration,  $\mathbf{g}_{\text{tot}}$ , can be computed as

$$\mathbf{g}_{\text{tot}} = -\nabla\Phi_{\text{tot}}, \quad (19)$$

where  $\Phi_{\text{tot}}$  is the global gravitational potential due to all of the gas in the simulation and is obtained directly from the simulation data. We estimate the acceleration due to self-gravity,  $\mathbf{g}_{\text{int}}$ , by a KD tree algorithm using only the mass contained inside the structure. We can then obtain the acceleration solely due to the surrounding medium by the vector subtraction of these two quantities.

$$\mathbf{g}_{\text{ext}} = \mathbf{g}_{\text{tot}} - \mathbf{g}_{\text{int}} \quad (20)$$

Note that  $\mathbf{g}_{\text{tot}}$  (and as a consequence  $\mathbf{g}_{\text{ext}}$ ) here is caused by the gas distribution, and does not include the galactic potential. The scale height of the galactic potential due to old stars in the simulations is 100 pc, much larger than our largest structures. We therefore neglect its effect.

If self-gravity is the only important term, then the  $\mathbf{g}_{\text{int}}$  and  $\mathbf{g}_{\text{tot}}$

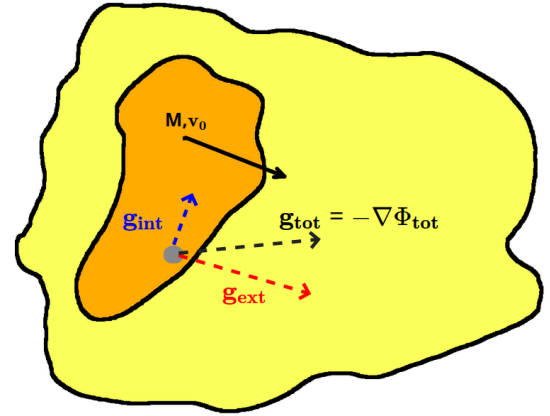


**Figure 11.** Sketch representing the internal and external gravitational acceleration. A given structure mass  $M$  and centre of mass velocity  $\mathbf{v}_0$  is embedded in a more diffuse surrounding medium. For each point inside the structure, we compute the net gravitational acceleration  $\mathbf{g}_{\text{tot}}$  as the negative gradient of the global potential  $\Phi_{\text{tot}}$ , and the self gravitational acceleration  $\mathbf{g}_{\text{int}}$  based on the mass distribution of the structure itself using a KD tree. The effect of solely the surrounding medium is then the vectorial subtraction of these two terms according to Eq. 20.

terms should be comparable, and the angle between them should peak at a value close to 0. The large-scale structures should also peak near zero, by virtue of the fact that there simply is little gas outside the structures to exert significant tidal forces.

We show the distribution of angles between these two terms, denoted by  $\cos^{-1}(\hat{\mathbf{g}}_{\text{tot}} \cdot \hat{\mathbf{g}}_{\text{int}})$ , as PDF computed over all cells for each dendrogram structure of one example cloud (MC1-HD at 3.5 Myr) in Fig. 12. Here,  $\hat{\mathbf{g}}_{\text{tot}}$  and  $\hat{\mathbf{g}}_{\text{int}}$  are the unit vectors of  $\mathbf{g}_{\text{tot}}$  and  $\mathbf{g}_{\text{int}}$ , respectively, i.e.

$$\hat{\mathbf{g}}_{\text{tot}} = \frac{\mathbf{g}_{\text{tot}}}{|\mathbf{g}_{\text{tot}}|}, \quad \hat{\mathbf{g}}_{\text{int}} = \frac{\mathbf{g}_{\text{int}}}{|\mathbf{g}_{\text{int}}|}. \quad (21)$$

The histogram of each individual dendrogram structure is shown by a grey line. If the angle between these two vectors is completely random, as could be the case if self-gravity is not at all important, then the histogram of angles should follow a distribution  $P(\theta) \propto \sin(\theta)$ . This is denoted by the dashed cyan line. The average behaviour for atomic, molecular, and dense molecular ( $\rho_{\text{thr}} > 10^{-20}$  g cm $^{-3}$ ) sub-structures for this particular cloud is shown in red, blue and yellow, respectively.

From the individual grey outlines, we see that for many structures, the angle between the two vectors is not random, and there is some preferential alignment. A few of the structures do indeed peak near 0, while there are also a significant number of structures where the angle

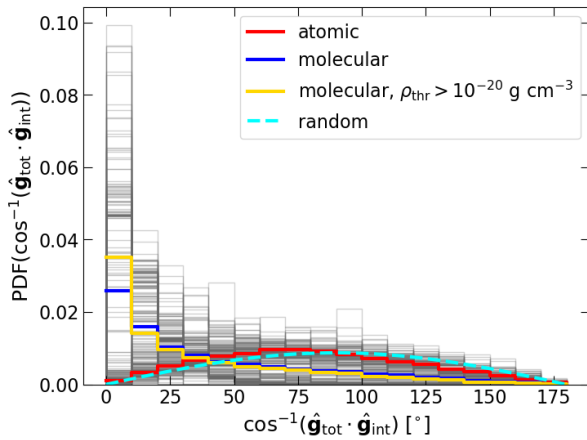


**Figure 12.** Histogram of angles between the self-gravitational acceleration  $\mathbf{g}_{\text{int}}$  and the total gravitational acceleration  $\mathbf{g}_{\text{tot}}$  due to gas both inside and outside the structure, for all different dendrogram structures of the cloud HD 1 at  $t_{\text{evol}} = 3.5$  Myr. The histogram for each individual structure is plotted with a grey line. The cyan dashed line shows how the distribution should be if these two vectors were randomly aligned (i.e. if self-gravity plays no role). The average for the atomic, molecular, and dense molecular structures is shown in red, blue, and yellow, respectively. We see that a preferential alignment between the two vectors is seen prominently for molecular structures.

distribution is relatively random. A clear distinction is seen when calculating the average behaviour for the molecular structures and the atomic structures, separately. The atomic structures show a behaviour which is in good agreement with the random line, suggesting that they are only marginally affected by their self-gravity. In contrast, the average behaviour of the molecular structures clearly shows that self-gravity plays a more pivotal role in their evolution.

We find consistent results when looking at the median angle distribution against  $\alpha_{\text{vir}}^{\text{vol}}$ , for all the different cloud structures in Fig. 13 (left panel). The median angle for a given sub-structure here is computed by obtaining the median for  $\cos^{-1}(\mathbf{g}_{\text{tot}} \cdot \mathbf{g}_{\text{int}})$  over all cells in the structure. The horizontal red band represents the marginally bound region ( $1 \leq \alpha_{\text{vir}}^{\text{vol}} < 2$ ), while the vertical dotted line represents the expected median for a completely random alignment, i.e. 90 degrees. We see a clear correlation between the median angle and the virial ratio, with smaller median angles corresponding to smaller virial ratios. Interestingly, there seem to be some structures, which are marginally bound but still have a relatively high median angle. These could possibly represent structures that are at least partially compressed due to tidal forces.

We find a similar picture if we compare the density weighted mean of the ratio of magnitudes of  $\mathbf{g}_{\text{int}}$  and  $\mathbf{g}_{\text{ext}}$  for each structure. This is shown in the right panel of Fig. 13, where we plot the log of the average of  $\frac{|\mathbf{g}_{\text{int}}|}{|\mathbf{g}_{\text{ext}}|}$  against  $R$ . We compute this by:

$$\left\langle \frac{|\mathbf{g}_{\text{int}}|}{|\mathbf{g}_{\text{ext}}|} \right\rangle = \frac{1}{M} \int_V \frac{|\mathbf{g}_{\text{int}}|}{|\mathbf{g}_{\text{ext}}|} \rho d^3r \quad (22)$$

The colorbar here represents  $\alpha_{\text{vir}}^{\text{vol}}$ , with bound structures ( $\alpha_{\text{vir}}^{\text{vol}} < 1$ ) marked with an additional black outline. We find that large scale ( $> 10$  pc) structures experience only a small effect from external gravity, owing to the fact that they represent almost the entire cloud and there is little mass outside to impart significant tidal influence. At smaller scales, we do continue to have structures where self-gravity is far

more important compared to the gravity of the surrounding medium, but we also find a large number of (predominantly atomic, but also molecular) structures where the external gravity can play an important role. There is also a clear trend that more bound structures tend to have stronger self-gravity, and therefore experience less influence due to the external medium. It is important to note that this analysis compares only gravity terms, and therefore does not tell us about the overall importance of gravity compared to other forces (see Section 4).

Finally, we attempt to directly compute the energy associated with the external gravitational field  $\mathbf{g}_{\text{ext}}$ . We estimate this from

$$E_{\text{PE}}^{\text{ext}} = \int_V \rho(\mathbf{r} - \mathbf{r}_0) \cdot \mathbf{g}_{\text{ext}} d^3r. \quad (23)$$

The comparison of  $E_{\text{PE}}^{\text{ext}}$  with the self-gravitating potential energy and kinetic energy at  $t_{\text{evol}} = 3.5$  Myr is seen in Fig. 14 for all sub-structures, both HD and MHD. The x-axis represents the size  $R$  of structure, while the colorbar plots the density threshold. The horizontal dotted line represents a value of 1 in the ratio for both panels. We see that  $E_{\text{PE}}^{\text{ext}}$  is smaller than the kinetic (right panel) or the self-gravitating potential energy (left panel) for almost all structures. This, however, hides the potentially dynamic effect tidal forces can have. If a structure is being partially compressed on one side and torn apart on the opposite side, in terms of energy these two effects would tend to cancel each other but the structure is actually being deformed. This can be captured by performing a more nuanced tidal analysis, which we do in the following.

## 5.2 Tidal analysis

The gravity of the external medium is important for a significant number of structures in our clouds. It is, however, unclear what exact effect the external gravity has. The structures in the simulations live in a chaotic environment, and therefore the net effect of the tides can cause shear motions, disrupting their possible collapse or hindering compression. Conversely, tidal effects may cause at least partial compression. To quantify the effect of the gravity of the medium surrounding the structure, we perform an analysis based on the tidal tensor (see e.g. Renaud et al. 2009, 2011).

For a gravitational potential field  $\Phi$ , the tidal tensor  $\mathbf{T}$  is defined such that

$$T_{ij} = -\partial_i \partial_j \Phi. \quad (24)$$

The eigenvalues of the tidal tensor encode the information related to deformation (compression/extension) occurring due to gravity at a certain point due to the local gravitational field. Because the tidal tensor is symmetric and real-valued, it can be written in orthogonal form. The diagonalized tidal tensor is given as,

$$\mathbf{T} = \begin{bmatrix} \lambda_1 & 0 & 0 \\ 0 & \lambda_2 & 0 \\ 0 & 0 & \lambda_3 \end{bmatrix} \quad (25)$$

where  $\lambda_i$  are its eigenvalues. The trace of the tidal tensor  $\text{Tr}(\mathbf{T}) = \sum_{i=1}^3 \lambda_i$  contains the local density information in the Poisson equation:

$$\text{Tr}(\mathbf{T}) = -\nabla^2 \Phi = -4\pi G \rho. \quad (26)$$

This implies that the trace is 0 if the point at which the tidal tensor is evaluated is outside the mass distribution.

For example, for a point of mass  $M$ , the tidal tensor at distance  $x$

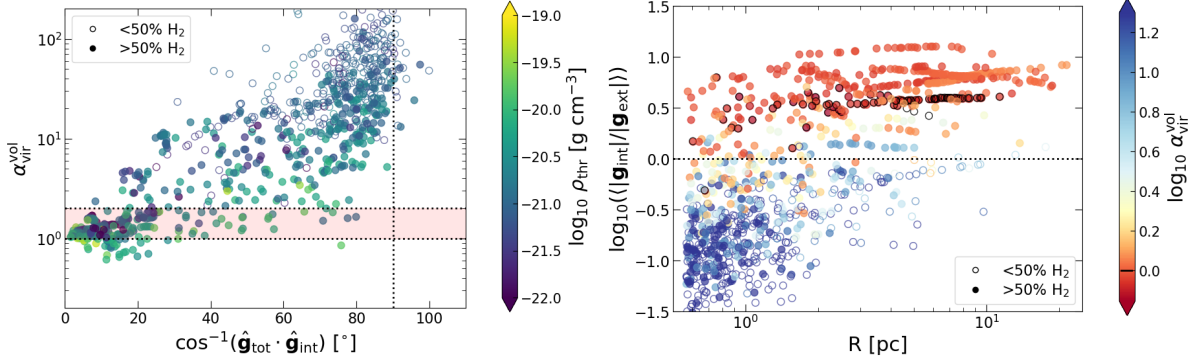


**Figure 13.** Left: The virial parameter  $\alpha_{\text{vir}}^{\text{vol}}$  of the structures, plotted against the median angle distribution between the self gravitational acceleration  $\mathbf{g}_{\text{int}}$  and the total gravitational acceleration  $\mathbf{g}_{\text{tot}}$ , for all clouds, both HD and MHD at  $t_{\text{evol}} = 3.5$  Myr. The red shaded region shows the region between marginally bound and virialized, while the vertical dotted line shows the expected value for a completely random alignment between  $\mathbf{g}_{\text{int}}$  and  $\mathbf{g}_{\text{tot}}$ . More bound structures have a preferential alignment between  $\mathbf{g}_{\text{int}}$  and  $\mathbf{g}_{\text{tot}}$ . Right: Average ratio of  $\mathbf{g}_{\text{int}}$  to the external gravitational acceleration  $\mathbf{g}_{\text{ext}}$ , plotted for each structure against its size, for all clouds at  $t_{\text{evol}} = 3.5$  Myr. The colorbar shows the virial ratio  $\alpha_{\text{vir}}^{\text{vol}}$ , and gravitationally bound structures are marked with a black circle. For the unbound, and mostly but not exclusively atomic structures, the external gravity seems to be more important compared to the self-gravity of the structures.

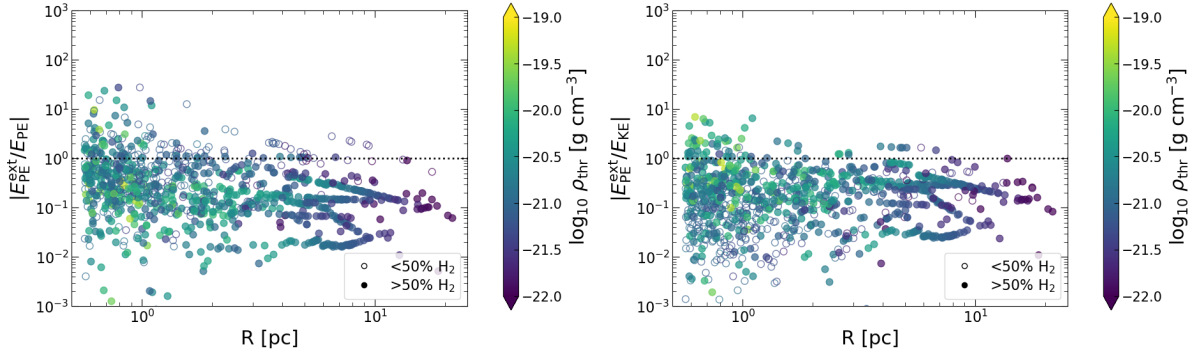


**Figure 14.** Ratio of the magnitudes of external gravitational energy  $E_{\text{PE}}^{\text{ext}}$  to the self gravitation potential energy (left) and to the kinetic energy (right) for all clouds, both HD and MHD, at  $t_{\text{evol}} = 3.5$  Myr. The potential energy due to the external medium is generally less for almost all structures compared to both potential and kinetic energy. This, however, masks compression and extension happening to the same structure due to the external medium, which would cancel out in the energy term but still deform the structure.

is given as:

$$\mathbf{T} = \begin{bmatrix} \frac{2GM}{x^3} & 0 & 0 \\ 0 & -\frac{GM}{x^3} & 0 \\ 0 & 0 & -\frac{GM}{x^3} \end{bmatrix} \quad (27)$$

The sign of the eigenvalues indicates whether the given mode is compressive or extensive, while the magnitude represents the strength of the respective compressive/extensive mode (see e.g. Renaud et al. 2009). A positive eigenvalue  $\lambda_i > 0$  implies that a clump of gas will expand along that particular eigen-direction due to the local gravitational field, while a negative eigenvalue of  $\lambda_i < 0$  implies the opposite. This does not of course automatically imply that the structure will successfully collapse or disperse along the given eigen-direction. The present analysis is done only on the gravitational field, and reflects the nature of gravitational deformation, in absence of all other resisting forces such as thermal or magnetic pressure.

For the purpose of our analysis, we are interested if an entire structure will compress/extend due to the gravitational field. The average tidal tensor for an entire structure can be computed as the

volume average of the tidal tensor at each point:

$$\langle \mathbf{T} \rangle_{ij} = \frac{1}{V} \int_V \partial_i g_j d^3r. \quad (28)$$

Similar to splitting the gravitational acceleration vector in the previous section, we can split the tidal tensor also into three parts: the tidal tensor due to only the matter inside the structure,  $\mathbf{T}_{\text{int}}$ , due to only matter distribution external to the structure,  $\mathbf{T}_{\text{ext}}$ , and their sum due to the entire matter distribution:

$$\langle \mathbf{T} \rangle_{\text{tot}} = \langle \mathbf{T} \rangle_{\text{int}} + \langle \mathbf{T} \rangle_{\text{ext}}. \quad (29)$$

Here,  $\langle \mathbf{T} \rangle_{\text{tot}}$  represents the net deformation due to both, the structure itself and its surroundings, while  $\langle \mathbf{T} \rangle_{\text{ext}}$  represents the deformation introduced solely due to the external medium. The trace of the three different tidal tensors are as follows:

$$\text{Tr}(\langle \mathbf{T} \rangle_{\text{tot}}) = -4\pi G \rho_{\text{avg}} \quad (30)$$

$$\text{Tr}(\langle \mathbf{T} \rangle_{\text{int}}) = -4\pi G \rho_{\text{avg}} \quad (31)$$

$$\text{Tr}(\langle \mathbf{T} \rangle_{\text{ext}}) = 0, \quad (32)$$

where  $\rho_{\text{avg}}$  is the average density computed in Eq. 10. We show in the

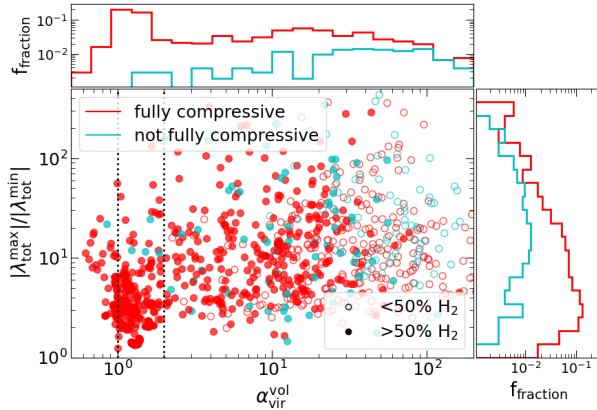


**Figure 15.** The ratio of the largest to the smallest eigenvalue of the tidal tensor  $\langle \mathbf{T} \rangle_{\text{tot}}$  plotted against  $\alpha_{\text{vir}}^{\text{vol}}$  of the structures, for all clouds at  $t_{\text{evol}} = 3.5$  Myr. The two vertical lines denote the marginally bound region ( $1 \leq \alpha_{\text{vir}}^{\text{vol}} < 2$ ). The red symbols represent fully compressive structures (all  $\lambda_i < 0$ ), while the cyan ones are structures which have at least extensive mode. The side-panels show the 1D distribution of the fraction of structures based on the distribution along that axis, and are normalized by the total number of structures. The  $\lambda_{\text{tot}}^{\text{max}}/\lambda_{\text{tot}}^{\text{min}}$  ratio represents the degree of anisotropy in the gravitational field. For most structures, the overall deformation due to gravity is still fully compressive, suggesting that disruptive tidal effects are not dominant. Structures with at least one extensive mode seem to experience a more anisotropic (higher  $|\lambda_{\text{tot}}^{\text{max}}|/|\lambda_{\text{tot}}^{\text{min}}|$ ) gravitational field. They are also more likely to be more unbound, while marginally or gravitationally bound structures are almost always fully compressive, with a few exceptions.

Appendix B that the traces are retrieved. An important consequence of Eqs. 30-32 is that  $\langle \mathbf{T} \rangle_{\text{ext}}$  must contain both compressive and extensive (disruptive) modes, corresponding to negative and positive  $\lambda_i$  respectively. In contrast,  $\langle \mathbf{T} \rangle_{\text{int}}$  and  $\langle \mathbf{T} \rangle_{\text{tot}}$  must contain at least one compressive mode, but might also be fully compressive.

In Fig. 15, we plot the ratio of the maximum to the minimum absolute eigenvalue of the total tidal tensor  $|\lambda_{\text{tot}}^{\text{max}}|/|\lambda_{\text{tot}}^{\text{min}}|$  against the virial ratio of the structures. These are computed as

$$|\lambda_{\text{tot}}^{\text{max}}| = \max(\{|\lambda_{i,\text{tot}}|\}) \quad (33)$$

$$|\lambda_{\text{tot}}^{\text{min}}| = \min(\{|\lambda_{i,\text{tot}}|\}), i = 1, 2, 3. \quad (34)$$

Since the eigenvalues can become negative, we consider their absolute values in order to disentangle the relative importance of tidal compression ( $\lambda < 0$ ) vs extension ( $\lambda > 0$ ). Fully compressive deformations (all three  $\lambda_i < 0$ ) are shown in red, while those with at least one extensive mode are shown in cyan. The two vertical dashed lines represent  $\alpha_{\text{vir}}^{\text{vol}} = 1$  and  $\alpha_{\text{vir}}^{\text{vol}} = 2$ . The top and right side-panels show the fraction  $f_{\text{fraction}}$  of structures against  $\alpha_{\text{vir}}^{\text{vol}}$  and  $|\lambda_{\text{tot}}^{\text{max}}|/|\lambda_{\text{tot}}^{\text{min}}|$ , respectively, for both fully compressive and partially extensive structures.

We first note that most structures have three compressive modes, suggesting that the inclusion of the surrounding clumpy medium, while modifying the nature of gravitational interaction, still results in compressive deformation due to the self-gravity. Note that this analysis is done on the gravity alone, and does not therefore imply that the structure is actually collapsing, only that this is the net effect the overall gravitational field will achieve.

We further find that the compression due to gravity is highly anisotropic, and on average appears to be more anisotropic (higher

$|\lambda_{\text{tot}}^{\text{max}}/\lambda_{\text{tot}}^{\text{min}}|$ ) for structures with at least one extensive mode (Fig. 15, right panel histogram). A higher anisotropy indicates that gravity is attempting to flatten or elongate these structures. Partially extensive structures also seem to experience such an elongating effect more strongly compared to fully compressive structures.

From Fig. 15, top panel histogram, we also see that structures which have at least one extensive mode, also tend to be more unbound. This raises the intriguing possibility that perhaps their high  $\alpha_{\text{vir}}^{\text{vol}}$  values are even generated by the highly anisotropic deformation introduced due to tides, by converting tidal energy into kinetic energy.

To investigate this possible scenario, and to quantify the relevance of the tidal force compared to other terms (such as self-gravity and turbulence), we perform a further timescale analysis based on the tidal tensor. For this purpose, we are interested in quantifying the relevant timescales and energies introduced by the external medium, and therefore use  $\langle \mathbf{T} \rangle_{\text{ext}}$  for our analysis.

The eigenvalues of the tidal tensor have units of  $[\text{time}]^{-2}$ , and can therefore directly be converted into a timescale. Assuming that the largest eigenvalue dominates the deformation of a given structure, we can define a tidal timescale which represents the typical deformation timescale of the given structure solely due to the external gravitational field as follows:

$$t_{\text{tidal}}^{\text{ext}} = (|\lambda_{\text{ext}}^{\text{max}}|)^{-1/2}, \quad (35)$$

where  $|\lambda_{\text{ext}}^{\text{max}}|$  is the maximum of the absolute eigenvalues  $|\lambda_{i,\text{ext}}|$ , similar to Eq. 33.

To compare this deformation timescale with the typical timescale of the gravity and turbulence, we use the free-fall time,  $t_{\text{ff}}$ , and the crossing time,  $t_{\text{crossing}}$ , respectively. The free fall time represents the timescale over which a uniform density spherical structure would collapse in the absence of any pressure forces, solely due to its own self-gravity:

$$t_{\text{ff}} = \sqrt{\frac{3\pi}{32G\rho_{\text{avg}}}}. \quad (36)$$

If the ratio  $t_{\text{tidal}}^{\text{ext}}/t_{\text{ff}} \gg 1$ , this implies that the self-gravity of the structure dominates and acts on a much shorter timescale compared to any deformation due to external tidal forces. In contrast, if  $t_{\text{tidal}}^{\text{ext}}/t_{\text{ff}} \ll 1$ , then tidal deformation is important in terms of modifying any possible collapse of a given structure.

Similarly, the crossing timescale is computed as

$$t_{\text{crossing}} = \frac{c}{\sigma_{1D}}, \quad (37)$$

where  $c$  is the shortest axis of the fitted ellipsoid (Eq. 4). The crossing timescale represents the timescale over which supersonic turbulence is established throughout the medium. In the absence of driving forces, supersonic turbulence is also expected to decay over  $t_{\text{crossing}}$  (Mac Low et al. 1998; Stone et al. 1998). If  $t_{\text{tidal}}^{\text{ext}}/t_{\text{crossing}} \gg 1$ , the turbulence dissipates on a much shorter timescale compared to the tidal deformation timescale. On the other hand, if  $t_{\text{tidal}}^{\text{ext}}/t_{\text{crossing}} \ll 1$ , the crossing timescale is much longer compared to the tidal timescale, and gravitational deformation occurs on a timescale short enough to possibly generate the high amount of kinetic energy seen in our energy analysis.

The behaviour of the two ratios against the virial ratio of the different structures is shown in Fig. 16 (top:  $t_{\text{tidal}}^{\text{ext}}/t_{\text{ff}}$ , middle:  $t_{\text{tidal}}^{\text{ext}}/t_{\text{crossing}}$ ). In both plots, the colorbar represents the size of the structures. The vertical dotted lines show the boundary between virialized and marginally bound. The circles with a black outline indicate

structures which have at least one extensive  $\lambda_i^{\text{tot}}$  (corresponding to the cyan points in Fig. 15).

We see that the ratio  $t_{\text{tidal}}^{\text{ext}}/t_{\text{ff}}$  becomes slightly higher with a lower  $\alpha_{\text{vir}}^{\text{vol}}$ , and therefore self-gravity becomes more and more important as we go to more bound structures. This agrees with the previous picture in Fig. 13, where the external gravity was magnitude-wise less important for larger scale, as well as more bound structures. Structures with at least one extensive mode have tidal timescales comparable to or slightly shorter than the free fall time.

The ratio  $t_{\text{tidal}}^{\text{ext}}/t_{\text{crossing}}$  has quite a different behaviour (Fig. 16, middle panel). For almost all structures, but especially for unbound structures, the crossing timescale is much shorter compared to the tidal timescale. This suggests that turbulence dissipates on a much shorter timescale compared to the gravitational deformation timescale introduced by tides and as such, tides cannot be the principal contributor to the high kinetic energy in the structures.

The difference in this average behaviour can be seen in a histogram of these two ratios in Fig. 16, bottom panel. Here, the distribution of  $t_{\text{tidal}}^{\text{ext}}/t_{\text{ff}}$  and  $t_{\text{tidal}}^{\text{ext}}/t_{\text{crossing}}$  are plotted as a PDF in red and cyan, respectively. The vertical dotted lines represent the mean of each distribution. We see that the distribution of  $t_{\text{tidal}}^{\text{ext}}/t_{\text{crossing}}$  is shifted to the right compared to the distribution of  $t_{\text{tidal}}^{\text{ext}}/t_{\text{ff}}$ , and in both cases the mean and most of the structures lie above a ratio of 1. Overall we find a scenario where  $t_{\text{crossing}} < t_{\text{tidal}}^{\text{ext}}$  for most of the structures, while  $t_{\text{ff}}$  is more comparable to  $t_{\text{tidal}}^{\text{ext}}$ . This suggests that turbulence acts on a short enough timescale to modify the structures as they evolve.

## 6 CONCLUSIONS

We perform a detailed energetic analysis of seven different simulated molecular clouds (5 with magnetic fields and 2 without) from the SILCC-Zoom simulations (Seifried et al. 2017). In these simulations, we study the evolution of the multi-phase interstellar medium in a supernova-driven, stratified galactic disc environment. We identify structures forming inside each cloud using a dendrogram algorithm, and trace the evolution of their statistical properties over 1.5 Myr during the early stages of cloud evolution before stellar feedback complicates the picture. We include a simple chemical network which allows us to follow the formation of  $\text{H}_2$  as the cloud assembles and as such, distinguish between mostly atomic ( $\text{H}_2$  mass fraction  $< 50\%$ ) and mostly molecular ( $\text{H}_2$  mass fraction  $> 50\%$ ) structures.

- We find that our clouds show a Larson-like power-law behaviour with significant systematic deviations for the densest dendrogram branches in both  $\sigma_{1D}$ -size and mass-size relations (Fig. 4). We further see that these deviations evolve over time from a roughly Larson-like law, suggesting that they emerge as gravity becomes more and more important. We observe that all sub-structures can be divided into roughly two kinds depending on their behaviour in the Heyer plot (Fig. 6); denser and molecular structures that roughly follow the Heyer line, and less dense and mostly atomic structures that show no trend with surface density.

- In terms of energetics, we find that the dynamics of large scale ( $\geq 10$  pc) structures, as well as smaller scale denser structures is primarily governed by the interplay between turbulence and gravity (Figs. 7 and 8). Thermal and magnetic energies are dynamically important only for more diffuse, mostly atomic structures. Our results are based on an analysis of the volume energy terms.

- From a virial analysis, we find that on the large scales, the dendrogram structures are unbound or marginally bound at earlier

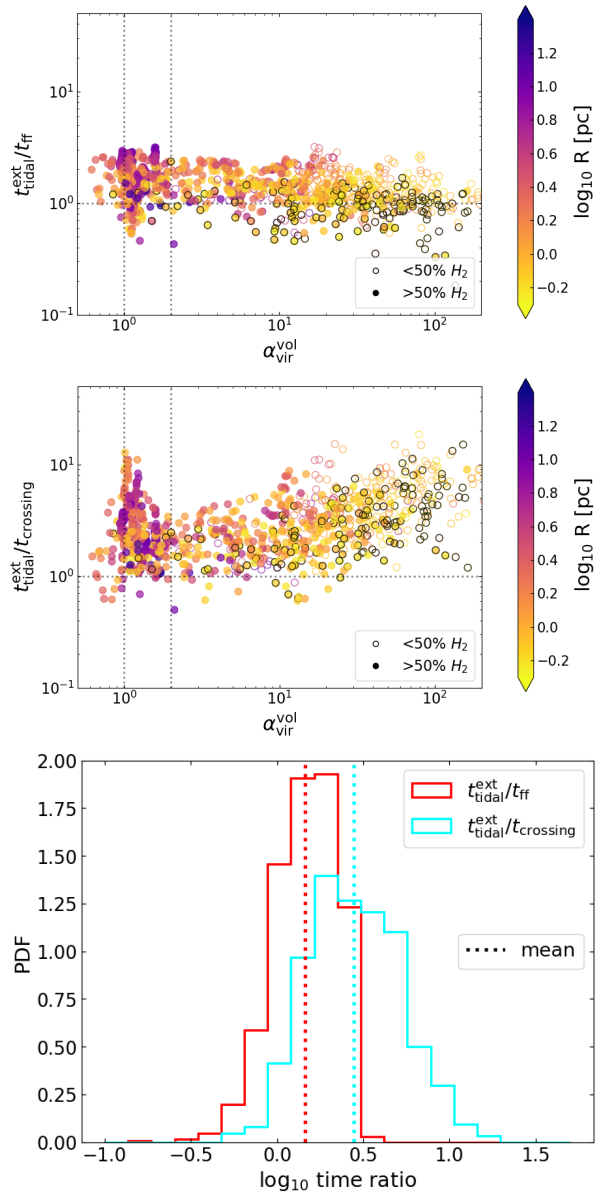


**Figure 16.** Ratio of the tidal deformation timescale due to  $\langle T \rangle_{\text{ext}}$ , to the gravitational free fall timescale (top) and the crossing time (middle), representing the turbulence decay timescale, plotted against the virial parameter  $\alpha_{\text{vir}}^{\text{vol}}$  of the substructures, for all clouds at  $t_{\text{evol}} = 3.5$  Myr. The colorbar represents the size of the structures. Structures which have at least one extensive mode (one  $\lambda_i^{\text{tot}} > 0$ ) are marked with a black circle. The vertical dotted lines represent the marginally bound region  $1 \leq \alpha_{\text{vir}}^{\text{vol}} < 2$  for the structures. The top plot shows that self-gravity is becoming more important compared to the tidal deformation timescale on average, for more bound structures. The bottom plot shows that the crossing time is shorter than the tidal deformation timescale for almost all structures, suggesting that tidal deformations due to the surrounding medium cannot be the primary source of turbulent energy. The histogram of the distribution of the two ratios,  $t_{\text{tidal}}^{\text{ext}}/t_{\text{crossing}}$  and  $t_{\text{tidal}}^{\text{ext}}/t_{\text{ff}}$ , with the means plotted in dotted vertical lines (bottom).

times, but become much closer to virialized over time. Denser, potentially star-forming structures emerge over time, suggesting that they are created by compression in a turbulent, marginally bound environment.

By performing a correlation analysis between the virial parameter and radial velocity tracing the inflow for each structure, we find that on the larger scales a more unbound structure is likely to have a stronger inflowing motion. This suggests that we see signs of supernova driven compression, rather than gravitational infall and is in agreement with the bubble-driven filament formation scenario proposed by [Inutsuka et al. \(2015\)](#).

- Finally, we attempt to assess the importance of gravitational tidal forces and their role in the dynamics of cloud sub-structures. We compare a given structure's self-gravity and the gravity due to its inhomogeneous surrounding medium by comparing the magnitude of, as well as the angle between, the two respective acceleration terms (Fig. 13). We find that the surrounding medium has some influence on a number of smaller scale unbound structures. Energetically, we find that the external gravitational energy is smaller in magnitude compared to both self-gravity and kinetic energy (Fig. 14).

To quantitatively evaluate the nature of the tidal field, we perform an analysis based on the tidal tensor. We find that the tidal effects are mostly compressive (Fig. 15). However, the gravitational field is highly anisotropic and even more so for structures which have extensive modes. Based on a timescale analysis, we find that timescales related to tidal deformation are generally longer compared to the turbulence decay timescale, suggesting that tidal deformations cannot be the primary source of generating kinetic energy in the structures (Fig. 16). However the tidal timescale is rather comparable to the freefall time, implying that the structures will deform as they collapse.

Overall, we find a structure formation scenario consistent with the gravo-turbulent scenario of structure formation, with bound structures emerging over time from a largely unbound or marginally bound medium. Magnetic and thermal energy seem to play a subservient role compared to turbulence and self-gravity, with gravitational tides modifying the nature of gravitational compression and leading to formation of more anisotropic, elongated structures.

## ACKNOWLEDGEMENTS

SG, SW and DS would like to acknowledge the support of Bonn-Cologne Graduate School (BCGS), which is funded through the German Excellence Initiative, as well as the DFG for funding through SFB 956 'Conditions and Impact of Star Formation' (subprojects C5 and C6). SDC is supported by the Ministry of Science and Technology (MoST) in Taiwan through grant MoST 108-2112-M-001-004-MY2. This research made use of *astrodendro* ([Robitaille et al. 2019](#)), a Python package to compute dendrograms of Astronomical data (<http://www.dendrograms.org/>); as well as *yt*, an open-source, permissively-licensed python package for analyzing and visualizing volumetric data (<https://yt-project.org/>). The FLASH code used in this work was partly developed by the Flash Center for Computational Science at the University of Chicago.

## DATA AVAILABILITY

The data underlying this article can be shared for selected scientific purposes after request to the corresponding author.

## REFERENCES

- Ballesteros-Paredes J., Klessen R. S., Mac Low M. M., Vazquez-Semadeni E., 2007, arXiv e-prints
- Ballesteros-Paredes J., Hartmann L. W., Vázquez-Semadeni E., Heitsch F., Zamora-Avilés M. A., 2011, *Monthly Notices of the Royal Astronomical Society*, 411, 65
- Bash F. N., Green E., Peters III W. L., 1977, *The Astrophysical Journal*, 217, 464
- Beck R., Wielebinski R., 2013, *Planets, Stars and Stellar Systems. Volume 5: Galactic Structure and Stellar Populations*, p. 641
- Blitz L., Fukui Y., Kawamura A., Leroy A., Mizuno N., Rosolowsky E., 2007, arXiv e-prints
- Bonnor W. B., 1956, *Monthly Notices of the Royal Astronomical Society*, 116, 351
- Bouchut F., Klingenberg C., Waagan K., 2007, *Numerische Mathematik*, 108, 7
- Bourke T. L., Myers P. C., Robinson G., Hyland A. R., 2001, *The Astrophysical Journal*, 554, 916
- Brunt C. M., 2003, *apj*, 583, 280
- Camacho V., Vázquez-Semadeni E., Ballesteros-Paredes J., Gómez G. C., Fall S. M., Mata-Chávez M. D., 2016, *The Astrophysical Journal*, 833, 113
- Chen H.-R. V., et al., 2019, *The Astrophysical Journal*, 875, 24
- Chevance M., et al., 2020, *Monthly Notices of the Royal Astronomical Society*, 493, 2872
- Chevance M., Krumholz M. R., McLeod A. F., Ostriker E. C., Rosolowsky E. W., Sternberg A., 2022, arXiv e-prints
- Colman T., Teyssier R., 2020, *Monthly Notices of the Royal Astronomical Society*, 492, 4727
- Crutcher R. M., 1999, *The Astrophysical Journal*, 520, 706
- Crutcher R. M., Wandelt B., Heiles C., Falgarone E., Troland T. H., 2010, *The Astrophysical Journal*, 725, 466
- Dame T. M., Elmegreen B. G., Cohen R. S., Thaddeus P., 1986, *The Astrophysical Journal*, 305, 892
- Derigs D., Winters A. R., Gassner G. J., Walch S., 2016, *Journal of Computational Physics*, 317, 223
- Derigs D., Winters A. R., Gassner G. J., Walch S., 2017, *Journal of Computational Physics*, 330, 624
- Derigs D., Winters A. R., Gassner G. J., Walch S., Böhm M., 2018, *Journal of Computational Physics*, 364, 420
- Dib S., Kim J., Vázquez-Semadeni E., Burkert A., Shadmehri M., 2007, *The Astrophysical Journal*, 661, 262
- Dobbs C. L., Burkert A., Pringle J. E., 2011, *Monthly Notices of the Royal Astronomical Society*, 413, 2935
- Draine B. T., 1978, *apjs*, 36, 595
- Dubey A., et al., 2008, in Pogorelov N. V., Audit E., Zank G. P., eds, *Astronomical Society of the Pacific Conference Series Vol. 385, Numerical Modeling of Space Plasma Flows*. p. 145
- Ebert R., 1955, *Zeitschrift für Astrophysik*, 37, 217
- Elmegreen B. G., 2000, *The Astrophysical Journal*, 530, 277
- Engargiola G., Plambeck R. L., Rosolowsky E., Blitz L., 2003, *The Astrophysical Journal Supplement Series*, 149, 343
- Falgarone E., Troland T. H., Crutcher R. M., Paubert G., 2008, *Astronomy and Astrophysics, Volume 487, Issue 1, 2008, pp.247-252*, 487, 247
- Federrath C., Klessen R. S., 2012, *The Astrophysical Journal*, 761, 156
- Fryxell B., et al., 2000, *The Astrophysical Journal Supplement Series*, 131, 273
- Genzel R., et al., 2010, *Monthly Notices of the Royal Astronomical Society*, 407, 2091
- Girichidis P., et al., 2016, *Monthly Notices of the Royal Astronomical Society*, 456, 3432
- Glover S. C. O., Mac Low M.-M., 2007, *The Astrophysical Journal Supplement Series*, 169, 239
- Glover S. C. O., Federrath C., Mac Low M.-M., Klessen R. S., 2010, *Monthly Notices of the Royal Astronomical Society*, 404, 2
- Goldreich P., Kwan J., 1974, *The Astrophysical Journal*, 189, 441
- Habing H. J., 1968, *Bulletin of the Astronomical Institutes of the Netherlands*,



- 19, 421
- Hacar A., Clark S. E., Heitsch F., Kainulainen J., Panopoulou G. V., Seifried D., R. S., 2022, arXiv e-prints
- Hartmann L., Ballesteros-Paredes J., Bergin E. A., 2001, *The Astrophysical Journal*, 562, 852
- Hennebelle P., Falgarone E., 2012, *Astronomy and Astrophysics Review*, 20, 55
- Heyer M., Krawczyk C., Duval J., Jackson J. M., 2009, *The Astrophysical Journal*, 699, 1092
- Hoyle F., 1953, *The Astrophysical Journal*, 118, 513
- Ibáñez-Mejía J. C., Mac Low M.-M., Klessen R. S., Baczynski C., 2017, *The Astrophysical Journal*, 850, 62
- Ibáñez-Mejía J. C., Mac Low M.-M., Klessen R. S., 2022, *The Astrophysical Journal*, 925, 196
- Inoue T., Inutsuka S.-i., 2009, *The Astrophysical Journal*, 704, 161
- Inutsuka S.-i., Inoue T., Iwasaki K., Hosokawa T., 2015, *Astronomy and Astrophysics*, 580, A49
- Izquierdo A. F., et al., 2021, *Monthly Notices of the Royal Astronomical Society*, 500, 5268
- Kawamura A., et al., 2009, *The Astrophysical Journal Supplement Series*, 184, 1
- Kendall M. G., 1938, *Biometrika*, 30, 81
- Kennicutt Jr. R. C., 1998, *The Astrophysical Journal*, 498, 541
- Kirk H., Myers P. C., Bourke T. L., Gutermuth R. A., Hedden A., Wilson G. W., 2013, *The Astrophysical Journal*, 766, 115
- Klessen R. S., 2001, *ApJ*, 556, 837
- Koyama H., Inutsuka S.-i., 2002, *The Astrophysical Journal*, 564, L97
- Kritsuk A. G., Lee C. T., Norman M. L., 2013, *Monthly Notices of the Royal Astronomical Society*, 436, 3247
- Krumholz M. R., Dekel A., McKee C. F., 2012, *The Astrophysical Journal*, 745, 69
- Kuznetsova A., Hartmann L., Ballesteros-Paredes J., 2015, *The Astrophysical Journal*, 815, 27
- Kuznetsova A., Hartmann L., Ballesteros-Paredes J., 2018, *Monthly Notices of the Royal Astronomical Society*, 473, 2372
- Larson R. B., 1981, *MNRAS*, 194, 809
- Lee Y.-N., Hennebelle P., 2018, *Astronomy & Astrophysics, Volume 611*, id.A89, <NUMPAGES>17</NUMPAGES> pp., 611, A89
- Leisawitz D., Bash F. N., Thaddeus P., 1989, *The Astrophysical Journal Supplement Series*, 70, 731
- Mac Low M.-M., Klessen R. S., 2004, *Reviews of Modern Physics*, 76, 125
- Mac Low M.-M., Klessen R. S., Burkert A., Smith M. D., 1998, *Physical Review Letters*, 80, 2754
- Mac Low M.-M., Burkert A., Ibáñez-Mejía J. C., 2017, *The Astrophysical Journal*, 847, L10
- McKee C. F., Ostriker E. C., 2007, *Annual Review of Astronomy and Astrophysics*, 45, 565
- McKee C. F., Zweibel E. G., 1992, *The Astrophysical Journal*, 399, 551
- Meidt S. E., et al., 2015, *The Astrophysical Journal*, 806, 72
- Mouschovias T. C., 1976a, *The Astrophysical Journal*, 206, 753
- Mouschovias T. C., 1976b, *The Astrophysical Journal*, 207, 141
- Murray N., 2011, *The Astrophysical Journal*, 729, 133
- Nelson R. P., Langer W. D., 1997, *The Astrophysical Journal*, 482, 796
- Orkisz J. H., et al., 2017, *A&A*, 599, A99
- Padoan P., Nordlund A., 2011, *The Astrophysical Journal*, 730, 40
- Padoan P., Pan L., Haugbølle T., Nordlund A., 2016, *The Astrophysical Journal*, 822, 11
- Peretto N., et al., 2014, *Astronomy & Astrophysics, Volume 561*, id.A83, <NUMPAGES>10</NUMPAGES> pp., 561, A83
- Renaud F., Boily C., Naab T., Theis C., 2009, *ApJ*, 706, 67
- Renaud F., Gieles M., Boily C. M., 2011, *Monthly Notices of the Royal Astronomical Society*, 418, 759
- Robitaille T., Rice T., Beaumont C., Ginsburg A., MacDonald B., Rosolowsky E., 2019, *Astrophysics Source Code Library*, p. ascl:1907.016
- Rosolowsky E. W., Pineda J. E., Kauffmann J., Goodman A. A., 2008, *The Astrophysical Journal*, 679, 1338
- Schmidt M., 1959, *The Astrophysical Journal*, 129, 243
- Seifried D., et al., 2017, *Monthly Notices of the Royal Astronomical Society*, 472, 4797
- Seifried D., Walch S., Haid S., Girichidis P., Naab T., 2018, *The Astrophysical Journal*, 855, 81
- Seifried D., Walch S., Reissl S., Ibáñez-Mejía J. C., 2019, *Monthly Notices of the Royal Astronomical Society*, 482, 2697
- Seifried D., Haid S., Walch S., Borchert E. M. A., Bisbas T. G., 2020, *Monthly Notices of the Royal Astronomical Society*, 492, 1465
- Shimajiri Y., André P., Palmeirim P., Arzoumanian D., Bracco A., Könyves V., Ntormousi E., Ladjelate B., 2019, *Astronomy & Astrophysics, Volume 623*, id.A16, <NUMPAGES>16</NUMPAGES> pp., 623, A16
- Solomon P. M., Rivolo A. R., Barrett J., Yahil A., 1987, *The Astrophysical Journal*, 319, 730
- Stone J. M., Ostriker E. C., Gammie C. F., 1998, *ApJ*, 508, L99
- Traficante A., et al., 2018, *Monthly Notices of the Royal Astronomical Society*, 477, 2220
- Troland T. H., Crutcher R. M., 2008, *The Astrophysical Journal*, 680, 457
- Truelove J. K., Klein R. I., McKee C. F., Holliman II J. H., Howell L. H., Greenough J. A., 1997, *ApJ*, 489, L179+
- Vázquez-Semadeni E., Gómez G. C., Jappsen A. K., Ballesteros-Paredes J., González R. F., Klessen R. S., 2007, *The Astrophysical Journal*, 657, 870
- Vázquez-Semadeni E., Gómez G. C., Jappsen A.-K., Ballesteros-Paredes J., Klessen R. S., 2009, *The Astrophysical Journal*, 707, 1023
- Vázquez-Semadeni E., González-Samaniego A., Colín P., 2017, *Monthly Notices of the Royal Astronomical Society*, 467, 1313
- Vázquez-Semadeni E., Palau A., Ballesteros-Paredes J., Gómez G. C., 2019, *Monthly Notices of the Royal Astronomical Society*, 490, 3061
- Waagan K., 2009, *Journal of Computational Physics*, 228, 8609
- Walch S., et al., 2015, *Monthly Notices of the Royal Astronomical Society*, 454, 238
- Wu J., Evans II N. J., Shirley Y. L., Knez C., 2010, *The Astrophysical Journal Supplement Series*, 188, 313
- Wünsch R., Walch S., Dinnbier F., Whitworth A., 2018, *Monthly Notices of the Royal Astronomical Society*, 475, 3393
- Zuckerman B., Evans II N. J., 1974, *ApJ*, 192, L149

## APPENDIX A: VELOCITY DISPERSION-SIZE DEPENDENCE ON THE VIRIAL RATIO

We highlight the evolution of Larson's velocity dispersion-size relation in relation to  $\alpha_{\text{vir}}^{\text{vol}}$  in Fig. A1 for all different MHD sub-structures at 2 Myr (Fig. A1, left) and 3.5 Myr (Fig. A1, right). We see that at 3.5 Myr structures deviating to form flatter branches are all bound or close to bound. However, the deviations are largely absent at earlier times.

## APPENDIX B: TRACE OF THE TIDAL TENSOR

The tidal tensor encodes the gravitational deformation at a given point. An estimated average tidal tensor, averaged over an entire sub-structure, therefore should encode the deformation behaviour of this entire mass element. One of the proofs of concept of this idea is to evaluate how well the trace corroborates to the average density of the structure (see Eq. 30).

From Fig. B1, top panel we see that the expected relation is indeed well retrieved for the total tidal tensor ( $\mathbf{T}_{\text{tot}}$ ). The trace for the external tidal tensor ( $\mathbf{T}_{\text{ext}}$ ) should ideally be 0, therefore any residual sum reflects the typical error in the estimate of the eigenvalue terms. However, these values are typically only 1% of the 1:1 line, and therefore adequately accurate for our calculations.

This paper has been typeset from a  $\text{\LaTeX}$  file prepared by the author.

20 *S. Ganguly et al.*

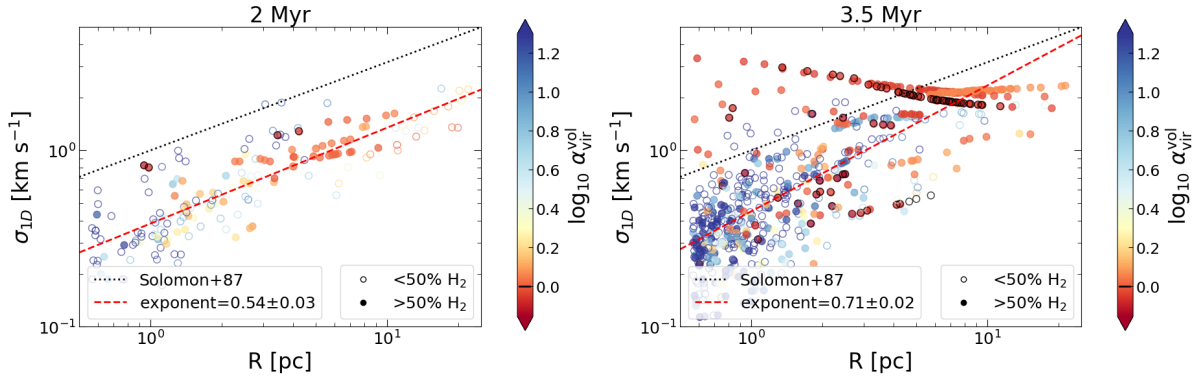


**Figure A1.**  $\sigma_{1D}$ - $R$  relation for all MHD sub-structures, at  $t_{\text{evol}} = 2$  (left) and 3.5 Myr (right). The colour bar represents  $\alpha_{\text{vir}}^{\text{vol}}$ , with structures with  $\alpha_{\text{vir}}^{\text{vol}} < 1$  being marked with an additional black outline.

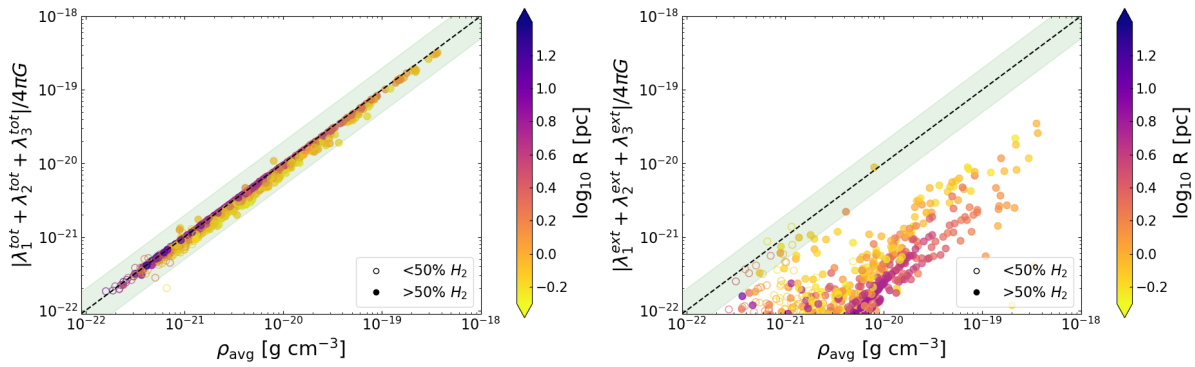


**Figure B1.** Trace of the averaged total tidal tensor ( $\langle \mathbf{T}_{\text{tot}} \rangle$ ) (left) and trace of the averaged external tidal tensor ( $\langle \mathbf{T}_{\text{ext}} \rangle$ ) (right), plotted against the average density, for all cloud sub-structures at  $t_{\text{evol}} = 3.5$  Myr. The dashed line represents a one to one line, and the green shaded region represents a factor of 2 in each direction. The trace of  $\langle \mathbf{T}_{\text{tot}} \rangle$  well reflects the average density. The trace of  $\langle \mathbf{T}_{\text{ext}} \rangle$  should ideally be 0, but is typically only 1% of the 1:1 line.

UNRAVELLING THE STRUCTURE OF MAGNETIZED  
MOLECULAR CLOUDS WITH SILCC-ZOOM: SHEETS,  
FILAMENTS AND FRAGMENTATION (PAPER II)

---

# Unravelling the structure of magnetized molecular clouds with SILCC-Zoom: sheets, filaments and fragmentation

Shashwata Ganguly,<sup>1\*</sup> S. Walch,<sup>1,2</sup> S. D. Clarke<sup>1,3</sup> D. Seifried<sup>1,2</sup> and M. Weis<sup>1</sup>

<sup>1</sup>*I. Physikalisches Institut, Universität zu Köln, Zùlpicher Str. 77, 50937 Köln, Germany*

<sup>2</sup>*Cologne Centre for Data and Simulation Science, University of Cologne, Cologne, Germany*

<sup>3</sup>*Academia Sinica, Institute of Astronomy and Astrophysics, Taipei, Taiwan*

Accepted XXX. Received YYY; in original form ZZZ

## ABSTRACT

To what extent magnetic fields affect how molecular clouds (MCs) fragment and create dense structures is an open question. We present a numerical study of cloud fragmentation using the SILCC-Zoom simulations. These simulations follow the self-consistent formation of MCs in a few hundred pc sized region of a stratified galactic disc; and include magnetic fields, self-gravity, supernova driven turbulence, as well as a non-equilibrium chemical network. To discern the role of magnetic fields in the time evolution of MCs, we study seven simulated clouds, five with magnetic fields and two without, for 1.5 Myr with a maximum resolution of 0.1 pc. Using a dendrogram we identify hierarchical structures which form within the clouds. We find that six out of seven clouds are sheet-like on the largest scales with filamentary structures embedded within, consistent with the bubble driven MC formation mechanism. Hydrodynamic simulations tend to produce more sheet-like structures, while presence of magnetic fields tends to increase filament formation somewhat. Analysing cloud energetics, we find that magnetic fields are dynamically important for less dense atomic structures, while the denser, potentially star forming structures are energetically dominated by self-gravity and turbulence. We further find the magnetic fields to have an overall "slow down" effect on cloud evolution and fragmentation.

**Key words:** MHD – methods: numerical – stars: formation – ISM: clouds – ISM: kinematics and dynamics

## 1 INTRODUCTION

Magnetic fields are ubiquitous in the interstellar medium or ISM (Crutcher et al. 2003; Heiles & Troland 2005; Fletcher et al. 2011; Beck 2015). Since the discovery of interstellar magnetic fields by Hiltner (1951) and Hall (1951), they have been known to be integral to the understanding of ISM dynamics. Magnetic fields, however, are also notoriously difficult to measure accurately as well as to model theoretically. Decades of painstaking observations offer us today unprecedented accuracy and scope in the measurement of magnetic fields for different phases in the ISM (Crutcher 1999; Bourke et al. 2001; Heiles & Crutcher 2005; Troland & Crutcher 2008; Crutcher 2012; Beck 2015; Planck Collaboration et al. 2020).

The exact nature of how magnetic fields affect molecular cloud (MC) formation and evolution is, however, an open question and subject of intense scrutiny (see e.g. reviews by Crutcher 2012; Hennebelle & Inutsuka 2019; Girichidis et al. 2020). Various numerical studies have performed detailed analysis on the interplay of magnetic fields with other factors (e.g. turbulence, thermal pressure) in order to determine how MCs are shaped, formed, and how they evolve (e.g. Heitsch et al. 2001; Federrath & Klessen 2012; Walch et al. 2015; Girichidis et al. 2016b; Seifried et al. 2017; Ibáñez-Mejía et al. 2022).

On galactic scales, ordered magnetic fields have been observed,

with there being a correlation between the direction of the spiral arms and the magnetic field (Beck 2009; Fletcher et al. 2011; Li & Henning 2011). In the diffuse ISM, the magnetic field strength  $B$  does not show any correlation with density for number densities of up to roughly  $300 \text{ cm}^{-3}$  (Crutcher et al. 2010). Above these densities, Crutcher et al. (2010) find  $B \propto \rho^\kappa$ , with  $\kappa \approx 2/3$ , though there remains considerable scatter in the observations.

The lack of correlation between the strength of the magnetic field and the density of the ambient medium implies that in the diffuse ISM, magnetic fields can channelize gas flows along the field lines and therefore determine the environment MCs form in. Pardi et al. (2017) show that magnetic fields are more likely to cause a smoother gas distribution, while Molina et al. (2012) find that they are more likely to affect the dynamics of lower density gas by broadening the density PDF. Magnetic fields can add to the thermal pressure exerted by the gas, and slow down formation of dense gas (Hill et al. 2012), as well as molecular gas (Girichidis et al. 2018). A strong enough magnetic field can prevent the collapse of a MC altogether (Mouschovias 1991; Spitzer 1978), or slow down cloud evolution (Heitsch et al. 2001; Padoan & Nordlund 2011; Federrath & Klessen 2012; Ibáñez-Mejía et al. 2022).

In terms of morphology, they can facilitate the formation of elongated filamentary structures (Hennebelle 2013), and are essential in understanding the filamentary nature of the ISM (see e.g. Bally et al. 1987; André et al. 2014).

B fields are likely to also affect fragmentation properties of clouds.

\* E-mail: ganguly@ph1.uni-koeln.de

Commerçon et al. (2011) find that cloud fragments in the presence of magnetic fields are more massive. Although the PDF of lower density gas is found to be broadened in presence of magnetic fields (Molina et al. 2012), this does not seem to, however, extend to the higher density end (Klessen & Burkert 2001; Slyz et al. 2005; Girichidis et al. 2014; Schneider et al. 2015).

In this present work, we perform a numerical investigation of the role magnetic fields play in forming and shaping density structures within MCs. We do a detailed analysis of realistic MC simulations based on the SILCC-Zoom simulations (Seifried et al. 2017) by comparing morphological, dynamical, and fragmentation properties in seven different simulated clouds, five with magnetic fields (magneto-hydrodynamic or MHD clouds) and two without (hydrodynamic or HD clouds).

The paper is structured as follows: in Section 2, we outline the numerical setup of the simulation. Section 3 discusses the procedure of identifying and classifying structures. We highlight the differences in a few bulk properties, such as differences in density PDFs, between the HD and MHD clouds in Section 4. The morphological properties of the obtained structures are presented in Section 5. We find all the MCs to be sheet-like on the largest (tens of parsecs) scales. On smaller scales, we see that the presence of magnetic fields suppress formation of spheroids, and somewhat enhance formation of filamentary over sheet-like sub-structures. In Section 6, we analyse the dynamics and energetic balance of magnetized structures and relate them to the fragmentation of cloud sub-structures. We find that the presence of magnetic fields slows down cloud evolution, and in particular leads to more massive fragments at low to intermediate densities ( $<100 \text{ cm}^{-3}$ ). Finally, we present the summary of our findings in Section 7.

## 2 NUMERICAL METHODS AND SIMULATION

We present results here based on the SILCC-Zoom simulations (Seifried et al. 2017). The SILCC-Zoom simulations are simulations of MCs with realistic boundary conditions, generated by embedding the clouds within the SILCC simulations of multi phase interstellar gas, thereby having realistic initial conditions (Walch et al. 2015; Girichidis et al. 2016a). In this section, we highlight some key features of the simulations. Further details regarding the simulations can be found in Seifried et al. (2017).

All simulations were executed using the adaptive mesh refinement code FLASH, version 4.3 (Fryxell et al. 2000; Dubey et al. 2008). We present results from runs both with and without magnetic fields. The MHD simulations showed are performed using an entropy-stable solver that guarantees minimum possible dissipation (Derigs et al. 2016, 2018). The hydrodynamic simulations have been performed using the MHD 'Bouchut 5-wave solver' (Bouchut et al. 2007; Waagan 2009) which guarantees positive entropy and density. The magnetic field strength has been set to zero for these runs.

All simulations include self gravity as well as an external galactic potential due to old stars. This external potential is calculated using the assumption of a stellar population density of  $\Sigma_{\text{star}} = 30 M_{\odot} \text{pc}^{-2}$ , a  $\text{sech}^2$  vertical profile and a scale height of 100 pc, according to Spitzer (1942). The self gravity of the gas is computed using a tree-based algorithm (Wünsch et al. 2018).

The entire simulation domain consists of a box of size  $500 \text{ pc} \times 500 \text{ pc} \times \pm 5 \text{ kpc}$ , with the long axis representing the vertical  $z$ -direction for a galactic disc. The box is set with periodic boundary conditions in the  $x$ - and  $y$ - directions, and outflow boundary condition in  $z$ -direction. The initial gas surface density is set to  $\Sigma_{\text{gas}} = 10 M_{\odot} \text{pc}^{-2}$  which corresponds to solar neighbourhood con-

ditions. The vertical distribution of the gas is modelled as a Gaussian, i.e.  $\rho = \rho_0 \exp(-z^2/2h_z^2)$ , where  $h_z=30 \text{ pc}$  is the scale height and  $\rho_0 = 9 \times 10^{-24} \text{ g cm}^{-3}$ . Initial gas temperature is set to 4500 K. For runs with magnetic fields, the magnetic field is initialized along the  $x$  direction, i.e.  $\mathbf{B} = (B_x, 0, 0)$  with  $B_x = B_{x,0} \sqrt{\rho(z)/\rho_0}$  and the magnetic field strength at the midplane  $B_{x,0} = 3 \mu\text{G}$ . The field strength is chosen to be in accordance with recent observations (e.g. Beck & Wielebinski 2013).

The turbulence in the simulations is generated by supernova explosions. The explosion rate is set to  $15 \text{ SNe Myr}^{-1}$ , which is consistent with Kennicutt-Schmidt relation of star formation rate for the used gas surface density (Schmidt 1959; Kennicutt 1998). 50% of the supernova are placed following a Gaussian random distribution along the  $z$ -direction up to a height of 50 pc, while the other 50% are placed at density peaks of the gas. This prescription of supernova driving creates a multi-phase turbulent ISM which can be used as initial condition for the zoom-in simulations (Walch et al. 2015; Girichidis et al. 2016a).

Apart from the dynamics of the gas, we also model its chemical evolution using a simplified non equilibrium chemical network based on hydrogen and carbon chemistry (Nelson & Langer (1997); Glover & Mac Low (2007); Glover et al. (2010)). For this purpose, we follow the abundance of  $\text{H}^+$ ,  $\text{H}$ ,  $\text{H}_2$ ,  $\text{CO}$ ,  $\text{C}^+$ ,  $\text{e}^-$ , and  $\text{O}$ . At the beginning of the simulation, all hydrogen in the disc midplane is neutral and carbon are in their ionized form (i.e.  $\text{H}$  and  $\text{C}^+$ , respectively).

To model the chemistry of the gas correctly, we include an interstellar radiation field (ISRF) of strength  $G_0 = 1.7$  Habing units (Habing 1968; Draine 1978). The attenuation of this radiation field is taken into consideration by computing the true optical depth inside any given point in the simulation domain. This is computed as follows:

$$A_{\text{V},3\text{D}} = -\frac{1}{2.5} \ln \left[ \frac{1}{N_{\text{PIX}}} \sum_{i=1}^{N_{\text{PIX}}} \exp \left( -2.5 \frac{N_{\text{H,tot},i}}{1.87 \times 10^{21} \text{ cm}^{-2}} \right) \right], \quad (1)$$

where the sum is carried over each HEALPIX pixel, with  $N_{\text{PIX}}$  being the total number of such pixels (usually 48), and  $N_{\text{H,tot},i}$  is the column density computed for the  $i$ th pixel. In essence, for any given point, we compute the column density along various lines of sight and use that for an effective  $A_{\text{V},3\text{D}}$ . The averaging is performed in an exponential manner because intensity of radiation decreases in an exponential manner due to gas column density along the line of sight. The calculation for this is done by the TREE-RAY OPTICAL DEPTH module developed by Wünsch et al. (2018).

In order to study forming MCs, all supernova explosions are stopped at a certain time  $t_0$ . Up to this point, the maximum grid resolution is 3.9 pc. At time  $t_0$ , different regions are identified for the zoom-in process, primarily due to their molecular gas content. The time  $t = t_0$  refers to the start of the evolution of the different clouds, and is set as evolution time  $t_{\text{evol}} = 0$ . The total simulation time  $t$  is related to the evolution time as

$$t = t_0 + t_{\text{evol}}. \quad (2)$$

From  $t_{\text{evol}} = 0$  on, in the select regions the AMR grid is allowed to refine to a higher resolution in order to capture structures forming as MCs. These regions are referred to as zoom-in regions and are of primary importance to us as sites of MCs. Each SILCC simulation we run two such "zoom-in" boxes simultaneously. The different MHD runs are seeded with a varying set of random supernovae, with all other initial conditions being identical. All runs present here have a maximum resolution of 0.125 pc. For the details of how the zoom-in process is achieved, see Seifried et al. (2017).

Run name	MHD	$t_0$ [Myr]	Total mass [ $10^4 M_\odot$ ]	H <sub>2</sub> mass [ $10^4 M_\odot$ ]	$\langle B \rangle$ [ $\mu\text{G}$ ]
MC1-HD	no	12	7.3	2.1	0
MC2-HD	no	12	5.4	1.6	0
MC1-MHD	yes	16	7.8	1.3	4.8
MC2-MHD	yes	16	6.2	0.86	3.9
(MC3-MHD) <sup>a</sup>	yes	16	2.0	0.19	2.0
MC4-MHD	yes	11.5	6.8	1.2	6.4
MC5-MHD	yes	11.5	10.1	1.6	6.8
MC6-MHD	yes	16	6.6	1.4	4.3

**Table 1.** Basic information on the eight analyzed simulations. From left to right we list the run name, whether magnetic fields are present or not, the time when the AMR "zoom-in" starts, as well as the total mass, molecular hydrogen mass and the average magnetic field strength at  $t_{\text{evol}} = 2$  Myr.

<sup>a</sup>We discard MC3-MHD from our further analysis because of its low molecular gas content and lack of interesting density features (see also Fig. A1).

### 3 CLASSIFICATION OF STRUCTURES

For the analysis presented in this work, we look at eight different cubic boxes of size 62.5 pc, each from a different SILCC zoom-in region. These boxes are chosen by visual inspection, in order to capture the most interesting features contained in each zoom-in region. For the purpose of this present work, we will refer to these cubic regions as MCs. They are named as MC1-HD and MC2-HD for the two hydrodynamic clouds, and MCx-MHD for the MHD clouds, where x is between one and six. We present some basic details of the different MCs in Table 1. A projected view of all the different MCs is added in Appendix A. For more information on the presented clouds, we refer the reader to Seifried et al. (2017) for the HD clouds and Seifried et al. (2019) for the MHD clouds.

We perform a detailed analysis of the different clouds, following their evolution from  $t_0 + 2$  Myr to  $t_0 + 3.5$  Myr, primarily focusing on the latter time. The beginning and the end time are chosen to look at relatively early stages of structure formation in the MCs, while still avoiding possible artefacts of the zoom in process itself.

#### 3.1 Structure identification

To identify structures in our MCs, we use a dendrogram algorithm (Rosolowsky et al. 2008). Dendrogram is a model independent method to determine hierarchical structures in two and three dimensions. Since we are interested in three dimensional structures, we perform the dendrogram analysis on 3-dimensional density cubes. We do not use the 3D AMR grid structure inherent in the data, but rather convert it into uniform mesh.

Given an initial density field,  $\rho$ , the dendrogram essentially depends on three free parameters: the initial starting threshold,  $\rho_0$ , the density jump,  $\Delta\rho$ , and the minimum number of cells that need to be included in any structure,  $N_{\text{cells}}$ . In addition, we can choose a pruning peak,  $\rho_{\text{prune}}$ , to allow the dendrogram to create new structures only when such a structure will have peak density  $\rho_{\text{peak}} > \rho_{\text{prune}}$ . Using these parameters, the dendrogram algorithm allows us to define volumes of gas as structures in a hierarchical tree, primarily defined by their threshold density  $\rho_{\text{thr}}$ , which is the minimum density value inside a given structure. This can be thought of as equivalent to contour values for two dimensional maps.

We build the dendrogram tree on the logarithmic density profile of the gas, and therefore have used density bins of  $\Delta\log_{10} \rho$ , rather than  $\Delta\rho$ . For probing both the higher and lower density ends of the data, we perform two dendrogram analyses on the same regions:

a higher density dendrogram analysis performed at a resolution of 0.125 pc for probing gas above densities of  $10^{-22} \text{ g cm}^{-3}$  (referred to as high-den), and a lower density analysis performed at 0.25 pc for gas between the densities of  $10^{-24}$  and  $10^{-22} \text{ g cm}^{-3}$  (referred to as low-den). The low-den values are computed as volume averaged values from the higher resolution grid. We present the dendrogram parameters used for both analyses in Table 2.

In addition to the difference in the basic parameters between the two dendrogram analyses, we remove all structures with  $\rho_{\text{thr}} > 10^{-22} \text{ g cm}^{-3}$  for the low-den analysis. This is done in order to avoid double counting of structures.

The parameter values mentioned in Table 2 have been chosen from a mixture of practical considerations, such as CPU memory, computation time, and through trial and error. We note that in principle the same analysis could be performed by a single dendrogram analysis at  $\rho_{\text{thr}} = 10^{-24} \text{ g cm}^{-3}$  at the highest resolution of 0.125 pc. However, the computation cost of such an analysis was prohibitive in our case. Combining the high-den and low-den dendrogram analyses allows us to probe a much higher density range than would be otherwise possible.

In terms of the parameters used, we have seen no unexpected change in the results by changing the free parameters within a reasonable range. We refer the reader to our companion paper (Ganguly et al., in prep.) for a more thorough discussion of the effect of altering the parameter values on the analysis. Overall, we find that changing the parameters leaves the statistical properties of the structures obtained virtually unaffected, but results in varying numbers of structures.

An example of the leaf density structures (structures that contain no further sub-structures) from the dendrogram analysis can be seen in Fig. 1, for MC3-MHD at  $t_{\text{evol}} = 3.5$  Myr, as contours over column density maps. The three panels show, from left to right, the cloud projected along the  $x$ -,  $y$ - and  $z$ -direction. The contours are drawn as projections of the 3D dendrogram structure outlines in the projected direction. We distinguish between structures depending on their molecular H<sub>2</sub> content, by plotting structures with over 50% of their total hydrogen mass in molecular form (referred to as molecular structures) in solid lines and otherwise in dashed lines (referred to as atomic structures).

Due to the nature of the dendrogram algorithm, there are some structures which touch the edge of the box. This can lead to structures whose morphology is determined by their proximity to the edge. To avoid this, we only analyze structures which have less than 5% of their surface cells touching any edge. This is relevant especially for the large-scale structures from the low-den dendrogram analysis.

#### 3.2 Structure classification

Once we obtain the tree of dendrogram density sub-structures, we aim to classify their morphology. For each structure, we compute an equivalent ellipsoid that has the same mass and the same moments of inertia (MOI) as the original structure. We then use the axes lengths of this equivalent ellipsoid to classify the shape of the different structures.

Let us consider a uniform density ellipsoid of mass  $M$  and semi-axes lengths  $a$ ,  $b$ ,  $c$  with  $a \geq b \geq c$ . The moments of inertia along

4 *S. Ganguly et al.*

dendrogram type	Resolution [pc]	$\rho_0$ [ $\text{g cm}^{-3}$ ]	$\Delta \log_{10} \rho$	$N_{\text{cells}}$	$\rho_{\text{prune}}$ [ $\text{g cm}^{-3}$ ]	additional criteria
high-den	0.125	$10^{-22}$	0.1	100	$10^{-21}$	None
low-den	0.25	$10^{-24}$	0.2	100	None	$\rho_{\text{thr}} < 10^{-22} \text{ g cm}^{-3}$

**Table 2.** Information on the parameters used for the two different kinds of dendrogram analyses. From left to right are: the type of dendrogram, the grid resolution at which it is performed, the starting density, the logarithmic density jump, the minimum number of cells in structures, the density of the pruning peak used, and if any additional criteria were used to select structures.

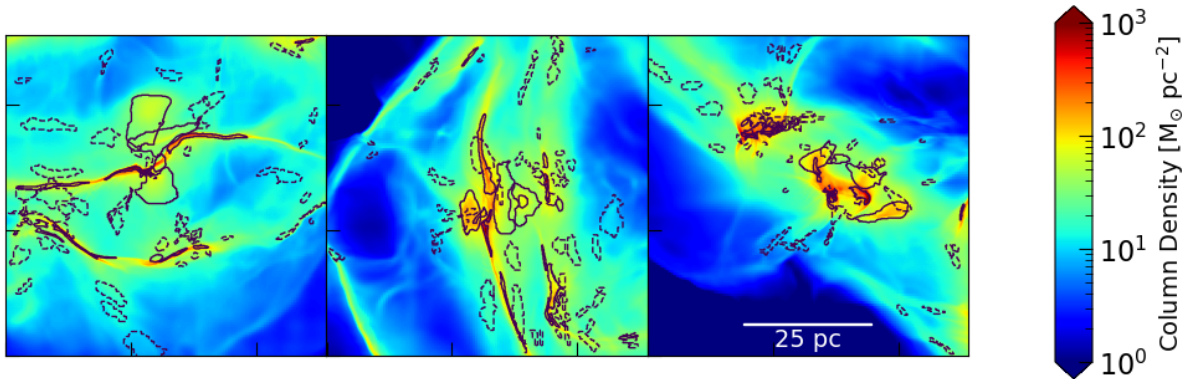


**Figure 1.** Left to right: Projections of MC3-MHD at  $t_{\text{evol}} = 3.5$  Myr along the  $x$ -,  $y$ -, and  $z$ -axis, respectively. The contours show the projections of the leaf dendrogram structures along the same axis. Molecular structures ( $> 50\%$   $\text{H}_2$  mass fraction) are plotted with solid, and atomic structures ( $< 50\%$   $\text{H}_2$  mass fraction) are plotted with dashed lines. The molecular structures nicely trace the dense spine of the two main filaments, while the atomic structures mostly represent the envelope.

the three principal axes will be given as follows:

$$\begin{aligned} I_a &= \frac{1}{5}M(b^2 + c^2), \\ I_b &= \frac{1}{5}M(c^2 + a^2), \\ I_c &= \frac{1}{5}M(a^2 + b^2), \end{aligned} \quad (3)$$

where  $I_c \geq I_b \geq I_a$ . If we now compute the principal moments of inertia of our given dendrogram structure to be  $A$ ,  $B$  and  $C$ , respectively, then the ellipsoid has an equivalent moment of inertia if

$$A = I_a, \quad B = I_b, \quad C = I_c. \quad (4)$$

This leads to the following equation for computing the axis lengths of the equivalent ellipsoids:

$$\begin{aligned} a &= \sqrt{\frac{5}{2M}(B + C - A)}, \\ b &= \sqrt{\frac{5}{2M}(C + A - B)}, \\ c &= \sqrt{\frac{5}{2M}(A + B - C)}. \end{aligned} \quad (5)$$

We then use the aspect ratio of the semi-axes of the ellipsoid and the position of its center of mass (COM) to categorize the different

structures into four categories: sheets, curved sheets (referred to as sheet\_c in this paper), filaments, and spheroids.

$$\begin{aligned} \text{sheet:} & \quad \frac{a}{b} \leq f_{\text{asp}}, \quad \frac{a}{c} > f_{\text{asp}} \\ \text{filament:} & \quad \frac{a}{b} > f_{\text{asp}} \\ \text{spheroidal:} & \quad \frac{a}{c} \leq f_{\text{asp}}, \quad \text{contains its own COM} \\ \text{sheet\_c:} & \quad \frac{a}{c} \leq f_{\text{asp}}, \quad \text{does not contain its own COM} \end{aligned} \quad (6)$$

where we set the aspect ratio factor  $f_{\text{asp}} = 3$ .

The inclusion of the COM criterion in addition to the ratio of the ellipsoid axes help us deal with especially the larger scale structures which can be highly curved. A highly curved sheet could have comparable MOI eigenvalues along the different eigen directions, but would not contain its own center. We highlight some visual examples of such highly curved sheet-like structures when we discuss the large scale morphology of our clouds in Fig. 4. In contrast to curved sheets, a spheroidal structure would contain its own COM.

Apart from using the normal moment of inertia, we also perform the classification by computing a volume weighted moment of inertia, where we compute the moment of inertia of the structures (the quantities  $A$ ,  $B$  and  $C$ ) by assuming the structure is of the same mass but with uniform density, but find statistically little to no difference in the resulting morphologies.

The discussion above highlights some possible caveats of our method. If we have a situation of multiple crossing filaments (hub-like structure), or parallel filaments joined by a more diffuse intermediate medium - the method will identify it as a sheet-like structure splitting into filaments in the dendrogram tree hierarchy. We must therefore

emphasise that our definition of sheet in this context is more general and contains also situations where multiple filamentary structures are connected by a more diffuse medium. Further, for highly curved structures, it is possible that the simple fit ellipsoid method may not result in a good description of the ellipsoid axis lengths.

#### 4 MASS DISTRIBUTION AND MAGNETIC FIELDS

We first consider the bulk properties of the different MCs to observe any difference between the hydrodynamic and MHD clouds. From Table 1, we see that the average magnetic field strength for the analyzed MHD clouds is relatively homogeneous, and varies between 3.9-6.8  $\mu\text{G}$ . The cloud masses, and their  $\text{H}_2$  masses are also within a factor of roughly 2 to each other (with the exception of MC3-MHD, see below). For a view of the time evolution of the total and  $\text{H}_2$  mass, as well as the  $\text{H}_2$  mass fraction, we refer the reader to Appendix A.

MC3-MHD stands out as having a much lower  $\text{H}_2$  mass and  $\text{H}_2$  mass fraction compared to the other clouds (Table 1). Visual inspection of this cloud shows that its structures are still diffuse and not as prominent, suggesting that it perhaps needs much longer to collapse, or may not collapse at all (see Fig. A1, bottom row left). Its molecular content remains at a constant roughly 10% level throughout the duration period of our analysis. Since we are interested primarily in the problem of density structures which go on to eventually form stars, we exclude MC3-MHD from further analysis considering its unevolved state and low molecular content.

It is of interest to note if the mass distribution in different clouds is affected by the presence of magnetic fields. This can be seen in Fig. 2, which shows the volume weighted density PDF of all different clouds at  $t_{\text{evol}} = 2$  Myr (top) and  $t_{\text{evol}} = 3.5$  Myr (bottom). Each line in the figures corresponds to the density PDF of a different cloud, with the two hydrodynamic clouds plotted in reddish lines. The two vertical dashed lines represent  $\rho = 10^{-24} \text{ g cm}^{-3}$  and  $\rho = 10^{-22} \text{ g cm}^{-3}$ , and set the boundaries of the low-den and high-den dendrogram analysis we perform (Table 2).

From Fig. 2, we see that at  $\rho < 10^{-24} \text{ g cm}^{-3}$  (corresponding roughly to number densities of  $\lesssim 1 \text{ cm}^{-3}$ ), the two hydrodynamic clouds have a much higher amount of gas compared to their MHD counterparts. The densities at these values often trace the "bubbles" blown by the supernovae in the original SILCC simulations. The difference in the PDFs could potentially indicate that the presence of magnetic fields help channel gas masses at these low densities more efficiently onto the denser envelope of the MCs. While interesting in their own right, in the present work we are interested in the role magnetic fields play on much denser MC sub-structures and therefore exclude these extremely low densities from our analysis.

In contrast to  $\rho < 10^{-24} \text{ g cm}^{-3}$ , at the intermediate density range between  $10^{-24}$  and  $10^{-22} \text{ g cm}^{-3}$ , corresponding to rough number densities of 1 and  $100 \text{ cm}^{-3}$ , respectively, we see that the MHD clouds contain much more gas. This is more prominent at  $t_{\text{evol}} = 2$  Myr, but remains also clearly visible at  $t_{\text{evol}} = 3.5$  Myr. This effect can also be visually seen in the column density plots of Fig. A1, where the denser parts of the hydrodynamic clouds seem to be embedded in a much rarer medium compared to their MHD counterparts. Magnetic fields in our simulations therefore play an important role in shaping the environment inside which denser, molecular, and potentially star forming structures live. This is consistent with the picture that magnetic fields affect the dynamics of lower density gas more significantly (Molina et al. 2012). We explore in more detail the exact role magnetic fields play in this regard when we look at the effect of magnetic fields on fragmentation properties in Section 6.3. We

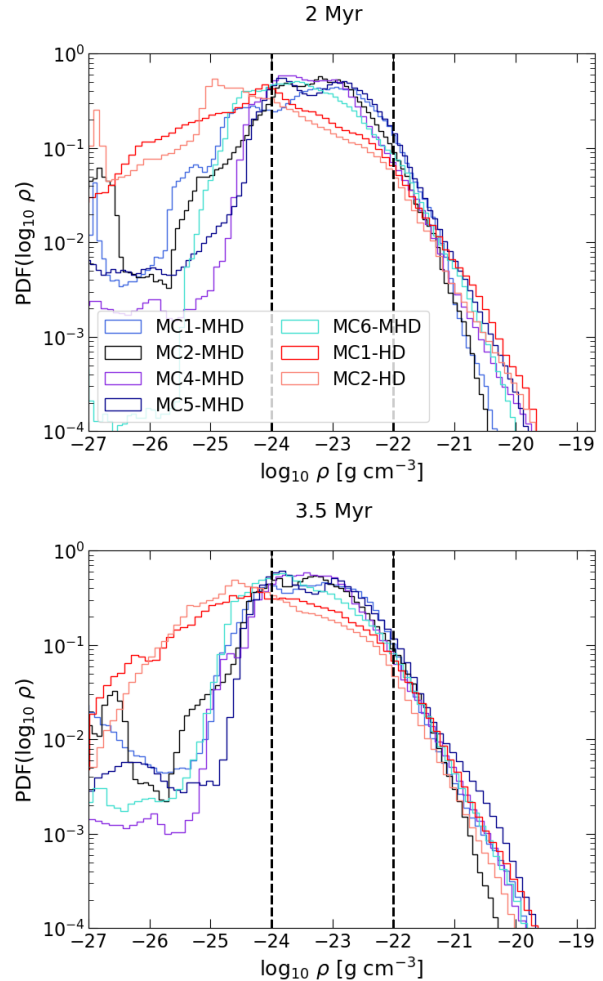


**Figure 2.** Density PDF for different HD and MHD clouds  $t_{\text{evol}} = 2$  Myr (top) and 3.5 Myr (bottom). The two hydrodynamic clouds are plotted in reddish lines. The vertical lines demarcate the boundaries of the high-den ( $> 10^{-22} \text{ g cm}^{-3}$ ) and the low-den (between  $10^{-24} - 10^{-22} \text{ g cm}^{-3}$ ) regions used for the dendrogram analyses (see also Table 2). The MHD clouds have more fraction of gas in the density range between roughly  $10^{-24}$  and  $10^{-22} \text{ g cm}^{-3}$ , or between approximately 1 and  $100 \text{ cm}^{-3}$ .

investigate the densities between  $10^{-24}$  and  $10^{-22} \text{ g cm}^{-3}$  through the low-den dendrogram analysis (Table 2). For  $\rho > 10^{-22} \text{ g cm}^{-3}$ , the density regime we with the dendrogram analysis at the highest resolution (0.125 pc), we see no obvious difference in the density PDF between the hydrodynamic and MHD clouds at earlier or later times. This is consistent with observations that column density PDFs show little to no change at higher column density ranges (Klessen & Burkert 2001; Slyz et al. 2005; Girichidis et al. 2014; Schneider et al. 2015). This naturally does not discount possible dynamical effects, which we explore further below.

The effects magnetic fields have on the cloud structures is naturally correlated to the field strength. The initial 3  $\mu\text{G}$  seed field in the original simulations is expected to magnify when we look at denser structures inside the MCs. The scaling behaviour of the magnetic



6 *S. Ganguly et al.*

field  $\mathbf{B}$  with  $\rho$ , is integral to understanding the importance of  $\mathbf{B}$  fields at different scales.

If contraction of gas happens exclusively along the magnetic field lines, this should lead to no dependency on the magnetic field strength relative to density, i.e.  $B \propto \rho^0$ . If magnetic field lines do contract with enhancement of gas density, then one expects a scaling similar to  $B \propto \rho^\kappa$ , with  $\kappa = 0.5, 0.67$  for strong and weak field limit, respectively (see e.g. the review by Hennebelle & Inutsuka 2019).

In the ISM, indeed the  $\kappa = 0$  relation is observed up to number densities of  $\sim 300 \text{ cm}^{-3}$  (Troland & Heiles 1986; Crutcher et al. 2010). This corresponds to densities of roughly  $1.1 \times 10^{-21} \text{ g cm}^{-3}$ , using a mean molecular weight of 2.35. Crutcher et al. (2010) find that above these densities, the data is consistent with  $\kappa = 2/3$ , with considerable scatter. The transition in power law is often associated with transitioning from a sub-Alfvénic (Alfvénic Mach number  $\mathcal{M}_A < 1$ ) to super-Alfvénic regime ( $\mathcal{M}_A > 1$ ).

For a given sub-structure, we can compute  $\mathcal{M}_A$  as

$$\mathcal{M}_A = \sigma_{1D} / v_A. \quad (7)$$

Here  $\sigma_{1D}$  is the one dimensional velocity dispersion and  $v_A$  is an estimate of the average Alfvén wave group velocity. For a structure of mass  $M$ , we compute  $\sigma_{1D}$  from

$$\sigma_{1D}^2 = \frac{1}{3M} \int_V \rho (\mathbf{v} - \mathbf{v}_0)^2 d^3r, \quad (8)$$

with  $\mathbf{v}_0$  being the center of mass velocity computed as

$$\mathbf{v}_0 = \frac{1}{M} \int_V \rho \mathbf{v} d^3r. \quad (9)$$

The integration is performed over the entire volume  $V$  of the given structure.

The Alfvén velocity can be compute as

$$v_A = \sqrt{\frac{\langle |\mathbf{B}|^2 \rangle}{4\pi\rho_{\text{avg}}}}. \quad (10)$$

The average density  $\rho_{\text{avg}}$  here is the volume averaged density, i.e.

$$\rho_{\text{avg}} = M/V. \quad (11)$$

$\langle |\mathbf{B}|^2 \rangle$  is the volume averaged square of the magnetic field  $\mathbf{B}$ ,

$$\langle |\mathbf{B}|^2 \rangle = \frac{1}{V} \int_V |\mathbf{B}|^2 d^3r. \quad (12)$$

The behaviour of the magnetic field strength with density can be seen for the MHD clouds in Fig. 3, where we plot the root mean squared magnetic field strength against the threshold (minimum) density  $\rho_{\text{thr}}$  for different dendrogram structures at  $t_{\text{evol}} = 3.5 \text{ Myr}$ . The different dendrogram structures are marked with filled or empty symbols depending on whether their molecular  $\text{H}_2$  mass percentage is greater or less than 50% of their total hydrogen mass. The colorbar here represents  $\mathcal{M}_A$ , as computed from Eq. 7. The reddish points represent super-Alfvénic structures, while the blueish points are sub-Alfvénic. The vertical dotted line at  $10^{-22} \text{ g cm}^{-3}$  represents the boundary between the points obtained from the low-den (left half) and high-den (right half) dendrogram analysis. The dash-dotted black line and the dotted power law represent the Crutcher et al. (2010) relation discussed previously and  $B \propto \rho^{0.5}$ , respectively. The red and blue solid lines represent the mean and median magnetic field strength at those densities in the simulation, while the cyan dashed line represents non linear least square best fit for points at the high density range ( $\rho_{\text{thr}} > 1.1 \times 10^{-21} \text{ g cm}^{-3}$ ).

Firstly, we note that the points at the high density range lie above the mean and median field at that density range. This can be explained

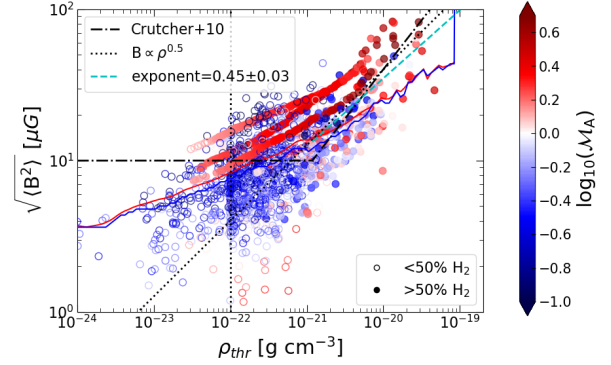


**Figure 3.** Relation between the root mean squared magnetic field and  $\rho_{\text{thr}}$  for all MHD clouds at  $t_{\text{evol}}=3.5 \text{ Myr}$ . The color bar represents the Alfvénic Mach number  $\mathcal{M}_A$ . The dash-dotted line represents the  $B$ - $\rho$  relation from Crutcher et al. (2010), while the dotted line represents a  $B \propto \rho^{0.5}$  power law. The red dashed line represents the best fit power law exponent for all points with  $\rho_{\text{thr}} > 1.1 \times 10^{-21} \text{ g cm}^{-3}$ . The blue and the red lines represent the evolution of the mean and median magnetic field against the density, respectively.

variable 1	variable 2	time [Myr]	p-value
$\rho_{\text{thr}} (\mathcal{M}_A > 1)$	$\rho_{\text{thr}} (\mathcal{M}_A \leq 1)$	2	$6 \times 10^{-4}$
		3.5	$5.2 \times 10^{-15}$

**Table 3.** The p-values of the 2 sample KS test for the density distribution of sub-Alfvénic and super-Alfvénic structures. We can see that the p-value is low for both 2 and 3.5 Myr, suggesting that sub-Alfvénic and super-Alfvénic structures (corresponding to bluish and reddish points in Fig. 3, respectively) have statistically significant differences in their density distributions.

by the fact that  $\rho_{\text{thr}}$  corresponds approximately to 3D density contour values, and is therefore lower than the average density. The higher density values are well consistent with the strong field limit expected relation of  $B \propto \rho^{0.5}$ . We will show in the next section (Section 5) that our structures are on average highly elongated, and magnetic fields clearly help deform the shape of the forming structures. It is therefore not unexpected that we find a shallower scaling compared to the weak field limit.

Finally, we see that while there is no clear transition from sub- to super-Alfvénic regime, there is clearly a trend that higher Alfvénic Mach numbers are obtained at the higher density end. This is also reproduced by a Kolmogorob-Smirnov (KS) 2 sample test between the  $\rho_{\text{thr}}$  distribution of  $\mathcal{M}_A > 1$  and  $\mathcal{M}_A \leq 1$  structures, which compares if two distributions belong to the same population (in this case, the same density distribution). If the p-value is larger than a certain value (typically 0.05), this represents that we cannot reject the null hypothesis that the sub-Alfvénic and super-Alfvénic structures have the same underlying density distribution. The p-values of the KS test for  $\rho_{\text{thr}}$  of sub-Alfvénic and super-Alfvénic structures can be seen in Table 3. We find the p-value to be very low ( $6 \times 10^{-4}$  at 2 Myr and  $5.2 \times 10^{-15}$  at 3.5 Myr), and can therefore reject the hypothesis that the sub-Alfvénic and super-Alfvénic structures have the same density distribution.

Overall, we find that the  $B$ - $\rho$  relation for the simulated structures is well consistent with observations, and enables us to draw relevant conclusions regarding the effects magnetic fields play in shaping and governing MC sub-structures.

## 5 MORPHOLOGY

Almost all clouds in our simulations tend to be identified as sheet or curved sheet-like on the larger scales, with filamentary networks embedded within. We present 3D renderings of three large scale cloud dendrogram structures in Fig. 4. In each case, we show the large scale structure in blue, and one of the primary embedded filamentary structures in red. The three rows correspond to MC1-MHD, MC5-MHD and MC6-MHD, with the different panels in each row showing different viewing angles. It is quite clear that especially at large scales, the structures are rather thin sheet-like, as classified by the algorithm. This is clearer in a video view, which can be found here<sup>1</sup>. We show here the largest structures from the high-den dendrogram analysis ( $\rho_0 = 10^{-22} \text{ g cm}^{-3}$ ) as they are on the maximum resolution and therefore capture the finer complexities of the cloud better. The large scale structures for the lower density dendrogram analysis follow the same trend.

The overall morphological trends obtained by our method is summarized in Fig. 5, where we plot the cumulative fraction of sheets, curved sheets, filaments and spheroidal structures against size  $R$  for all structures in the two hydrodynamic clouds (Fig. 5, left panel) and the five MHD clouds (Fig. 5, right panel) at  $t_{\text{evol}} = 3.5 \text{ Myr}$ .

We estimate the size of the structures simply from the volume  $V$  as:

$$R = V^{1/3}. \quad (13)$$

We find that spheroidal structures, shown in green, are in general less numerous compared to sheet-like or filamentary structures. Moreover, we see that the MHD clouds consist of even less fraction of spheroidal structures compared to their hydrodynamic counterparts. Sheets (including curved sheets) seem to be the most abundant for all clouds, though the fraction of filaments is considerably higher for the MHD counterparts.

Gravitational collapse naturally proceeds anisotropically and tends to create elongated structures. However, we show in our companion paper that most of our cloud structures are unbound or only marginally bound. Such being the case, gravity cannot be the principal contributor to forming elongated structures and we must therefore identify other methods as possible primary reasons for the lack of spheroidal structures.

Shock compression and turbulence are two such methods to produce elongated structures (see e.g. Inoue & Inutsuka (2016) for shock compression, Federrath (2016) for turbulence). Due to the anisotropic nature of MHD turbulence, the presence of magnetic fields is naturally prone to form even more elongated structures (see, for example, Hennebelle & Inutsuka (2019)). This is consistent with what we find.

Sheets and filaments are both elongated structures. It is interesting, however, that for the hydrodynamic clouds, sheets are by far the most numerous contributor whereas for the MHD clouds filaments and sheets are more comparable in total number. This is consistent with the results of Hennebelle (2013), who investigate setups of both decaying supersonic turbulence and colliding flow, and find that their simulations tend to produce more sheet-like structures for hydrodynamical simulations, and more filamentary structures for MHD simulations.

Overall, we see primarily sheet like MCs with an abundance of elongated structures (filamentary or sheet-like), irrespective of whether the simulation contains magnetic fields or not. Sheets are generally more numerous, likely representing the fact that we trace a large number of structures belonging to the sheet-like

atomic envelope of the MCs. The presence of magnetic fields, however, tends to somewhat increase the fraction of filamentary over sheet-like structures, and decrease the number of spheroidal structures.

The morphological trend among MC structures at these scales is of paramount importance in relation to how the MCs themselves form. The multi phase ISM in the SILCC simulations (and therefore also the SILCC-Zoom simulations) is primarily a product of multiple supernova driven expansions. The MCs in the simulations themselves form primarily at the shells or intersections of such expanding supernova bubbles. The large scale sheets we see, therefore, can be interpreted as tracing these shells, with a complex network of different morphological trends contained within. This picture is consistent with the bubble driven structure formation scenario (Koyama & Inutsuka 2000; Inoue & Inutsuka 2009; Inutsuka et al. 2015), where supernova expansions drive out large bubbles, and at the dense HI shell of these bubbles, MCs form due to multiple compressions.

Our results overall indicate that the extended structures that host the dense potential star forming structures in the MCs seem to be sheet-like in nature. In previous observational works, Kalberla et al. (2016) have argued that the cold, neutral hydrogen in the ISM is organized in sheet-like structures. Investigating the L1495 region of the Taurus molecular cloud, Arzoumanian et al. (2018) report evidences of extended sheet-like structures. Our findings here are in line with both observations.

## 6 DYNAMICS AND FRAGMENTATION

### 6.1 Dynamics of sub-structures

We are also interested in assessing the energetic relevance of magnetic fields over different length scales in the MCs, especially with respect to potentially star forming structures. For this purpose, we compute the volume term of the magnetic energy and compare it to the kinetic and potential energies.

The magnetic energy of a structure is computed as

$$E_B = \int_V \frac{1}{8\pi} |\mathbf{B}|^2 d^3r, \quad (14)$$

where the integration is computed over the entire volume  $V$  of the structure. The kinetic energy is computed using the following relation:

$$E_{KE} = \frac{1}{2} \int_V \rho (\mathbf{v} - \mathbf{v}_0)^2 d^3r. \quad (15)$$

Here  $\mathbf{v}_0$  is the center of mass velocity computed from Eq. 9. The self gravitating potential energy of a given structure is obtained using the following relation:

$$E_{PE} = -\frac{1}{2} G \int_V \int_V \frac{\rho(\mathbf{r})\rho(\mathbf{r}')}{|\mathbf{r} - \mathbf{r}'|} d^3r d^3r', \quad (16)$$

where  $G$  is the universal gravitational constant. We compute the self gravity of each dendrogram structure using a KD-tree algorithm instead of an  $O(N^2)$  direct computation.

We show the relative importance of magnetic fields with respect to potential and kinetic energy in the left and right panel of Fig. 6, respectively, for all MHD cloud structures at  $t_{\text{evol}} = 3.5 \text{ Myr}$ . For both plots, the x-axis represents the density threshold  $\rho_{\text{thr}}$ , and the y-axis represents  $E_B/|E_{PE}|$  (left) and  $E_B/|E_{KE}|$  (right). The colorbar indicates  $\log_{10} R$ , with larger sizes corresponding to darker colors. Different types of structures are plotted with different symbols. The

<sup>1</sup> [https://hera.ph1.uni-koeln.de/~ganguly/silcc\\_zoom/](https://hera.ph1.uni-koeln.de/~ganguly/silcc_zoom/)

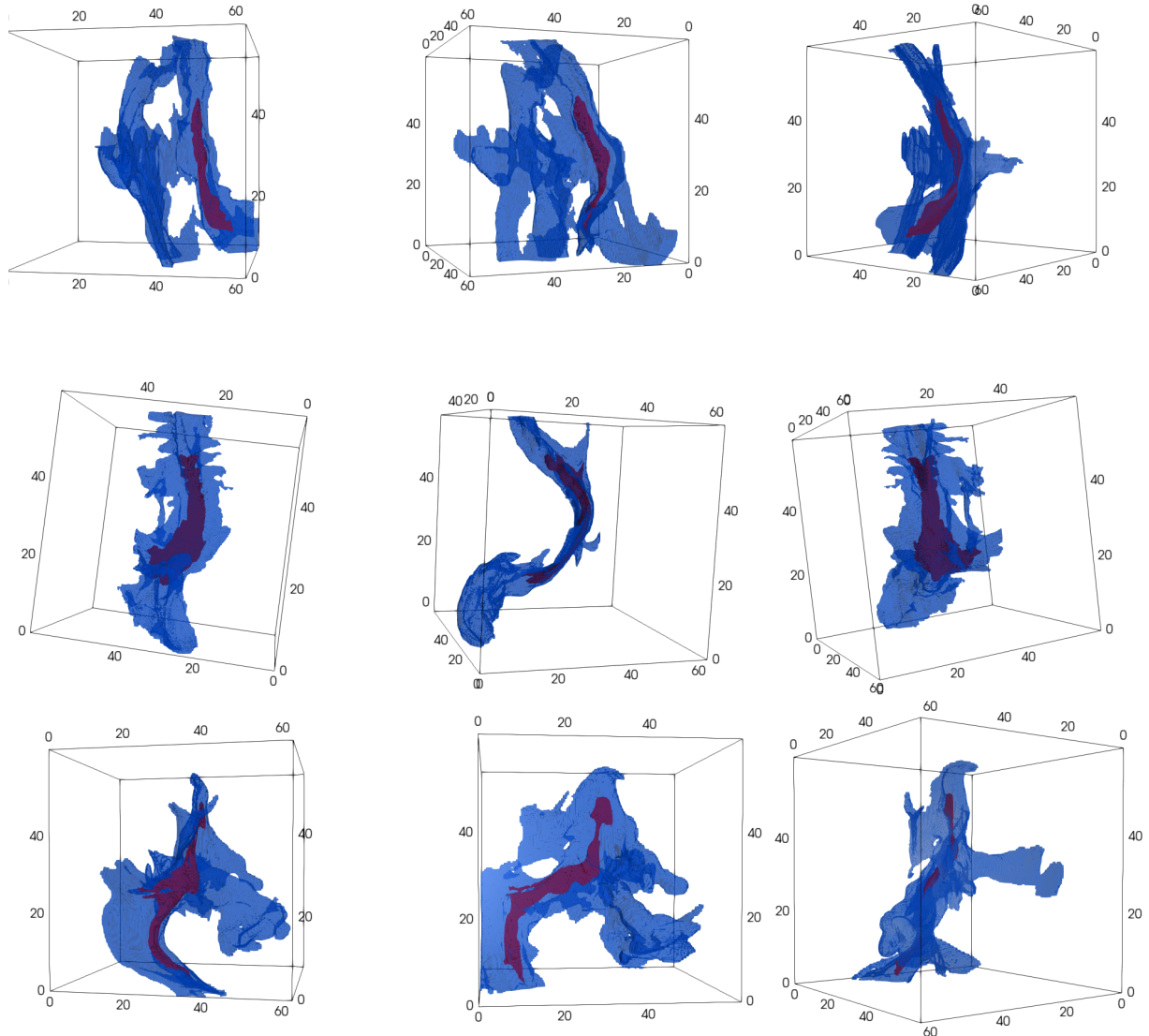


**Figure 4.** 3D rendering of example large scale dendrogram structures from the high-den dendrogram analysis for MC1-MHD (top row), MC5-MHD (middle row) and MC6-MHD (bottom row), from different angles. The blue structures represent the large scale sheet or curved sheet like structures, while the embedded red structures show one of the more prominent embedded filaments. The units in the axes are in parsec. A video link for the various structures can be found [here](#).

vertical line is drawn at  $10^{-22} \text{ g cm}^{-3}$ , dividing the plot into points obtained by the low-den and high-den dendrogram analysis. The horizontal dotted line represents a value of 1, where the magnetic energy is magnitude wise equal to the potential or kinetic energy. The dash-dotted line is a power law proportional to  $\rho^{-1/2}$ . The side panes to the right and top of each plot show the marginalized distribution of the structures over the corresponding energy ratio and  $\rho_{\text{thr}}$ , respectively. The different colored lines in the side panes represent different morphological fractions  $f_{\text{fraction}}$ .

We firstly note that for large scale structures, the magnetic energy tends to become comparable to potential and kinetic energies, but slowly becomes one to two orders of magnitudes less when looking

at the denser structures. There are, however, a larger number of mostly atomic, small-scale structures where the magnetic pressure is stronger compared to both potential and kinetic energies.

There seems to be a trend roughly similar to  $\rho^{-1/2}$  for scaling of the energy ratio as we follow certain branches that go from larger scale and less dense structures, to denser and potentially star forming structures. This implies that for the present scenario, magnetic field becomes less important as we go deeper into the MCs themselves.

We can explore the implications of such possible scaling relations using Larson’s  $\sigma_{\text{1D}}$ -size, and mass-size relations (Larson 1981; Solomon et al. 1987). Let us assume that our dendrogram structures

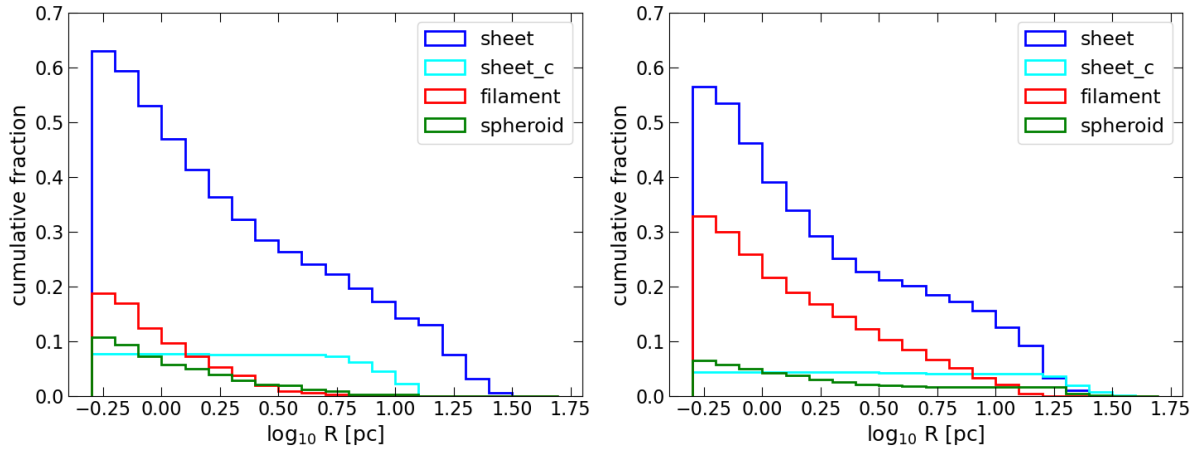


**Figure 5.** Cumulative histogram of different morphologies (sheets, curved sheets, filaments, or spheroids) for all HD (left) and MHD (right) clouds at  $t_{\text{evol}} = 3.5$  Myr. 6 out of the 7 analyzed clouds are sheet-like on large scales, with filamentary networks embedded inside. Spheroidal structures are rarer in presence of magnetic fields. The hydrodynamic simulations produce more sheets than filaments, while the MHD runs tend to have a relative increase in fraction of filaments.

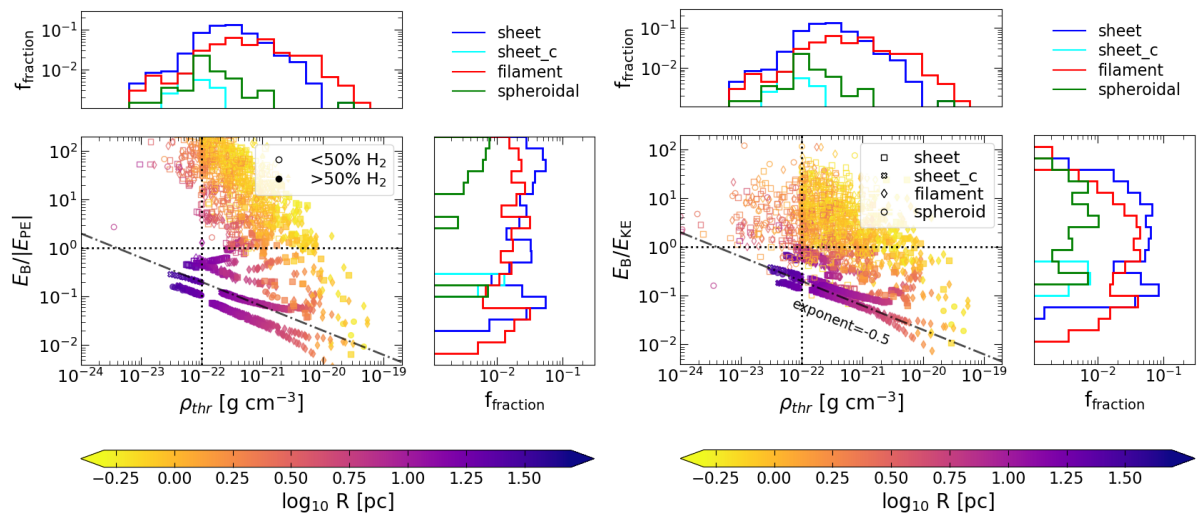


**Figure 6.** Ratio of magnetic energy to self gravitating potential energy (left) and to kinetic energy (right) plotted against the density threshold for different MHD dendrogram structures at time  $t_{\text{evol}} = 3.5$  Myr. The color bar represents the size of the various structures. A line proportional to  $\rho^{-1/2}$  is plotted in dash-dotted lines. The top and the right panels show the marginalized distribution of the fraction of structures over the density and the respective energy ratio, respectively, divided into their structure type.

follow the following scaling relations,

$$\sigma_{\text{1D}} \propto R^n, \quad (17)$$

$$M \propto R^\beta, \quad (18)$$

as well as  $B \propto \rho^\kappa$  with  $\kappa \geq 0$ , as already discussed in Section 4. Using the relation that  $M \propto \rho R^3$ , we can estimate that the ratios  $E_B/E_{\text{PE}}$  and  $E_B/E_{\text{KE}}$  have the following dependencies on density:

$$E_B/E_{\text{PE}} \propto \rho^{2(\kappa-1)+\frac{2}{3-\beta}}, \quad (19)$$

$$E_B/E_{\text{KE}} \propto \rho^{2\kappa-1+\frac{2n}{3-\beta}}. \quad (20)$$

If we use typical parameters from Larson's relations and put  $n =$

$1/2$ ,  $\beta = 2$ , we find that both ratios reduce to

$$E_B/E_{\text{PE}} \propto \rho^{2\kappa}, \quad (21)$$

$$E_B/E_{\text{KE}} \propto \rho^{2\kappa}. \quad (22)$$

As  $\kappa \geq 0$ , it is impossible to achieve a negative slope in the  $E_B/|E_{\text{PE}}|$  and  $E_B/E_{\text{KE}}$  relations using structures following Larson's relations. The structures that follow an energy ratio proportional to  $\rho^{-1/2}$  must therefore necessarily depart from Larson's relations. In our companion paper, we show that indeed the gravity dominated dendrogram branches depart from Larson's relations and show a much flatter scaling. Note that this is only true for the structures that actually follow

this  $\rho^{-1/2}$  trend. The diffuse atomic structures that show little to no trend with density can be fully consistent with the Larson relations.

From the marginal distributions, we find no obvious trend in the morphology of the structures over either  $\rho_{\text{thr}}$  or the energy ratios. This suggests that the different morphological configurations are created by the same formation mechanism.

There also seems to be a difference in the energy ratios between atomic and molecular structures. This can be clearly seen in the average behaviour of these ratios over time (Fig. 7). Fig. 7 plots the time evolution of the average value of  $E_B/|E_{\text{PE}}|$  (left) and  $E_B/E_{\text{KE}}$  (right) for all atomic (red), molecular (blue), and dense molecular (yellow) structures from the MHD clouds, where we note dense molecular structures to be structures that are both molecular and have  $\rho_{\text{thr}} > 10^{-20} \text{ g cm}^{-3}$ . The error bars here represent the standard error on the mean. From Fig. 7, we find that there is a clear distinction regarding how strong magnetic energy is for atomic and molecular structures, particularly with respect to potential energy. As we increase in molecular fraction and density, the magnetic energy becomes less and less important. There also does not seem to be a clear trend in the evolution of these ratios over time.

The relatively less importance of magnetic energy for dense structures compared to potential or kinetic energy suggests that while magnetic fields help determine the morphology of cloud structures across different scales, the dynamics of particularly the denser structures, and ultimately of potential star formation, is determined by the interaction between gravity and turbulence. We explore this interplay between turbulence and gravity in much greater detail in our companion paper by means of a virial analysis.

Magnetic fields can change in what kind of environment denser structures sit in (i.e. by making the surrounding envelope "fluffier"), and shape the structures and affect the nature of gas flow that forms these structures. This is clearly seen by the large number of (mostly atomic) structures where magnetic energy is comparable or even orders of magnitude larger compared to self-gravity or kinetic energy. However, the dynamically subservient magnetic fields at higher densities is consistent with the lack of discernible difference in the density PDFs between hydrodynamic and MHD clouds (Fig. 2), as well as observations that the high density power law tails of column density PDFs, representing star forming gas, is virtually unaffected by the presence of magnetic fields (see.g. [Klessen & Burkert 2001](#); [Girichidis et al. 2014](#); [Schneider et al. 2015](#)).

## 6.2 Magnetic surface energy

In the previous section, we have discussed the magnetic pressure term in comparison to self-gravity and kinetic energy. The magnetic pressure relates to the stretching and compression of magnetic field lines, and does not take into account the effect of curvature in the field.

The magnetic surface term can be computed as an integral over the surface of a given structure  $S$  as follows:

$$E_B^{\text{surface}} = \oint_S (\mathbf{r} - \mathbf{r}_0) \mathbf{T} \hat{\mathbf{n}} dS. \quad (23)$$

Here  $\mathbf{r}_0$  is the center of mass,  $\hat{\mathbf{n}}$  is the surface normal vector pointing outwards, and  $\mathbf{T}$  is the Maxwell stress tensor, which can be written as follows for ideal MHD (as electric fields are zero):

$$\mathbf{T} = \frac{1}{4\pi} \left( \mathbf{B} \otimes \mathbf{B} - \frac{1}{2} |\mathbf{B}|^2 \hat{\mathbf{I}} \right). \quad (24)$$

$\hat{\mathbf{I}}$  is here a second order identity matrix.

We evaluate Eq. 23 as a volume integral using the Gauss' divergence theorem for convenience. This gives us the following relation:

$$E_B^{\text{surface}} = -E_B + \int_V (\mathbf{r} - \mathbf{r}_0) \cdot \nabla \mathbf{T} dV \quad (25)$$

From Eq. 25, we can see that  $E_B^{\text{surface}}$  can be both positive or negative. When it is positive, it adds to the magnetic pressure term and acts as a dispersive term. In contrast, when  $E_B^{\text{surface}} < 0$ , it acts as a confining term.

The importance of  $E_B^{\text{surface}}$  with respect to the the volume term  $E_B$  can be seen in Fig. 8, left panel, which plots the magnitude of the ratio of  $E_B^{\text{surface}}/E_B$  to the density threshold of the cloud sub-structures for all MHD clouds at  $t_{\text{evol}} = 3.5$  Myr. Structures where  $E_B^{\text{surface}}$  helps disperse them ( $E_B^{\text{surface}} > 0$ ) are marked in red, while structures where  $E_B^{\text{surface}}$  acts as a confining term ( $E_B^{\text{surface}} < 0$ ) are marked in cyan. The vertical dotted line marks the difference between the results of the low-den and high-den dendrogram runs at  $\rho = 10^{-22} \text{ g cm}^{-3}$ , as in the previous plots. The horizontal dotted line represents a value of one, where the volume and surface term are magnitude wise equally important. The top and side panels show the marginalized distribution of the fraction of structures, marginalized over  $\rho_{\text{thr}}$  and  $|E_B^{\text{surface}}/E_B|$ , respectively.

From the marginalized distributions, we see that roughly equivalent number of structures have  $E_B^{\text{surface}}$  as a confining and dispersive term, with confinement slightly outweighing number of structures where the surface term is dispersive. On average the magnetic surface term seems to be slightly less than or comparable to  $E_B$ , though there are significant number of structures where the surface term magnitude wise exceeds the volume term. This implies that for diffuse and mostly atomic structures, where magnetic energy is comparable or dominant, the surface term is important. This is especially relevant when  $E_B^{\text{surface}}$  acts as a confining term. However, for dense structures, where the magnetic pressure energy is one to two order of magnitudes less compared to potential and kinetic energy, the surface term is unlikely to affect the dynamics significantly.

The behaviour of the confining nature of the surface term can be seen in the right panel of Fig. 8, which plots the magnitude of  $(E_B^{\text{surface}} + E_B)/E_{\text{PE}}$  against the ratio of magnetic pressure energy to self-gravity,  $E_B/E_{\text{PE}}$ , for all MHD cloud sub-structures at  $t_{\text{evol}} = 3.5$  Myr. The color bar here represents the size of the structures. The horizontal and vertical dotted lines both represent a value of unity along the  $y$ - and  $x$ - axes, respectively. The dashed line represents a 1:1 line, and the shaded region around it represents a factor of 2 in each direction. Structures in the shaded region represent those where the magnetic surface energy is not significant compared to the volume energy. Structures with strong dispersive  $E_B^{\text{surface}}$  terms lie above the 1:1 line, while points that lie below the 1:1 line represent structures where  $E_B^{\text{surface}}$  is confining in nature. Most interesting here are points that lie in the bottom right quadrant of the plot. They represent structures where the magnetic pressure  $E_B$  is higher compared to the self-gravity, and would be completely unbound in a traditional virial analysis. However, the confining  $E_B^{\text{surface}}$  term is strong enough that the overall magnetic contribution becomes far less, thus allowing for a sort of "magnetic confinement".

Two examples of structures belonging to MC2-MHD, that exhibit such magnetic confinement, are plotted in Fig. 9, as black contour lines over a density slice along the  $x$ -direction. The background color here represents the logarithmic density scale, while the planar magnetic field component direction is shown using the line integral convolution (LIC) technique. For both structures, we mention the magnitude of the  $E_B/E_{\text{PE}}$  and  $(E_B^{\text{surface}} + E_B)/E_{\text{PE}}$  ratios in the figure

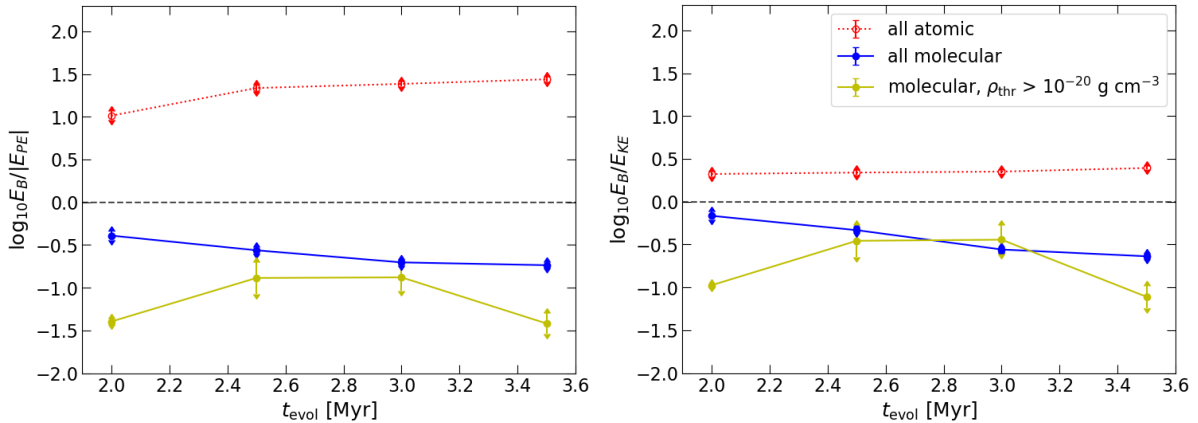


**Figure 7.** Evolution of mean of the ratio of magnetic to potential energy (left) and kinetic energy (right) over time. The different colors represent atomic, molecular, and dense molecular (molecular and  $\rho_{\text{thr}} > 10^{-20} \text{ g cm}^{-3}$ ) structures in red, blue, and yellow, respectively. The errors bars are the standard errors on the mean. For denser and molecular structures, magnetic energy is less important compared to potential or kinetic energies. The atomic structures, representing more the envelope, have high magnetic energies, especially compared to self-gravity.

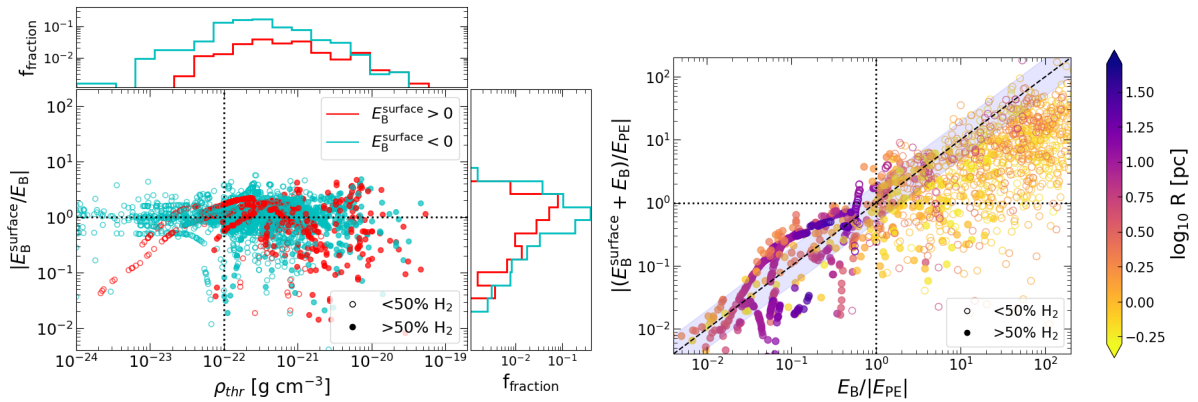


**Figure 8.** Left: Ratio of the absolute value of the magnetic surface to volume energy, plotted against the density threshold. The different colors represent whether the magnetic surface term is positive and resists collapse or negative and helps collapse. The magnetic surface energy seems to be as relevant as the volume energy term, and for more than half of the structures acts as a confining term. Right: The ratio of the total magnetic energy (surface and volume) to the self-gravitating potential energy, plotted against the magnetic volume energy to the self-gravitating potential energy. The dashed line represents a 1:1 ratio, and the shaded region represents a factor of 2. For many small scale atomic structures, magnetic surface term seems to be important as a possible confining force.

title. As can be clearly seen, the magnetic surface term reduces the  $|(E_B^{\text{surface}} + E_B)/E_{\text{PE}}|$  ratio to less than one. However, this naturally does not take into account other energy terms, i.e. kinetic and thermal energy.

### 6.3 Fragmentation

Finally, we attempt to disentangle what, if any, effects magnetic fields can have in terms of fragmentation properties of their parent clouds. For this purpose, we study the numbers and masses of different fragments, represented by leaf sub-structures (i.e. structures containing no further sub-structures) in our dendrogram analysis.

Representing fragments by the leaves in the dendrogram analysis suffers from the caveat of depending on the dendrogram parameters. Increasing the minimum number of cells required in a dendrogram structure, for example, would naturally reduce the number of fragments and increase their masses. The absolute values of the masses

and numbers we find, therefore, are sensitive to the parameter values we have used. However, since we have used the exact same parameters for each HD and MHD run, the relative difference between the average behaviour of the HD and MHD clouds is of significance.

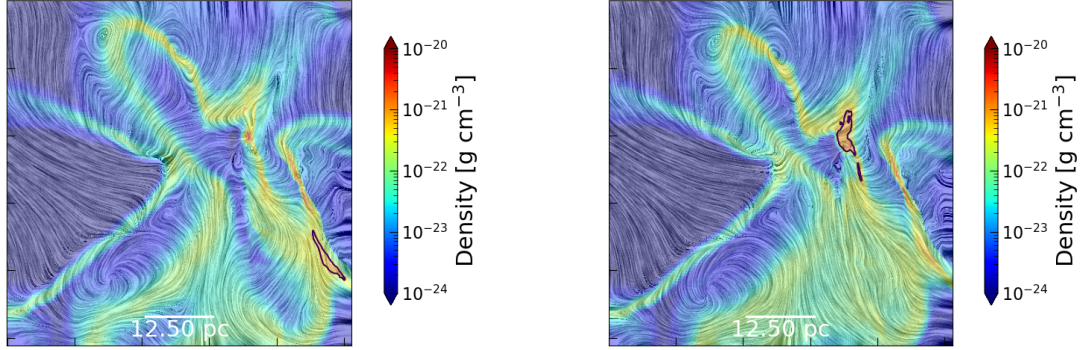
With this caveat in mind, let us look at the fragmentation properties of our dendrogram structures. We study the behaviour of the numbers and masses of leaf fragments in Fig. 10.

Fig. 10, top row, plots the cumulative distribution of the average number of leaf structures  $\langle N_{\text{structure}}^{\text{leaf}} \rangle$  at different  $\rho_{\text{thr}}$  for both HD (blue) and MHD (red) clouds. The three panels show a time evolution from left to right at  $t_{\text{evol}} = 2, 2.5$  and  $3.5$  Myr, respectively. The number of leaves is normalized by the total number of HD and MHD clouds (2 for HD, 5 for MHD). The vertical line at  $10^{-22} \text{ g cm}^{-3}$  marks the difference between the low-den and the high-den dendrogram analysis.

We see that at  $t_{\text{evol}} = 2$  and  $2.5$  Myr, up until densities of somewhere between  $10^{-23}$  and  $10^{-22} \text{ g cm}^{-3}$ , the HD and MHD clouds

12 *S. Ganguly et al.*

$$|E_B/E_{PE}| = 4.57, |(E_B + E_B^{\text{surface}})/E_{PE}| = 0.13 \quad |E_B/E_{PE}| = 1.36, |(E_B + E_B^{\text{surface}})/E_{PE}| = 0.95$$



**Figure 9.** Two examples of structures confined by  $E_B^{\text{surface}}$  from MC2-MHD, plotted as black contours over density slices along the  $x$ -direction, at  $t_{\text{evol}} = 3.5$  Myr. The colormap is the logarithmic density, and the direction of the planar magnetic field is plotted as line integral convolution. The relevant energy ratios are plotted in the title.

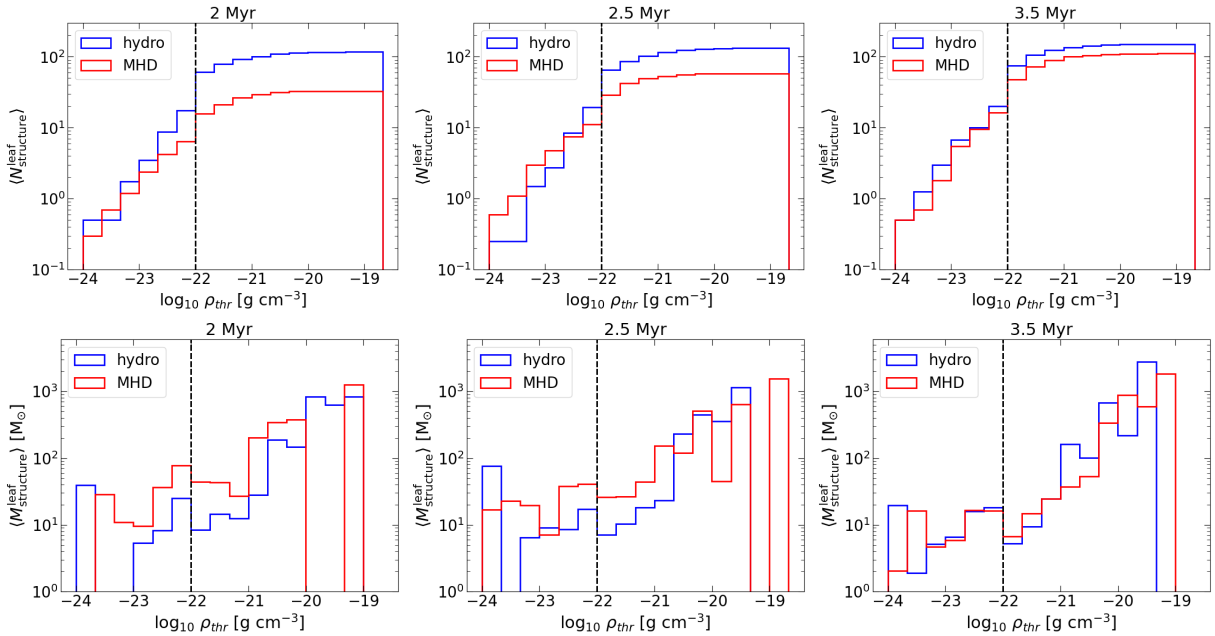


**Figure 10. Top row, left to right:** Cumulative distribution of the average number of leaf structures against  $\rho_{\text{thr}}$  for HD and MHD clouds at  $t_{\text{evol}} = 2, 2.5, 3.5$  Myr, respectively. The hydrodynamic clouds have on average more new structures forming at earlier times, but this distinction slowly disappears later on. **Bottom row, left to right:** Distribution of average mass of leaf structures for both HD and MHD clouds at  $t_{\text{evol}} = 2, 2.5, 3.5$  Myr, respectively. The leaf structures, representing fragments, are more massive for MHD clouds at earlier times, while this distinction mostly disappears later on.

form roughly similar number of leaf fragments. However, at higher densities,  $\langle N_{\text{structure}}^{\text{leaf}} \rangle$  is much higher for hydrodynamic clouds. This difference largely disappears at 3.5 Myr.

This suggests that the formation of structures is slowed down at higher densities in presence of magnetic fields. At lower densities of up to  $\sim 10^{-22}$   $\text{g cm}^{-3}$ , this difference is mostly absent.

It is also interesting to note, if there exists difference in the mass of the fragments that form in presence of magnetic fields. This can be seen in Fig. 10, bottom row, where we plot the average mass of the forming leaf structures over different  $\rho_{\text{thr}}$  for HD and MHD

structures. Similar to the top row, the panels show a time evolution. The vertical dashed line demarcates the same difference as in the top row.

We see that for densities of up to a few times  $10^{-22}$   $\text{g cm}^{-3}$ , the MHD fragments are more massive compared to their hydrodynamic counterparts, even though their number is roughly equal (see discussion above). This is prominent at  $t_{\text{evol}} = 2$  and 2.5 Myr, and is much less striking at 3.5 Myr. For  $\rho_{\text{thr}} > 10^{-21}$   $\text{g cm}^{-3}$ , we do not seem to see any such systematic difference. This is in line with Fig. 2, where we saw that the difference in PDFs between the hydrodynamic and

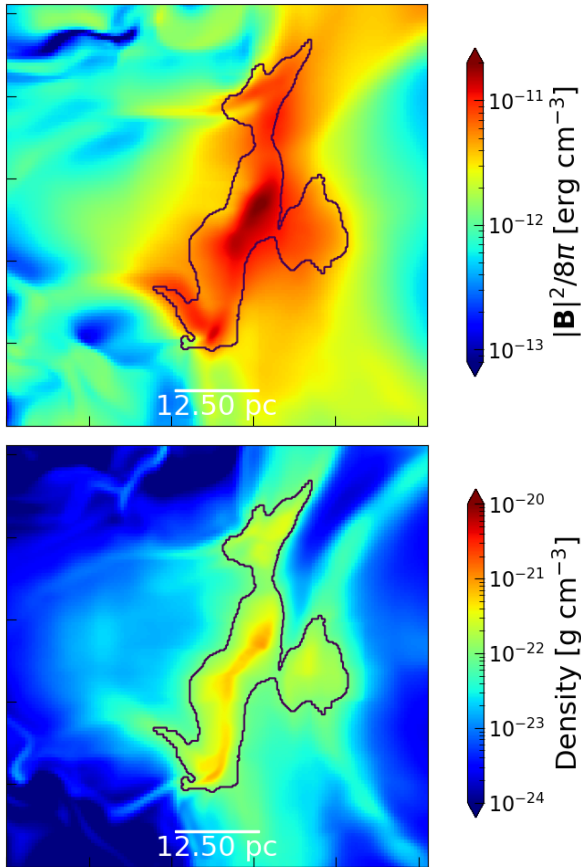


**Figure 11. Top:** A map of the distribution of magnetic pressure  $|B|^2/8\pi$  in a slice plot for one larger scale structure from MC1-MHD at  $t_{\text{evol}} = 2$  Myr. The contour of the structure is plotted with a black outline. Significant variations in magnetic pressure is seen, corresponding to the strength of the magnetic force. **Bottom:** Density slice of the same contour to guide the eye.

MHD clouds at the intermediate density ranges of the cloud envelope was most striking at  $t_{\text{evol}} = 2$  Myr, and less so later on.

All combined, from Fig. 10, we find a picture where at densities of up to roughly  $\rho_{\text{thr}} = 10^{-22}$  g cm $^{-3}$ , both HD and MHD clouds form similar numbers of fragments. The MHD fragments, however, are on average more massive. This is consistent with the result that magnetic fields affect the dynamics of lower density gas more (Molina et al. 2012).

We also see from behaviour of both the number and mass of sub-structures that the differences between the HD and MHD clouds largely disappear over time. This suggests that the magnetic fields have a "slow down" effect on the evolution of the cloud. This effect is related to the strength of the magnetic field, and the variations therein. To highlight the variations in the strength of the B field, in the top panel of Fig. 11, we plot the magnetic pressure for an example slice of cloud MC1-MHD at  $t_{\text{evol}} = 2$  Myr. We also plot a density map of the same slice in Fig. 11, bottom panel to guide the eye. In each case, we show the projected outline of a representative larger scale dendrogram structure as black contours.

To estimate an order of magnitude value of this slow down effect

from the variations in magnetic pressure, we attempt to estimate a timescale depending on its gradient:

$$\tau_B = \sqrt{\frac{2c}{\frac{|\nabla|B|^2|}{8\pi\rho_{\text{thr}}}}} \quad (26)$$

Here  $c$  is the shortest semi axis of the fitted ellipsoid from Eq. 5, and  $\langle\nabla|B|^2\rangle$  is the gradient of the magnetic pressure term, averaged over the volume of a given sub-structure, i.e.

$$\langle\nabla|B|^2\rangle = \int_V \nabla|B|^2 d^3r. \quad (27)$$

$\tau_B$  gives us a measure of the timescale over which the magnetic pressure can significantly change a structure. It is motivated by the fact that from an acceleration vector  $\mathbf{g}$  and a distance  $S$ , we can estimate a timescale as  $(S/|\mathbf{g}|)^{1/2}$ . If the magnetic field is constant, then  $\tau_B \rightarrow \infty$ . To estimate over what timescale this can have an effect on our cloud, we take an average of  $\tau_B$  over all "trunk" structures (i.e. structures that do not have any further parents and typically represent the largest scale structures) from the low-den dendrogram analysis. This leads to a value of  $\tau_B = 1.9 \pm 1.0$  Myr, which is roughly consistent with what we seem to see in terms of fragmentation.

We emphasize, however, that this is an order of magnitude calculation and any true attempt at estimating the slow down needs to take into account the other acceleration terms, such as from gravity and thermal pressure.

## 7 CONCLUSIONS

We investigate the role magnetic fields play in determining the morphology, energetics, and fragmentation properties of young molecular clouds by performing a detailed analysis on seven different simulated clouds (five with magnetic fields, and two without) from the SILCC Zoom simulations. These simulations are geared to study the evolution of the multi-phase interstellar medium in a supernova-driven, turbulent, stratified galactic disc environment. To identify forming structures, we use a dendrogram algorithm, and trace the statistical properties of the identified structures. We include a simple chemical network which allows us to follow the formation of H $_2$  as the cloud assembles and thereby distinguish between mostly atomic (H $_2$  mass fraction < 50%) and mostly molecular (H $_2$  mass fraction > 50%) structures.

We observe that the MHD clouds are fluffier and have more intermediate density gas between number densities of roughly 1 – 100 cm $^{-3}$ , compared to their hydrodynamic counterparts. Lack of magnetic fields then result in the denser structures of the hydrodynamic clouds being surrounded by a comparatively rarer envelope.

In terms of morphology, we find that almost all of the clouds are sheet-like, suggesting that they form due to compression caused by expanding supernova shells, or where shells from multiple supernovae cross. This is consistent with the bubble driven filament formation scenario of MCs (Koyama & Inutsuka 2000; Inoue & Inutsuka 2009; Inutsuka et al. 2015) and support observations of sheet-like envelopes around denser filamentary structures (Kalberla et al. 2016; Arzoumanian et al. 2018).

We find spheroidal structures in the simulations to be rare in general, and rarer still for clouds with magnetic fields, suggesting that B fields affect and enhance the already present anisotropy of structure formation. We further see that the runs with magnetic fields have roughly comparable fraction of filaments and sheets, while the hydrodynamic runs produce more sheet-like structures compared to filaments.



Energetically, magnetic fields in our simulations are important for less dense and mostly, but not exclusively, atomic structures. The dynamics for larger cloud-scale structures, as well as for smaller scale and potentially star forming structures, is dominated by the interplay of turbulence and gravity. We see no clear trend between morphology and relative importance of magnetic fields, suggesting that different morphologies have similar dynamic origins. By investigating the magnetic surface energy term, we find that for most structures, it acts in a confining manner and even leads to some low density, magnetically confined structures.

By studying the numbers and masses of forming cloud fragments, we find that at densities below roughly  $10^{-22}$  g cm $^{-3}$ , the presence of magnetic fields helps create more massive fragments, but generally do not result in an increased number of such structures. Instead of altering the nature of fragmentation, magnetic fields seem to rather slow down the fragmentation procedure.

Overall we find a scenario where magnetic fields significantly affect the flows and fragmentation in the lower density gas, channeling flows and thereby affecting both the morphology of the forming structures as well as slowing down the formation of dense gas. Once the dense structures form, however, the further evolution and fragmentation of the dense gas seems to be mostly unaffected by the magnetic fields.

#### ACKNOWLEDGEMENTS

SG, SW and DS would like to acknowledge the support of Bonn-Cologne Graduate School (BCGS), which is funded through the German Excellence Initiative, as well as the DFG for funding through SFB 956 'Conditions and Impact of Star Formation' (sub-projects C5 and C6). SDC is supported by the Ministry of Science and Technology (MoST) in Taiwan through grant MoST 108-2112-M-001-004-MY2. This research made use of *astrodendro*, a Python package to compute dendrograms of Astronomical data (<http://www.dendrograms.org/>); as well as *yt*, an open-source, permissively-licensed python package for analyzing and visualizing volumetric data (<https://yt-project.org/>). The 3D renderings in Fig. 4 were computed using *paraview*. The FLASH code used in this work was partly developed by the Flash Center for Computational Science at the University of Chicago.

#### DATA AVAILABILITY

The data underlying this article can be shared for selected scientific purposes after request to the corresponding author.

#### REFERENCES

- André P., Di Francesco J., Ward-Thompson D., Inutsuka S. I., Pudritz R. E., Pineda J. E., 2014, From Filamentary Networks to Dense Cores in Molecular Clouds: Toward a New Paradigm for Star Formation. eprint: arXiv:1312.6232, doi:10.2458/azu\_uapress\_9780816531240-ch002, <https://ui.adsabs.harvard.edu/abs/2014prpl.conf...27A>
- Arzoumanian D., Shimajiri Y., Inutsuka S.-i., Inoue T., Tachihara K., 2018, *Publications of the Astronomical Society of Japan*, 70, 96
- Bally J., Stark A. A., Wilson R. W., Henkel C., 1987, *The Astrophysical Journal Supplement Series*, 65, 13
- Beck R., 2009, *Astrophysics and Space Sciences Transactions*, 5, 43
- Beck R., 2015, *The Astronomy and Astrophysics Review, Volume 24, article id.4*, <NUMPAGES>57</NUMPAGES> pp., 24, 4

- Beck R., Wielebinski R., 2013, *Planets, Stars and Stellar Systems. Volume 5: Galactic Structure and Stellar Populations*, p. 641
- Bouchut F., Klingenberg C., Waagan K., 2007, *Numerische Mathematik*, 108, 7
- Bourke T. L., Myers P. C., Robinson G., Hyland A. R., 2001, *The Astrophysical Journal*, 554, 916
- Commerçon B., Hennebelle P., Henning T., 2011, *The Astrophysical Journal*, 742, L9
- Crutcher R. M., 1999, *The Astrophysical Journal*, 520, 706
- Crutcher R. M., 2012, *Annual Review of Astronomy and Astrophysics*, vol. 50, p.29-63, 50, 29
- Crutcher R., Heiles C., Troland T., 2003, *Turbulence and Magnetic Fields in Astrophysics*, 614, 155
- Crutcher R. M., Wandelt B., Heiles C., Falgarone E., Troland T. H., 2010, *The Astrophysical Journal*, 725, 466
- Derigs D., Winters A. R., Gassner G. J., Walch S., 2016, *Journal of Computational Physics*, 317, 223
- Derigs D., Winters A. R., Gassner G. J., Walch S., Bohm M., 2018, *Journal of Computational Physics*, 364, 420
- Draine B. T., 1978, *Apjs*, 36, 595
- Dubey A., et al., 2008, in Pogorelov N. V., Audit E., Zank G. P., eds, *Astronomical Society of the Pacific Conference Series Vol. 385, Numerical Modeling of Space Plasma Flows*. p. 145
- Federrath C., 2016, *Monthly Notices of the Royal Astronomical Society*, 457, 375
- Federrath C., Klessen R. S., 2012, *The Astrophysical Journal*, 761, 156
- Fletcher A., Beck R., Shukurov A., Berkhuijsen E. M., Horellou C., 2011, *Monthly Notices of the Royal Astronomical Society*, 412, 2396
- Fryxell B., et al., 2000, *The Astrophysical Journal Supplement Series*, 131, 273
- Girichidis P., Konstandin L., Whitworth A. P., Klessen R. S., 2014, *The Astrophysical Journal*, 781, 91
- Girichidis P., et al., 2016a, *Monthly Notices of the Royal Astronomical Society*, 456, 3432
- Girichidis P., et al., 2016b, *Apjl*, 816, L19
- Girichidis P., Seifried D., Naab T., Peters T., Walch S., Wunsch R., Glover S. C. O., Klessen R. S., 2018, *Monthly Notices of the Royal Astronomical Society*, 480, 3511
- Girichidis P., et al., 2020, *Space Science Reviews*, 216, 68
- Glover S. C. O., Mac Low M.-M., 2007, *The Astrophysical Journal Supplement Series*, 169, 239
- Glover S. C. O., Federrath C., Mac Low M.-M., Klessen R. S., 2010, *Monthly Notices of the Royal Astronomical Society*, 404, 2
- Habing H. J., 1968, *Bulletin of the Astronomical Institutes of the Netherlands*, 19, 421
- Hall J. S., 1951, *The Astronomical Journal*, 56, 40
- Heiles C., Crutcher R., 2005, *Cosmic Magnetic Fields*, 664, 137
- Heiles C., Troland T. H., 2005, *The Astrophysical Journal*, 624, 773
- Heitsch F., Zweibel E. G., Mac Low M.-M., Li P., Norman M. L., 2001, *The Astrophysical Journal*, 561, 800
- Hennebelle P., 2013, *Astronomy and Astrophysics*, 556, A153
- Hennebelle P., Inutsuka S.-i., 2019, *Frontiers in Astronomy and Space Sciences*, 6, 5
- Hill A. S., Joungh M. R., Mac Low M.-M., Benjamin R. A., Haffner L. M., Klingenberg C., Waagan K., 2012, *The Astrophysical Journal*, 750, 104
- Hiltner W. A., 1951, *The Astrophysical Journal*, 114, 241
- Ibáñez-Mejía J. C., Mac Low M.-M., Klessen R. S., 2022, *The Astrophysical Journal*, 925, 196
- Inoue T., Inutsuka S.-i., 2009, *The Astrophysical Journal*, 704, 161
- Inoue T., Inutsuka S.-i., 2016, *The Astrophysical Journal*, 833, 10
- Inutsuka S.-i., Inoue T., Iwasaki K., Hosokawa T., 2015, *Astronomy and Astrophysics*, 580, A49
- Kalberla P. M. W., Kerp J., Haud U., Winkel B., Ben Bekhti N., Flöer L., Lenz D., 2016, *The Astrophysical Journal*, 821, 117
- Kennicutt Jr. R. C., 1998, *The Astrophysical Journal*, 498, 541
- Klessen R. S., Burkert A., 2001, *The Astrophysical Journal*, 549, 386
- Koyama H., Inutsuka S.-i., 2000, *The Astrophysical Journal*, 532, 980
- Larson R. B., 1981, *mnras*, 194, 809

- Li H.-B., Henning T., 2011, *Nature*, 479, 499
- Molina F. Z., Glover S. C. O., Federrath C., Klessen R. S., 2012, *Monthly Notices of the Royal Astronomical Society*, 423, 2680
- Mouschovias T. C., 1991, *The Astrophysical Journal*, 373, 169
- Nelson R. P., Langer W. D., 1997, *The Astrophysical Journal*, 482, 796
- Padoan P., Nordlund A., 2011, *The Astrophysical Journal*, 730, 40
- Pardi A., et al., 2017, *Monthly Notices of the Royal Astronomical Society*, 465, 4611
- Planck Collaboration P., et al., 2020, *Astronomy and Astrophysics*, 641, A12
- Rosolowsky E. W., Pineda J. E., Kauffmann J., Goodman A. A., 2008, *The Astrophysical Journal*, 679, 1338
- Schmidt M., 1959, *The Astrophysical Journal*, 129, 243
- Schneider N., et al., 2015, *Astronomy & Astrophysics, Volume 578, id.A29, <NUMPAGES>17</NUMPAGES> pp.*, 578, A29
- Seifried D., et al., 2017, *Monthly Notices of the Royal Astronomical Society*, 472, 4797
- Seifried D., Walch S., Reissl S., Ibáñez-Mejía J. C., 2019, *Monthly Notices of the Royal Astronomical Society*, 482, 2697
- Slyz A. D., Devriendt J. E. G., Bryan G., Silk J., 2005, *Monthly Notices of the Royal Astronomical Society*, 356, 737
- Solomon P. M., Rivolo A. R., Barrett J., Yahil A., 1987, *The Astrophysical Journal*, 319, 730
- Spitzer Jr. L., 1942, *The Astrophysical Journal*, 95, 329
- Spitzer L., 1978, Physical processes in the interstellar medium, [doi:10.1002/9783527617722](https://ui.adsabs.harvard.edu/abs/1978ppim.book.....S), <https://ui.adsabs.harvard.edu/abs/1978ppim.book.....S>
- Troland T. H., Crutcher R. M., 2008, *The Astrophysical Journal*, 680, 457
- Troland T. H., Heiles C., 1986, *The Astrophysical Journal*, 301, 339
- Waagan K., 2009, *Journal of Computational Physics*, 228, 8609
- Walch S., et al., 2015, *Monthly Notices of the Royal Astronomical Society*, 454, 238
- Wünsch R., Walch S., Dinnbier F., Whitworth A., 2018, *Monthly Notices of the Royal Astronomical Society*, 475, 3393

#### APPENDIX A: BASIC INFORMATION OF CLOUDS

We present here some basic properties of the different analyzed molecular clouds. Fig. A1 plots the column density projections of all different clouds, both HD and MHD. Fig. A2 plots the total and H<sub>2</sub> mass of the different MCs in the left panel, and the H<sub>2</sub> mass fraction in the right panel.

This paper has been typeset from a  $\text{\TeX}/\text{\LaTeX}$  file prepared by the author.

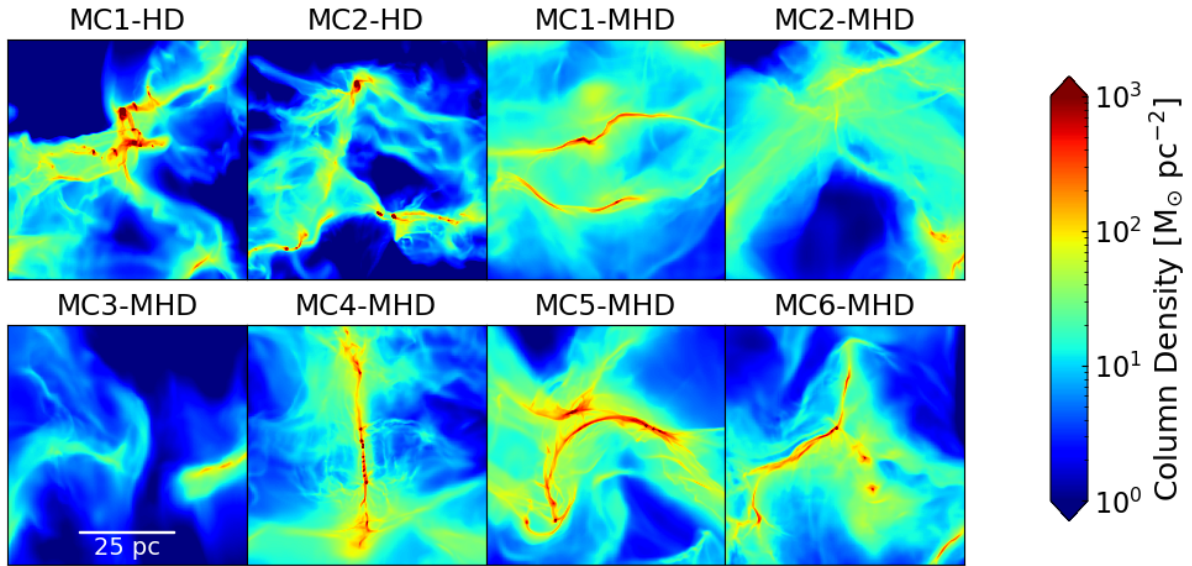


**Figure A1.** Column density projection along the x axis for different molecular clouds at  $t_{\text{evol}} = 3.5$  Myr. The MHD clouds have typically more diffuse emission. Note that we have excluded MC3-MHD from further analysis due to its low molecular content (see Fig. A2).

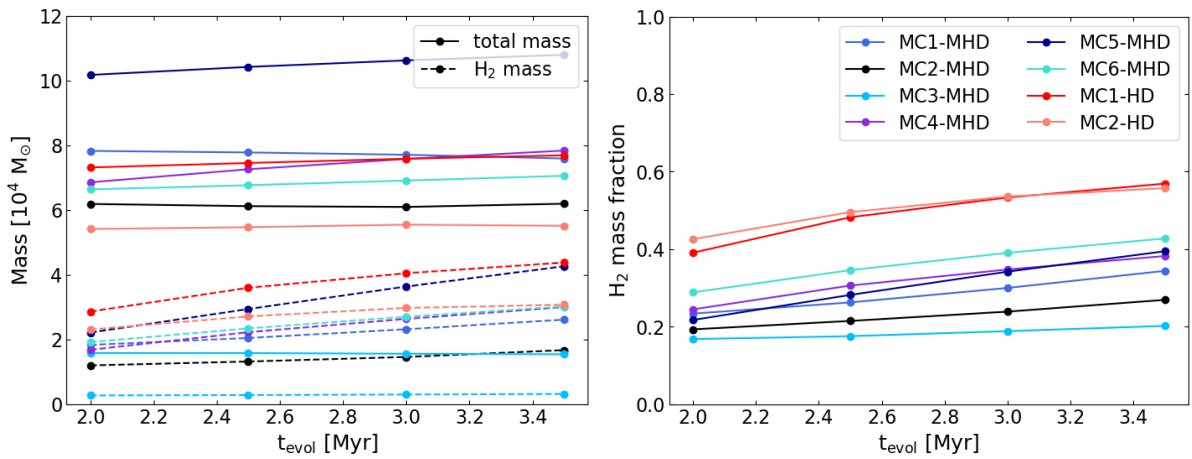


**Figure A2. Left:** Time evolution of total mass and total  $\text{H}_2$  mass in the different molecular clouds, both HD and MHD, from  $t_{\text{evol}} = 2$  to 3.5 Myr. The solid lines represent the total mass, and the dashed lines represent the  $\text{H}_2$  mass. **Right:**  $\text{H}_2$  mass fraction for the same clouds, both HD and MHD. The two HD clouds are plotted in reddish lines. Apart from MC3-MHD, which we discard due to its low molecular gas mass, the other MHD and HD and clouds have comparable masses. The two HD clouds however, have a much higher  $\text{H}_2$  mass fraction.

## SUB-STRUCTURES IN SILCC DEEP-ZOOM

---

In the research presented in the previous chapters, we have investigated results on the early stages of molecular cloud evolution, focusing on cloud scale structures, from few tens of parsecs down to about half a parsec. We have looked at the dynamical behaviour connected to potential and kinetic energy, the effect of magnetic fields on the different density regimes in the cloud, and traced the morphological evolution of sub-structures across scales.

The SILCC deep-zoom simulations, which have been implemented and run as part of this thesis, allow us to probe much smaller scales and offer a resolution up to sixteen times better. The resolution of the SILCC deep-zoom runs, compared to that of the SILCC-Zoom runs, can be seen in Table 6.1.

simulation type	box size	maximum refinement level	maximum resolution
SILCC-Zoom	~100 pc	10	0.125 pc
SILCC deep-zoom	~50 pc	14	0.0078 pc

Table 6.1: Comparison of the maximum resolution attainable in SILCC-Zoom and SILCC deep-zoom simulations.

The results in this chapter can roughly be divided into two interlinked types: results on dynamics, and on morphology. The layout of this chapter is as follows: in Section 6.1, we motivate the types of questions that the new simulations allow us to answer. We follow this up with a general overview of the different analyzed regions and their bulk properties in Section 6.2. In Section 6.3, we perform a full virial analysis of the cloud sub-structures. This is followed by a discussion of the morphology of the deep-zoom structures in Section 6.4, focusing primarily on filaments and core-like sub-structures. Finally, we summarize the results of the chapter in Section 6.5.

### 6.1

#### THE SCOPE OF THE DEEP-ZOOM SIMULATIONS

The dynamics of the interstellar medium spans many orders of magnitudes in both length and density scales. Galactic dynamics influences the formation of molecular clouds. The molecular clouds, themselves tens or even hundreds of parsecs in size, seem to be permeated by filamentary structures in observations (Molinari et al., 2010; André et al., 2010, 2014; Hacar et al., 2022). Filaments are assumed to form under different conditions, and their dynamical behaviour is likely to reflect the difference in their parent environments (e.g. Hacar et al., 2022). Many filaments in observations are threaded by core-like structures (André et al., 2010; Arzoumanian et al., 2013; Könyves et al., 2015; Marsh et al., 2016; Clarke et al., 2017), the sites of star formation.

With the SILCC-Zoom results (Chapters 4 and 5), we were able to probe the dynamics of cloud scale ( $\sim 1$  pc and above) structures. We could resolve down to roughly parsec scale sub-structures (the smallest structures in our SILCC-Zoom dendrogram analysis has a size of  $\sim 0.5$  pc) and analyze their dynamics. However, many filaments in observations tend to have a width of  $\sim 0.1$  parsec (Arzoumanian et al., 2011, 2019), although it is a matter of debate whether this is an observational limitation (e.g. Panopoulou et al., 2017).

The superior resolution of the SILCC deep-zoom simulations allows us to resolve such possible forming filaments, and investigate sub-parsec scale structures that form inside them in a realistic ISM simulation of a much larger scale. This is relevant, as most investigations into fragmentation of filaments rely on smaller scale, more idealized simulations (e.g. Clarke et al., 2017). Investigating the SILCC deep-zoom simulations, therefore, gives us insight into the dynamics of MC sub-structures on filamentary scales.

What kind of physics can we hope to investigate from this? We can look into, for example, different processes of filament formation and fragmentation (see Section 1.3.2 for a brief overview), and investigate if there are dynamical differences in filaments that are created through different pathways. By connecting the results with the larger scale SILCC-Zoom simulations (chapters 4 and 5), we can attempt to understand the hierarchical behaviour of forming structures. In the previous chapters, we have seen the dynamical dominance of gravity and kinetic energy - and we can attempt to disentangle whether this changes once we are inside the supposed filaments. We can, for example, investigate if we are able to resolve the scales at which gravity takes over. The scenario of embedded cores inside filaments suggests that we should have a filament to core transition scale. The deep-zoom simulations potentially allow us investigate these scales.

Summarizing the discussion above, we highlight the different questions being investigated in the remainder of this chapter:

- What is the principal method of structure formation for the scales investigated here ( $\sim 0.03 - 3$  pc), and how is it different from cloud scales? (Section 6.3)
- Are the sub-parsec scale structures we see here bound at all? If so, to what degree, and by which dynamical component, are they primarily bound by? (Section 6.3)
- What is the morphological distribution of the sub-structures observed here? How is it similar to, or different from cloud scale morphological distributions seen in Chapter 5? (Section 6.4)
- Do we see a transition scale from filaments to cores? (Section 6.4)
- What is the nature of accretion for the cores and filaments seen in the simulations? Are they reflected also in their dynamical differences? (Section 6.4)

The short discussion above highlights some of the questions that we have attempted to answer in the next sections. We present further possible work, beyond the scope of the present thesis in the outlook in Chapter 7.

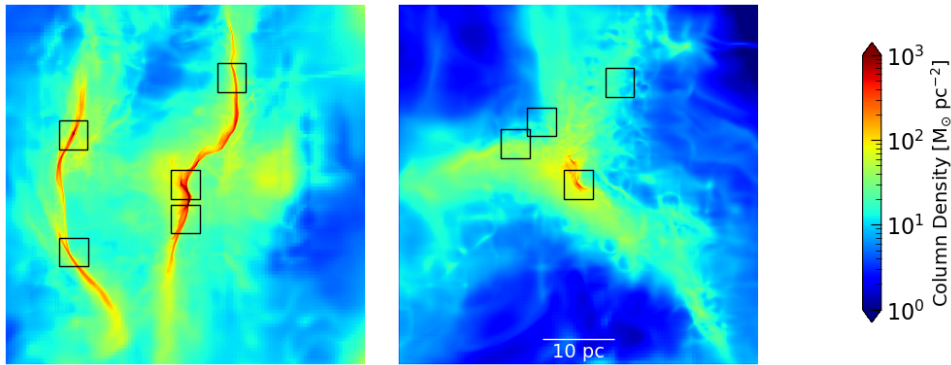


Figure 9: The two clouds in the SILCC deep-zoom simulations, MC1-MHD (left) and MC2-MHD (right), projected along the  $x$ -axis, at  $t_{\text{deep}} = 0.8$  Myr. The square boxes represent the projection of the  $4 \text{ (pc)}^3$  analyzed regions. MC1-MHD shows denser and more developed structures, while MC2-MHD is more extended and diffuse.

## 6.2

### GENERAL OVERVIEW

The SILCC deep-zoom simulations are performed by restarting the SILCC-Zoom simulations with embedded high refinement boxes. As discussed in Section 2.3.3, for any considerations of time evolution of the deep-zoom simulations, we use the evolution time  $t_{\text{deep}}$ , which is set to zero at the start of the deep-zoom refinement.

The two different clouds analyzed for the purpose of the deep-zoom simulations can be seen in Fig. 9. The left panel shows the cloud MC1-MHD, which has two prominent elongated structures. Throughout this chapter, we will often refer to these two regions as the left and right region, respectively. In contrast, MC2-MHD shows a more diffuse and extended gas distribution, and is likely lagging behind in terms of developing dense structures. In each case, we point out some of the regions we use for the dendrogram analysis as black squares plotted over the column density maps. Note that the deep-zoom region is  $\sim (50 \text{ pc})^3$  in size, much larger than the analyzed boxes shown in Fig. 9. A projected view of each of the analyzed regions can be found in Fig. 10.

The naming convention of the analyzed regions is as follows: they are named MC $x$ -MHD-R $a$ , MC $x$ -MHD-R $b$  and so on, where  $x=1,2$  refers to the two molecular clouds. Further, since MC1-MHD has two clearly distinctive regions as discussed above (also see Fig. 9, left panel), we pick regions such that MC1-MHD-R $a$  and MC1-MHD-R $b$  belong to the left region, while regions MC1-MHD-R $c,d,e$  belong to the right region.

The dense structures in the simulations are reached by gradual refinement of the grid, starting from relatively early stages of the SILCC-Zoom simulations. This can be seen in Fig. 11, where we see the gradual refinement and evolution of the right region from MC1-MHD. We further see that the right region seems to move from the left to right in the projected view over time. This is a result of it experiencing a general larger scale flow in the simulated ISM. We will show later on that the right region represents shock compressed structures compressed by ISM flows, themselves likely originating from old supernovae exploding in the original SILCC simulations. Please note that the region in Fig. 11 is larger in scale compared to any

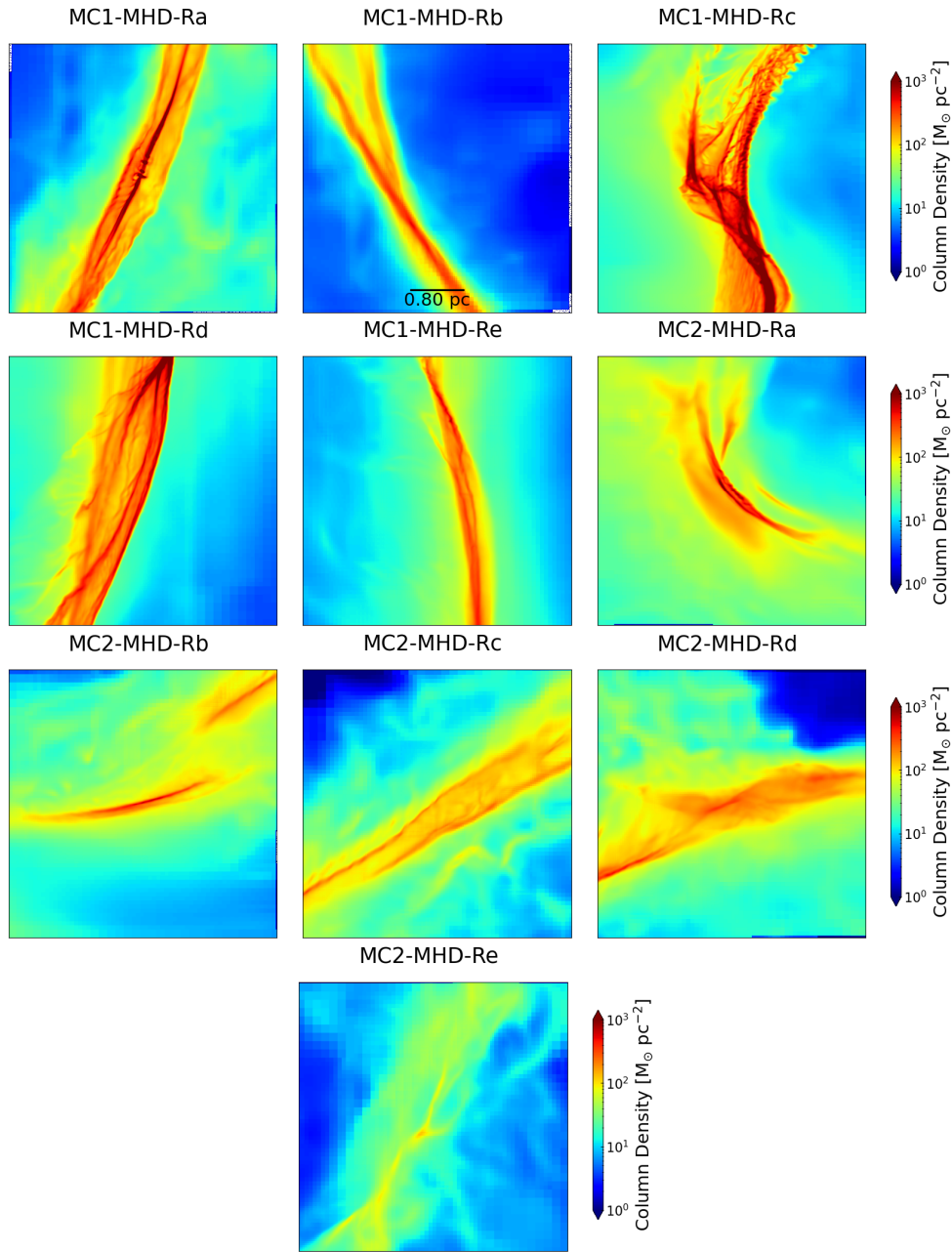


Figure 10: The different regions analyzed in the dendrogram analysis, projected along the  $x$ -axis at  $t_{\text{deep}} = 0.8$  Myr.

of the analyzed regions shown in Fig. 10, and is only shown to illustrate the gradual refinement procedure.

#### *Analyzed regions*

To identify structures inside the SILCC deep-zoom boxes, we perform a dendrogram analysis on the 3D density cubes corresponding to each region in Fig. 10. Similar to the analysis presented in previous chapters, we use *astrodendro* for this purpose. The regions are picked by considering different portions of the clouds by visual inspection. The list of these regions, along with some basic properties such

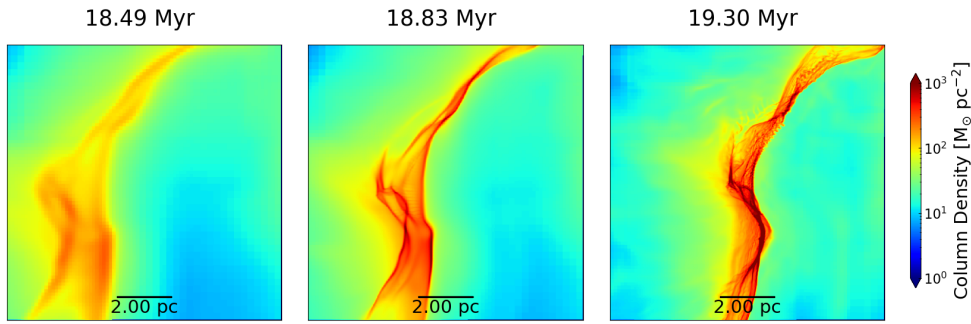


Figure 11: **Left to right:** Gradual refinement of the right region for the cloud MC1-MHD, projected along the x-axis. The time shown here is in the total simulation time  $t$ . The left panel corresponds to just after the refinement process has started, and the right panel is the end time we principally analyze. Note that the region shown in this figure is larger than the analyzed regions (highlighted as black square boxes in Fig. 9), and is only for the purpose of illustrating the refinement.

Cloud	Region	Total mass [ $M_{\odot}$ ]	$H_2$ mass [ $M_{\odot}$ ]	$H_2$ mass fraction	peak density [ $g\ cm^{-3}$ ]
MC1-MHD	MC1-MHD-Ra	985	568	0.81	$1.2 \times 10^{-15}$
	MC1-MHD-Rb	426	201	0.66	$8.4 \times 10^{-20}$
	MC1-MHD-Rc	1572	954	0.85	$6.3 \times 10^{-17}$
	MC1-MHD-Rd	1186	661	0.78	$1.2 \times 10^{-17}$
	MC1-MHD-Re	545	245	0.63	$4.6 \times 10^{-19}$
MC2-MHD	MC2-MHD-Ra	805	445	0.77	$2.0 \times 10^{-18}$
	MC2-MHD-Rb	611	322	0.74	$7.3 \times 10^{-19}$
	MC2-MHD-Rc	628	329	0.73	$8.8 \times 10^{-20}$
	MC2-MHD-Rd	781	454	0.81	$2.5 \times 10^{-19}$
	MC2-MHD-Re	270	67	0.35	$9.5 \times 10^{-20}$

Table 6.2: Summary of some bulk properties of the different regions analyzed using a dendrogram analysis at  $t_{\text{deep}} = 0.8$  Myr. Each region is of size  $(4\ \text{pc})^3$ .

as total and  $H_2$  mass, can be found in Table 6.2.

The size  $(4\ \text{pc})^3$  of the boxes is chosen out of a mixture of practical considerations, and to be consistent with the SILCC-Zoom results. In the SILCC-Zoom analysis, the smallest structures analyzed had a size of  $\sim 0.5\ \text{pc}$ . A  $4\ \text{pc}$  sized box allows us to overlap with the intermediate to small scale structures in SILCC-Zoom, and therefore allows us to extend and compare the results. A larger box could not be chosen, however, primarily due to considerations of computer memory required for the dendrogram algorithm.

#### *Dendrogram parameters*

In order to analyze the sub-structures in the selected regions, an important choice is to set the three dendrogram parameters: starting threshold  $\rho_0$ , density jump  $\Delta\rho$ , minimum number of cells  $N_{\text{cells}}$ . We refer to Section 2.4.1 for a detailed description of the parameters.

Since in the deep-zoom simulations, we are interested in denser structures, which were potentially not well resolved in the SILCC-Zoom analysis, we pick a higher  $\rho_0$  and a higher  $\Delta\rho$  compared to the SILCC-Zoom parameters. These para-



meters, and their comparison to the parameters used in the previous analysis (see paper I for example), are listed in Table 6.3.

From our analysis of the SILCC-Zoom simulations, we have learned that changing the dendrogram parameters does not affect the statistical properties of the structures. Therefore, while the number of structures may well change significantly depending on our choice of parameters, their overall statistical behaviour should remain relatively unchanged.

Simulation	$\rho_0$ [g cm <sup>-3</sup> ]	$\log_{10}\Delta\rho$	$N_{\text{cells}}$	pruning peak [g cm <sup>-3</sup> ]	size scale [pc]
SILCC-Zoom	10 <sup>-22</sup>	0.1	100	None/10 <sup>-21</sup>	~0.5-60
SILCC deep-zoom	10 <sup>-20</sup>	0.1	100	None	~0.03-3

Table 6.3: Comparison of the parameters used for the SILCC deep-zoom simulations, as opposed to the SILCC-Zoom simulations.

### *Time evolution*

In the present work, we have not performed a time series analysis of the results. All results from here on, unless otherwise stated, refer to  $t_{\text{deep}} = 0.8$  Myr.

## 6.3

### VIRIAL ANALYSIS

Once we obtain our dendrogram tree, we attempt to first analyze the energetics of the given structures using a full virial analysis. The details of the different virial volume and surface term can be found in Section 2.4.3. We investigate if structures from different analyzed regions are dominated by the same force, or exhibit very different energetic behaviours. The total number of structures from different regions, sub-divided by their leading energy term (i.e. which of the energy terms is magnitude-wise the largest), can be found in Table 6.4. Let us consider the different energy terms individually.

#### 6.3.1

##### STRUCTURES DOMINATED BY KINETIC ENERGY

In terms of the overall number of structures, structures dominated by the surface kinetic energy term or ram pressure ( $E_{\text{KE}}^{\text{surface}}$ ) form the single largest fraction (98 of 292, almost 34%). However, we see stark regional divisiveness depending on the region. Most of the ram pressure dominated structures are situated in MC1-MHD-Rc, which is the central dense part of the right region of MC1-MHD (see Fig. 9, left panel). This entire region, as we have noted before, seems to move from left to right in the projected view. The high kinetic surface term could represent therefore the "headwind" from this motion and help confine structures.

Indeed, this is true for most of the kinetically confined structures on the right region of MC1-MHD. An example of such a structure can be seen in Fig. 12, left panel, where we plot the slice of one of the ram pressure dominated structures in black contour lines, plotted over the corresponding density slice. The velocity vector in the plane  $\mathbf{v}_{\text{plane}}$  is plotted using arrows, with the reference arrow representing a velocity of 1 km s<sup>-1</sup>. The heading of the figure shows the full virial ratio  $\alpha_{\text{vir}}$  (as defined in Eq. 2.57), and the virial ratio obtained by considering only the volume

Region	Total structures	Leading energy term							
		$E_{PE}$	$E_{PE}^{ext}$	$E_{KE}$	$E_{KE}^{surface}$	$E_{TE}$	$E_{TE}^{surface}$	$E_B$	$E_B^{surface}$
MC1-MHD-Ra	39	21	2	0	0	14	0	1	1
MC1-MHD-Rb	5	1	0	0	1	2	0	0	1
MC1-MHD-Rc	175	17	14	1	77	40	0	11	15
MC1-MHD-Rd	17	1	6	0	6	4	0	0	0
MC1-MHD-Re	9	1	0	0	5	2	0	0	1
MC2-MHD-Ra	10	5	0	0	0	5	0	0	0
MC2-MHD-Rb	3	2	0	0	1	0	0	0	0
MC2-MHD-Rc	17	1	0	0	7	8	0	0	1
MC2-MHD-Rd	11	5	0	1	0	2	0	2	1
MC2-MHD-Re	6	0	0	0	1	0	0	2	3
Total	292	54	22	2	98	77	0	16	23

Table 6.4: The number of dendrogram structures in each analyzed deep-zoom region, sub-categorized by their leading energy term in the virial analysis, at  $t_{deep} = 0.8$  Myr.

terms ( $\alpha_{vir}^{vol}$ , from Eq. 2.58). We can see that the velocity flow to the left of the structure is strongly towards the right of the figure, while the velocity flow to the right changes direction and is much smaller in magnitude. This implies that the dense structure is essentially a shock layer. Here, the negative sign of  $\alpha_{vir}$  implies that the surface terms (specifically  $E_{KE}^{surface}$  in this case) are important.

For a minority of structures, as for the one shown in Fig. 12, right panel, the kinetic confinement seems to represent a converging flow rather than a shock front. In this case, multiple flows from different regions converge on the filamentary structure, and the filamentary structure itself likely represents the local longitudinal mass flow.

Interestingly, structures dominated by the volume term of the kinetic energy are almost absent (only 2 of 292). The velocity dispersion inside the structures themselves is mostly therefore not significant compared to its surface component.

### 6.3.2

#### STRUCTURES DOMINATED BY THERMAL ENERGY

Structures dominated by the volume term of the thermal energy ( $E_{TE}$ ) represent more than a quarter of the total structures (77 of 292 or 26%). They are more ubiquitous, appearing in both regions of MC1-MHD, as well as in MC2-MHD. They represent mostly smaller scale and relatively less dense structures. This can be seen in the left panel of Fig. 13, which plots the threshold density  $\rho_{thr}$  against size  $R$  of the different structures.

The discrete color bar here represents the structures with the magnitude wise leading energy term. For each energy, the darker color represents the volume term, while the lighter color represents the surface or external term (for example,  $E_{PE}$  dominated structures are shown in red, while  $E_{PE}^{ext}$  dominated structures are shown in salmon).

We can see that the thermal pressure dominated structures (dark green) seem to represent more the smaller scale, less dense end of all structures. We will later also demonstrate when computing the virial ratio (Fig. 18), that almost all the thermally dominated structures are unbound, and are likely representative of density fluctuations in the gas flow.

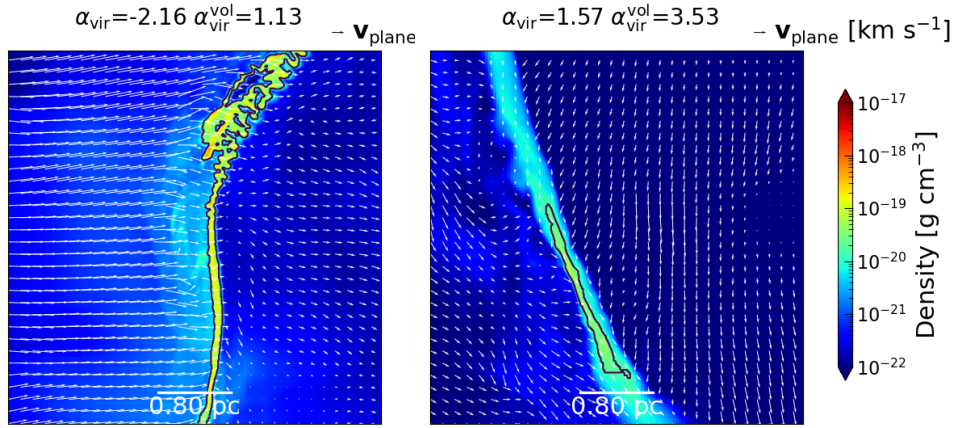


Figure 12: Two examples of kinetically bound structures, overplotted over density slices as black contours with the velocity field shown in white arrows, the length of the marker arrow representing a velocity of  $1 \text{ km s}^{-1}$ . The two structures belong to MC1-MHD-Rc (left) and MC1-MHD-Rb (right), respectively. The left structure represents shock compression, which represents the majority of kinetically bound structures. The right panel represents a rare example where the structure seems to be kinetically compressed more from converging flows onto the filament.

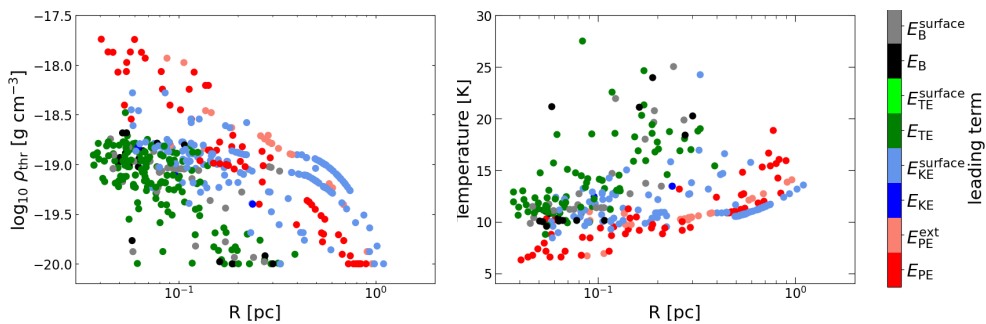


Figure 13:  $\rho_{\text{thr}}$  vs size  $R$  (left) and mean temperature distribution of (right) all deep-zoom structures at  $t_{\text{deep}} = 0.8 \text{ Myr}$ . The discrete colorbar represents the leading energy term in the virial equation. Thermal pressure dominated structures are typically small scale, and of lower densities.

The abundance of relatively less dense, thermally dominated structures is, however, in stark contrast to the energetics of the SILCC-Zoom structures discussed in the previous chapters. The source of this thermal energy could possibly be related to heating due to dynamic compressions of the velocity field.

Fig. 13, right panel shows the temperature distribution of the different structures against  $R$ , with the colorbar representing the leading energy term as discussed previously. We can see that the thermally dominant structures have a mean temperature only slightly above structures dominated by the other energy terms. The highest average temperatures we find here are of the order of  $\sim 25$  K, reflecting the fact that we are capturing the dynamics of highly dense and molecular gas.

Another interesting point to note is the absence of structures dominated by the surface term of thermal energy (light green in color bar, see also Table 6.4). Such structures could potentially represent thermal confinement, where stark temperature gradients between a structure and its surroundings confines a volume of gas. Such temperature gradients can be created by a nearby radiation source, such as a forming protostar. Since all gas is well resolved up to the analyzed time in our simulations, and no potential protostars have formed yet, the lack of thermally confined structures is expected and consistent with the overall picture. In future work, it would be interesting to note if such structures appear with the onset of stellar feedback.

### 6.3.3

#### STRUCTURES DOMINATED BY MAGNETIC ENERGY

For the ideal MHD equations, the volume term of the magnetic energy, associated with magnetic pressure, reflects the fact that when magnetic field lines are drawn closer together, this exerts a force perpendicular to the field lines. This pressure acts as a repellent against collapse of structures.

A small fraction of structures in our simulations are dominated by magnetic pressure energy  $E_B$  (16 out of 292, or  $\sim 5\%$ ). This is consistent with our previous SILCC-Zoom analysis, where we found only a few diffuse, atomic structures to be magnetically dominated. In the  $\rho_{\text{thr}}-R$  plot of Fig. 13, these structures are plotted in black and also tend to represent mostly smaller scale structures.

Just as the stretching or squeezing of magnetic field lines is associated with the volume term  $E_B$ , one can associate the magnetic surface term  $E_B^{\text{surface}}$  with the curvature of the field.  $E_B^{\text{surface}}$  can represent, for example, torsion of field lines and can be both positive and attempt to disperse the structure, or negative and act as a confining force. In fact, we find that structures dominated by their magnetic surface term are slightly more abundant (23 of 292 or  $\sim 8\%$ ) compared to volume magnetic energy dominated structures. Two such examples where the magnetic surface energy is the dominating virial term and helps confine the structures are shown in Fig. 14.

In Fig. 14, contour of the chosen dendrogram structures are plotted in black solid lines over a density slice. The wavy pattern represents the direction of the planar magnetic field and is plotted using the line integral convolution technique (Cabral & Leedom, 1993). The structure in the left panel represents the somewhat rarer example where the magnetic confinement force is strong enough to bind the structure ( $\alpha_{\text{vir}} < 0$ ). Typically, however, the magnetic surface term mostly manages to reduce the degree of unboundness. Such an example is shown in 14, right panel.

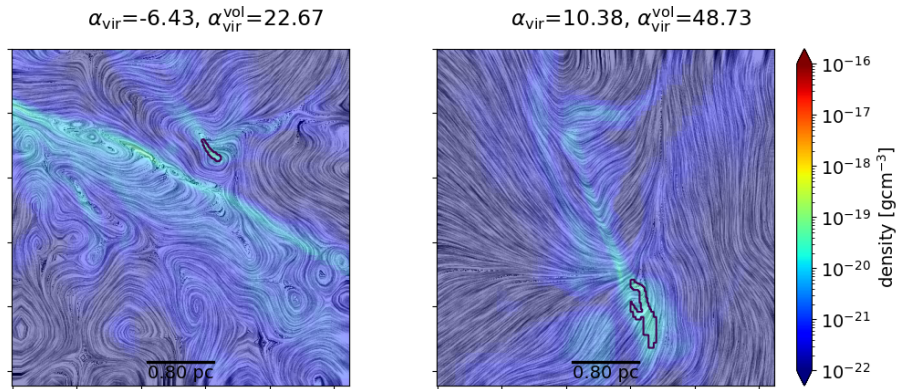


Figure 14: Two examples of structures where the magnetic field helps confine structures, overplotted as black contours over density slices. The morphology of the planar component of the magnetic field is plotted using a line integral convolution. The two structures belong to MC2-MHD-Rc (left) and MC2-MHD-Re (right), respectively. In the first case, the structure really is confined, while in the second case the magnetic field merely helps the structure become less unbound. Note that any magnetic confinement must be associated with bending of magnetic field lines.

#### 6.3.4

##### STRUCTURES DOMINATED BY GRAVITATIONAL ENERGY

Structures dominated by gravitational energy can be both self-gravity dominated ( $E_{PE}$ ), or dominated by tidal forces ( $E_{PE}^{ext}$ ). In a sense, structures dominated and bound by self-gravity are the most interesting for the purpose of star formation - as any structure that forms stars has to eventually become self-gravitating. While not overwhelmingly dominant, we find a significant number of such structures from Table 6.4 (54 of 292 or 18%). Most of such self-gravitating structures belong to the MC1-MHD regions. This is likely due to the fact that MC1-MHD is further developed at the time of analysis, has more prominent structures, and therefore has started to form structures that are bound by their own self-gravity. We show two examples of such structures, as well as the surrounding velocity field in Fig. 15.

The left panel of Fig. 15 represents a large scale filamentary structure of MC1-MHD-Ra. The entire structure is self-gravity dominated and close to virialized. The filamentary structure also shows signs of fragmenting into cores - however, this can be misleading as it is only a slice plot. We analyze this more in the next section (Section 6.4), while discussing the morphology of structures. The velocity flow around the structure shows no overall larger scale flow, but rather low density gas falling onto the filament.

In contrast, the other self-gravity dominated structure on the right hand panel of Fig. 15 belongs to the shock dominated right region of MC1-MHD (MC1-MHD-Rc). It represents shock compressed gas that became dense enough to become self-gravitating.

##### *"Family tree" of gravitationally dominated structures*

The completely different velocity structure in the two highlighted regions of Fig. 15 suggests that the origin of gravitationally bound structures in the two cases are potentially different. We can understand the mechanism of emergence of gravitational

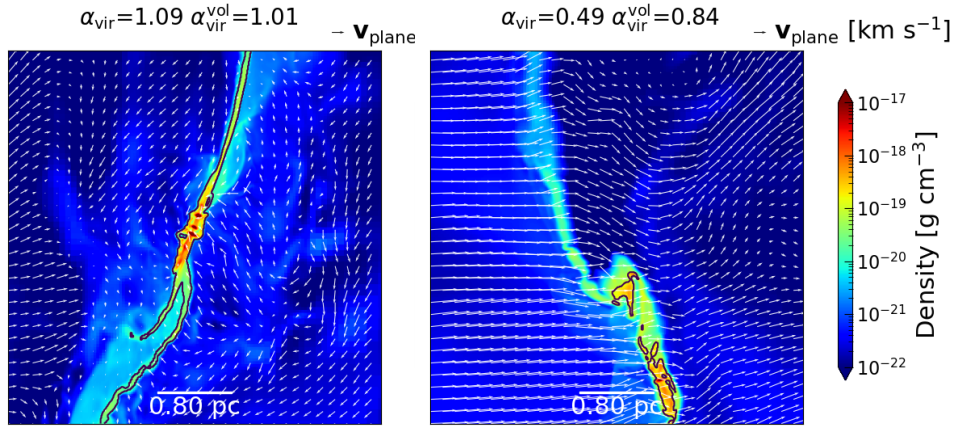


Figure 15: Two examples of structures where self-gravity dominates, overplotted as black contours over density slices. The planar component of the velocity field is plotted using arrows. The two structures belong to MC1-MHD-Ra (left) and MC1-MHD-Rc (right), respectively. In the left panel, gravity drives the nearby velocity field. The right panel corresponds to a scenario where shock compression creates dense enough structures so that gravity eventually takes over.

structures by studying the "family tree" of gravitationally bound leaf structures. This is done by tracing the dominant energy term of small scale gravity dominated structures, along with all their parents, right up to the largest scale ancestor.

This is shown in Fig. 16. The x-axis here is the size  $R$ , and the y-axis represents the density threshold. The small scale leaf structures we start with are to the left-most. From left to right, we trace the energetic behaviour of the parent structures, all the way to the largest structure of the corresponding deep-zoom regions. The dotted lines joining the structures represent the hierarchy of the dendrogram tree (i.e. a smaller scale structure is the child of the larger structure that it is joined to towards its right). For MC1-MHD-Ra (Fig. 16, left panel) the entire family of structures, all the way up to the largest scale structures, is dominated by gravity. We can therefore say that the entire region has become gravity dominated already, and at least up to parsec scales, we do not trace the larger scale flows that created the filamentary structures anymore.

In contrast, for MC1-MHD-Rc (Fig. 16, right panel), we find that the small scale gravitationally dominated leaf structures are connected to larger structures confined by ram pressure. The shock compression therefore helps create these denser and potentially star forming structures.

#### *Two ways to form small scale gravitationally bound structures*

What Fig. 16 illustrates is a rather remarkable result, so let us ponder its implications for a moment longer. The two panels of Fig. 16 illustrate two ways of forming small scale gravitational structures: by a traditional gravitational fragmentation (Fig. 16, left panel), and by shock compression leading to self-gravitating structures (Fig. 16, right panel). While discussing the morphologies in Section 6.4, we will show that the family tree of the gravity dominated structures also show a transition of filament fragmenting into cores.

Finally, apart from self-gravitating structures, we see that parts of the branches in Fig. 16 are also dominated by  $E_{PE}^{ext}$ , the gravity of the surrounding medium.

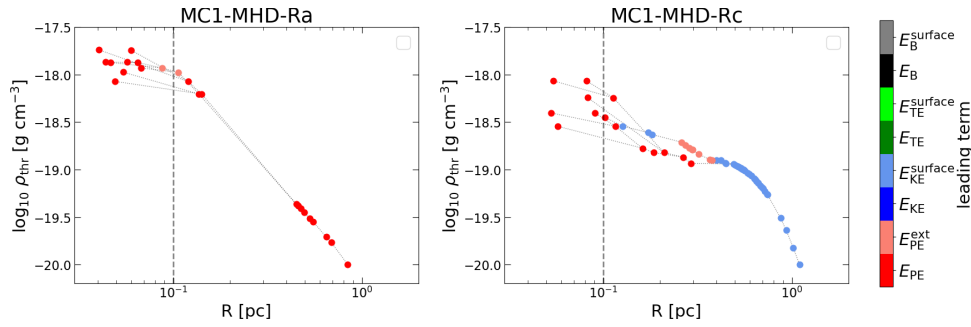


Figure 16:  $\rho_{\text{thr}}$  vs size  $R$  for only the gravity dominated leaf structures and their parent structures for MC1-MHD-Ra (left) and MC1-MHD-Rc (right) at  $t_{\text{deep}} = 0.8$  Myr. The lines join the leaf through the largest structures and represent the family tree of the gravity dominated leaf structures. MC1-MHD-Ra is gravity dominated upto the largest scale sub-structures, while the small scale self-gravity dominated structures in MC1-MHD-Rc are part of larger scale ram pressure dominated structures.

This relates to positioning of nearby dense structures which can deform the local gravitational field and exert significant influence on the structures. A couple of such examples are shown in Fig. 17 - from MC1-MHD-Ra (left) and MC1-MHD-Rd (right), respectively.

Fig. 17, left panel shows a typical scenario of tidal effects. The dense core of the filamentary structure of the left filament of MC1-MHD has dense structures nearby, and this results in structures in experiencing tidal forces. This is also reflected in the virial ratio of the structure - while  $\alpha_{\text{vir}}^{\text{vol}}$  suggests that the structure is completely bound, including the tidal effects, we see that  $\alpha_{\text{vir}}$  is, in fact, greater than 1.

The structure in Fig. 17, right panel, experiences something similar. The region MC1-MHD-Rd is located just below the hub-like densest part of the right filamentary region of MC1-MHD (see Fig. 9, left panel). It therefore experiences a dispersive pull from mass of gas just above its upper boundary.

### 6.3.5

#### VIRIAL BALANCE

So far we have discussed the different virial terms separately, and we have pointed out some examples of structures dominated by various energetic components. Let us now attempt to put all the terms together and systematically look at the virial balance.

From the analysis so far, we see a stark contrast between the left region of MC1-MHD, which is more gravity dominated, and the right region, which is more shock compressed. For the full virial analysis, therefore, we split the structures into three groups: MC1-MHD-Ra,b (left region of MC1-MHD), MC1-MHD-Rc,d,e (right region of MC1-MHD), and all regions of MC2-MHD. The three regions can be seen in Fig. 18, left, right, and bottom panel, respectively.

The x-axes in all panels of Fig. 18 plot the logarithm of the absolute value of  $\alpha_{\text{vir}}$ , while the y-axis plots  $W + \Theta_{\text{VT}}$ , the total sum of the right hand side of the virial equation of 2.37. We remind the reader that the term  $\Theta_{\text{VT}}$  includes both the volume and surface terms of magnetic, thermal, and kinetic energy. Let us now attempt to understand the positioning of the four quadrants. For an overview on the implication of the different quadrants, please see the explanatory Fig. 8.

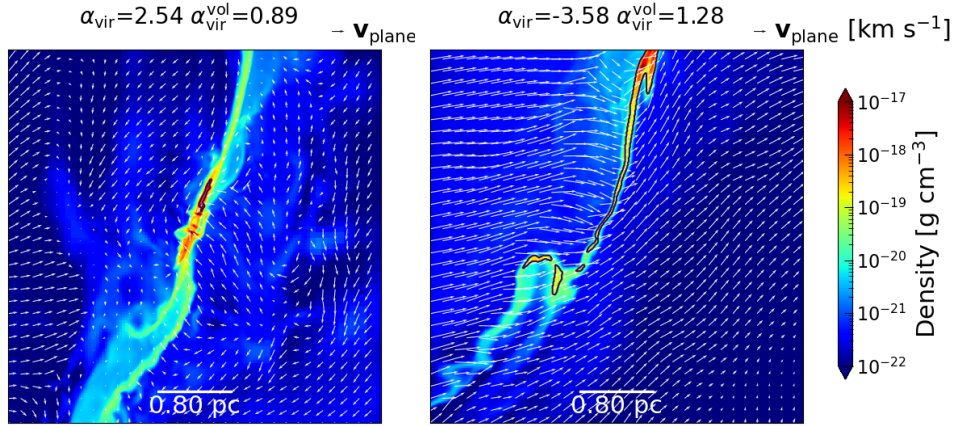


Figure 17: Two examples of structures where external gravity attempts to disperse the structure, overplotted as black contours over density slices. The planar component of the velocity field is plotted using arrows. The two structures belong to MC1-MHD-Ra (left) and MC1-MHD-Rd (right), respectively. The left panel corresponds to our typical understanding of tidal forces, where the structure is being stretched due to presence of nearby dense structures. In the right panel, the strong velocity field helps confine the structure, despite tidal effects.

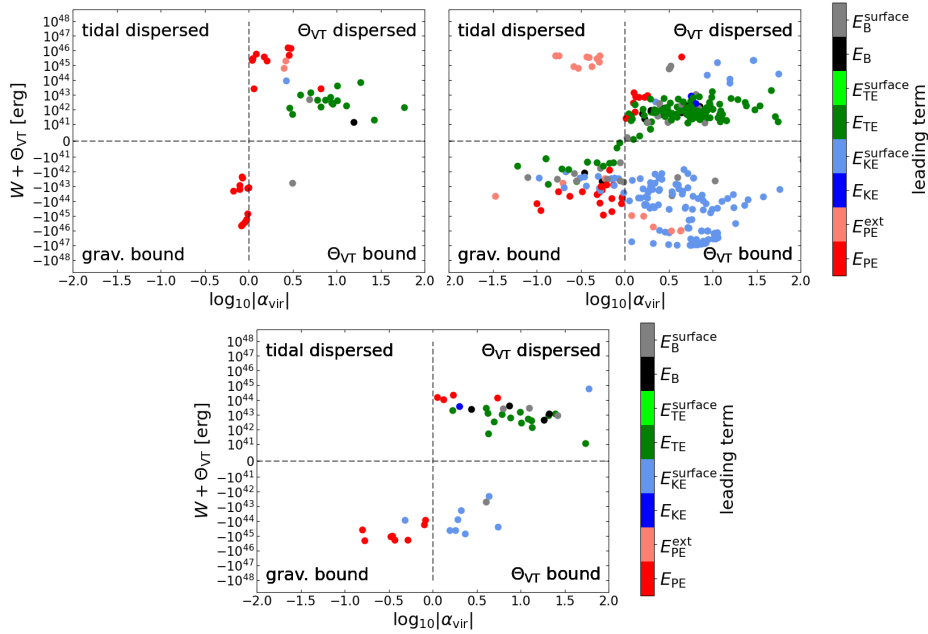


Figure 18: The absolute virial ratio plotted against the overall energetic balance for MC1-MHD left region (top left), MC1-MHD right region (top right) and MC2-MHD (bottom) at  $t_{\text{deep}} = 0.8$  Myr. The right filament of MC1-MHD is mostly compressed by ram pressure. In contrast, the left filament is more gravity dominated.



For the left region of MC1-MHD (Fig. 18, top left panel), almost all bound structures ( $W + \Theta_{VT} < 0$ ) are dominated by self-gravity. A few of the unbound structures are still gravity dominated, implying that they are kept from collapsing by the combined effect of the turbulent, thermal, and magnetic pressure. The thermally dominated structures are all unbound and likely represent momentary density enhancements. We remind the reader that the dynamics captured in this method is the instantaneous virial balance and therefore suffers from effects of instantaneous fluctuations in the gas flow.

In contrast, for the right region of MC1-MHD (Fig. 18, top right panel), we see a large number of structures instantaneously compressed and bound by the surface term of the kinetic energy (lower right quadrant,  $W + \Theta_{VT} < 0$  and  $|\alpha_{vir}| > 1$ ). A few of the structures are compressed enough to become self-gravity dominated and collapsing, examples of which we have seen before in Fig. 16. Further, we also find some structures where the tidal force is strong enough to attempt to disperse the structures (upper left quadrant). The thermal structures are again mostly unbound (with a few notable exceptions) and likely realizations of turbulent compressions, where the regular velocity of the shock has decayed into thermal energy.

In contrast to the mostly gravity dominated left region and mostly ram pressure dominated right region of MC1-MHD, the MC2-MHD regions show a mixture of both (Fig. 18, bottom panel). The number of structures are fewer in number, and the regions are still somewhat behind in evolutionary stage compared to MC1-MHD. Nonetheless, an overall similar trend is seen. Thermal structures are exclusively unbound, while most self-gravity dominated structures are bound and collapsing.

Overall, the virial analysis therefore shows us regions dominated by different forces. Each region contains both structures which are bound and collapsing, as well as structures which represent density fluctuations and will likely disperse. Strong disparity is seen between the two prominent structures of MC1-MHD, with one showing more quiescent gravitational collapse, while the other representing structures becoming gravitationally bound through shock compressions.

It is to be noted that while we have grouped the structures according to their most dominant energy term, it is likely that most of the structures are not overwhelmingly dominated by a single term, but rather their energetic evolution follows from the delicate balance of different virial terms.

## 6.4

### MORPHOLOGY OF STRUCTURES

The above discussion concludes our analysis of the virial terms. Let us now classify the dendrogram structures according to their morphologies, and attempt to relate it to their energetics. Similar to in paper II, we here classify the morphologies of our structures into sheets (including curved sheets), filaments, and spheroids using their moment of inertia tensor (see Section 2.4.1 for details).

The number of different types of morphologies found for the different analyzed regions is summarized in Table 6.5. Let us firstly note that there are no curved sheets detected by the algorithm at all. This is in keeping with the conclusions of paper II, where we saw curved sheets only on the scales of tens of parsecs, where our large scale structures traced the shells of the supernova blown bubbles.

From Table 6.5, we further find that sheets and filaments make up most of the structures, with filaments slightly more numerous compared to sheets. This is also

Region	Total	sheet	sheet_c	filament	spheroidal
MC1-MHD-Ra	39	16	0	19	4
MC1-MHD-Rb	5	2	0	3	0
MC1-MHD-Rc	175	93	0	76	6
MC1-MHD-Rd	17	2	0	15	0
MC1-MHD-Re	9	0	0	9	0
MC2-MHD-Ra	10	6	0	4	0
MC2-MHD-Rb	3	0	0	3	0
MC2-MHD-Rc	17	12	0	5	0
MC2-MHD-Rd	11	2	0	8	1
MC2-MHD-Re	6	0	0	6	0
Total	292	133	0	148	11

Table 6.5: The number of dendrogram structures sorted by their structure type for each analyzed region, at  $t_{\text{deep}} = 0.8$  Myr.

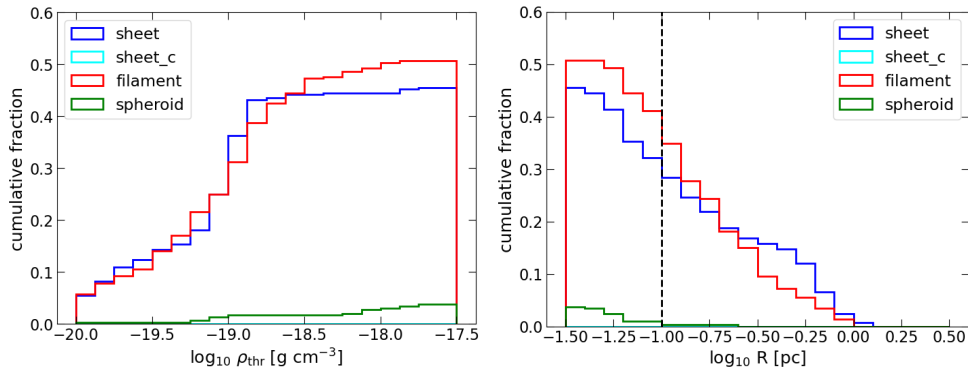


Figure 19: The cumulative distribution of the types of structures, plotted against  $\rho_{\text{thr}}$  (left), and against  $R$  (right) for all dendrogram structures at  $t_{\text{deep}} = 0.8$  Myr. Filaments are slightly more common than sheets, while cores appear only at a length scale of  $\sim 0.1$  pc or smaller.

consistent with the SILCC-Zoom results, where we found mostly elongated structures, with sheets slightly more numerous compared to filaments.

We can see the distribution of the different types of structures across density ranges in the left panel of Fig. 19, which shows the cumulative distribution of the fraction of structures against  $\rho_{\text{thr}}$ . We see that up to densities of  $\log_{10} \rho_{\text{thr}} \approx -18.5$ , sheets and filaments are more or less equally common. Above these densities, filaments and spheroidal structures become more numerous. This suggests that our denser structures are more likely to be filamentary or core-like structures, rather than sheets. From paper II, we have seen that our clouds are mostly embedded inside sheet-like envelopes. It is therefore not surprising that many of the less dense structures we trace are sheet-like.

It is interesting to see how the different morphologies are distributed across length scales. This can be seen in the right panel of Fig. 19, which shows the cumulative distribution of the fraction of structures against size  $R$ . The vertical dashed line represents  $R = 0.1$  pc.

Firstly, we note that at smaller scales, filaments tend to become more numerous compared to sheets. The difference, however, is not very dramatic. The most interesting feature of Fig. 19 is rather the emergence of spheroidal structures at length scales of  $\sim 0.1$  pc. Let us have a closer look at this 0.1 parsec length scale by

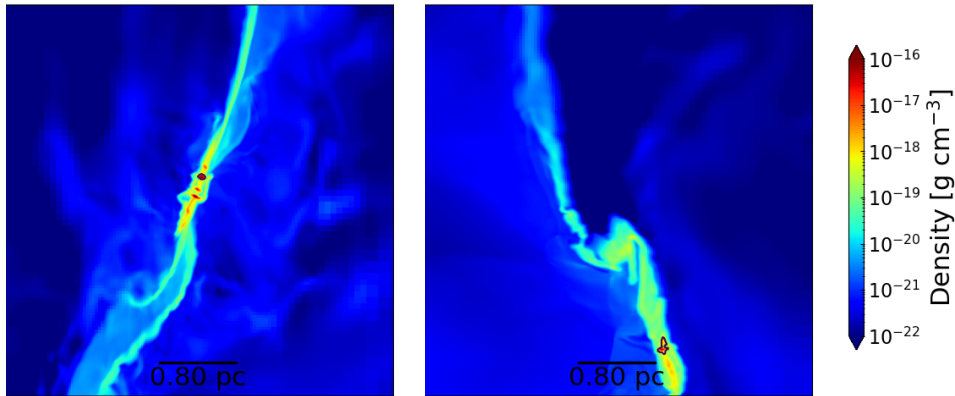


Figure 20: Two examples of small scale core-like structures, plotted as black contours over density slices from the region MC1-MHD-Ra (left) and MC1-MHD-Rc (right) at  $t_{\text{deep}} = 0.8$  Myr. In both cases the cores seem to be a part of a filamentary structure. For the left figure, a series of distinct cores can be seen lined up next to each other.

studying the core-like structures in more detail.

#### 6.4.1

##### CORES

In the classical scenario of star formation, molecular clouds consist of filaments (e.g. [Arzoumanian et al., 2011](#)). Star formation occurs in spheroidal cores inside the filaments ([André et al., 2010](#)). It has been highly debated whether filaments in molecular clouds have a typical width or not (e.g. [Panopoulou et al., 2017](#)). If filaments indeed have a typical width of around  $\sim 0.1$  pc, this implies that the cores inside them, that are potential sites of star formation, also have a typical size-scale of  $\sim 0.1$  pc. In this context, the appearance of spheroidal structures at roughly  $\sim 0.1$  pc is interesting.

A couple of examples of such core-like structures can be seen in Fig. 20. The selected core-like structures are plotted as black contour lines over a density slice map, and belong to the regions MC1-MHD-Ra (left) and MC1-MHD-Rc (right), respectively.

For MC1-MHD-Ra, it seems from the projection that even apart from the structure marked, there are a few cores lined up neatly inside a filament. For MC1-MHD-Rc, we see a similar picture. Apart from the selected core-like structure, we see nearby density enhancements with a hint of fragmentation. To investigate whether this is somehow a projection effect, we can simply use our "family tree" technique, and trace the parent structures.

In Fig. 21, we plot the different spheroidal structures, with all their parent structures for MC1-MHD-Ra (left) and MC1-MHD-Rc (right), respectively. The different types of structures are represented by different symbols: square (sheet), diamond (filament) and circle (spheroid). The discrete color bar represents the dominant energy term as in plots from the previous Section 6.3. In both cases, we find that the denser, gravitationally dominated cores are embedded inside parent filaments. In case of MC1-MHD-Ra, we see gravity dominating cores and filaments all the way up to our largest scales. For MC1-MHD-Rc, we find instances of  $E_{\text{TE}}$  and  $E_{\text{B}}^{\text{surface}}$  dominant cores, although they seem to not necessarily be embedded inside fila-

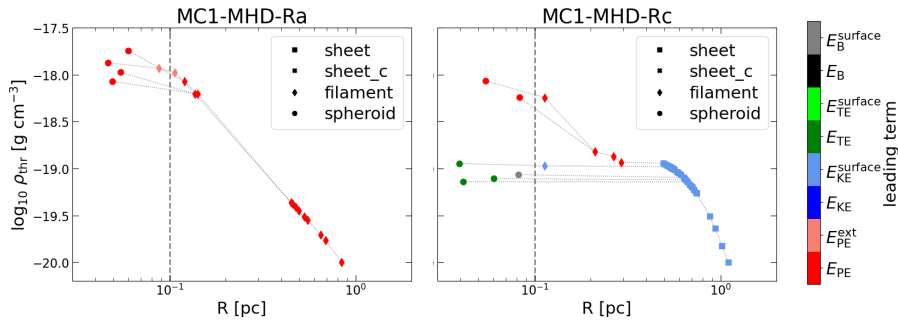


Figure 21:  $\rho_{\text{thr}}$  vs  $R$  plot for spheroidal leaf structures and all their parents for MC1-MHD-Ra (left) and MC1-MHD-Rc (right) at  $t_{\text{deep}} = 0.8$  Myr. The different structure types are marked with different symbols. The dotted lines joining the points trace the family tree of the structures, from left to right. The parents of all gravitationally dominated spheroidal structures are identified as filaments.

ments. All the core-like structures in MC1-MHD-Rc are eventually connected to kinetically dominated larger scale sheets.

#### *Filament to core transition?*

We therefore indeed see a filament to core transition for the gravity dominated structures at around  $\sim 0.1$  pc. However, the transition is not a "clean" transition, in the sense that relatively less dense, non-gravity dominated core-like sub-structures seem to be embedded inside both filaments and sheets. The potential observability of such less dense core-like structures is also a further question. Finally, we must note that we have here very small number statistics and must exercise caution regarding conclusions. It would be relevant to see if also in future simulations, we see the gravitationally dominant dense cores to be embedded exclusively inside filaments.

#### *Accretion properties*

It is also interesting to note the nature of accretion for the different core-like structures. Are they all growing in mass? Are they accreting homogeneously, or through filamentary channels? How well can theoretical models of gravitational accretion, such as Bondi-Hoyle accretion (Hoyle & Lyttleton, 1941; Bondi, 1952), explain their accretion rate? This is relevant in the discussion of how cores form and grow in mass (see Section 1.3.2).

We can estimate the instantaneous mass accretion rate  $\dot{M}$  of a given structures as the mass influx through the surface of the structure.

$$\dot{M} = - \oint_S \rho(\mathbf{v} - \mathbf{v}_0) \cdot d\mathbf{S}, \quad (6.1)$$

where  $\mathbf{v}_0$  is the center of mass velocity of the structure and the negative sign ensures that  $\dot{M} > 0$  when mass is inflowing. For ease of computation, we convert this to a volume integral using the Gauss' divergence theorem,

$$\dot{M} = - \int_V \nabla \cdot \rho(\mathbf{v} - \mathbf{v}_0) dV. \quad (6.2)$$

All the core-like structures identified in the simulations accrete mass ( $\dot{M} > 0$ ). The

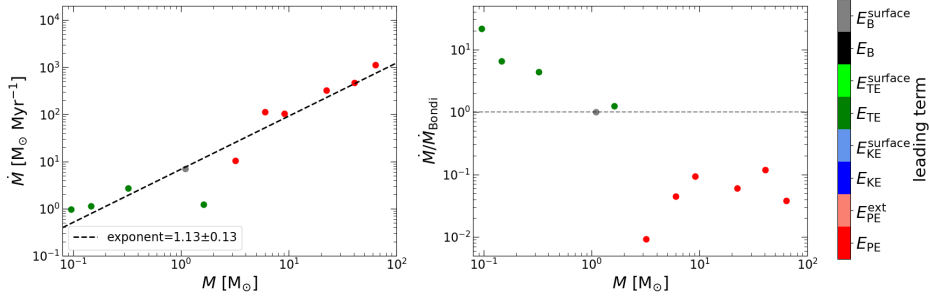


Figure 22: **Left:**  $\dot{M}$  against  $M$ , plotted for all core-like structures. They follow a power law relation similar to  $\dot{M} \propto M^{1.13 \pm 0.13}$ , considerably shallower than  $\dot{M} \propto M^2$  expected from Bondi accretion for a constant ambient medium density. **Right:** Ratio of  $\dot{M}$  to Bondi accretion rate  $\dot{M}_{\text{Bondi}}$  plotted against mass  $M$  for all core-like structures. The gravitationally dominating cores accrete considerably slower, while the core-like structures dominated by other energies accrete faster.

mass accretion rate for the different core-like structures can be seen in Fig. 22, left panel, which plots the mass accretion rate  $\dot{M}$  against the mass of different spheroids. The black dashed line plots the best fit power law, obtained by using a linear least squares fit on the logarithm of the data. The power law fit is given by:

$$\dot{M} \propto M^{1.13 \pm 0.13}. \quad (6.3)$$

It is of interest to compare the accretion rate to accretion such as Bondi-Hoyle accretion. This estimates the accretion rate for spherical accretion in a uniform density ambient medium and is given as follows:

$$\dot{M}_{\text{Bondi}} = \frac{\pi \rho_{\text{amb}} G^2 M^2}{c_{s,\text{amb}}^3}, \quad (6.4)$$

where  $\rho_{\text{amb}}$  and  $c_{s,\text{amb}}$  are the density and sound speed of the ambient medium, respectively. For a constant ambient medium density, we expect  $\dot{M} \propto M^2$  from Eq. 6.4. Our scaling seems to be considerably shallower. However, from Fig. 21, we know that our structures sit in considerably different ambient densities. We therefore estimate the Bondi accretion rate for our different core-like structures by calculating their ambient medium density and sound speed. We assume  $\rho_{\text{thr}} \approx \rho_{\text{amb}}$  and estimate the sound speed of the ambient medium as follows:

$$c_{s,\text{amb}} = \sqrt{\frac{P_{\text{avg}}}{\rho_{\text{thr}}}}, \quad (6.5)$$

where  $P_{\text{avg}}$  is the average thermal pressure of the structure and we have assumed pressure equilibrium between the structure and the surrounding. Note that the sound speed is calculated using an isothermal equation of state.

The ratio of  $\dot{M}$  over  $\dot{M}_{\text{Bondi}}$ , representing the comparison of the observed accretion rate to that of Bondi accretion, is plotted against the mass of the core-like structures in Fig. 22, right panel. The horizontal dotted line here represents a value of one, where  $\dot{M} = \dot{M}_{\text{Bondi}}$ .

We can see that all the gravity dominated core-like structures accrete below the

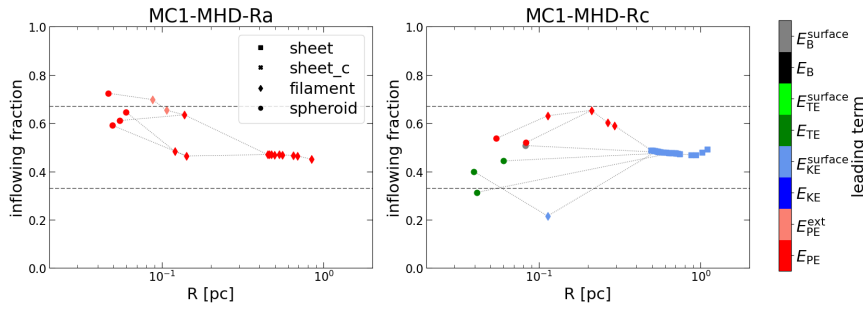


Figure 23: Fraction of surface cells with inflowing mass as defined in Eq. 6.7, against the size for all spheroidal structures and their parents for MC1-MHD-Ra (left) and MC1-MHD-Rc (right). The connecting dotted lines represent the family tree of the structures. The two horizontal dashed lines represent values of  $1/3$  and  $2/3$ .

Bondi limit, by at least an order of magnitude. In contrast, all the non-gravity dominated core-like structures lie typically above the Bondi line, with a couple lying almost on top.

Bondi accretion is expected for a spherical structure accreting in a quiescent ambient density medium. The departures from Bondi-like accretion therefore represent the importance the different dynamical forces other than gravity have. The non-gravity dominated spheroids likely lie at converging points in the flow, and therefore are able to accrete at a much higher rate. We further show in the next section that their accretion is also highly anisotropic.

#### *Homogeneous vs inhomogeneous accretion*

The discussion above clearly illustrates that the accretion of the core-like simulations do not conform to spherical accretion. It is, however, nonetheless interesting to note the degree of departure from homogeneity in terms of accretion. For homogeneous accretion, we expect all the cells at the surface of the structure to have inflowing velocity, i.e.

$$(\mathbf{v} - \mathbf{v}_0) \cdot d\mathbf{S} < 0 \quad (6.6)$$

at each point on the surface  $S$ . We compute therefore the fraction of cells with inflowing velocities as follows:

$$\text{inflowing fraction} = \frac{\text{surface cells where } (\mathbf{v} - \mathbf{v}_0) \cdot d\mathbf{S} < 0}{\text{all surface cells}}. \quad (6.7)$$

For completely homogeneous accretion, this value should be equal to one. A smaller value represents that the structures accrete mass through narrow channels, likely filamentary flows that feed the structures. We can see the behaviour of this fraction for all the core-like structures, as well as their parents, in Fig. 23. The panel on the left plots the inflowing fraction for the family tree of the core-like structures for MC1-MHD-Ra, while the right panel shows the same for MC1-MHD-Rc. As in previous family tree plots, the hierarchy of the structures is shown by connected lines. The two horizontal dashed lines plot an inflowing fraction value of  $1/3$  and  $2/3$ , respectively.

For both MC1-MHD-Ra and MC1-MHD-Rc, we see that the larger scale structures have an inflowing fraction of roughly 50%. For MC1-MHD-Ra, this fraction grows progressively as we go to smaller scales, and is close to  $\sim 2/3$  for the spher-

oidal core-like structures. We therefore here see a trend of transition towards more homogeneous accretion.

Such a trend is absent for the spheroidal structures of MC1-MHD-Rc. The non-gravity dominated core-like structures have an inflowing fraction of 50% or less, suggesting that they accrete inhomogeneously. Interestingly, even the gravity dominated structures in this case show a similar trend. This is likely related to the fact that the larger structure here is a shock layer, and therefore retains strong anisotropy in terms of morphology and mass flow, even for the densest structures.

While none of the regions show close to idealized homogeneous accretion, we can see here that the two regions of MC1-MHD again have markedly different behaviours, the smaller gravity bound structures for the left region of MC1-MHD tend to become progressively more homogeneously accreting, while this is absent for the right region.

The nature and rate of mass accretion has consequences for discussions related to how cores grow more massive (see Section 1.3.2). Classical theories of competitive accretion often rely on Bondi-like spherical accretion (Krumholz, 2015). Padoan et al. (2020) proposes that inertial flows following filamentary channels feed the mass onto massive cores. While the small number statistics and lack of time evolution of the accretion rate here prevents us from drawing definitive conclusions, the positioning of all gravitationally bound cores inside filaments (Fig. 21), the much shallower accretion rate compared to Bondi accretion (Fig. 22), and the signatures of inhomogeneous accretion (Fig. 23) suggest that our primary findings are more indicative of turbulent flows through filamentary channels. However, the fact that the small-scale gravitationally bound cores in MC1-MHD-Ra become progressively more homogeneously accreting compared to their parent structures perhaps suggests that for MC1-MHD-Ra, a mixture of both methods could be at play. The distinction of the two possibilities can be investigated further with more core-like structures in future simulations.

#### 6.4.2

##### FILAMENTS

The discussion above concludes our analysis on the core-like structures forming in the SILCC deep-zoom simulations. Despite the relatively small number statistics (eleven core-like structures in total, of which six are dominated by self-gravity), we were able to find a number of interesting results regarding the scale dependence of their morphology, and their accretion properties.

The number of filaments, in contrast to cores, is far higher. Indeed, we see an abundance of filamentary structures in both SILCC-Zoom and SILCC deep-zoom results. Most such structures do not seem to host embedded cores. In this section, we investigate the properties related to fragmentation and accretion of the filaments.

##### *Measure of length and radius*

So far, while denoting the size of structures, we have used the cubic root of the total volume. Structures identified as filaments can often be long and narrow, and therefore we must find a better measurement of the length and radius.

For this purpose, we use the axes lengths of our moment of inertia fit ellipsoid used to identify the structures as filaments in the first place (see Section 2.4.1 for details).

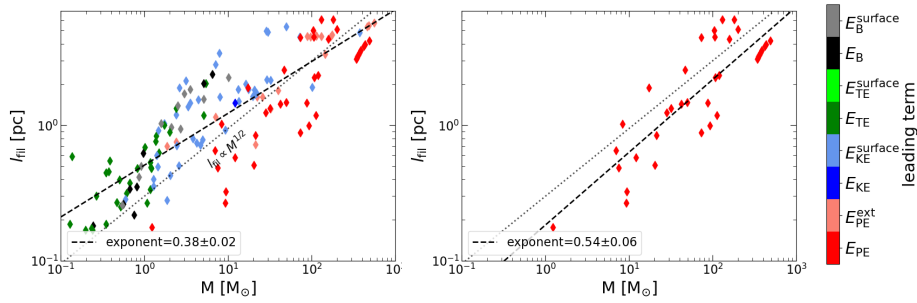


Figure 24: Mass-length relation for all (left) and only gravity dominated (right) deep zoom filaments at  $t_{\text{deep}} = 0.8$  Myr. The dotted line represents  $l_{\text{fil}} \propto M^{1/2}$ . The dashed line represents the best fit in each case.

From the fitted ellipsoid, we have the length of the three semi-axes to be  $a$ ,  $b$  and  $c$ , with  $a \geq b \geq c$ . From this consideration, we define the length  $l_{\text{fil}}$  and radius  $r_{\text{fil}}$  of the filament as follows:

$$l_{\text{fil}} = 2a, \quad (6.8)$$

$$r_{\text{fil}} = \sqrt{bc}. \quad (6.9)$$

As the mass of the structure (here filament) is  $M$ , this allows us to define the line mass of the filament  $\lambda_{\text{fil}}$  as

$$\lambda_{\text{fil}} = \frac{M}{l_{\text{fil}}}. \quad (6.10)$$

#### *The deep-zoom filaments compared to observations*

Filaments in observations span from large-scale hundreds of parsec giant filaments (Mattern et al., 2018) to sub-pc scale dense fibres (Hacar et al., 2018). It is interesting to note how the masses, lengths, line masses and accretion rates of our sub-pc and parsec scale SILCC deep-zoom filaments compare to that of observations. We note, however, that there are important differences in how filament properties are determined in observations compared to how we calculate them here.

**Mass-length relation:** The mass-length relation of filaments is of great importance in determining how filaments fragment. Consider a parent filament of mass  $M$  and length  $l_{\text{fil}}$ . If the filament fragments longitudinally, as is expected from simple isothermal filaments that become gravitationally unstable (e.g. Ostriker, 1964), then the line masses of the filament fragments remain the same as the parent filament, and  $l_{\text{fil}} \propto M$  should be observed.

In practice, this is not seen. Observational filaments tend to follow a relation  $l_{\text{fil}} \propto M^{1/2}$  (e.g. Hacar et al., 2022). We present the relation between the length and mass of all deep-zoom filaments in the left panel of Fig. 24. The dotted line here represents  $l_{\text{fil}} \propto M^{1/2}$ , while the dashed line represents the best-fit, using a linear least squares method on the logarithm of the data. We can see that the points follow the general trend of  $l_{\text{fil}} \propto M^{1/2}$  with considerable scatter, resulting in the power law becoming overall shallower (an exponent of 0.38).

However, this is partly due to the different types of dynamically dominant filaments that we find. Hacar et al. (2022) argue that different observational filaments follow slightly different power law lines in the mass-length relation, corresponding



to their different mass accretion rates. As such, filaments that accrete at a higher rate should populate more the lower end of the mass-length plane. We will show later on (in Fig. 26) that the gravity dominated filaments, which have a tendency to be situated more in the lower part of Fig. 24, indeed accrete at a faster rate compared to, for example, the thermally dominated filaments. If we fit only the self-gravitating filaments in the mass-length plane (Fig. 24, right panel), we find  $l_{\text{fil}} \propto M^{0.54 \pm 0.06}$ , consistent with the power law exponent of 0.5 within error limits.

**Line mass of filaments:** As filaments populate a large range of both masses and length scales, they are often related to each other by their line masses. For a self-gravitating filament, fragmentation occurs when the filament's line mass exceeds the thermal critical line mass  $\lambda_{\text{crit}}$ , given by

$$\lambda_{\text{crit}} = \frac{2c_s^2}{G}. \quad (6.11)$$

We estimate the sound speed  $c_s$  of a given filamentary structure as:

$$c_s = \sqrt{\frac{P_{\text{avg}}}{\rho_{\text{avg}}}}. \quad (6.12)$$

We remind the reader that  $P_{\text{avg}}$  and  $\rho_{\text{avg}}$  are the volume averaged thermal pressure and density, respectively.

The line mass  $\lambda_{\text{fil}}$ , and its ratio to the critical line mass for different filamentary structures are plotted in Fig. 25 as a function of the filament radius  $r_{\text{fil}}$ , in the top left and top right panel, respectively. They essentially differ due to the temperature difference of the various structures, and we therefore plot the average temperature of the sub-structures in Fig. 25, bottom panel, to guide the eye.

From the top left and top right panel of Fig. 25, we firstly note that the simulated filaments do not have a typical 0.1 pc width. While the median value of  $r_{\text{fil}}$  is around 0.1 pc, there is a scatter of more than an order of magnitude. Secondly, we see that the gravity dominated filaments are typically with the highest line mass, consistent with the fact that they occupy more the lower end of the mass-length plot. Further, almost all the filaments above their critical line mass are gravity (both self-gravity and tidal effects) dominated. This is striking, especially given the fact that the manner in which we defined gravitationally dominant structures is independent of any consideration regarding the theory of critical line masses.

In future work, it will be relevant to compare the line mass and critical masses found here to observed filaments, as well as look at how much the estimate of line mass here is affected by projection.

**Accretion properties:** The previous analysis shows us that the gravity dominated filaments stand out when we estimate their line masses. Another question worth investigating is the rate and nature of filamentary accretion. For a filament, estimates of accretion rates are usually considered per unit length, to account for the different length scales of the various filaments. Thus, we can define the instantaneous accretion rate as

$$\dot{\lambda}_{\text{fil}} = \frac{\dot{M}}{l_{\text{fil}}}, \quad (6.13)$$

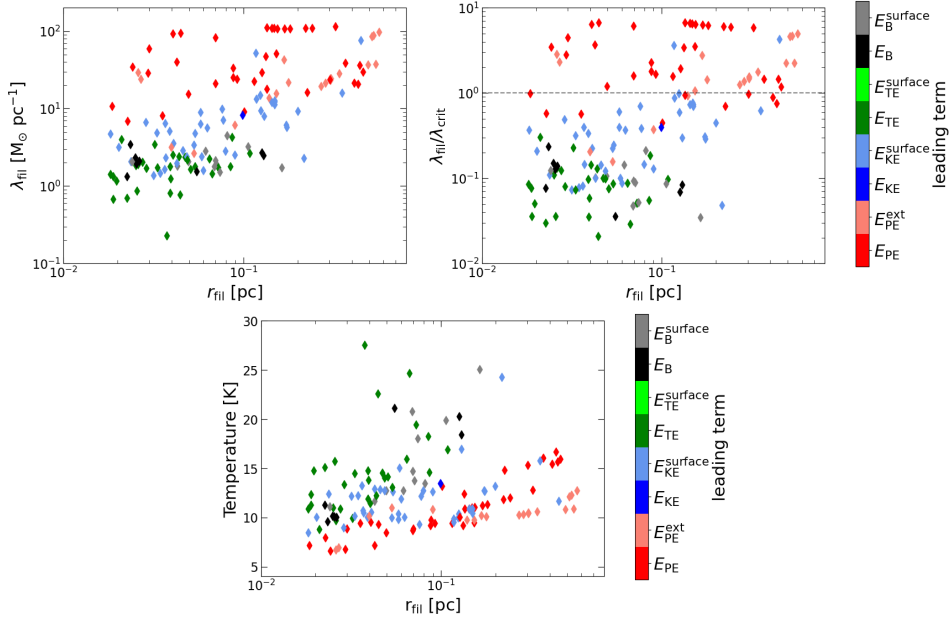


Figure 25: **Top left:** Line mass of the filamentary structures. **Top right:** Ratio of line mass to the thermal critical line mass. The horizontal line represents a value of 1 **Bottom:** Distribution of temperatures for the various filaments. All plots plotted against the filament radius  $r_{\text{fil}}$ . We see that the gravity dominated filaments have typically the lowest temperatures, the highest line masses, and consist of mostly filaments above the critical line mass line.

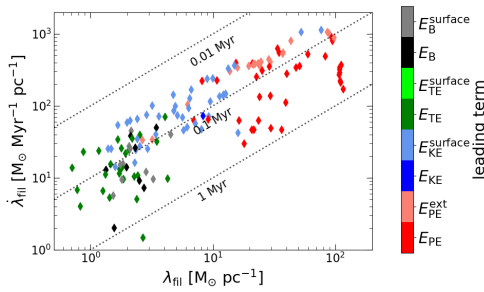


Figure 26:  $\dot{\lambda}_{\text{fil}}$  vs  $\lambda_{\text{fil}}$  for all accreting filaments ( $\dot{\lambda}_{\text{fil}} > 0$ ). The dotted lines represent different constant  $\tau_{\text{acc}}$ . The gravity dominated filaments accrete at a higher rate, and the accretion timescale for all the structures is around  $\tau_{\text{acc}} \sim 0.1$  Myr, with considerable scatter.

([Rivera-Ingraham et al., 2021](#)).

The behaviour of  $\dot{\lambda}_{\text{fil}}$  against  $\lambda_{\text{fil}}$  for our filamentary structures can be seen in Fig. 26. Here we have chosen only filaments that are accreting ( $\dot{\lambda}_{\text{fil}} > 0$ ), which are virtually all the filaments (146 out of 148). The dotted lines represent lines of constant  $\tau_{\text{acc}}$  at (from above to below) 0.01, 0.1 and 1 Myr, respectively.

Firstly, we note that  $\dot{\lambda}_{\text{fil}}$  varies in our case from a few  $M_{\odot} \text{ Myr}^{-1} \text{ pc}^{-1}$  to around a thousand  $M_{\odot} \text{ Myr}^{-1} \text{ pc}^{-1}$ . The estimated accretion rates for the fastest accreting

where we estimate  $\dot{M}$  similar to the core-like structures, from Eq. 6.1. In observations, estimates of  $\dot{\lambda}_{\text{fil}}$  are typically between few tens to few hundreds  $M_{\odot} \text{ Myr}^{-1} \text{ pc}^{-1}$  ([Kirk et al., 2013](#); [Palmeirim et al., 2013](#); [Bonne et al., 2020](#)). Further, from the accretion rate  $\dot{\lambda}_{\text{fil}}$ , one can define an accretion timescale for the filaments as

$$\tau_{\text{acc}} = \frac{\lambda_{\text{fil}}}{\dot{\lambda}_{\text{fil}}}. \quad (6.14)$$

$\tau_{\text{acc}}$  defines the typical time over which the filaments change their properties through accretion. Estimates of  $\tau_{\text{acc}}$  in observation are around roughly a Myr ([Rivera-Ingraham et al., 2017](#); [Gong](#)

structures is slightly higher than observations. Moreover, we do indeed see that the gravity dominated filaments have typically a higher accretion rate, consistent with their position in the lower half of the mass-length plane in Fig. 24.

Overall, we find that despite some scatter, all the structures roughly follow  $\tau_{\text{acc}} \approx 0.1$  Myr. This value is lower than observed estimates of  $\sim 1$  Myr, but consistent within limits given the scatter.

#### *Nature of filamentary accretion*

Another interesting point to note, along with the rate of accretion, is in what manner accretion is taking place. Are the accretion flows occurring longitudinally along the filament, or onto them? Do the filaments accrete roughly uniformly, or more from their ends? Many observations show filaments tending to show end dominated collapse (Beuther et al., 2015; Kainulainen et al., 2016; Bhadari et al., 2020), where the mass flow is primarily through the two edges of the filaments.

To investigate this, we study the accretion profile of filaments by investigating which part of their surface they accrete most mass from. To this end, we use the following method: Firstly, we choose filaments which are overall accreting ( $\dot{M} > 0$ ). We compute then the distance from the center of mass  $\mathbf{r}_0$  of the filament to each surface cell  $\mathbf{r}_S$ . We only select cells along which the structure is accreting mass by using Eq. 6.6. Since the filaments are of different lengths, we normalize this distance using the estimated length of the filament  $l_{\text{fil}}$ . The distance measure is then given by

$$d_S = |\mathbf{r}_S - \mathbf{r}_0|/l_{\text{fil}}. \quad (6.15)$$

The distribution of  $d_S$  gives us the accretion profile of a given filament. The distribution of  $d_S$  should vary roughly between 0 and 1/2, with values higher than 1/2 resulting primarily from the inhomogeneity of the filament, such as the COM not being in the center. However, even for an ideal, straight filament, the exact range of  $d_S$  depends on the aspect ratio of the filament. We can define this aspect ratio as,

$$f_{\text{asp}} = \frac{l_{\text{fil}}}{2r_{\text{fil}}}, \quad (6.16)$$

where the factor 2 is due to the fact that we are considering the diameter of the filament for calculating the aspect ratio. The minimum and maximum values of  $d_S$  is given by

$$\min(d_S) = \frac{r_{\text{fil}}}{l_{\text{fil}}} = \frac{1}{2f_{\text{asp}}}, \quad (6.17)$$

$$\max(d_S) = \frac{\sqrt{r_{\text{fil}}^2 + l_{\text{fil}}^2/4}}{l_{\text{fil}}} = \frac{1}{2} \sqrt{1 + \frac{1}{f_{\text{asp}}^2}}, \quad (6.18)$$

which reduce to 0 and 1/2, respectively, for an infinitely thin filament ( $f_{\text{asp}} \rightarrow \infty$ ). For a uniform cylinder accreting only through its edges, then, the distribution of  $d_S$  should peak at close to 1/2. For uniform cylindrical accretion, a derivation of how the PDF of  $d_S$  would be distributed is provided in Appendix A.1.

In Fig. 27, we plot the cumulative PDFs of different accreting filaments as a function of  $d_S$ . We separate between filaments dominated by different energy terms, as they could potentially have different modes of accretion. The top row shows the PDF for gravity dominant accreting filaments of MC1-MHD-Ra (top row, left), and MC1-MHD-Rc (top row, right). The bottom row shows the PDF of filaments

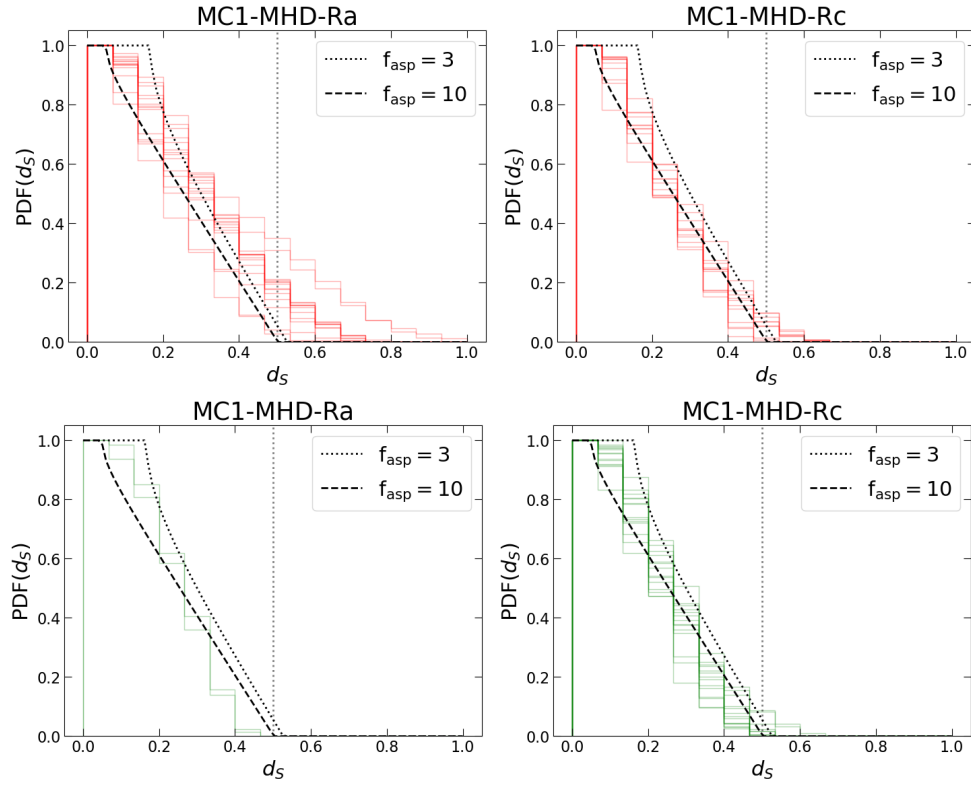


Figure 27: PDF of the distance measure  $d_S$  for different accreting filaments dominated by  $E_{PE}$  (red) and  $E_{TE}$  (green). Each solid line shows the distribution for an individual filament. The dotted and the dashed lines show expected PDFs for uniformly cylindrically accreting filaments with aspect ratios  $f_{asp} = 3$  and 10, respectively. **Top row:** Gravity dominated filaments in MC1-MHD-Ra (left) and MC1-MHD-Rc (right). **Bottom row:** Thermally dominated filaments in MC1-MHD-Ra (left) and MC1-MHD-Rc (right).  $d_S$  measures the normalized distance from the COM of a structure to an accreting surface cell (Eq. 6.15).

dominated by the thermal energy, for the same regions. In each case, the accretion profile of individual filaments are shown in solid colors (top row: gravity dominated filaments in red, bottom row: thermally dominated filaments in green). The expected distribution for filaments experiencing uniform cylindrical inflow is also shown for two aspect ratios:  $f_{\text{asp}} = 3$  (dotted lines) and  $f_{\text{asp}} = 10$  (dashed lines) (see Appendix A.1 for derivation). Note that due to the lack of angular dependence in the definition of  $d_S$ , it is not possible to distinguish azimuthal variations in the flow strength using  $d_S$  (for example, between, cylindrical and planar compressive flows, which would have similar profiles).

The PDF for each structure is weighed by the mass inflow rate  $\dot{M}$  through the cells. This ensures that we do not only count the number of accreting cells for the PDF, but rather take into account the amount of mass that flows through them.

From Fig. 27, we firstly note that even for theoretical uniformly accreting filaments (dashed and dotted lines), there is some difference depending on the aspect ratio, particularly at low  $d_S$ . This is due to the fact that the minimum value  $d_S$  can reach is given by  $1/2f_{\text{asp}}$  (Eq. 6.17).

From Fig. 27, we further see that thermally dominated structures from both MC1-MHD-Ra and MC1-MHD-Rc (bottom row), as well as self-gravity dominated structures in MC1-MHD-Rc (top row, right) follow more or less the behaviour expected from a uniformly accreting filament. This is different from how the gravity dominated filaments in MC1-MHD-Ra behave, where there is clearly higher accretion at high  $d_S$ , corresponding to longitudinal flows.

While it is difficult to conclude from this analysis whether we see signatures of end-dominated collapse for MC1-MHD-Ra, no less because of the limited  $(4 \text{ pc})^3$  sized box, it is quite clear that they do experience a more longitudinal flow. The difference in the accretion profile of the self-gravitating structures between MC1-MHD-Ra and MC-MHD-Rc likely also relate to the different mechanisms through which they evolve, through gravitational collapse and shock compression, respectively. This could potentially also explain why the gravitational core-like structures situated inside the two regions also experience significantly different nature of accretion (Fig. 23) - if the gravity dominated MC1-MHD-Ra experiences longitudinal flow as well as infall onto the filament, this could potentially explain why the cores that sit inside tend to accrete more homogeneously.

The similarity between the the thermally dominated filaments of both MC1-MHD-Ra and MC1-MHD-Rc, and the gravity dominated filaments of MC1-MHD-Rc is also worth pointing out. This likely indicates that they form in a similar way, i.e. through shocks, and in a different manner to how the gravity dominated filaments in MC1-MHD-Ra form.

Overall, we find filaments in the SILCC deep-zoom simulations which have comparable masses, lengths, line masses, and comparable or slightly higher accretion rates to observed filaments. The dynamical differences of the filaments are reflected in the aforementioned properties, as well as in the manner in which they accrete. Self-gravitating filaments formed through dynamical compression seem to retain the accretion properties of the shocked layer that created them, thus distinguishing them from filaments formed through gravtational fragmentation, which show signs of longitudinal flows. However, it is unclear to what extent the flow patterns are evolving over time. For example, do the self-gravitating filaments formed through shock compression eventually evolve to have longitudinal flows? In this regard, a time series analysis of the data could be potentially interesting.

## 6.5

## SUMMARY

This brings the results of this chapter to an end. In this chapter, we have investigated the dynamics and morphology of sub-pc scale structures in early evolutionary stages of two simulated molecular clouds, obtained through the SILCC deep-zoom simulations that have been implemented and run as part of the present thesis. We have investigated structures in the range of  $\sim 0.03$ -3 pc, which extends the results obtained in the previous chapters to smaller length scales.

- We have investigated the principal dynamics of structure formation at these scales. We find that self-gravity and shock compression are the two main methods that lead to the dense structures. The two regions of the MC1-MHD clearly show the differences in the formation scenario.

By performing a virial analysis based on the virial equation (Eq. 2.57), we have demonstrated that many structures are confined by the surface terms, and that especially the kinetic surface term, expressing ram pressure, is very important for structure formation in certain regions. We also find quite a few thermally dominated structures, which likely represent dissipated heat from converging flows.

- We have further performed a thorough investigation of the morphological behaviour of the different sub-structures. Core-like structures, although a small fraction of the total number, tend to appear at length scales of  $\sim 0.1$  pc. Elongated structures such as filaments and sheets seem to, however, be the overwhelming majority of forming structures. Compared to the SILCC-Zoom results in paper II, where the number of sheets were significantly higher compared to filaments, here the filaments slightly outnumber sheets, especially at higher densities - suggesting that in these analysis we are able to probe more the denser, filamentary part embedded inside the larger scale sheet-like clouds.

By studying the hierarchical behaviour of the spheroidal core-like structures, we have found that the gravitationally dominated cores seem to be embedded inside filaments. In case of MC1-MHD-Rc, the gravity dominated filaments are further situated inside a kinetically dominated, sheet-like shocked layer.

The accretion rate of the gravitationally dominated cores are at least an order of magnitude below what is expected from spherical accretion (Bondi, 1952). However, for MC1-MHD-Ra, we see that as we go to smaller scales, the accretion does tend towards a more homogeneous accretion, which could point to the presence of both longitudinal and transverse flows in their parent filaments (see also below). This trend of increasing homogeneity is absent for the gravity dominated core-like structures of MC1-MHD-Rc.

The abundant filamentary structures in the simulations are consistent with observational relations in terms of position in the mass-length plane, line masses, and accretion rates. A large fraction of the filaments are dominated by gravity, although there are a number of thermal and ram pressure dominated structures. Almost all of the gravity dominated filaments are super critical in terms of the thermal critical line mass. The typical accretion timescale of the filaments is around  $\sim 0.1$  Myr, with considerable scatter.

And finally, by studying the accretion profile of different gravitationally and thermally dominated filaments, we conclude that while most filaments in our simulations tend to show signatures of accretion onto the filaments, the gravity dominated filaments in MC1-MHD-Ra show in addition signs of longitudinal flow.

## SUMMARY AND CONCLUSION

## 7.1

## SUMMARY

This present work investigates various aspects of the hierarchical nature of structure formation occurring inside molecular clouds through numerical simulations. The results of papers I and II are based on the SILCC-Zoom simulations, which study formation of dense, molecular gas with a resolution of  $\sim 0.1$  pc in a supernova-driven, turbulent interstellar medium in a stratified galactic disc with the size of a few hundred parsecs. Chapter 6 is based on the SILCC deep-zoom simulations, which are a natural extension of the SILCC-Zoom simulations and investigate structure formation at sub-parsec scales.

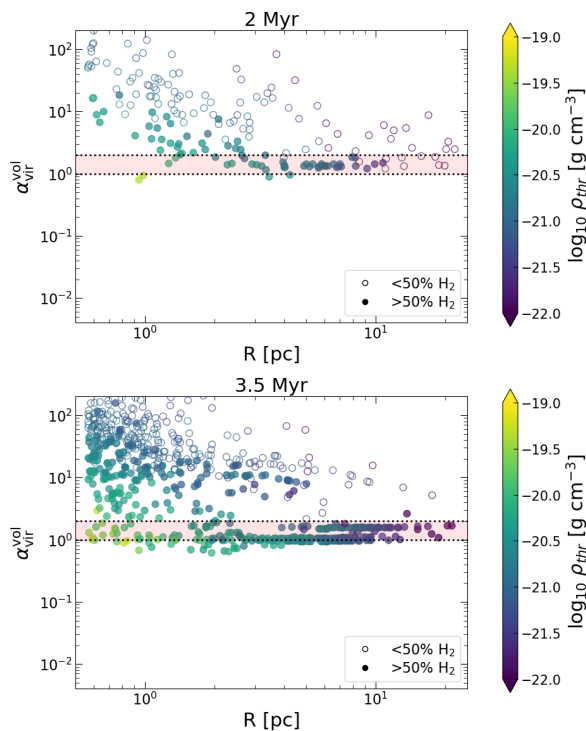


Figure 28: Two panels from Fig. 8, bottom panel, in **paper I** showing the evolution of  $\alpha_{\text{vir}}^{\text{vol}}$  (Eq. 2.58) for MHD sub-structures at  $t_{\text{evol}} = 2$  Myr (top) and 3.5 Myr (bottom). Bound structures appear over time below the  $\alpha_{\text{vir}}^{\text{vol}} = 1$  line.

$\alpha_{\text{vir}}^{\text{vol}}$  (Eq. 2.58) against the size  $R$  of the structures at two different times.

In **paper I**, we investigate two competing scenarios of structure formation in young molecular clouds, the gravo-turbulent and the global hierarchical collapse scenario (see Section 1.3.2). We identify hierarchical density structures using the technique of dendrograms and analyze their energetics using the virial theorem. Our cloud sub-structures follow a Larson-like power law between their velocity dispersion and size at earlier times, but show considerable departure as gravity becomes dynamically important. Energetically, we notice that our clouds are primarily dominated by gravity and kinetic energy. From a virial analysis, we find that gravitationally bound structures emerge over time from a largely marginally bound environment. This can be seen for the MHD clouds in Fig. 28, which shows the behaviour of the virial parameter



We further see some signatures of larger scale compressive flows, likely driven by expanding shells from the supernovae that exploded in the original SILCC simulations. The formation of bound structures over time, the emergence of gravity as a dynamically dominant force for the densest sub-structures, and the signatures of larger scale inflows driving turbulence lead us to conclude that we see a structure formation scenario consistent with the gravo-turbulent scenario of fragmentation.

We extend the traditional virial analysis by considering tidal effects due to the gas surrounding a forming sub-structure. To this end, we compare the gravitational acceleration due to self-gravity and tidal forces directly and also perform a deformation analysis based on the tidal tensor. We find that the external gravity, while making gravitational deformation more anisotropic, does not seem to be disruptive for a majority of the sub-structures. By performing a time scale analysis between the turbulent decay timescale and the tidal deformation timescale, we further find that tidal effects due to the external medium are not acting on a short enough timescale to sustain turbulent motions and therefore cannot be a primary source of kinetic energy in molecular clouds.

**Paper II** considers in detail the importance of magnetic fields in determining the morphology, fragmentation, and dynamics of molecular cloud sub-structures. To this end, we extend our dendrogram analysis by considering structures at much lower densities ( $\gtrsim 1 \text{ cm}^{-3}$ ), corresponding to the atomic envelope surrounding the dense molecular gas. We model the morphology of the hierarchical structures as ellipsoids with equal moments of inertial and classify the structures into sheets, curved sheets, filaments, and spheroids based on the aspect ratios of the ellipsoid axes.

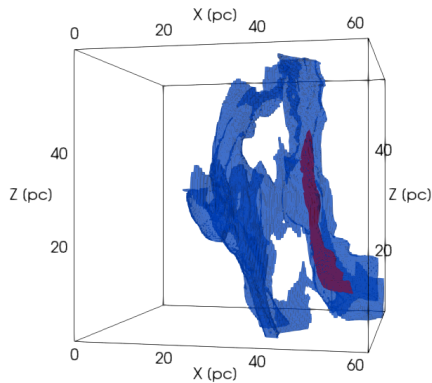


Figure 29: Panel from Fig. 4 in **paper II** showing the 3D view of the sheet-like nature of the cloud MC1-MHD (in blue) and a prominent filamentary structure inside (in red).

We find that our clouds are mostly sheet-like on large scales, likely representing the fact that they trace expanding supernova bubbles (see Fig. 29). This corroborates the findings of paper I, which found the molecular clouds experiencing larger scale compressive flows. By studying the fraction of different morphological structures, we find that the presence of magnetic fields tends to decrease the number of spheroidal structures (from  $\sim 10\%$  to  $\sim 5\%$  in presence of magnetic fields, see Fig. 5 of paper II) and somewhat enhance filament formation (from  $\sim 20\%$  to over  $30\%$ , see same figure). Dynamically, we see that the magnetic energy is comparable to, or larger than, both self-gravity and turbulence in the low density regime, but unimportant for denser, potentially star forming structures.

We study the fragmentation of the medium by considering the number and mass of leaf dendrogram structures, i.e. structures that contain no further sub-structures inside them. By studying the time evolution of the distribution of such leaf structures, we find that magnetic fields essentially seem to have a "slow down" effect

on the fragmentation of forming clouds and delay the formation of denser sub-structures.

**Chapter 6** extends the morphological and dynamical results found in papers I and II to sub-pc scales. We investigate the dynamics of hierarchically forming structures in  $\sim 0.03$ -3 pc scales by considering the full virial theorem, and find that two distinct regions: (1) quiescent, gravity dominated (2) ram pressure confined. We find small-scale gravitationally bound structures emerging both from fragmentation of self-gravitating filaments, as well as through dynamic compression.

We apply a similar morphological analysis as in paper II and find evidence of core-like structures forming inside filaments at  $\sim 0.1$  pc scales. In the dynamically compressed region, the filamentary structures seem to be embedded in a larger sheet-like shocked layer. We investigate the accretion properties of the forming core-like structures and find that they follow  $\dot{M} \propto M^{1.13}$ , a power law shallower compared to what is expected from spherical accretion ( $\dot{M} \propto M^2$ ). In addition, the accretion profiles of the cores are mostly inhomogeneous, with a hint towards homogeneity for the cores in the more quiescent, gravity dominated region. We further investigate filaments, and find that the masses, lengths, line masses and accretion rates of the sub-pc and pc scale filaments are comparable to observations. By studying the nature of mass accretion for the filaments, we infer that the accretion profiles of most filaments match gas inflow onto the filaments, with hints of longitudinal flow for the more quiescent, self-gravitating filaments in the gravity dominated region.

## 7.2

### CONCLUSION

Molecular clouds are nurseries of star formation. The dynamic state of molecular clouds has direct and significant consequences for the multi-scale collapse, fragmentation, and structure formation in the dense ISM (e.g. [Chevance et al., 2022](#)). This present work attempts to answer key questions, as highlighted in Chapter 1, related to structure formation in the early stages of a cloud's evolution.

For this thesis, we analyze existing cloud-scale SILCC-Zoom simulations, and in addition implement and run the SILCC deep-zoom simulations that allow us to probe the formation of sub-pc scale filaments and cores. We identify density enhancements in the simulations as structures using a dendrogram algorithm and study their hierarchical behaviour.

Concerning the dynamics of cloud scale sub-structures, we demonstrate that the simulated clouds are dominated by turbulence and gravity, with magnetic fields and thermal pressure playing subservient roles. Our findings suggest that the clouds inherit turbulent motions from larger scale supernova-driven flows and support the idea of the formation of dense, elongated structures by multiple compressions from supernova-driven bubbles ([Inutsuka et al., 2015](#)).

We extend this idea of molecular clouds tracing supernova shells by showing that our clouds are sheet-like on the largest scales, with filamentary networks embedded within. This supports observational claims of sheet-like envelopes around dense, filamentary structures ([Arzoumanian et al., 2018](#)). By studying the behaviour of magnetic fields in detail, we show that magnetic fields tend to "slow down" structure formation, affect the fragmentation in lower density gas, and change how cloud structures are shaped by affecting gas flows. Our results, however, also seem to in-

dicates that they are dynamically unimportant for further evolution of the dense and potentially star-forming structures.

We expand the results to sub-pc scale filaments using the novel SILCC deep-zoom simulations and find two distinct forms of how dense, small scale, gravitationally bound structures emerge - through gravitational fragmentation, as well as turbulent compression. This is of direct relevance to ongoing debates regarding how various filaments form (e.g. [Hacar et al., 2022](#)). We demonstrate the emergence of self-consistently formed spheroidal cores at  $\sim 0.1$  pc scales, starting from a simulated stratified galactic disc of a few hundred parsecs. By investigating the accretion properties of the forming filaments and cores, we in addition find that the nature of accretion reflects the dynamic state of the structures, as well as their formation history.

The self-consistent modelling of the highly dynamical, multi-scale ISM is a challenging task. In this work, we have attempted to disentangle the different forces that dominate different scales inside molecular clouds and understand the consequences using realistic ISM simulations. Overall, we find highly dynamic molecular clouds created through compressions in rarefied gas. The gas flow is affected and channeled through magnetic fields which, however, become less important at higher densities. As we probe the denser filamentary structures at sub-pc scales, different regions tend to show different behaviours - with both self-gravitating and kinetically compressed regions leading to small-scale cores. These cores feed and accrete in a mostly inhomogeneous manner from the dynamic environment, and will act as the birthplaces of eventual stars.

### 7.3 OUTLOOK

We propose that the present work can be extended in three critical, interconnected directions. In terms of simulations, they can be varied to include more detailed physics. In paper II, we investigate the effects of magnetic fields and conclude that they are dynamically mostly unimportant in the dense, star forming gas. However, magnetic field strengths vary throughout the Galaxy, and it would be interesting to note how different large-scale seed magnetic fields (in particular, stronger fields than the  $3 \mu\text{G}$  initial field used for the present work) propagate down the size-scales and influence fragmentation and structure formation.

Related to the deep-zoom simulations, a number of parameters need to be varied in order to obtain a better statistical sample and get a more robust view of structure formation at these scales. The first step of this could be to evolve the clouds further, and include the effects of stellar feedback on the forming structures. The inclusion of feedback has been extensively performed for the cloud scale SILCC-Zoom simulations, but remain absent for the newer deep-zoom runs.

In the densest structures of the SILCC deep-zoom runs, we reach densities at which non-ideal MHD effects, such as ambipolar diffusion, could start to become important. A further possibility in this direction would then be to include the modelling of such non-ideal effects, possibly in combination with stronger seed-field strengths.

The entire analysis of this thesis was done based on the method of dendrograms. While dendrograms give us an easy, model independent way to identify structures as density enhancements and allow us to capture the hierarchical nature

of the medium at a given time, they are ill-suited for tracing the time evolution of a given sub-structure. This is relevant for obtaining a more dynamic view of structure formation. The inclusion of time evolution can perhaps be done by combining the dendrogram approach with tracer particles, i.e. particles that trace the time evolution of a certain parcel of gas. The combination of the two approaches potentially could allow us the benefit of both - capture the hierarchical, as well as the time varying nature of the simulated medium.

The identification of 3D volumes of gas allows one to compute many properties of the medium simply and accurately. However, it is not immediately clear how this translates to 2D projected views an observer would find. For example, would the larger scale flows be detected in projected views? How does the viewing angle affect our conclusions for sheet-like molecular clouds? A third critical direction, in particular related to the deep-zoom simulations, could then be to potentially attempt to bridge the gap between the 3D properties and their 2D projections. This can be carried out in two rather complimentary manners: by creating synthetic emission maps of the simulations and comparing them directly to observations, and by projecting the 3D dendrogram structures into 2D and attempting to see what properties related to the dynamics of the original cloud structures remain despite projection effects.

# A

## APPENDIX

---

### A.1

#### DISTANCE MEASURE FOR UNIFORMLY ACCRETING IDEAL FILAMENTS

To understand the behaviour of the distance measure  $d_S$  (Eq. 6.15), let us consider the case of a uniform density filament with length  $l_{\text{fil}}$  and radius  $r_{\text{fil}}$ , that is accreting cylindrically and homogeneously. The aspect ratio of the filament is given by

$$f_{\text{asp}} = l_{\text{fil}}/2r_{\text{fil}},$$

where the factor 2 comes from considering the diameter for calculating the aspect ratio. If the filament is of infinite thickness, then  $f_{\text{asp}} \rightarrow \infty$ . As a consequence, the distribution of mass accretion would be uniform between  $d_S = 0$  (at the position of the center of mass) and  $d_S = 1/2$  (corresponding to the edge of the filament). The cumulative PDF in this case will be given by

$$\begin{aligned} F(d_S) &= 1 - 2d_S, & 0 < d_S < 1/2, \\ &= 0, & \text{otherwise,} \end{aligned}$$

where we compute the cumulative PDF from higher to lower values (i.e.  $F(d_S) = 1$  at  $d_S = 0$ ). However, for a filament which is not infinitely thin,  $d_S$  is not uniformly distributed. For a straight, uniform density filament, the minimum and maximum value that  $d_S$  can reach is given by

$$\begin{aligned} \min(d_S) &= \frac{r_{\text{fil}}}{l_{\text{fil}}} = \frac{1}{2f_{\text{asp}}}, \\ \max(d_S) &= \frac{\sqrt{r_{\text{fil}}^2 + l_{\text{fil}}^2/4}}{l_{\text{fil}}} = \frac{1}{2} \sqrt{1 + \frac{1}{f_{\text{asp}}^2}}, \end{aligned}$$

which is consequence of considering the nearest and furthest point of a cylinder from the center of mass. For  $f_{\text{asp}} = \infty$ , they reduce to 0 and 1/2, respectively. For uniform cylindrical converging flow onto the filament, the cumulative PDF of  $d_S$  is given by

$$\begin{aligned} F(d_S) &= 1 - \sqrt{4d_S^2 - \frac{1}{f_{\text{asp}}^2}}, & \min(d_S) < d_S < \max(d_S), \\ &= 0, & \text{otherwise,} \end{aligned}$$

which again reduces to the case for the ideal infinitely thin filament for  $f_{\text{asp}} = \infty$ . Note that the distribution here comes from considering the fact that if we consider a point on the surface of the filament with cylindrical coordinates  $(r, \theta, z)$ ,

$$d_S = \frac{\sqrt{r^2 + z^2}}{l_{\text{fil}}},$$

where  $z$  is the height of the considered point. For uniform flow onto the filament,  $z$  is uniformly distributed (i.e. if we consider rings at different heights along the filament, they all have the same inflowing mass).

$$f(z) = \begin{cases} \frac{1}{l_{\text{fil}}}, & -l_{\text{fil}}/2 < z < l_{\text{fil}}/2, \\ 0 & \text{otherwise.} \end{cases}$$

The distribution of  $d_S$  can be therefore obtained from the following transformation:

$$f(d_S) = f(z(d_S)) \left| \frac{dz(d_S)}{dd_S} \right|.$$

And the cumulative function of  $d_S$  is then obtained as

$$F(d_S) = \int_{d_S}^{\infty} f(d_S) dd_S.$$

## ABBREVIATIONS

---

<b>AMR</b>	Adaptive mesh refinement
<b>CMF</b>	Core mass function
<b>CNM</b>	Cold neutral medium
<b>COM</b>	Center of mass
<b>GHC</b>	Global hierarchical collapse
<b>GMC</b>	Giant molecular cloud
<b>GT</b>	Gravo turbulent
<b>HD</b>	Hydrodynamics
<b>HIM</b>	Hot ionized medium
<b>IMF</b>	Initial mass function
<b>ISM</b>	Interstellar medium
<b>ISRF</b>	Interstellar radiation field
<b>KS</b>	Kennicutt-Schmidt
<b>LIC</b>	Line integral convolution
<b>MC</b>	Molecular cloud
<b>MHD</b>	Magnetohydrodynamics
<b>UV</b>	Ultraviolet
<b>WIM</b>	Warm ionized medium
<b>WNM</b>	Warm neutral medium

## BIBLIOGRAPHY

---

- Agertz, O. & Kravtsov, A. V., On the Interplay between Star Formation and Feedback in Galaxy Formation Simulations. 2015, *The Astrophysical Journal*, 804, 18, aDS Bibcode: 2015ApJ...804...18A
- Ambartsumian, V. A., Stellar Associations. 1949, *Astronomicheskii Zhurnal*, 26, 3, aDS Bibcode: 1949AZh....26....3A
- André, P., Belloche, A., Motte, F., & Peretto, N., The initial conditions of star formation in the Ophiuchus main cloud: Kinematics of the protocluster condensations. 2007, *Astronomy and Astrophysics*, Volume 472, Issue 2, September III 2007, pp.519-535, 472, 519
- André, P., Di Francesco, J., Ward-Thompson, D., et al. 2014, From Filamentary Networks to Dense Cores in Molecular Clouds: Toward a New Paradigm for Star Formation (eprint: arXiv:1312.6232), conference Name: Protostars and Planets VI Pages: 27 ADS Bibcode: 2014prpl.conf...27A
- André, P., Men'shchikov, A., Bontemps, S., et al., From filamentary clouds to prestellar cores to the stellar IMF: Initial highlights from the Herschel Gould Belt Survey. 2010, *Astronomy and Astrophysics*, Volume 518, id.L102, <NUMPAGES>7</NUMPAGES> pp., 518, L102
- Arthur, S. J., Kurtz, S. E., Franco, J., & Albarrán, M. Y., The Effects of Dust on Compact and Ultracompact H II Regions. 2004, *The Astrophysical Journal*, 608, 282, aDS Bibcode: 2004ApJ...608..282A
- Arzoumanian, D., André, P., Didelon, P., et al., Characterizing interstellar filaments with Herschel in IC 5146. 2011, *Astronomy & Astrophysics*, Volume 529, id.L6, <NUMPAGES>9</NUMPAGES> pp., 529, L6
- Arzoumanian, D., André, P., Könyves, V., et al., Characterizing the properties of nearby molecular filaments observed with Herschel. 2019, *Astronomy & Astrophysics*, Volume 621, id.A42, <NUMPAGES>31</NUMPAGES> pp., 621, A42
- Arzoumanian, D., André, P., Peretto, N., & Könyves, V., Formation and evolution of interstellar filaments. Hints from velocity dispersion measurements. 2013, *Astronomy & Astrophysics*, Volume 553, id.A119, <NUMPAGES>15</NUMPAGES> pp., 553, A119
- Arzoumanian, D., Shimajiri, Y., Inutsuka, S.-i., Inoue, T., & Tachihara, K., Molecular filament formation and filament-cloud interaction: Hints from Nobeyama 45 m telescope observations. 2018, *Publications of the Astronomical Society of Japan*, 70, 96, aDS Bibcode: 2018PASJ...70...96A
- Atkins, P. & Friedman, R. 2010, *Molecular Quantum Mechanics - Peter W. Atkins, Ronald S. Friedman - Oxford University Press*
- Bakes, E. L. O. & Tielens, A. G. G. M., The Photoelectric Heating Mechanism for Very Small Graphitic Grains and Polycyclic Aromatic Hydrocarbons. 1994, *The Astrophysical Journal*, 427, 822, aDS Bibcode: 1994ApJ...427..822B



- Ballesteros-Paredes, J. & Hartmann, L., Remarks on Rapid vs. Slow Star Formation. 2007, *Revista Mexicana de Astronomía y Astrofísica*, 43, 123, aDS Bibcode: 2007RMxAA..43..123B
- Ballesteros-Paredes, J., Hartmann, L. W., Vázquez-Semadeni, E., Heitsch, F., & Zamora-Avilés, M. A., Gravity or turbulence? Velocity dispersion-size relation. 2011, *Monthly Notices of the Royal Astronomical Society*, 411, 65, aDS Bibcode: 2011MNRAS.411..65B
- Ballesteros-Paredes, J., Klessen, R. S., Mac Low, M. M., & Vazquez-Semadeni, E. 2007, *Molecular Cloud Turbulence and Star Formation* (eprint: arXiv:astro-ph/0603357), conference Name: Protostars and Planets V Pages: 63 ADS Bibcode: 2007prpl.conf...63B
- Banerjee, R., Vázquez-Semadeni, E., Hennebelle, P., & Klessen, R. S., Clump morphology and evolution in MHD simulations of molecular cloud formation. 2009, *Monthly Notices of the Royal Astronomical Society*, 398, 1082, aDS Bibcode: 2009MNRAS.398.1082B
- Beck, R. & Wielebinski, R., *Magnetic Fields in Galaxies*. 2013, *Planets, Stars and Stellar Systems. Volume 5: Galactic Structure and Stellar Populations*, 641
- Becklin, E. E. & Neugebauer, G., Observations of an Infrared Star in the Orion Nebula. 1967, *The Astrophysical Journal*, 147, 799, aDS Bibcode: 1967ApJ...147..799B
- Benedettini, M., Schisano, E., Pezzuto, S., et al., Filaments in the Lupus molecular clouds. 2015, *Monthly Notices of the Royal Astronomical Society*, 453, 2036, aDS Bibcode: 2015MNRAS.453.2036B
- Beuther, H., Ragan, S. E., Johnston, K., et al., Filament fragmentation in high-mass star formation. 2015, *Astronomy & Astrophysics*, Volume 584, id.A67, <NUMPAGES>12</NUMPAGES> pp., 584, A67
- Bhadari, N. K., Dewangan, L. K., Pirogov, L. E., & Ojha, D. K., Star-forming Sites IC 446 and IC 447: An Outcome of End-dominated Collapse of Monoceros R1 Filament. 2020, *The Astrophysical Journal*, 899, 167, aDS Bibcode: 2020ApJ...899..167B
- Black, J. H. & Dalgarno, A., Models of interstellar clouds. I. The Zeta Ophiuchi cloud. 1977, *The Astrophysical Journal Supplement Series*, 34, 405, aDS Bibcode: 1977ApJS...34..405B
- Blitz, L., Fukui, Y., Kawamura, A., et al. 2007, *Giant Molecular Clouds in Local Group Galaxies* (eprint: arXiv:astro-ph/0602600), conference Name: Protostars and Planets V Pages: 81 ADS Bibcode: 2007prpl.conf...81B
- Bolatto, A. D., Leroy, A. K., Rosolowsky, E., Walter, F., & Blitz, L., The Resolved Properties of Extragalactic Giant Molecular Clouds. 2008, *The Astrophysical Journal*, 686, 948, aDS Bibcode: 2008ApJ...686..948B
- Bondi, H., On spherically symmetrical accretion. 1952, *Monthly Notices of the Royal Astronomical Society*, 112, 195, aDS Bibcode: 1952MNRAS.112..195B
- Bonne, L., Bontemps, S., Schneider, N., et al., Formation of the Musca filament: evidence for asymmetries in the accretion flow due to a cloud-cloud collision. 2020, *Astronomy & Astrophysics*, Volume 644, id.A27, <NUMPAGES>23</NUMPAGES> pp., 644, A27

- Bouchut, F., Klingenberg, C., & Waagan, K., A multiwave approximate Riemann solver for ideal MHD based on relaxation. I: theoretical framework. 2007, *Numerische Mathematik*, 108, 7, publisher: Springer-Verlag
- Bouchut, F., Klingenberg, C., & Waagan, K., A multiwave approximate Riemann solver for ideal MHD based on relaxation II: numerical implementation with 3 and 5 waves. 2010, *Numerische Mathematik*, 115, 647
- Bourke, T. L., Myers, P. C., Robinson, G., & Hyland, A. R., New OH Zeeman Measurements of Magnetic Field Strengths in Molecular Clouds. 2001, *The Astrophysical Journal*, 554, 916, aDS Bibcode: 2001ApJ...554..916B
- Burkert, A. & Hartmann, L., Collapse and Fragmentation in Finite Sheets. 2004, *The Astrophysical Journal*, 616, 288, aDS Bibcode: 2004ApJ...616..288B
- Burton, M. G., Hollenbach, D. J., & Tielens, A. G. G. M., Line Emission from Clumpy Photodissociation Regions. 1990, *The Astrophysical Journal*, 365, 620, aDS Bibcode: 1990ApJ...365..620B
- Cabral, B. & Leedom, L. C. 1993, in *Proceedings of the 20th annual conference on Computer graphics and interactive techniques, SIGGRAPH '93* (New York, NY, USA: Association for Computing Machinery), 263–270
- Camacho, V., Vázquez-Semadeni, E., Ballesteros-Paredes, J., et al., Energy Budget of Forming Clumps in Numerical Simulations of Collapsing Clouds. 2016, *The Astrophysical Journal*, 833, 113
- Caselli, P., Walmsley, C. M., Terzieva, R., & Herbst, E., The Ionization Fraction in Dense Cloud Cores. 1998, *The Astrophysical Journal*, 499, 234, aDS Bibcode: 1998ApJ...499..234C
- Chandrasekhar, S. & Fermi, E., Problems of Gravitational Stability in the Presence of a Magnetic Field. 1953, *The Astrophysical Journal*, 118, 116, aDS Bibcode: 1953ApJ...118..116C
- Chen, H.-R. V., Zhang, Q., Wright, M. C. H., et al., Filamentary Accretion Flows in the Infrared Dark Cloud G14.225-0.506 Revealed by ALMA. 2019, *The Astrophysical Journal*, 875, 24, aDS Bibcode: 2019ApJ...875...24C
- Chevance, M., Krumholz, M. R., McLeod, A. F., et al., The Life and Times of Giant Molecular Clouds. 2022, arXiv:2203.09570 [astro-ph], arXiv: 2203.09570
- Choudhuri, A. R. 1998, *The physics of fluids and plasmas : an introduction for astrophysicists /*, publication Title: *The physics of fluids and plasmas : an introduction for astrophysicists /* Arnab Rai Choudhuri. New York : Cambridge University Press ADS Bibcode: 1998pfpp..book.....C
- Cioffi, D. F., McKee, C. F., & Bertschinger, E., Dynamics of Radiative Supernova Remnants. 1988, *The Astrophysical Journal*, 334, 252, aDS Bibcode: 1988ApJ...334..252C
- Clarke, S. D., Whitworth, A. P., Duarte-Cabral, A., & Hubber, D. A., Filamentary fragmentation in a turbulent medium. 2017, *Monthly Notices of the Royal Astronomical Society*, 468, 2489, aDS Bibcode: 2017MNRAS.468.2489C

- Clarke, S. D., Whitworth, A. P., & Hubber, D. A., Perturbation growth in accreting filaments. 2016, *Monthly Notices of the Royal Astronomical Society*, 458, 319, aDS Bibcode: 2016MNRAS.458..319C
- Colman, T. & Teyssier, R., On the origin of the peak of the stellar initial mass function: exploring the tidal screening theory. 2020, *Monthly Notices of the Royal Astronomical Society*, 492, 4727, aDS Bibcode: 2020MNRAS.492.4727C
- Commerçon, B., Hennebelle, P., & Henning, T., Collapse of Massive Magnetized Dense Cores Using Radiation Magnetohydrodynamics: Early Fragmentation Inhibition. 2011, *The Astrophysical Journal*, 742, L9, aDS Bibcode: 2011ApJ...742L...9C
- Crutcher, R. M., Magnetic Fields in Molecular Clouds: Observations Confront Theory. 1999, *The Astrophysical Journal*, 520, 706, aDS Bibcode: 1999ApJ...520..706C
- Crutcher, R. M., Magnetic Fields in Molecular Clouds. 2012, *Annual Review of Astronomy and Astrophysics*, vol. 50, p.29-63, 50, 29
- Crutcher, R. M., Hakobian, N., & Troland, T. H., Testing Magnetic Star Formation Theory. 2009, *The Astrophysical Journal*, 692, 844, aDS Bibcode: 2009ApJ...692..844C
- Crutcher, R. M. & Troland, T. H., OH Zeeman Measurement of the Magnetic Field in the L1544 Core. 2000, *The Astrophysical Journal*, 537, L139, aDS Bibcode: 2000ApJ...537L.139C
- Crutcher, R. M., Wandelt, B., Heiles, C., Falgarone, E., & Troland, T. H., Magnetic Fields in Interstellar Clouds from Zeeman Observations: Inference of Total Field Strengths by Bayesian Analysis. 2010, *The Astrophysical Journal*, 725, 466, aDS Bibcode: 2010ApJ...725..466C
- Dame, T. M., Elmegreen, B. G., Cohen, R. S., & Thaddeus, P., The Largest Molecular Cloud Complexes in the First Galactic Quadrant. 1986, *The Astrophysical Journal*, 305, 892, aDS Bibcode: 1986ApJ...305..892D
- Derigs, D., Winters, A. R., Gassner, G. J., & Walch, S., A novel high-order, entropy stable, 3D AMR MHD solver with guaranteed positive pressure. 2016, *Journal of Computational Physics*, 317, 223, aDS Bibcode: 2016JCoPh.317..223D
- Derigs, D., Winters, A. R., Gassner, G. J., & Walch, S., A novel averaging technique for discrete entropy-stable dissipation operators for ideal MHD. 2017, *Journal of Computational Physics*, 330, 624, aDS Bibcode: 2017JCoPh.330..624D
- Derigs, D., Winters, A. R., Gassner, G. J., Walch, S., & Bohm, M., Ideal GLM-MHD: About the entropy consistent nine-wave magnetic field divergence diminishing ideal magnetohydrodynamics equations. 2018, *Journal of Computational Physics*, 364, 420, aDS Bibcode: 2018JCoPh.364..420D
- Dib, S., Kim, J., Vázquez-Semadeni, E., Burkert, A., & Shadmehri, M., The Virial Balance of Clumps and Cores in Molecular Clouds. 2007, *The Astrophysical Journal*, 661, 262, aDS Bibcode: 2007ApJ...661..262D
- Dobbs, C. L., Krumholz, M. R., Ballesteros-Paredes, J., et al. 2014, Formation of Molecular Clouds and Global Conditions for Star Formation (eprint: arXiv:1312.3223), conference Name: Protostars and Planets VI Pages: 3 ADS Bibcode: 2014prpl.conf....3D

- Draine, B. T., Photoelectric heating of interstellar gas. 1978, *\apjs*, 36, 595
- Draine, B. T. 2011, *Physics of the Interstellar and Intergalactic Medium*, publication Title: *Physics of the Interstellar and Intergalactic Medium* by Bruce T. Draine. Princeton University Press ADS Bibcode: 2011piim.book.....D
- Draine, B. T. & Bertoldi, F., Structure of Stationary Photodissociation Fronts. 1996, *The Astrophysical Journal*, 468, 269, aDS Bibcode: 1996ApJ...468..269D
- Draine, B. T. & Lee, H. M., Optical Properties of Interstellar Graphite and Silicate Grains. 1984, *The Astrophysical Journal*, 285, 89, aDS Bibcode: 1984ApJ...285...89D
- Dubey, A., Fisher, R., Graziani, C., et al., Challenges of Extreme Computing using the FLASH code. 2008, 385, 145, conference Name: Numerical Modeling of Space Plasma Flows
- Elmegreen, B. G., Magnetic diffusion and ionization fractions in dense molecular clouds: the role of charged grains. 1979, *The Astrophysical Journal*, 232, 729, aDS Bibcode: 1979ApJ...232..729E
- Elmegreen, B. G., Star Formation in a Crossing Time. 2000, *The Astrophysical Journal*, 530, 277, aDS Bibcode: 2000ApJ...530..277E
- Elmegreen, B. G. & Scalo, J., Interstellar Turbulence I: Observations and Processes. 2004, *Annual Review of Astronomy & Astrophysics*, vol. 42, Issue 1, pp.211-273, 42, 211
- Falgarone, E., Pety, J., & Hily-Blant, P., The Neutral Atomic Phases of the Interstellar Medium. 1995, *The Astrophysical Journal*, 443, 152
- Federrath, C., Sur, S., Schleicher, D. R. G., Banerjee, R., & Klessen, R. S., A New Jeans Resolution Criterion for (M)HD Simulations of Self-gravitating Gas: Application to Magnetic Field Amplification by Gravity-driven Turbulence. 2011, *\apj*, 731, 62, *\_eprint*: 1102.0266
- Ferrière, K., Gillard, W., & Jean, P., Spatial distribution of interstellar gas in the innermost 3 kpc of our galaxy. 2007, *Astronomy and Astrophysics*, Volume 467, Issue 2, May IV 2007, pp.611-627, 467, 611
- Ferrière, K. M., The interstellar environment of our galaxy. 2001, *Reviews of Modern Physics*, 73, 1031, aDS Bibcode: 2001RvMP...73.1031F
- Field, G. B., Thermal Instability. 1965, *The Astrophysical Journal*, 142, 531, aDS Bibcode: 1965ApJ...142..531F
- Field, G. B., Goldsmith, D. W., & Habing, H. J., Cosmic-Ray Heating of the Interstellar Gas. 1969, *The Astrophysical Journal*, 155, L149, aDS Bibcode: 1969ApJ...155L.149F
- Fixsen, D. J. & Mather, J. C., The Spectral Results of the Far-Infrared Absolute Spectrophotometer Instrument on COBE. 2002, *The Astrophysical Journal*, 581, 817, aDS Bibcode: 2002ApJ...581..817F
- Flower, D. R., Le Bourlot, J., Pineau des Forêts, G., & Cabrit, S., The contributions of J-type shocks to the H<sub>2</sub> emission from molecular outflow sources. 2003, *Monthly Notices of the Royal Astronomical Society*, 341, 70, aDS Bibcode: 2003MNRAS.341...70F

- Fryxell, B., Olson, K., Ricker, P., et al., FLASH: An Adaptive Mesh Hydrodynamics Code for Modeling Astrophysical Thermonuclear Flashes. 2000, *The Astrophysical Journal Supplement Series*, 131, 273
- Gaensler, B. M., Madsen, G. J., Chatterjee, S., & Mao, S. A., The Vertical Structure of Warm Ionised Gas in the Milky Way. 2008, *Publications of the Astronomical Society of Australia*, 25, 184, aDS Bibcode: 2008PASA...25..184G
- Gatto, A., Walch, S., Low, M. M. M., et al., Modelling the supernova-driven ISM in different environments. 2015, *Monthly Notices of the Royal Astronomical Society*, 449, 1057, aDS Bibcode: 2015MNRAS.449.1057G
- Geen, S., Rosdahl, J., Blaizot, J., Devriendt, J., & Slyz, A., A detailed study of feedback from a massive star. 2015, *Monthly Notices of the Royal Astronomical Society*, 448, 3248, aDS Bibcode: 2015MNRAS.448.3248G
- Genzel, R., Tacconi, L. J., Gracia-Carpio, J., et al., A study of the gas-star formation relation over cosmic time. 2010, *Monthly Notices of the Royal Astronomical Society*, 407, 2091, aDS Bibcode: 2010MNRAS.407.2091G
- Girichidis, P., Seifried, D., Naab, T., et al., The SILCC project - V. The impact of magnetic fields on the chemistry and the formation of molecular clouds. 2018, *Monthly Notices of the Royal Astronomical Society*, 480, 3511, aDS Bibcode: 2018MNRAS.480.3511G
- Girichidis, P., Walch, S., Naab, T., et al., The SILCC (Simulating the LifeCycle of molecular Clouds) project - II. Dynamical evolution of the supernova-driven ISM and the launching of outflows. 2016, *\mnras*, 456, 3432, *\_eprint*: 1508.06646
- Glassgold, A. E. & Langer, W. D., Heating of Molecular-Hydrogen Clouds by Cosmic Rays and X-Rays. 1973, *The Astrophysical Journal*, 186, 859, aDS Bibcode: 1973ApJ...186..859G
- Glover, S. C. O., Federrath, C., Mac Low, M. M., & Klessen, R. S., Modelling CO formation in the turbulent interstellar medium. 2010, *Monthly Notices of the Royal Astronomical Society*, 404, 2, aDS Bibcode: 2010MNRAS.404....2G
- Glover, S. C. O. & Mac Low, M.-M., Simulating the Formation of Molecular Clouds. I. Slow Formation by Gravitational Collapse from Static Initial Conditions. 2007a, *The Astrophysical Journal Supplement Series*, 169, 239
- Glover, S. C. O. & Mac Low, M.-M., Simulating the Formation of Molecular Clouds. II. Rapid Formation from Turbulent Initial Conditions. 2007b, *\apj*, 659, 1317, *\_eprint*: arXiv:astro-ph/0605121
- Gnat, O. & Ferland, G. J., Ion-by-ion Cooling Efficiencies. 2012, *The Astrophysical Journal Supplement Series*, 199, 20, aDS Bibcode: 2012ApJS..199...20G
- Goicoechea, J. R., Pety, J., Gerin, M., Hily-Blant, P., & Le Bourlot, J., The ionization fraction gradient across the Horsehead edge: an archetype for molecular clouds. 2009, *Astronomy and Astrophysics*, 498, 771
- Goldreich, P. & Kwan, J., Molecular Clouds. 1974, *The Astrophysical Journal*, 189, 441, aDS Bibcode: 1974ApJ...189..441G

- Goldreich, P. & Kylafis, N. D., On mapping the magnetic field direction in molecular clouds by polarization measurements. 1981, *The Astrophysical Journal*, 243, L75, aDS Bibcode: 1981ApJ...243L..75G
- Goldreich, P. & Sridhar, S., Toward a Theory of Interstellar Turbulence. II. Strong Alfvénic Turbulence. 1995, *The Astrophysical Journal*, 438, 763, aDS Bibcode: 1995ApJ...438..763G
- Goldsmith, P. F., Molecular Depletion and Thermal Balance in Dark Cloud Cores. 2001, *The Astrophysical Journal*, 557, 736, aDS Bibcode: 2001ApJ...557..736G
- Goldsmith, P. F. & Langer, W. D., Molecular cooling and thermal balance of dense interstellar clouds. 1978, *The Astrophysical Journal*, 222, 881, aDS Bibcode: 1978ApJ...222..881G
- Gong, Y., Belloche, A., Du, F. J., et al., Physical and chemical structure of the Serpens filament: Fast formation and gravity-driven accretion. 2021, *Astronomy & Astrophysics*, Volume 646, id.A170, <NUMPAGES>25</NUMPAGES> pp., 646, A170
- Goossens, M. 2003, *Astrophysics and Space Science Library*, Vol. 294, *An Introduction to Plasma Astrophysics and Magnetohydrodynamics* (Dordrecht: Springer Netherlands)
- Gould, R. J. & Salpeter, E. E., The Interstellar Abundance of the Hydrogen Molecule. I. Basic Processes. 1963, *The Astrophysical Journal*, 138, 393, aDS Bibcode: 1963ApJ...138..393G
- Gritschneder, M., Naab, T., Walch, S., Burkert, A., & Heitsch, F., Driving Turbulence and Triggering Star Formation by Ionizing Radiation. 2009, *The Astrophysical Journal*, 694, L26, aDS Bibcode: 2009ApJ...694L..26G
- Habing, H. J., The interstellar radiation density between 912 Å and 2400 Å. 1968, *Bulletin of the Astronomical Institutes of the Netherlands*, 19, 421, aDS Bibcode: 1968BAN....19..421H
- Hacar, A., Clark, S. E., Heitsch, F., et al., Initial Conditions for Star Formation: A Physical Description of the Filamentary ISM. 2022, arXiv:2203.09562 [astro-ph], arXiv: 2203.09562
- Hacar, A., Tafalla, M., Forbrich, J., et al., An ALMA study of the Orion Integral Filament. I. Evidence for narrow fibers in a massive cloud. 2018, *Astronomy & Astrophysics*, Volume 610, id.A77, <NUMPAGES>24</NUMPAGES> pp., 610, A77
- Haffner, L. M., Dettmar, R. J., Beckman, J. E., et al., The warm ionized medium in spiral galaxies. 2009, *Reviews of Modern Physics*, 81, 969, aDS Bibcode: 2009RvMP...81..969H
- Haid, S., Walch, S., Naab, T., et al., Supernova blast waves in wind-blown bubbles, turbulent, and power-law ambient media. 2016, *Monthly Notices of the Royal Astronomical Society*, 460, 2962, aDS Bibcode: 2016MNRAS.460.2962H
- Hall, J. S., Some polarization measurements in the Pleiades and Orion regions. 1951, *The Astronomical Journal*, 56, 40, aDS Bibcode: 1951AJ.....56...40H

- Hartmann, L., Ballesteros-Paredes, J., & Bergin, E. A., Rapid Formation of Molecular Clouds and Stars in the Solar Neighborhood. 2001, *The Astrophysical Journal*, 562, 852, aDS Bibcode: 2001ApJ...562..852H
- Hartmann, L. & Burkert, A., On the Structure of the Orion A Cloud and the Formation of the Orion Nebula Cluster. 2007, *The Astrophysical Journal*, 654, 988, aDS Bibcode: 2007ApJ...654..988H
- Heiles, C. & Troland, T. H., The Millennium Arecibo 21 Centimeter Absorption-Line Survey. IV. Statistics of Magnetic Field, Column Density, and Turbulence. 2005, *The Astrophysical Journal*, 624, 773, aDS Bibcode: 2005ApJ...624..773H
- Heithausen, A., Bensch, F., Stutzki, J., Falgarone, E., & Panis, J. F., How Small Were the First Cosmological Objects? 1997, *The Astrophysical Journal*, 474, 1
- Heitsch, F., Gravitational Infall onto Molecular Filaments. II. Externally Pressurized Cylinders. 2013, *The Astrophysical Journal*, 776, 62, aDS Bibcode: 2013ApJ...776...62H
- Heitsch, F., Ballesteros-Paredes, J., & Hartmann, L., Gravitational Collapse and Filament Formation: Comparison with the Pipe Nebula. 2009, *The Astrophysical Journal*, 704, 1735, aDS Bibcode: 2009ApJ...704.1735H
- Heitsch, F. & Hartmann, L., Rapid Molecular Cloud and Star Formation: Mechanisms and Movies. 2008, *The Astrophysical Journal*, 689, 290, aDS Bibcode: 2008ApJ...689..290H
- Heitsch, F., Mac Low, M.-M., & Klessen, R. S., Gravitational Collapse in Turbulent Molecular Clouds. II. Magnetohydrodynamical Turbulence. 2001, *The Astrophysical Journal*, 547, 280, aDS Bibcode: 2001ApJ...547..280H
- Hennebelle, P., Banerjee, R., Vázquez-Semadeni, E., Klessen, R. S., & Audit, E., From the warm magnetized atomic medium to molecular clouds. 2008, *Astronomy and Astrophysics*, 486, L43
- Hennebelle, P. & Chabrier, G., Analytical Theory for the Initial Mass Function: CO Clumps and Prestellar Cores. 2008, *The Astrophysical Journal*, 684, 395, aDS Bibcode: 2008ApJ...684..395H
- Hennebelle, P. & Falgarone, E., Turbulent molecular clouds. 2012, *Astronomy and Astrophysics Review*, 20, 55
- Hennebelle, P. & Inutsuka, S.-i., The role of magnetic field in molecular cloud formation and evolution. 2019, *Frontiers in Astronomy and Space Sciences*, 6, 5, aDS Bibcode: 2019FrASS...6....5H
- Heyer, M. & Dame, T. M., Molecular Clouds in the Milky Way. 2015, *Annual Review of Astronomy and Astrophysics*, vol. 53, p.583-629, 53, 583
- Heyer, M., Krawczyk, C., Duval, J., & Jackson, J. M., Re-Examining Larson's Scaling Relationships in Galactic Molecular Clouds. 2009, *The Astrophysical Journal*, 699, 1092, aDS Bibcode: 2009ApJ...699.1092H
- Heyer, M. H., Carpenter, J. M., & Snell, R. L., The Equilibrium State of Molecular Regions in the Outer Galaxy. 2001, *The Astrophysical Journal*, 551, 852, aDS Bibcode: 2001ApJ...551..852H

- Hildebrand, R. H., The determination of cloud masses and dust characteristics from submillimetre thermal emission. 1983, *Quarterly Journal of the Royal Astronomical Society*, 24, 267, aDS Bibcode: 1983QJRAS..24..267H
- Hill, A. S., Joung, M. R., Mac Low, M.-M., et al., Vertical Structure of a Supernova-driven Turbulent, Magnetized Interstellar Medium. 2012, *The Astrophysical Journal*, 750, 104, aDS Bibcode: 2012ApJ...750..104H
- Hiltner, W. A., Polarization of Stellar Radiation. III. The Polarization of 841 Stars. 1951, *The Astrophysical Journal*, 114, 241, aDS Bibcode: 1951ApJ...114..241H
- Hollenbach, D. & McKee, C. F., Molecule formation and infrared emission in fast interstellar shocks. I. Physical processes. 1979, *The Astrophysical Journal Supplement Series*, 41, 555, aDS Bibcode: 1979ApJS...41..555H
- Hollenbach, D. & McKee, C. F., Molecule Formation and Infrared Emission in Fast Interstellar Shocks. III. Results for J Shocks in Molecular Clouds. 1989, *The Astrophysical Journal*, 342, 306, aDS Bibcode: 1989ApJ...342..306H
- Hopkins, P. F., The stellar initial mass function, core mass function and the last-crossing distribution. 2012, *Monthly Notices of the Royal Astronomical Society*, 423, 2037, aDS Bibcode: 2012MNRAS.423.2037H
- Hosokawa, T. & Inutsuka, S.-i., Dynamical Expansion of Ionization and Dissociation Front around a Massive Star. II. On the Generality of Triggered Star Formation. 2006, *The Astrophysical Journal*, 646, 240, aDS Bibcode: 2006ApJ...646..240H
- Hoyle, F. & Ellis, G. R. A., On the Existence of an Ionized Layer about the Galactic Plane. 1963, *Australian Journal of Physics*, 16, 1, aDS Bibcode: 1963AuJPh..16....1H
- Hoyle, F. & Lyttleton, R. A., On the accretion theory of stellar evolution. 1941, *Monthly Notices of the Royal Astronomical Society*, 101, 227, aDS Bibcode: 1941MNRAS.101..227H
- Iffrig, O. & Hennebelle, P., Mutual influence of supernovae and molecular clouds. 2015, *Astronomy & Astrophysics*, Volume 576, id.A95, <NUMPAGES>13</NUMPAGES> pp., 576, A95
- Inoue, T. & Fukui, Y., Formation of Massive Molecular Cloud Cores by Cloud-Cloud Collision. 2013, *The Astrophysical Journal*, 774, L31, aDS Bibcode: 2013ApJ...774L..31I
- Inutsuka, S.-i., Inoue, T., Iwasaki, K., & Hosokawa, T., The formation and destruction of molecular clouds and galactic star formation. An origin for the cloud mass function and star formation efficiency. 2015, *A&A*, 580, A49, eprint: 1505.04696
- Inutsuka, S.-I. & Miyama, S. M., Self-similar Solutions and the Stability of Collapsing Isothermal Filaments. 1992, *The Astrophysical Journal*, 388, 392, aDS Bibcode: 1992ApJ...388..392I
- Janka, H.-T., Explosion Mechanisms of Core-Collapse Supernovae. 2012, *Annual Review of Nuclear and Particle Science*, 62, 407, aDS Bibcode: 2012ARNPS..62..407J
- Jenkins, E. B., The Fractional Ionization of the Warm Neutral Interstellar Medium. 2013, *The Astrophysical Journal*, 764, 25, aDS Bibcode: 2013ApJ...764...25J



- Kainulainen, J., Hacar, A., Alves, J., et al., Gravitational fragmentation caught in the act: the filamentary Musca molecular cloud. 2016, *Astronomy & Astrophysics*, Volume 586, id.A27, <NUMPAGES>13</NUMPAGES> pp., 586, A27
- Kalberla, P. M. W. & Kerp, J., The HI Distribution of the Milky Way. 2009, *Annual Review of Astronomy and Astrophysics*, 47, 27
- Kauffmann, J., Pillai, T., & Goldsmith, P. F., Low Virial Parameters in Molecular Clouds: Implications for High-mass Star Formation and Magnetic Fields. 2013, *The Astrophysical Journal*, 779, 185, aDS Bibcode: 2013ApJ...779..185K
- Kawamura, A., Mizuno, Y., Minamidani, T., et al., The Second Survey of the Molecular Clouds in the Large Magellanic Cloud by NANTEN. II. Star Formation. 2009, *The Astrophysical Journal Supplement Series*, 184, 1, aDS Bibcode: 2009ApJS..184....1K
- Kegel, W. H., The interpretation of correlations between observed parameters of molecular clouds. 1989, *Astronomy and Astrophysics (ISSN 0004-6361)*, vol. 225, no. 2, Nov. 1989, p. 517-520., 225, 517
- Kennicutt, Jr., R. C., The Global Schmidt Law in Star-forming Galaxies. 1998, *The Astrophysical Journal*, 498, 541, aDS Bibcode: 1998ApJ...498..541K
- Kirk, H., Johnstone, D., & Tafalla, M., Dynamics of Dense Cores in the Perseus Molecular Cloud. 2007, *The Astrophysical Journal*, 668, 1042, aDS Bibcode: 2007ApJ...668.1042K
- Kirk, H., Myers, P. C., Bourke, T. L., et al., Filamentary Accretion Flows in the Embedded Serpens South Protocluster. 2013, *The Astrophysical Journal*, 766, 115, aDS Bibcode: 2013ApJ...766..115K
- Klessen, R. S. & Burkert, A., The Formation of Stellar Clusters: Gaussian Cloud Conditions. II. 2001, *The Astrophysical Journal*, 549, 386, aDS Bibcode: 2001ApJ...549..386K
- Klessen, R. S. & Glover, S. C. O., Physical Processes in the Interstellar Medium. 2016, *Saas-Fee Advanced Course*, 43, 85, aDS Bibcode: 2016SAAS...43...85K
- Koda, J., Scoville, N., Sawada, T., et al., Dynamically Driven Evolution of the Interstellar Medium in M51. 2009, *The Astrophysical Journal*, 700, L132, aDS Bibcode: 2009ApJ...700L.132K
- Kolmogorov, A., The Local Structure of Turbulence in Incompressible Viscous Fluid for Very Large Reynolds' Numbers. 1941, *Akademiia Nauk SSSR Doklady*, 30, 301, aDS Bibcode: 1941DoSSR..30..301K
- Kounkel, M., Covey, K., Suárez, G., et al., The APOGEE-2 Survey of the Orion Star-forming Complex. II. Six-dimensional Structure. 2018, *The Astronomical Journal*, 156, 84, aDS Bibcode: 2018AJ....156...84K
- Kramer, C., Alves, J., Lada, C. J., et al., Depletion of CO in a cold dense cloud core of IC 5146. 1999, *Astronomy and Astrophysics*, v.342, p.257-270 (1999), 342, 257
- Kroupa, P., On the variation of the initial mass function. 2001, *Monthly Notices of the Royal Astronomical Society*, 322, 231, aDS Bibcode: 2001MNRAS.322..231K

- Krumholz, M. R. 2015, Notes on Star Formation, Tech. rep., publication Title: arXiv e-prints ADS Bibcode: 2015arXiv151103457K Type: article
- Krumholz, M. R., Dekel, A., & McKee, C. F., A Universal, Local Star Formation Law in Galactic Clouds, nearby Galaxies, High-redshift Disks, and Starbursts. 2012, *The Astrophysical Journal*, 745, 69, aDS Bibcode: 2012ApJ...745...69K
- Krumholz, M. R. & Matzner, C. D., The Dynamics of Radiation-pressure-dominated H II Regions. 2009, *The Astrophysical Journal*, 703, 1352, aDS Bibcode: 2009ApJ...703.1352K
- Krumholz, M. R., McKee, C. F., & Tumlinson, J., The Atomic-to-Molecular Transition in Galaxies. I. An Analytic Approximation for Photodissociation Fronts in Finite Clouds. 2008, *The Astrophysical Journal*, 689, 865, aDS Bibcode: 2008ApJ...689..865K
- Kunz, M. W. & Mouschovias, T. C., The non-isothermal stage of magnetic star formation - II. Results. 2010, *Monthly Notices of the Royal Astronomical Society*, 408, 322, aDS Bibcode: 2010MNRAS.408..322K
- Kwan, J. H., Gatley, I., Merrill, K. M., Probst, R., & Weintraub, D. A., On the molecular hydrogen emission at the Orion Nebula. 1977, *The Astrophysical Journal*, 216, 713, aDS Bibcode: 1977ApJ...216..713K
- Könyves, V., André, P., Men'shchikov, A., et al., A census of dense cores in the Aquila cloud complex: SPIRE/PACS observations from the Herschel Gould Belt survey. 2015, *Astronomy & Astrophysics*, Volume 584, id.A91, <NUMPAGES>33</NUMPAGES> pp., 584, A91
- Landau, L. D. & Lifshitz, E. M. 1959, Fluid mechanics, publication Title: Course of theoretical physics ADS Bibcode: 1959flme.book.....L
- Larson, R. B., Turbulence and star formation in molecular clouds. 1981, *Monthly Notices of the Royal Astronomical Society*, 194, 809, aDS Bibcode: 1981MNRAS.194..809L
- Lee, Y.-N. & Hennebelle, P., Stellar mass spectrum within massive collapsing clumps. II. Thermodynamics and tidal forces of the first Larson core. A robust mechanism for the peak of the IMF. 2018, *Astronomy & Astrophysics*, Volume 611, id.A89, <NUMPAGES>17</NUMPAGES> pp., 611, A89
- Leroy, A. K., Bolatto, A. D., Ostriker, E. C., et al., ALMA Reveals the Molecular Medium Fueling the Nearest Nuclear Starburst. 2015, *The Astrophysical Journal*, 801, 25, aDS Bibcode: 2015ApJ...801...25L
- Leung, C. M., Radiation transport in dense interstellar dust clouds. 1975, *The Astrophysical Journal*, 199, 340, aDS Bibcode: 1975ApJ...199..340L
- Li, G.-X., Urquhart, J. S., Leurini, S., et al., ATLASGAL: A Galaxy-wide sample of dense filamentary structures. 2016, *Astronomy & Astrophysics*, Volume 591, id.A5, <NUMPAGES>24</NUMPAGES> pp., 591, A5
- Li, H.-B. & Henning, T., The alignment of molecular cloud magnetic fields with the spiral arms in M33. 2011, *Nature*, 479, 499, aDS Bibcode: 2011Natur.479..499L

- Li, Z.-Y., Krasnopolsky, R., & Shang, H., Non-ideal MHD Effects and Magnetic Braking Catastrophe in Protostellar Disk Formation. 2011, *The Astrophysical Journal*, 738, 180, aDS Bibcode: 2011ApJ...738..180L
- Lim, B., Hong, J., Yun, H.-S., et al., The Origin of a Distributed Stellar Population in the Star-forming Region W4. 2020, *The Astrophysical Journal*, 899, 121, aDS Bibcode: 2020ApJ...899..121L
- Löhner, R., An adaptive finite element scheme for transient problems in CFD. 1987, *Computer Methods in Applied Mechanics and Engineering*, 61, 323
- Mac Low, M.-M. & Klessen, R. S., Control of star formation by supersonic turbulence. 2004, *Reviews of Modern Physics*, 76, 125, aDS Bibcode: 2004RvMP...76..125M
- Mac Low, M.-M., Klessen, R. S., Burkert, A., & Smith, M. D., Kinetic Energy Decay Rates of Supersonic and Super-Alfvénic Turbulence in Star-Forming Clouds. 1998, *Physical Review Letters*, 80, 2754, aDS Bibcode: 1998PhRvL..80.2754M
- MacNeice, P., Olson, K. M., Mobarry, C., de Fainchtein, R., & Packer, C., PARAMESH: A parallel adaptive mesh refinement community toolkit. 2000, *Computer Physics Communications*, 126, 330
- Marsh, K. A., Kirk, J. M., André, P., et al., A census of dense cores in the Taurus L1495 cloud from the Herschel. 2016, *Monthly Notices of the Royal Astronomical Society*, 459, 342, aDS Bibcode: 2016MNRAS.459..342M
- Mathis, J. S., Rumpl, W., & Nordsieck, K. H., The size distribution of interstellar grains. 1977, *The Astrophysical Journal*, 217, 425, aDS Bibcode: 1977ApJ...217..425M
- Mattern, M., Kauffmann, J., Csengeri, T., et al., SEDIGISM: the kinematics of ATLASGAL filaments. 2018, *Astronomy & Astrophysics*, Volume 619, id.A166, <NUMPAGES>24</NUMPAGES> pp., 619, A166
- McKee, C. F. & Ostriker, E. C., Theory of Star Formation. 2007, *Annual Review of Astronomy and Astrophysics*, 45, 565
- McKee, C. F. & Ostriker, J. P., A theory of the interstellar medium: three components regulated by supernova explosions in an inhomogeneous substrate. 1977, *The Astrophysical Journal*, 218, 148, aDS Bibcode: 1977ApJ...218..148M
- McKee, C. F. & Zweibel, E. G., On the Virial Theorem for Turbulent Molecular Clouds. 1992, *The Astrophysical Journal*, 399, 551, aDS Bibcode: 1992ApJ...399..551M
- Mierkiewicz, E. J., Reynolds, R. J., Roesler, F. L., Harlander, J. M., & Jaehnig, K. P., Detection of Diffuse Interstellar [O II] Emission from the Milky Way Using Spatial Heterodyne Spectroscopy. 2006, *The Astrophysical Journal*, 650, L63, aDS Bibcode: 2006ApJ...650L..63M
- Mocz, P., Vogelsberger, M., Robles, V. H., et al., Galaxy formation with BECDM - I. Turbulence and relaxation of idealized haloes. 2017, *Monthly Notices of the Royal Astronomical Society*, 471, 4559, aDS Bibcode: 2017MNRAS.471.4559M

- Molinari, S., Swinyard, B., Bally, J., et al., Clouds, filaments, and protostars: The Herschel Hi-GAL Milky Way. 2010, *Astronomy and Astrophysics*, Volume 518, id.L100, <NUMPAGES>5</NUMPAGES> pp., 518, L100
- Murray, N., Star Formation Efficiencies and Lifetimes of Giant Molecular Clouds in the Milky Way. 2011, *The Astrophysical Journal*, 729, 133, aDS Bibcode: 2011ApJ...729..133M
- Murray, N., Ménard, B., & Thompson, T. A., Radiation Pressure from Massive Star Clusters as a Launching Mechanism for Super-galactic Winds. 2011, *The Astrophysical Journal*, 735, 66, aDS Bibcode: 2011ApJ...735...66M
- Murray, N., Quataert, E., & Thompson, T. A., On the Maximum Luminosity of Galaxies and Their Central Black Holes: Feedback from Momentum-driven Winds. 2005, *The Astrophysical Journal*, 618, 569, aDS Bibcode: 2005ApJ...618..569M
- Murray, N., Quataert, E., & Thompson, T. A., The Disruption of Giant Molecular Clouds by Radiation Pressure & the Efficiency of Star Formation in Galaxies. 2010, *The Astrophysical Journal*, 709, 191, aDS Bibcode: 2010ApJ...709..191M
- Myers, P. C., Dense cores in dark clouds. III. Subsonic turbulence. 1983, *The Astrophysical Journal*, 270, 105, aDS Bibcode: 1983ApJ...270..105M
- Myers, P. C., Filamentary Structure of Star-forming Complexes. 2009, *The Astrophysical Journal*, 700, 1609, aDS Bibcode: 2009ApJ...700.1609M
- Naab, T. & Ostriker, J. P., Theoretical Challenges in Galaxy Formation. 2017, *Annual Review of Astronomy and Astrophysics*, vol. 55, issue 1, pp. 59-109, 55, 59
- Nakamura, F. & Li, Z.-Y., Magnetically Regulated Star Formation in Three Dimensions: The Case of the Taurus Molecular Cloud Complex. 2008, *The Astrophysical Journal*, 687, 354, aDS Bibcode: 2008ApJ...687..354N
- Nakano, T., Nishi, R., & Umebayashi, T., Mechanism of Magnetic Flux Loss in Molecular Clouds. 2002, *The Astrophysical Journal*, 573, 199, aDS Bibcode: 2002ApJ...573..199N
- Nelson, R. P. & Langer, W. D., The Dynamics of Low-Mass Molecular Clouds in External Radiation Fields. 1997, *\apj*, 482, 796
- Nishi, R., Nakano, T., & Umebayashi, T., Magnetic Flux Loss from Interstellar Clouds with Various Grain-Size Distributions. 1991, *The Astrophysical Journal*, 368, 181, aDS Bibcode: 1991ApJ...368..181N
- Oort, J. H., Outline of a theory on the origin and acceleration of interstellar clouds and O associations. 1954, *Bulletin of the Astronomical Institutes of the Netherlands*, 12, 177, aDS Bibcode: 1954BAN....12..177O
- Ossenkopf-Okada, V. & Stepanov, R., Measuring the filamentary structure of interstellar clouds through wavelets. 2019, *Astronomy & Astrophysics*, Volume 621, id.A5, <NUMPAGES>36</NUMPAGES> pp., 621, A5
- Ostriker, J., The Equilibrium of Polytropic and Isothermal Cylinders. 1964, *The Astrophysical Journal*, 140, 1056, aDS Bibcode: 1964ApJ...140.1056O

- Padoan, P. & Nordlund, A., The Stellar Initial Mass Function from Turbulent Fragmentation. 2002, *The Astrophysical Journal*, 576, 870, aDS Bibcode: 2002ApJ...576..870P
- Padoan, P., Nordlund, A., & Jones, B. J. T., The universality of the stellar initial mass function. 1997, *Monthly Notices of the Royal Astronomical Society*, 288, 145, aDS Bibcode: 1997MNRAS.288..145P
- Padoan, P., Pan, L., Haugbølle, T., & Nordlund, A., Supernova Driving. I. The Origin of Molecular Cloud Turbulence. 2016, *The Astrophysical Journal*, 822, 11, aDS Bibcode: 2016ApJ...822...11P
- Padoan, P., Pan, L., Juvela, M., Haugbølle, T., & Nordlund, A., The Origin of Massive Stars: The Inertial-inflow Model. 2020, *The Astrophysical Journal*, 900, 82, aDS Bibcode: 2020ApJ...900...82P
- Palmeirim, P., André, P., Kirk, J., et al., Herschel view of the Taurus B211/3 filament and striations: evidence of filamentary growth? 2013, *Astronomy & Astrophysics*, Volume 550, id.A38, <NUMPAGES>9</NUMPAGES> pp., 550, A38
- Panopoulou, G. V., Psaradaki, I., Skalidis, R., Tassis, K., & Andrews, J. J., A closer look at the 'characteristic' width of molecular cloud filaments. 2017, *Monthly Notices of the Royal Astronomical Society*, 466, 2529, aDS Bibcode: 2017MNRAS.466.2529P
- Parker, E. N., The Dynamical State of the Interstellar Gas and Field. 1966, *The Astrophysical Journal*, 145, 811, aDS Bibcode: 1966ApJ...145..811P
- Planck Collaboration, P., Ade, P. a. R., Aghanim, N., et al., Planck intermediate results. XXXV. Probing the role of the magnetic field in the formation of structure in molecular clouds. 2016, *Astronomy and Astrophysics*, 586, A138
- Planck Collaboration, P., Aghanim, N., Akrami, Y., et al., Planck 2018 results. XII. Galactic astrophysics using polarized dust emission. 2020, *Astronomy and Astrophysics*, 641, A12
- Puls, J., Kudritzki, R.-P., Herrero, A., et al., O-star mass-loss and wind momentum rates in the Galaxy and the Magellanic Clouds Observations and theoretical predictions. 1996, *Astronomy and Astrophysics*, v.305, p.171, 305, 171
- Reynolds, R. J., The Column Density and Scale Height of Free Electrons in the Galactic Disk. 1989, *The Astrophysical Journal*, 339, L29, aDS Bibcode: 1989ApJ...339L..29R
- Reynolds, R. J., Scherb, F., & Roesler, F. L., Observations of Diffuse Galactic HA and [n II] Emission. 1973, *The Astrophysical Journal*, 185, 869, aDS Bibcode: 1973ApJ...185..869R
- Rivera-Ingraham, A., Ristorcelli, I., Juvela, M., et al., Galactic cold cores. VIII. Filament formation and evolution: Filament properties in context with evolutionary models. 2017, *Astronomy & Astrophysics*, Volume 601, id.A94, <NUMPAGES>9</NUMPAGES> pp., 601, A94
- Robitaille, T., Rice, T., Beaumont, C., et al., astrodendro: Astronomical data dendrogram creator. 2019, *Astrophysics Source Code Library*, ascl:1907.016, aDS Bibcode: 2019ascl.soft07016R

- Rolleston, W. R. J., Smartt, S. J., Dufton, P. L., & Ryans, R. S. I., The Hi Distribution of the Milky Way. 2009, *Annual Review of Astronomy and Astrophysics*, 47, 27
- Rosolowsky, E., The Mass Spectra of Giant Molecular Clouds in the Local Group. 2005, *Publications of the Astronomical Society of the Pacific*, 117, 1403, aDS Bibcode: 2005PASP..117.1403R
- Rosolowsky, E. W., Pineda, J. E., Foster, J. B., et al., An Ammonia Spectral Atlas of Dense Cores in Perseus. 2008a, *The Astrophysical Journal Supplement Series*, 175, 509, aDS Bibcode: 2008ApJS..175..509R
- Rosolowsky, E. W., Pineda, J. E., Kauffmann, J., & Goodman, A. A., Structural Analysis of Molecular Clouds: Dendrograms. 2008b, *apj*, 679, 1338, eprint: 0802.2944
- Rudolph, A. L., Fich, M., Bell, G. R., et al., Abundance Gradients in the Galaxy. 2006, *The Astrophysical Journal Supplement Series*, 162, 346, aDS Bibcode: 2006ApJS..162..346R
- Sales, L. V., Marinacci, F., Springel, V., & Petkova, M., Stellar feedback by radiation pressure and photoionization. 2014, *Monthly Notices of the Royal Astronomical Society*, 439, 2990, aDS Bibcode: 2014MNRAS.439.2990S
- Salpeter, E. E., The Luminosity Function and Stellar Evolution. 1955, *The Astrophysical Journal*, 121, 161, aDS Bibcode: 1955ApJ...121..161S
- Scalo, J., Perception of interstellar structure - Facing complexity. 1990, 162, 151, conference Name: Physical Processes in Fragmentation and Star Formation ADS Bibcode: 1990ASSL..162..151S
- Schneider, N., Csengeri, T., Klessen, R. S., et al., Understanding star formation in molecular clouds. II. Signatures of gravitational collapse of IRDCs. 2015, *Astronomy & Astrophysics*, Volume 578, id.A29, <NUMPAGES>17</NUMPAGES> pp., 578, A29
- Schuller, F., Csengeri, T., Urquhart, J. S., et al., SEDIGISM: Structure, excitation, and dynamics of the inner Galactic interstellar medium. 2017, *Astronomy & Astrophysics*, Volume 601, id.A124, <NUMPAGES>25</NUMPAGES> pp., 601, A124
- Schuller, F., Menten, K. M., Contreras, Y., et al., ATLASGAL - The APEX telescope large area survey of the galaxy at 870  $\mu\text{m}$ . 2009, *Astronomy and Astrophysics*, Volume 504, Issue 2, 2009, pp.415-427, 504, 415
- Scoville, N. Z. & Hersh, K., Collisional growth of giant molecular clouds. 1979, *The Astrophysical Journal*, 229, 578, aDS Bibcode: 1979ApJ...229..578S
- Seifried, D., Schmidt, W., & Niemeyer, J. C., Forced turbulence in thermally bistable gas: a parameter study. 2011, *Astronomy and Astrophysics*, Volume 526, id.A14, <NUMPAGES>13</NUMPAGES> pp., 526, A14
- Seifried, D., Walch, S., Girichidis, P., et al., SILCC-Zoom: the dynamic and chemical evolution of molecular clouds. 2017, *Monthly Notices of the Royal Astronomical Society*, 472, 4797

- Seifried, D., Walch, S., Reissl, S., & Ibáñez-Mejía, J. C., SILCC-Zoom: Polarization and depolarization in molecular clouds. 2019, *Monthly Notices of the Royal Astronomical Society*, 482, 2697, aDS Bibcode: 2019MNRAS.482.2697S
- Shadmehri, M., Vázquez-Semadeni, E., & Ballesteros-Paredes, J., Virial Theorem Analysis of 3D Numerical Simulations of MHD Self-Gravitating Turbulence. 2002, 276, 190, conference Name: Seeing Through the Dust: The Detection of HI and the Exploration of the ISM in Galaxies Place: eprint: arXiv:astro-ph/0111574 ADS Bibcode: 2002ASPC..276..190S
- Shimajiri, Y., André, P., Palmeirim, P., et al., Probing accretion of ambient cloud material into the Taurus B211/B213 filament. 2019, *Astronomy & Astrophysics*, Volume 623, id.A16, <NUMPAGES>16</NUMPAGES> pp., 623, A16
- Slyz, A. D., Devriendt, J. E. G., Bryan, G., & Silk, J., Towards simulating star formation in the interstellar medium. 2005, *Monthly Notices of the Royal Astronomical Society*, 356, 737, aDS Bibcode: 2005MNRAS.356..737S
- Smith, R. J., Glover, S. C. O., & Klessen, R. S., On the nature of star-forming filaments - I. Filament morphologies. 2014, *Monthly Notices of the Royal Astronomical Society*, 445, 2900, aDS Bibcode: 2014MNRAS.445.2900S
- Solomon, P. M., Rivolo, A. R., Barrett, J., & Yahil, A., Mass, Luminosity, and Line Width Relations of Galactic Molecular Clouds. 1987, *The Astrophysical Journal*, 319, 730, aDS Bibcode: 1987ApJ...319..730S
- Spitzer, L. 1978, *Physical processes in the interstellar medium*, publication Title: A Wiley-Interscience Publication ADS Bibcode: 1978ppim.book.....S
- Spitzer, Jr., L., *The Dynamics of the Interstellar Medium. III. Galactic Distribution.* 1942, *The Astrophysical Journal*, 95, 329
- Stahler, S. W. & Palla, F. 2004, *The Formation of Stars*, publication Title: The Formation of Stars ADS Bibcode: 2004fost.book.....S
- Stodólkiewicz, J. S., On the Gravitational Instability of Some Magneto-Hydrodynamical Systems of Astrophysical Interest. Part III. 1963, *Acta Astronomica*, 13, 30, aDS Bibcode: 1963AcA....13...30S
- Stone, J. M., Ostriker, E. C., & Gammie, C. F., Dissipation in Compressible Magnetohydrodynamic Turbulence. 1998, *The Astrophysical Journal*, 508, L99, aDS Bibcode: 1998ApJ...508L..99S
- Strömgren, B., *The Physical State of Interstellar Hydrogen.* 1939, *The Astrophysical Journal*, 89, 526, aDS Bibcode: 1939ApJ....89..526S
- Suri, S., Sánchez-Monge, A., Schilke, P., et al., The CARMA-NRO Orion Survey. Filamentary structure as seen in C<sup>18</sup>O emission. 2019, *Astronomy & Astrophysics*, Volume 623, id.A142, <NUMPAGES>18</NUMPAGES> pp., 623, A142
- Swiggum, C., D'Onghia, E., Alves, J., et al., Evidence for Radial Expansion at the Core of the Orion Complex with Gaia EDR3. 2021, *The Astrophysical Journal*, 917, 21, aDS Bibcode: 2021ApJ...917...21S
- Tan, J. C., Krumholz, M. R., & McKee, C. F., *Equilibrium Star Cluster Formation.* 2006, *The Astrophysical Journal*, 641, L121, aDS Bibcode: 2006ApJ...641L.121T

- Tassis, K., Dowell, C. D., Hildebrand, R. H., Kirby, L., & Vaillancourt, J. E., Statistical Assessment of Shapes and Magnetic Field Orientations in Molecular Clouds through Polarization Observations. 2009, *Monthly Notices of the Royal Astronomical Society*, 399, 1681, aDS Bibcode: 2009MNRAS.399.1681T
- Tegmark, M., Silk, J., Rees, M. J., et al., How Small Were the First Cosmological Objects? 1997, *The Astrophysical Journal*, 474, 1, aDS Bibcode: 1997ApJ...474....1T
- Tielens, A. G. G. M. 2005, *The Physics and Chemistry of the Interstellar Medium*, publication Title: *The Physics and Chemistry of the Interstellar Medium* ADS Bibcode: 2005pcim.book.....T
- Troland, T. H. & Crutcher, R. M., Magnetic Fields in Dark Cloud Cores: Arecibo OH Zeeman Observations. 2008, *The Astrophysical Journal*, 680, 457, aDS Bibcode: 2008ApJ...680..457T
- Troland, T. H. & Heiles, C., Interstellar Magnetic Field Strengths and Gas Densities: Observational and Theoretical Perspectives. 1986, *The Astrophysical Journal*, 301, 339, aDS Bibcode: 1986ApJ...301..339T
- Truelove, J. K., Klein, R. I., McKee, C. F., et al., The Jeans Condition: A New Constraint on Spatial Resolution in Simulations of Isothermal Self-gravitational Hydrodynamics. 1997, *ApJ*, 489, L179+
- Vázquez-Semadeni, E., Colín, P., Gómez, G. C., Ballesteros-Paredes, J., & Watson, A. W., Molecular Cloud Evolution. III. Accretion Versus Stellar Feedback. 2010, *The Astrophysical Journal*, 715, 1302, aDS Bibcode: 2010ApJ...715.1302V
- Vázquez-Semadeni, E., González-Samaniego, A., & Colín, P., Hierarchical star cluster assembly in globally collapsing molecular clouds. 2017, *Monthly Notices of the Royal Astronomical Society*, 467, 1313, aDS Bibcode: 2017MNRAS.467.1313V
- Vázquez-Semadeni, E., Gómez, G. C., Jappsen, A. K., et al., Molecular Cloud Evolution. II. From Cloud Formation to the Early Stages of Star Formation in Decaying Conditions. 2007, *The Astrophysical Journal*, 657, 870, aDS Bibcode: 2007ApJ...657..870V
- Vázquez-Semadeni, E., Gómez, G. C., Jappsen, A. K., Ballesteros-Paredes, J., & Klessen, R. S., High- and Low-Mass Star-Forming Regions from Hierarchical Gravitational Fragmentation. High Local Star Formation Rates with Low Global Efficiencies. 2009, *The Astrophysical Journal*, 707, 1023, aDS Bibcode: 2009ApJ...707.1023V
- Vázquez-Semadeni, E., Palau, A., Ballesteros-Paredes, J., Gómez, G. C., & Zamora-Avilés, M., Global hierarchical collapse in molecular clouds. Towards a comprehensive scenario. 2019, *Monthly Notices of the Royal Astronomical Society*, 490, 3061, aDS Bibcode: 2019MNRAS.490.3061V
- Waagan, K., A positive MUSCL-Hancock scheme for ideal magnetohydrodynamics. 2009, *Journal of Computational Physics*, 228, 8609
- Waagan, K., Federrath, C., & Klingenberg, C., A robust numerical scheme for highly compressible magnetohydrodynamics: Nonlinear stability, implementation and tests. 2011, *Journal of Computational Physics*, 230, 3331, [\\_eprint: 1101.3007](#)



- Wada, K., Meurer, G., & Norman, C. A., Gravity-driven Turbulence in Galactic Disks. 2002, *The Astrophysical Journal*, 577, 197, aDS Bibcode: 2002ApJ...577..197W
- Walch, S., Girichidis, P., Naab, T., et al., The SILCC (SIMulating the LifeCYcle of molecular Clouds) project - I. Chemical evolution of the supernova-driven ISM. 2015, *\mnras*, 454, 238, *\_eprint*: 1412.2749
- Wardle, M., Star Formation and the Hall Effect. 2004, *Astrophysics and Space Science*, 292, 317
- Weingartner, J. C. & Draine, B. T., Dust Grain-Size Distributions and Extinction in the Milky Way, Large Magellanic Cloud, and Small Magellanic Cloud. 2001, *The Astrophysical Journal*, 548, 296, aDS Bibcode: 2001ApJ...548..296W
- Wolfire, M. G., Hollenbach, D., & McKee, C. F., The Dark Molecular Gas. 2010, *The Astrophysical Journal*, 716, 1191, aDS Bibcode: 2010ApJ...716.1191W
- Wolfire, M. G., Hollenbach, D., McKee, C. F., Tielens, A. G. G. M., & Bakes, E. L. O., The Neutral Atomic Phases of the Interstellar Medium. 1995, *The Astrophysical Journal*, 443, 152, aDS Bibcode: 1995ApJ...443..152W
- Wolfire, M. G., McKee, C. F., Hollenbach, D., & Tielens, A. G. G. M., Neutral Atomic Phases of the Interstellar Medium in the Galaxy. 2003, *The Astrophysical Journal*, 587, 278, aDS Bibcode: 2003ApJ...587..278W
- Wünsch, R., Walch, S., Dinnbier, F., & Whitworth, A., Tree-based solvers for adaptive mesh refinement code FLASH - I: gravity and optical depths. 2018, *Monthly Notices of the Royal Astronomical Society*, 475, 3393
- Zuckerman, B. & Evans, II, N. J., Models of Massive Molecular Clouds. 1974, *The Astrophysical Journal*, 192, L149, aDS Bibcode: 1974ApJ...192L.149Z
- Zuckerman, B. & Palmer, P., Radio radiation from interstellar molecules. 1974, *Annual Review of Astronomy and Astrophysics*, 12, 279

#### DATA AVAILABILITY

The data underlying this thesis will be shared on reasonable request to the supervisor.

## ACKNOWLEDGEMENTS

I would like to thank my supervisor, Prof. Stefanie Walch-Gassner for her scientific support and encouragement. I would also like to extend my thanks to my second supervisor, Prof. Peter Schilke and the head of my thesis committee Prof. Susanne Crewell for agreeing to supervise this work. I have always received help and sound advice from my TAC members, Dr. Volker Ossenkopf-Okada, and Dr. Alvaro Sacherz-Monge, and for that I am truly grateful.

For new ideas related to work, I am greatly indebted to Seamus and Daniel, who have always found the time to discuss ideas and complications with me. I would also like to thank Marco, Stefano, Agniva, Katya, Seamus, Alvaro, and Kaustav for proof-reading the thesis, as well as suggesting helpful scientific and organizational ideas.

Special thanks go to Giulia, Persis, Annika, Alvaro, Nassim, Szymon, Jigisha, and Birka, who were always there with a helpful word of encouragement or the time for a coffee whenever needed; and to Paul whom I could always turn to for questions related to the bureaucracy of the thesis. I thank all my friends who have given me the mental fortitude for the times that have been difficult.

I would like to thank my parents, Gautam and Shampa for their unwavering belief and support in me. And finally, I would like to thank Urmimala, without whose love, support, and patience, this effort would hardly have been possible.

This work, and the past three years have been difficult in many regards. I am grateful to everyone who supported me in some way through this step, even if I could not always return it. I am also thankful to myself for always trying to do the best I could in my limited capacity throughout the last three years.

## SELBSTSTÄNDIGKEITSERKLÄRUNG

Hiermit versichere ich an Eides statt, dass ich die vorliegende Dissertation selbstständig und ohne die Benutzung anderer als der angegebenen Hilfsmittel und Literatur angefertigt habe. Alle Stellen, die wörtlich oder sinngemäß aus veröffentlichten und nicht veröffentlichten Werken dem Wortlaut oder dem Sinn nach entnommen wurden, sind als solche kenntlich gemacht. Ich versichere an Eides statt, dass diese Dissertation noch keiner anderen Fakultät oder Universität zur Prüfung vorgelegen hat; dass sie - abgesehen von unten angegebenen Teilpublikationen und eingebundenen Artikeln und Manuskripten - noch nicht veröffentlicht worden ist sowie, dass ich eine Veröffentlichung der Dissertation vor Abschluss der Promotion nicht ohne Genehmigung des Promotionsausschusses vornehmen werde. Die Bestimmungen dieser Ordnung sind mir bekannt. Darüber hinaus erkläre ich hiermit, dass ich die Ordnung zur Sicherung guter wissenschaftlicher Praxis und zum Umgang mit wissenschaftlichem Fehlverhalten der Universität zu Köln gelesen und sie bei der Durchführung der Dissertation zugrundeliegenden Arbeiten und der schriftlich verfassten Dissertation beachtet habe und verpflichte mich hiermit, die dort genannten Vorgaben bei allen wissenschaftlichen Tätigkeiten zu beachten und umzusetzen. Ich versichere, dass die eingereichte elektronische Fassung der eingereichten Druckfassung vollständig entspricht."

Teilpublikationen:

- *SILCC-Zoom: the dynamic balance in molecular cloud substructures* (Ganguly et al., in prep., 2022)
- *Unravelling the structure of magnetized molecular clouds with SILCC-Zoom: sheets, filaments and fragmentation* (Ganguly et al., in prep., 2022)

Köln, den 03.04.2022



(Shashwata Ganguly)



# Shashwata Ganguly

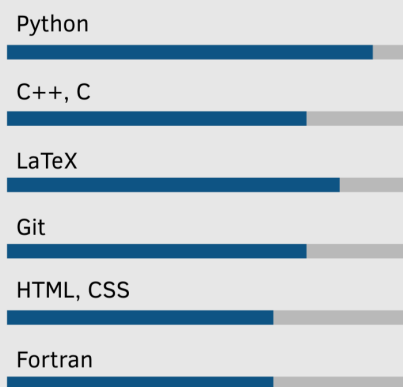
Doctoral researcher

- 1 December, 1995
- Cologne, Germany
- +49 15774038117
- sasata95@gmail.com

## About me

I am a finishing PhD student, with 6 years of experience in working with programming and big data in academic research. I am hard working, friendly, and always willing to take on new challenges. I take great joy in working in a team and helping others, but am also comfortable in handling individual responsibilities as a result of my academic training.

## Technical skills



## Soft skills

- public speaking+9
- social skills+8
- leadership+7
- adaptability+8
- problem solving+7

(\*)[The skill scale is from 0 (Fundamental Awareness) to 10 (Expert).]

## Professional interests

Programming, problem solving, research, communication, conflict management.

## Education

- since 2019 Ph.D. candidate in Computational Astrophysics University of Cologne  
*Deep zoom simulations of molecular clouds.*
- 2016-2019 M.Sc. summa cum laude University of Cologne  
Physics major, specialization in computational Astrophysics
- 2013-2016 B.Sc. gold medalist Presidency University  
Physics major
- 2011-2013 High school  
11th in board exams among 700,000 students

## Key projects

- 2021-2022 The effect of magnetic fields on molecular clouds Ph.D. project  
I was the principal investigator in trying to use different python tools to look in-depth into how astronomical clouds collapse to form stars.
- 2020 N-body code to simulate the solar system Teaching project  
I wrote a python code to simulate N-body systems such as the solar system as part of teaching. Find this and other such small codes here.
- 2018-2019 Implementation of meshless finite scheme Masters thesis  
I implemented a new computational scheme to compute astronomical fluid dynamical problems using C++.

## Publications

- 2022 SILCC-Zoom: the dynamic balance in molecular cloud substructures (Ganguly et al., in prep., 2022)
- 2022 Unravelling the structure of magnetized molecular clouds with SILCC-Zoom: sheets, filaments and fragmentation (Ganguly et al., in prep., 2022)

## Awards and fellowships

- 2016 BCGS honors branch fellowship
- 2016 Gold medalist for securing highest marks in Bachelors
- 2016 4th in all India Joint Entrance Screening Test (JEST)
- 2016 11th in all India Joint Admission test for Masters (JAM)
- 2015 Indian Academy of Sciences summer fellow
- 2013 DST inspire fellow for being top 1% at higher secondary level

## Internships and workshops

- 2021 Presenter, conference, Midwest magnetic fields conference
- 2020 Presenter, conference, German Astronomical Society
- 2020 Participant, workshop, deep learning for language analysis
- 2019 Participant, workshop, skills for project leaders/managers
- 2018 Participant, summer school, Cosmology school Krakow
- 2015 Summer intern, Indian Institute of Astrophysics

## Other information

### Organisational

- 2020 Elected president of SFB Students' Council
- 2020 Organiser of Astronomy on Tap, Cologne
- 2018 Principal organiser of a small book club in Cologne

### Public relations

- 2020 Public talk at Presidency University, "A star is born: the life cycle of molecular clouds"